

# Arbeitsbericht NAB 16-24

**Thermo-Hydro-Mechanical  
Postmortem Analysis of bentonite  
performed at CIEMAT**

September 2018

M. V. Villar, R. J. Iglesias, C. Gutiérrez-Álvarez,  
B. Carbonell, R. Campos, G. Campos,  
P. L. Martín & B. Castro

**National Cooperative  
for the Disposal of  
Radioactive Waste**

Hardstrasse 73  
P.O. Box 280  
5430 Wettingen  
Switzerland  
Tel. +41 56 437 11 11  
[www.nagra.ch](http://www.nagra.ch)



# Arbeitsbericht NAB 16-24

## Thermo-Hydro-Mechanical Postmortem Analysis of bentonite performed at CIEMAT

September 2018

M. V. Villar, R. J. Iglesias, C. Gutiérrez-Álvarez,  
B. Carbonell, R. Campos, G. Campos,  
P. L. Martín & B. Castro

### KEYWORDS

FEDEX-DP, bentonite properties, THM analysis,  
buffer performance

**National Cooperative  
for the Disposal of  
Radioactive Waste**

Hardstrasse 73  
P.O. Box 280  
5430 Wettingen  
Switzerland  
Tel. +41 56 437 11 11  
[www.nagra.ch](http://www.nagra.ch)

Nagra Arbeitsberichte ("Working Reports") present the results of work in progress that have not necessarily been subject to a comprehensive review. They are intended to provide rapid dissemination of current information.

This report was prepared on behalf of Nagra. The viewpoints presented and conclusions reached are those of the author(s) and do not necessarily represent those of Nagra.

"Copyright © 2019 by Nagra, Wettingen (Switzerland) / All rights reserved.

All parts of this work are protected by copyright. Any utilisation outwith the remit of the copyright law is unlawful and liable to prosecution. This applies in particular to translations, storage and processing in electronic systems and programs, microfilms, reproductions, etc."

## Table of Contents

<b>Table of Contents</b> .....	<b>I</b>
<b>List of Tables</b> .....	<b>II</b>
<b>List of Figures</b> .....	<b>IV</b>
<b>1 Introduction</b> .....	<b>1</b>
<b>2 Dismantling of the barrier and bentonite sampling</b> .....	<b>7</b>
<b>3 Methodology</b> .....	<b>17</b>
3.1 Basic properties .....	19
3.1.1 Thermal conductivity .....	19
3.1.2 Suction measurement .....	21
3.1.3 Water content and dry density .....	22
3.1.4 Specific weight of solid particles .....	24
3.1.5 Measurement of basal spacing .....	24
3.1.6 Pore size distribution .....	25
3.1.7 Specific surface area .....	26
3.2 Hydraulic properties .....	26
3.2.1 Water retention curves .....	26
3.2.2 Hydraulic conductivity .....	28
3.2.3 Gas permeability .....	30
3.3 Mechanical properties .....	36
3.3.1 Swelling under load tests .....	36
3.3.2 Swelling pressure .....	37
3.3.3 Swelling pressure and permeability tests .....	37
3.3.4 Consolidation tests .....	39
<b>4 Results</b> .....	<b>43</b>
4.1 Calculating the degree of saturation .....	43
4.2 Basic properties .....	43
4.2.1 Water content and dry density .....	48
4.2.2 Specific weight of solid particles .....	54
4.2.3 Suction measurement .....	54
4.2.4 Interlayer space .....	57
4.2.5 Pore size distribution .....	61
4.2.6 Specific surface area .....	71
4.3 Thermal conductivity .....	73
4.4 Hydraulic properties .....	75
4.4.1 Water retention curve .....	75
4.4.2 Hydraulic conductivity .....	86
4.4.3 Gas permeability .....	95

4.4.3.1	Low-pressure equipment (LP) .....	98
4.4.3.2	High-pressure equipment.....	101
4.4.3.3	Summary and discussion .....	106
4.5	Mechanical properties.....	120
4.5.1	Swelling deformation tests .....	120
4.5.2	Swelling pressure (and hydraulic conductivity) .....	133
4.5.3	Volume change behaviour on loading .....	137
<b>5</b>	<b>Summary and discussion.....</b>	<b>155</b>
5.1	Physical state and microstructure .....	156
5.2	Thermo-hydro-mechanical properties.....	157
5.2.1	Thermal properties.....	158
5.2.2	Hydraulic properties .....	158
5.2.3	Mechanical properties.....	160
5.3	Conclusion.....	161
<b>6</b>	<b>Acknowledgements .....</b>	<b>163</b>
<b>7</b>	<b>References.....</b>	<b>165</b>

## List of Tables

Tab. 1:	Dimensions of the blocks shown in Fig. 3 (Fuentes-Cantillana & García-Siñeriz 1998).....	3
Tab. 2:	Temperatures (°C) measured in the bentonite barrier before dismantling (1: 2002, Bárcena et al. 2006; 2: 2015, Martínez et al. 2016).....	5
Tab. 3:	Samples received by CIEMAT from the FEBEX-DP dismantling for THM analyses.....	9
Tab. 4:	Summary of blocks sampled at CIEMAT for THM and THG determinations .....	12
Tab. 5:	Summary of cores used at CIEMAT for gas permeability determinations.....	14
Tab. 6:	Characteristics of the experimental setups used for the gas permeability tests .....	31
Tab. 7:	Summary of properties determined in the blocks sampled in sections S36, S44 and S47 .....	44
Tab. 8:	Summary of properties determined in the blocks sampled in sections S53, S57 and S59 .....	46
Tab. 9:	Pore size distribution obtained with MIP of samples from section S36 ( <i>n</i> : porosity, <i>e</i> : void ratio).....	64
Tab. 10:	Pore size distribution obtained with MIP of samples from section S47 ( <i>n</i> : porosity, <i>e</i> : void ratio).....	65
Tab. 11:	Pore size distribution obtained with MIP of samples from section S53 ( <i>n</i> : porosity, <i>e</i> : void ratio).....	66

Tab. 12:	Pore size distribution obtained with MIP of samples from section S59 (n: porosity, e: void ratio).....	67
Tab. 13:	Results of the water retention curves with samples from section S47.....	76
Tab. 14:	Results of the water retention curves with samples from section S53.....	78
Tab. 15:	Results of the water retention curves with samples from section S59.....	79
Tab. 16:	Results of the hydraulic conductivity measurements of the samples in Fig. 81 .....	89
Tab. 17:	Results of the hydraulic conductivity determinations performed in samples from section S47 .....	91
Tab. 18:	Results of the hydraulic conductivity determinations performed in samples from section S53 .....	92
Tab. 19:	Characteristics of the bentonite samples used for gas permeability tests .....	96
Tab. 20:	Results of the gas permeability tests performed in the low-pressure setup .....	99
Tab. 21:	Range of pressures applied with the high-pressure equipment.....	101
Tab. 22:	Results of the gas permeability tests in core samples from section S44.....	107
Tab. 23:	Results of the gas permeability tests in core samples from section S47.....	109
Tab. 24:	Results of the gas permeability tests in core samples from section S36 and drilled samples from section S53.....	110
Tab. 25:	Results of the swelling under load tests with samples of section S36.....	122
Tab. 26:	Results of the swelling under load tests with samples of section S47.....	122
Tab. 27:	Results of the swelling under load tests with samples of section S53.....	122
Tab. 28:	Results of the swelling under load tests with samples of section S36 in contact with shotcrete .....	128
Tab. 29:	Results of the swelling under load tests with oxidised samples of sections S36 and S59 .....	128
Tab. 30:	Results of the swelling pressure tests .....	133
Tab. 31:	Results of the hydraulic conductivity tests in the high-pressure oedometer.....	136
Tab. 32:	Initial conditions of the samples used in the oedometer tests.....	138
Tab. 33:	Results of the oedometer tests in sample BB-47-7-2 (external ring), performed under suction 4 MPa (test ended by clay extrusion and specimen damage) .....	139
Tab. 34:	Results of the oedometer tests in sample BB-47-4-1 (external ring), performed under a suction pressure of 4 MPa.....	139
Tab. 35:	Results of the oedometer tests in sample BB-47-4-2 (external ring), performed under a suction pressure of 2 MPa.....	140
Tab. 36:	Results of the oedometer tests in sample BB-47-8-2 (middle ring), performed under a suction pressure of 21 MPa.....	140
Tab. 37:	Results of the oedometer tests in sample BB-47-9-1(internal ring), performed under a suction pressure of 28 MPa .....	141
Tab. 38:	Results of the oedometer tests in sample BB-47-9-2 (internal ring), performed under a suction pressure of 33 MPa .....	141

Tab. 39:	Apparent preconsolidation stress ( $\sigma_v^*$ ), pre-yield ( $\kappa$ ) and post-yield ( $\lambda$ ) compressibility determined from the oedometer tests under constant suction for untreated and retrieved samples.....	150
Tab. 40:	Pore size distribution obtained by MIP and basal spacing after the consolidation tests.....	151

## List of Figures

Fig. 1:	General layout of the in-situ test during phase I, including instrumented sections (ENRESA 2000) .....	2
Fig. 2:	Geometry of the clay barrier in the FEBEX in-situ test at GTS (ENRESA 2000).....	2
Fig. 3:	Geometry of the different kinds of blocks (Fuentes-Cantillana & García-Siñeriz 1998).....	3
Fig. 4:	General layout of the in-situ test during phase II, including instrumented sections (ENRESA 2006) .....	4
Fig. 5:	Appearance of the bentonite barrier after extraction of heater #1 in 2005 and of heater #2 in 2015 .....	7
Fig. 6:	Water content distribution in a vertical longitudinal section (Villar et al. 2016a).....	8
Fig. 7:	Dry density distribution in a vertical longitudinal section (Villar et al. 2016a) .....	8
Fig. 8:	Degree of saturation distribution in a vertical longitudinal section (Villar et al. 2016a) (inexact values because of solid specific weight and water density uncertainties) .....	8
Fig. 9:	Distribution of sampling sections for THM-THG and interfaces studies of CIEMAT (modified from Bárcena & García-Siñeriz 2015).....	10
Fig. 10:	Position of blocks received at CIEMAT for THM and THG tests in sampling sections S36, S47, S53 and S59 (the position of blocks BB-36-7 and BB-36-9 is interchanged) (Bárcena & García-Siñeriz 2015).....	11
Fig. 11:	References for the radii along which the blocks were taken .....	14
Fig. 12:	RH-controlled room for the storage of samples.....	15
Fig. 13:	Relative humidity and temperature in the storage room.....	15
Fig. 14:	Measurement of thermal conductivity, relative humidity and moisture before sampling the blocks .....	17
Fig. 15:	Sectioning of blocks for THM and THG determinations .....	18
Fig. 16:	Drilling of a block to obtain subsamples 1 (closest to the granite) and 2 (closest to the gallery axis) for HM determinations .....	18
Fig. 17:	Sectioning of the THM part of a block before packaging and final storage.....	19
Fig. 18:	Kemtherm QTM-D3 conductivity meter with probe and standard plates .....	19
Fig. 19:	Schematic representation of the psychrometers.....	21

Fig. 20:	Psychrometers inserted into a block prior to unpacking.....	22
Fig. 21:	Location in the blocks of sampling positions for water content and dry density (and most of the other determinations) .....	23
Fig. 22:	Determination of sample volume by immersion in mercury .....	23
Fig. 23:	Equipment used for the determination of N <sub>2</sub> sorption isotherms (Micromeritics ASAP 2020).....	26
Fig. 24:	Schematic representation of the constant volume cell for WRC determination (left) and desiccator with perforated cells inside (right).....	27
Fig. 25:	Schematic representation of the setup for permeability measurement of expansive soils (using an oil/water pump to apply injection pressure and a pressure/volume controller for backpressure application and outflow measurement).....	28
Fig. 26:	Drilling of cores to obtain samples for the hydraulic conductivity tests .....	29
Fig. 27:	Appearance of the samples drilled from the blocks inside the permeability cell rings .....	29
Fig. 28:	Sample drilled on site at the contact between blocks (left) and in the laboratory (right).....	31
Fig. 29:	Sample preparation: adjusting the diameter.....	32
Fig. 30:	Appearance of a specimen prepared for gas test with interface between blocks.....	32
Fig. 31:	Schematic representation of the low-pressure gas permeability system.....	33
Fig. 32:	Experimental setup of the high confining pressure line (HCP) (CF: coalescing filter, FPC: forward-pressure controller, BPC: back-pressure controller, MFM: mass flow meter).....	35
Fig. 33:	Schematic cross-section of an oedometric cell (left) and daily measurement of electrical conductivity of the water in the cell (right) .....	36
Fig. 34:	Appearance of the base and the upper part of a sample inserted in the oedometer ring.....	37
Fig. 35:	Schematic layout and picture of the high-pressure oedometric equipment .....	39
Fig. 36:	Schematic cross-section of an oedometric cell with vessel for solutions .....	40
Fig. 37:	Suction-controlled oedometer cells installed in the frames to perform high pressure consolidation tests .....	40
Fig. 38:	Preparation of samples for the consolidation tests.....	41
Fig. 39:	Water content and dry density measured in the laboratory in blocks taken from section S36 (the sampling radii are indicated in the legend according to Fig. 11).....	49
Fig. 40:	Water content and dry density measured in the laboratory in blocks taken from section S47 (the sampling radii are indicated in the legend according to Fig. 11).....	49
Fig. 41:	Water content and dry density measured in the laboratory in blocks taken from section S53 (the sampling radii are indicated in the legend according to Fig. 11).....	49

Fig. 42:	Water content and dry density measured in the laboratory in blocks taken from section S59 (the sampling radii are indicated in the legend according to Fig. 11).....	50
Fig. 43:	Relationship between the water content determined in subsamples 1 and 2 of the blocks in the laboratory as a function of the time since their retrieval at GTS (filled symbols, sections S47 and S53). The values for time 0 correspond to the average value for this relationship obtained in the blocks of nearby sections analysed on site (S45-S49 and S52) .....	51
Fig. 44:	Comparison of water content and dry density measured in close-by sections S36 (CIEMAT's lab, filled symbols and small crosses) and S37 (on site). The sampling radii are indicated in the legend according to Fig. 11 .....	52
Fig. 45:	Comparison of water content and dry density measured in close-by sections S47 (CIEMAT's lab, filled symbols and small crosses) and S49 (on site) . The sampling radii are indicated in the legend according to Fig. 11 .....	52
Fig. 46:	Comparison of water content and dry density measured in close-by sections S59 (CIEMAT's lab, filled symbols and small crosses) and S58 (on site) . The sampling radii are indicated in the legend according to Fig. 11 .....	53
Fig. 47:	Microwave measurement of the moisture of blocks .....	53
Fig. 48:	Specific weight of solid particles determined in samples from different sampling sections.....	54
Fig. 49:	Total suction values measured in blocks from different sampling sections at CIEMAT's laboratory.....	55
Fig. 50:	Relationship between suction and water content and suction and degree of saturation in the blocks sampled at CIEMAT's laboratory .....	56
Fig. 51:	Relationship between suction values measured and water content and degree of saturation in the blocks sampled at CIEMAT's laboratory (range of dry density indicated in $\text{g/cm}^3$ ) .....	56
Fig. 52:	Basal spacing of the smectite in FEBEX-DP samples of different sections as a function of the distance to the axis .....	58
Fig. 53:	Basal spacing of the smectite in FEBEX-DP samples of different sections as a function of water content (the figure on the right is an enlargement).....	58
Fig. 54:	Profile fitting of the XRD pattern of samples from radius B in section S47 (Gutiérrez-Nebot 2016a). The distance to the axis of the gallery is indicated in parentheses .....	60
Fig. 55:	Relation between the intensities of the main and secondary reflections of the basal spacing for samples of different sections .....	60
Fig. 56:	Basal spacings of FEBEX samples saturated in different ways with deionised water (Villar et al. 2012, 2016b) and of samples from the FEBEX-DP .....	61
Fig. 57:	Pore size distribution of samples from radius B-C in section S36 .....	62
Fig. 58:	Pore size distribution of samples from radius E-F in section S47 .....	63
Fig. 59:	Pore size distribution of samples from radius E-F in section S53 .....	63
Fig. 60:	Pore size distribution of samples from radius D in section S59 .....	64

Fig. 61:	Comparison of the porosity determined by MIP and calculated from the dry density and specific weight in Tab. 7 and Tab. 8 for different sampling sections .....	69
Fig. 62:	Void ratio along three radii of section S36 (the solid and dotted thick horizontal lines indicate the values of pores larger and smaller than 50 nm, respectively, for the reference FEBEX compacted at 1.6 g/cm <sup>3</sup> with 14% water content) .....	70
Fig. 63:	Void ratio along three radii of section S47 (the solid and dotted thick horizontal lines indicate the values of pores larger and smaller than 50 nm, respectively, for the reference FEBEX compacted at 1.6 g/cm <sup>3</sup> with 14% water content) .....	70
Fig. 64:	Void ratio along three radii of section S53 (the solid and dotted thick horizontal lines indicate the values of pores larger and smaller than 50 nm, respectively, for the reference FEBEX compacted at 1.6 g/cm <sup>3</sup> with 14% water content) .....	71
Fig. 65:	Void ratio along three radii of section S59 (the solid and dotted thick horizontal lines indicate the values of pores larger and smaller than 50 nm, respectively, for the reference FEBEX compacted at 1.6 g/cm <sup>3</sup> with 14% water content) .....	71
Fig. 66:	BET specific surface area of samples taken along a radius from different sections (the dotted line indicates the value for the reference FEBEX bentonite) .....	72
Fig. 67:	BET specific surface area of the reference FEBEX and of samples taken along a radius from different sections as a function of their water content at the time of dismantling .....	72
Fig. 68:	Thermal conductivity measured on blocks taken from different sampling sections .....	73
Fig. 69:	Thermal conductivity measured for different sections as a function of degree of saturation .....	74
Fig. 70:	Dependence of thermal conductivity measured in blocks on water content and dry density (symbols) and empirical relationships for FEBEX reference bentonite (lines) .....	74
Fig. 71:	Location of samples used for water retention curve determination .....	76
Fig. 72:	Water retention curves determined for samples of section S47. The highest suction value for each sample (largest symbols) is that measured in the block from which it was trimmed and reported in Tab. 7 .....	81
Fig. 73:	Water retention curves determined for samples of section S53. The highest suction value for each sample (largest symbols) is that measured in the block from which it was trimmed and reported in Tab. 8 .....	81
Fig. 74:	Water retention curves determined for samples of section S59. The highest suction value for each sample (largest symbols) is that measured in the block from which it was trimmed and reported in Tab. 8 .....	82
Fig. 75:	Water retention curves of samples located at 57 cm from the gallery axis in sections S47 and S53 .....	83

Fig. 76:	Water retention curves of samples located at 67 cm from the gallery axis in sections S47 and S53 and 5 cm from the gallery axis in section S59.....	83
Fig. 77:	Water retention curves obtained by measuring the suction pressure of blocks with different water content values (subchapter 4.2.3, filled symbols) and obtained in cells (this subchapter, empty symbols) .....	84
Fig. 78:	Water retention curves obtained in cells for the reference bentonite compacted at different dry densities (filled symbols) and for the FEBEX-DP samples (this report, empty symbols) .....	85
Fig. 79:	Location of samples used for hydraulic conductivity tests.....	86
Fig. 80:	Comparison of the dry density measured in adjacent samples in the same block and the dry density of the samples trimmed for permeability tests.....	87
Fig. 81:	Water intake during saturation of samples from sections S47 and S53.....	87
Fig. 82:	Water outflow during the permeability tests of two samples. The hydraulic gradients applied are indicated in the legends (m/m) .....	88
Fig. 83:	Hydraulic conductivity of samples from section S47 as a function of the hydraulic gradient applied .....	89
Fig. 84:	Hydraulic conductivity of samples from section S53 as a function of the hydraulic gradient applied .....	90
Fig. 85:	Hydraulic conductivity of samples from section S47 and S53 taken along different radii (the dry density of the specimens is indicated in $\text{g/cm}^3$ ) .....	93
Fig. 86:	Hydraulic conductivity of samples from different sections and radii (indicated in the legend) and empirical correlation for untreated FEBEX bentonite obtained with Eq. 10 (solid line, the dashed lines indicate the expected range of variation, 30%) .....	94
Fig. 87:	Comparison between the hydraulic conductivity measured and that corresponding to samples of the reference bentonite of the same dry density obtained with Eq. 10. The distance to the gallery axis of each sample is indicated in cm.....	95
Fig. 88:	Location of the samples tested for gas permeability (the actual position of the cores differs in some cases from the one in the Sampling Book (Bárcena & García-Siñeriz 2015). Samples from section S53 were drilled in the laboratory.....	97
Fig. 89:	Pressure decrease in the gas tank during testing of two samples of section S44 taken at ~61 cm from the gallery axis (sample BC-44-2 with an interface) under two different confining pressures .....	98
Fig. 90:	Effective permeability values obtained in the low-pressure equipment as a function of the position in the barrier. The arrows point to samples with interface .....	100
Fig. 91:	Effective permeability values obtained in the low-pressure equipment as a function of the degree of saturation. The arrows point to samples with interface .....	100
Fig. 92:	Interface in a sample from the external ring (indicated by an arrow, BC-44-6) and from the inner ring (BC-44-2) .....	101
Fig. 93:	Pressure path followed in the LCP setup for sample BC-44-4 .....	103

Fig. 94:	Evolution of gas effective permeability at constant confining pressure (left) and constant injection pressure (right) for sample BC-44-4 (the duration of longer steps is indicated in hours) .....	103
Fig. 95:	Pressure path followed in the HP-US setup for sample BC-47-4.....	104
Fig. 96:	Evolution of confining pressure and of pressure on the upstream and downstream vessels during test BC-47-4.....	105
Fig. 97:	Evolution of gas effective permeability ( $k_{ig} \cdot k_{rg}$ ) for sample BC-47-4 as a function of confining pressure .....	105
Fig. 98:	Evolution of gas permeability at constant confining pressure for sample BC-47-4 (the duration of longer steps is indicated in hours) .....	106
Fig. 99:	Initial and final appearance of sample BC-47-4 (the arrows indicate the same position before and after testing) .....	106
Fig. 100:	Effective gas permeability measured at constant confining pressure of 0.6 MPa in the HP setup. The sample reference, dry density, water content and degree of saturation are indicated in the legend .....	112
Fig. 101:	Effective gas permeability measured at constant confining pressure of 1 MPa in the HP setup. The sample reference, dry density, water content and degree of saturation are indicated in the legend .....	113
Fig. 102:	Change of effective permeability with increasing confining pressure in samples of section S44 (the values are the average of all steps in which confining pressure was the same, irrespective of the injection pressure) .....	114
Fig. 103:	Change of effective permeability with increasing confining pressure in samples of section S47 (the values are the average of all steps in which confining pressure was the same, irrespective of the injection pressure) .....	114
Fig. 104:	Change of effective permeability with increasing confining pressure in samples of sections S36 (the values are the average of all steps in which confining pressure was the same, irrespective of the injection pressure) .....	115
Fig. 105:	Change of gas effective permeability with increase/decrease of confining pressure for samples of section S44. The sample reference, dry density, water content and degree of saturation are indicated in the legend .....	116
Fig. 106:	Change of gas effective permeability with increase/decrease of confining pressure for samples of section S47. The sample reference, dry density, water content and degree of saturation are indicated in the legend .....	116
Fig. 107:	Effect of confining pressure on gas effective permeability for samples with and without interface (The accessible void ratio plotted is the initial one. The values for confining pressure 0.6 and 1.0 MPa were obtained in the LP and HP setups).....	117
Fig. 108:	Gas permeability as a function of the accessible void ratio for FEBEX samples tested during the FEBEX and FORGE projects and for FEBEX-DP samples with and without interface (Eq. 11) .....	119
Fig. 109:	Gas permeability as a function of the accessible void ratio for FEBEX samples tested during the FEBEX and FORGE projects and for FEBEX-DP samples with and without interface (enlargement of Fig. 108; Eq. 11).....	119
Fig. 110:	Location of samples used for the swelling capacity tests .....	120

Fig. 111:	Decrease of samples' density caused by the processes of trimming and fitting into the oedometer cells.....	121
Fig. 112:	Evolution of vertical strain during the swelling under 0.5 MPa stress for samples of section S36.....	123
Fig. 113:	Evolution of vertical strain during the swelling under 0.5 MPa stress for samples of section S47.....	124
Fig. 114:	Evolution of vertical strain during the swelling under 0.5 MPa stress for samples of section S53.....	124
Fig. 115:	Final vertical strain for samples of different sections saturated under vertical stress 0.5 MPa.....	125
Fig. 116:	Comparison between the vertical strain measured at the end of the swelling under load tests and the strain corresponding to equivalent samples of the reference bentonite tested under the same conditions obtained with Eq. 12. The distance to the gallery axis of each sample is indicated in cm .....	126
Fig. 117:	Evolution of electrical conductivity of the water in the oedometer cell during swelling under 0.5 MPa stress for samples of section S53.....	127
Fig. 118:	Evolution of vertical strain and electrical conductivity of water in the oedometer cell during swelling under 0.5 MPa stress for two samples of section S53.....	127
Fig. 119:	Evolution of vertical strain during the swelling under 0.5 or 0.05 MPa vertical stress for samples of section S36 in contact with shotcrete.....	129
Fig. 120:	Evolution of vertical strain during the swelling under 0.5 MPa vertical stress for samples drilled on oxidised bentonite.....	129
Fig. 121:	Location of samples (2a and 2b) drilled close to the liner in block BB-36-3.....	130
Fig. 122:	Drilling of sample BB-59-8-2 in an area affected by the oxidation of an extensometer.....	130
Fig. 123:	Final vertical strain for samples of different sections taken close to interfaces and saturated under vertical stress 0.5 MPa.....	131
Fig. 124:	Comparison between the vertical strain measured at the end of the swelling under load tests and the strain corresponding to equivalent samples of the reference bentonite tested under the same conditions. Samples taken close to interfaces.....	132
Fig. 125:	Evolution of electrical conductivity of the water in the oedometer cell during the swelling stress for samples of section S36 taken in contact with the shotcrete (see Tab. 28 for characteristics of the tests).....	132
Fig. 126:	Evolution of swelling pressure of samples saturated with deionised water in the high-pressure oedometer (the distance to the gallery axis is indicated in the legend) .....	134
Fig. 127:	Relationship between suction measured in the blocks and swelling pressure for specimens trimmed from the blocks (Tab. 30).....	135
Fig. 128:	Relationship between swelling pressure and dry density for the samples tested (the lines correspond to the empirical correlation for the reference bentonite in Eq. 13).....	136

Fig. 129: Hydraulic conductivity measured as described in 4.4.2 (filled symbols) and after the swelling pressure tests (in the two cases only the values obtained for hydraulic gradients higher than 10000 m/m are included) ..... 137

Fig. 130: Location of samples used for the oedometer tests ..... 138

Fig. 131: Sample BB-47-7-2 extruding out of the oedometer ring after loading step at 17 MPa..... 142

Fig. 132: Evolution of strain during the different steps of the process of loading under a suction pressure of 4 MPa for sample BB-47-7-2 (see Fig. 110 for location of sample) ..... 143

Fig. 133: Evolution of strain during the different steps of the process of loading under a suction pressure of 4 MPa for sample BB-47-4-1(see Fig. 110 for location of sample) ..... 143

Fig. 134: Evolution of strain during the different steps of the process of loading under a suction pressure of 2 MPa for sample BB-47-4-2 (see Fig. 110 for location of sample) ..... 144

Fig. 135: Evolution of strain during the different steps of the process of loading under a suction pressure of 21 MPa for sample BB-47-8-2 (see Fig. 110 for location of sample) ..... 144

Fig. 136: Evolution of strain during the different steps of the process of loading under a suction pressure of 28 MPa for sample BB-47-9-1 (see Fig. 110 for location of sample) ..... 145

Fig. 137: Evolution of strain during the different steps of the process of loading under a suction pressure of 33 MPa for sample BB-47-9-2 (see Fig. 110 for location of sample) ..... 145

Fig. 138: Water permeability obtained by back-analysis of the oedometer tests and by direct measurement under controlled gradient (subchapter 3.2.2). The lines correspond to the empirical relation for untreated FEBEX (Eq. 10) ..... 146

Fig. 139: Oedometric curves of the tests performed in samples from section S47 (the distance from the axis of the gallery is indicated in the legend)..... 147

Fig. 140: Determination of the vertical preconsolidation stress of samples from radius D in section S47 using the Casagrande method..... 148

Fig. 141: Determination of the vertical preconsolidation stress of samples from radius E-F in section S47 using the Casagrande method..... 149

Fig. 142: Apparent preconsolidation stress estimated from the oedometer tests using two methods for samples trimmed from the blocks retrieved (FEBEX-DP) and for compacted samples of the reference bentonite..... 150

Fig. 143: Pre ( $\kappa$ ) and post-yield ( $\lambda$ ) compressibility values estimated from the oedometer tests ..... 151

Fig. 144: Pore size distribution before and after the oedometer tests for samples of section S47..... 152

Fig. 145: Void ratio corresponding to different pore sizes before and after the oedometer tests for samples of section S47 ..... 152

Fig. 146: Basal reflection before and after the oedometer tests for samples of section S47 ..... 153



## 1 Introduction

The FEBEX project (Full-scale Engineered Barriers Experiment) studies the behaviour of components in the near-field for a high-level radioactive waste (HLW) repository in crystalline rock. The project was based on the Spanish reference concept for disposal of radioactive waste in crystalline rock (AGP Granito): the waste canisters are placed horizontally in drifts and surrounded by a clay barrier constructed from highly-compacted bentonite blocks (ENRESA 1995). As part of this project, an “in-situ” test, under natural conditions and at full scale, was performed at the Grimsel Test Site (GTS, Switzerland), an underground laboratory managed by NAGRA (ENRESA 2000, 2006). The thermal effect of the waste was simulated by means of heaters, whereas hydration was natural. The test was monitored, thereby obtaining data on the evolution of temperature, total pressure, water content, water pressure, displacements and other parameters continuously, in different parts of the barrier and the host rock. This information is then used to compare with the predictions of the thermo-hydro-mechanical (THM) and thermo-hydro-geochemical (THG) models.

The basic components of the test (Fig. 1) were: the gallery, measuring 70 m in length and 2.3 m in diameter, excavated through the Aare granite; the heating system, made up of two heaters placed inside a liner installed concentrically with the gallery and separated from each other by a 1.0 m distance, with dimensions and weights analogous to those of the real canisters. The clay barrier is formed by blocks of compacted bentonite; the instrumentation, the monitoring and control system for data acquisition as well as supervision and control of the test both run autonomously and remotely from Madrid. Up to 632 sensors of very diverse types were initially installed for monitoring the different thermo-hydro-mechanical processes that occurred in both the clay barrier and the surrounding rock throughout the entire life of the test. The gallery was closed by a concrete plug.

The clay barrier consisted of FEBEX bentonite, which was extracted from the Cortijo de Archidona deposit (Almería, Spain). The physico-chemical properties of the FEBEX bentonite, as well as its most relevant thermo-hydro-mechanical and geochemical characteristics obtained during the projects FEBEX I and II were summarised in the final reports of the project (ENRESA 2000, 2006) and later documents (Villar & Gómez-Espina 2009). To build the clay barrier, various types of blocks were manufactured from the bentonite in the shape of 12-cm thick circular crown sectors. The blocks were arranged in vertical slices consisting of concentric rings. In the heater areas the interior ring was in contact with the steel liner, whereas in the non-heater areas a core of bentonite blocks replaced the heaters (Fig. 2). The geometry and dimensions of the blocks are shown in Fig. 2, Fig. 3 and Tab. 1. The thickness of the bentonite barrier in the heater areas was 65 cm (distance from liner to granite). The bentonite slices were numbered from the back of the gallery towards the front, and those in which sensors were installed were called “instrumented sections” and given a distinctive reference letter. The backfilled area was sealed with a plain concrete plug placed into a recess excavated in the rock.

The blocks were obtained by uniaxial compaction of the FEBEX clay with its hygroscopic water content at pressures between 40 and 45 MPa, resulting in dry densities of 1.69-1.70 g/cm<sup>3</sup>. The initial dry density of the blocks was selected by taking into account the probable volume of the construction gaps and the need to have a barrier with an average dry density of 1.60 g/cm<sup>3</sup> (ENRESA 2000).

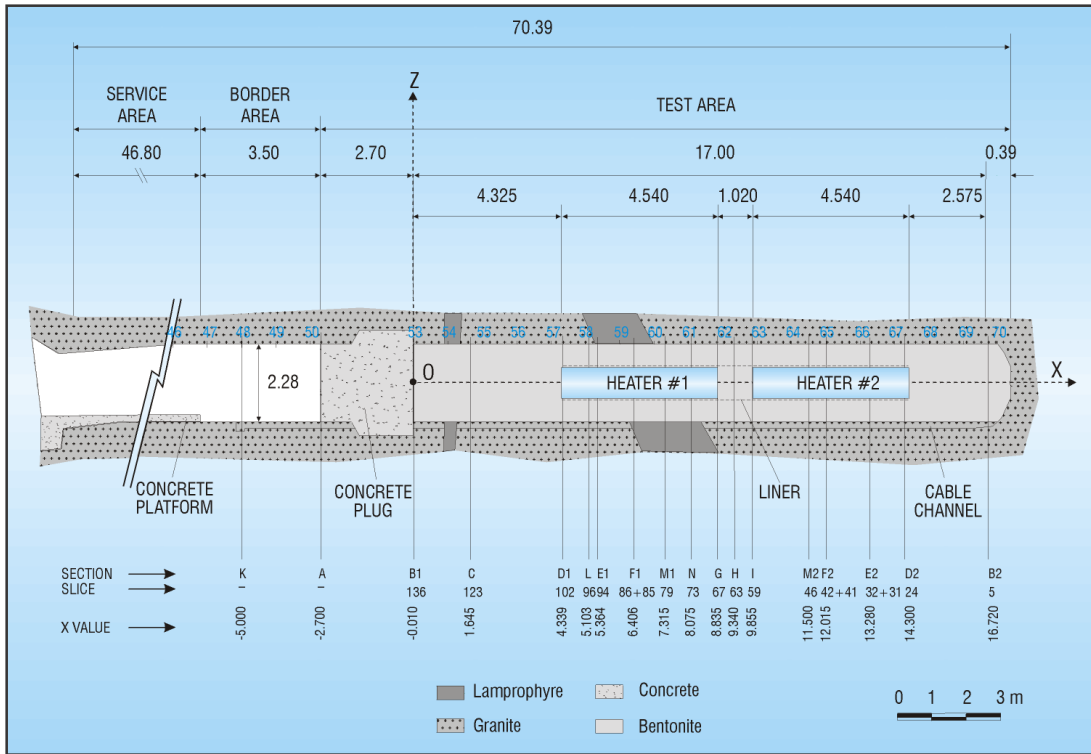


Fig. 1: General layout of the in-situ test during phase I, including instrumented sections (ENRESA 2000)

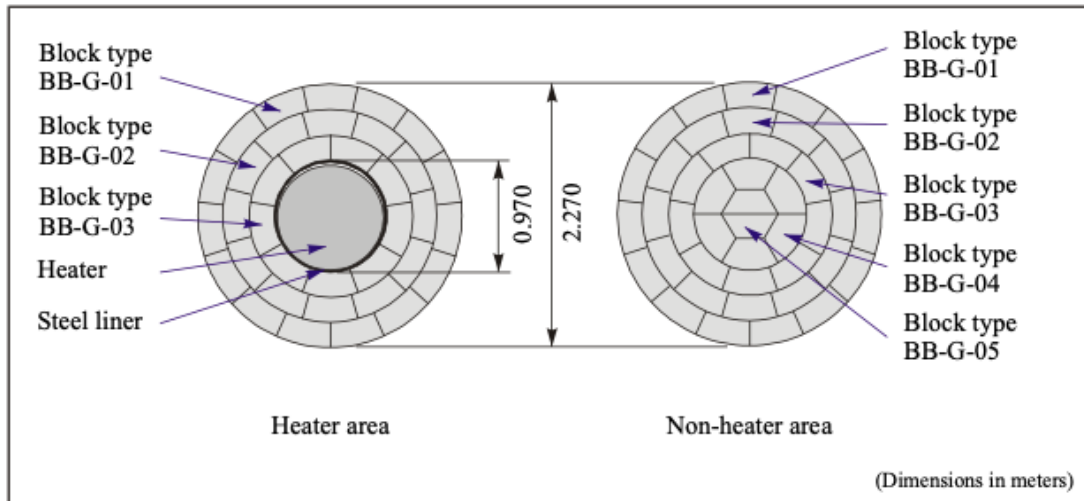


Fig. 2: Geometry of the clay barrier in the FEBEX in-situ test at GTS (ENRESA 2000)

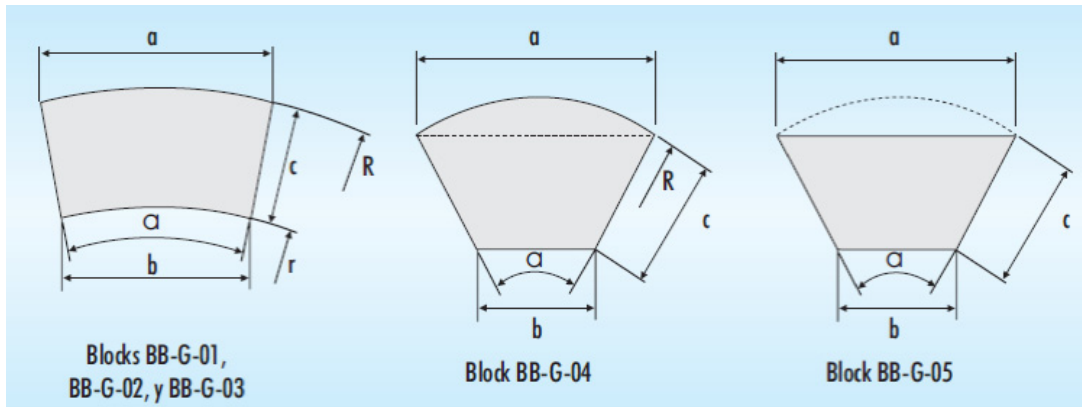


Fig. 3: Geometry of the different kinds of blocks (Fuentes-Cantillana & García-Siñeriz 1998)

Tab. 1: Dimensions of the blocks shown in Fig. 3 (Fuentes-Cantillana & García-Siñeriz 1998)

Block type	External radius R (mm)	Internal radius r (mm)	R-r (mm)	Blocks per slice	Thickness (mm)
BB-G-01	1135.0	918.3	216.7	15	125.0
BB-G-02	918.3	701.7	216.7	12	125.0
BB-G-03	701.7	485.0	216.7	9	125.0
BB-G-04	485.0	242.5 <sup>a</sup>	216.7	6	125.0
BB-G-05	242.5	0.0	216.7	2	125.0

<sup>a</sup> radius of central hexagon

The heating stage of the in-situ test began on 27 February 1997. The power of the heaters was adjusted to keep the temperatures at the liner surface at 100°C. After five years of uninterrupted heating at constant temperature, the heater closer to the gallery entrance (Heater #1) was switched off (February 2002). In the following months this heater and all the bentonite and instruments preceding and surrounding it were extracted (Bárcena et al. 2003). A large number of bentonite samples were also taken for analysis in different laboratories (Villar 2006). The remaining part of the experiment was sealed with a new sprayed shotcrete plug. New sensors were installed in the buffer through the shotcrete plug, and a second operational phase started with the test configuration shown in Fig. 4. It shows how the buffer and all components were removed up to a distance of 2 metres from Heater #2 to minimize disturbance of the non-dismantled area. A dummy steel cylinder with a length of 1 m was inserted in the void left by Heater #1 in the centre of the buffer.

The test continued running until April 2015, when Heater #2 was switched off and the dismantling operations started. Many sensors were in operation until the end of the experiment,

which allowed following the evolution of some thermo-hydro-mechanical variables during the second operational phase (Martínez et al. 2016). In particular, the temperatures measured at the different instrumented sections indicated in Fig. 4 just before dismantling are shown in Tab. 2, along with those measured just before the partial dismantling in 2002. The location of sensors in the bentonite rings is given according to Fig. 2.

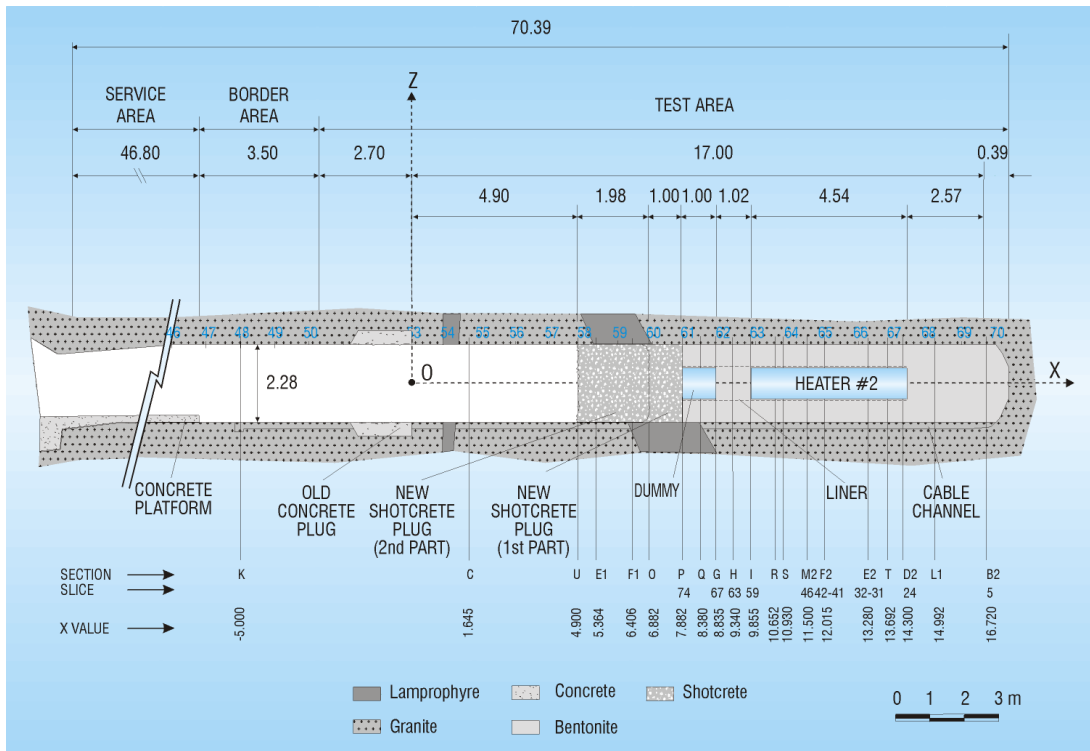


Fig. 4: General layout of the in-situ test during phase II, including instrumented sections (ENRESA 2006)

Tab. 2: Temperatures (°C) measured in the bentonite barrier before dismantling (1: 2002, B rcena et al. 2006; 2: 2015, Mart nez et al. 2016)

	Date	Section G (1 m from heater)	Section I (heater front)	Section S (1 m into heater zone)	Section F2 (middle of heater)	Section D2 (heater rear end)	Section B2 (gallery end)
Outer ring (BB-G-01)	1	44-46	44-45			36-38	21-23
	2	30-34	37-39			36-37	22
Intermediate ring (BB-G-02)	1	58-60	58-61			51-53	
	2	34-39	54-63	72	71-73	54-56	
Inner ring 1 (BB-G-03)	1	80-84	84-88		95-100	82-90	
	2	36-43	84-87	93	94-99	83-88	
Inner ring 2 (BB-G-04)							21-23
							20-22
Core (BB-G-05)	1	100-104					21-23
	2						22

The dismantling operations included demolishing the shotcrete plug and removing all bentonite surrounding the heater on all sides. A large number of samples from all types of material were taken for analysis.

In particular, clay samples were taken to characterise the solid and liquid phases, in order to confirm predictions and validate existing models of THM and THG processes. The aims of these post-mortem analyses were:

- Analyse the physical, physico-chemical, mineralogical, chemical and textural changes that occurred in the clay through heating and hydration, taking also into account the effect of joints.
- Analyse the physical, physico-chemical, mineralogical, chemical and textural changes occurred in the clay through interaction with different interfaces (shotcrete, granite, metal components).
- Analyse the chemical evolution of the bentonite pore water.
- Supply data to validate and check the capacity of the numerical codes (THM and THG) being developed to predict the bentonite behaviour in an engineered barrier.

A large part of the samples were sent to CIEMAT and received between the 7 and 21 August 2015. The characterisation planning, i.e. the kind and number of tests to be performed by CIEMAT, was detailed in CIEMAT (2014).

This document collects the results obtained by CIEMAT referring to the THM characterisation of the samples. Many of these results are also summarised and included in the synthesis report collecting results of the bentonite characterisation obtained by all the project partners NAB-16-017 (Villar 2018). The results concerning the mineralogical and geochemical characterisation are reported in the NAB-16-025 (Fernández et al. 2018).

## 2 Dismantling of the barrier and bentonite sampling

The test continued running until, when Heater #2 was switched off. Some days earlier, demolition of the shotcrete plug had started; buffer removal and sampling took place between 8 May and 5 August 2015, when temperature in the area affected by the dismantling had diminished to a level compatible with manual works (25-30 °C). This means that when the first bentonite section was sampled, the heater had been switched-off for 14 days, and as sampling proceeded towards the back of the gallery, the longer the cooling period had been for these samples. During the dismantling operation, bentonite, rock, relevant interfaces, sensors, metallic components and tracers were extensively sampled, allowing the analysis of the barrier condition after 18 years of heating and natural hydration, as described in NAB16-011 (García-Siñeriz et al. 2016). All details about the sampling program are given in NAB15-014 (Bárcena & García-Siñeriz 2015).

Upon exposure, the bentonite sections presented a consistent appearance; although the joints between blocks were in most cases visible, all construction gaps were sealed, even the big apertures hewn in the bentonite for inserting bunches of cable (Fig. 5). Differences in coloration of the bentonite related to the variations of its water content were observed, the outer rings of the barrier having darker colours.



Fig. 5: Appearance of the bentonite barrier after extraction of heater #1 in 2005 and of heater #2 in 2015

The on-site determinations performed during dismantling showed that the physical condition of the bentonite along the barrier had changed during operation, as a result of hydration and of the different temperatures to which the bentonite had been subjected (Tab. 2). Water content and dry density gradients, both across the vertical sections and along the gallery, had been generated (Villar et al. 2016a). Fig. 6 to Fig. 8 show the final distribution of dry density, water content and degree of saturation along the barrier obtained from the on-site determinations. It is clear that the initial conditions of the samples received by the different laboratories depended on the exact location along the barrier of the sampling section from which they were taken, as well as on the position of a particular sample with respect to the axis of the gallery. The main differences occurred between sections located around the heater (sections S42 to S53) as opposed to cool areas.

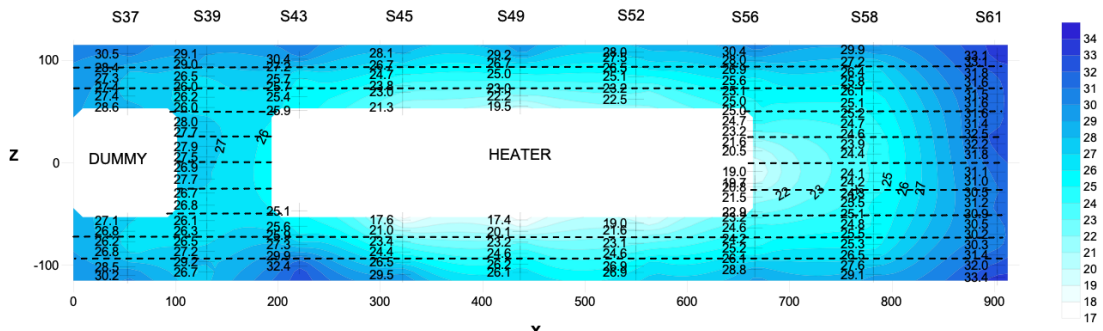


Fig. 6: Water content distribution in a vertical longitudinal section (Villar et al. 2016a)

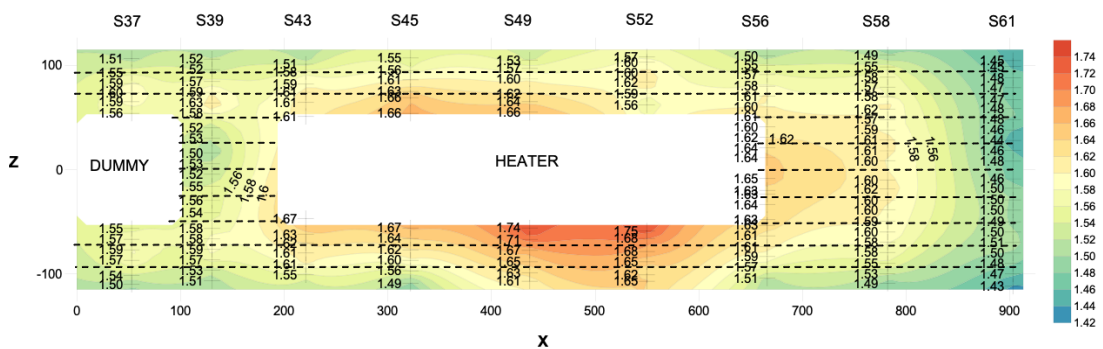


Fig. 7: Dry density distribution in a vertical longitudinal section (Villar et al. 2016a)

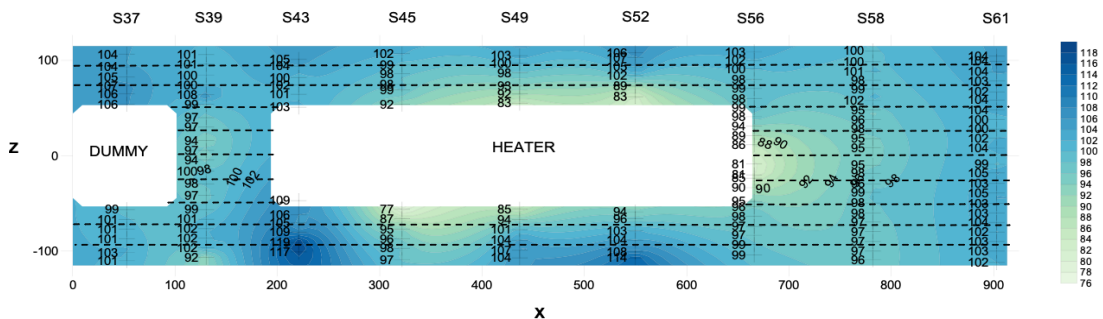


Fig. 8: Degree of saturation distribution in a vertical longitudinal section (Villar et al. 2016a) (inexact values because of solid specific weight and water density uncertainties)

The location of the bentonite sampling points was positioned to allow a good representation of physico-chemical alterations and the hydration distribution. The sampling took place in vertical sections normal to the axis of the tunnel, and in each section several samples were taken along different radii. Following the same terminology used during installation of the experiment and during the first dismantling, the term bentonite "slice" refers to the vertical slices of bentonite blocks as they were installed. These were numbered during the installation of the barrier in 1997 as they were put in place: from slice 1, at the back of the gallery, to slice 136, at the front of the barrier in contact with the first concrete plug, the last one installed. The term "section" refers to the vertical sampling sections in which samples of any kind were taken during dismantling. They were numbered from the entrance of the gallery towards the back of it, and the numbering

started in the first dismantling. Hence, sampling sections S1 to S30 were sampled in 2002, and sampling sections S31 to S61 were sampled in 2015. For this reason, there were more slices than sampling sections, because not all bentonite slices were sampled. Besides, a sampling section could include two or three slices.

According to the Sampling Book (Bárcena & García-Siñeriz 2015), the bentonite samples sent to CIEMAT were taken from the vertical sections detailed in Tab. 3 and Fig. 9. The exact location of the samples inside each section is shown in Fig. 10.

Tab. 3: Samples received by CIEMAT from the FEBEX-DP dismantling for THM analyses

Sampling section	x-coordinate (m)	Tests
S36	7.950	THM-THG (9 blocks and 5 cores) Filter paper
S42	9.855	Canister/bentonite interaction (2 cores) Piece of block in contact with cables (not foreseen) 3 bulky samples in contact with pipes
S44	10.610	THM-THG (9 blocks (two of them taken as 8 cores) and 7 cores) and 4 samples of bentonite adhered to the liner 2 bulky samples in contact with pipes
S47	11.755	THM-THG (9 blocks and 6 cores) and bentonite adhered to the liner
S50	12.647	THM-THG (6 blocks (2 of them taken as 4 cores and fragment) and 6 cores) and 3 samples of bentonite adhered to the liner. 8 samples of iodide in filter papers
S51	13.280	Tracers B, Eu, Re, Se, I (6 blocks), 8 samples of FP
S53	13.795	THM-THG (9 blocks (3 of them as cores and fragment) and 6 cores) and 3 samples of bentonite adhered to the liner
S57	14.930	THM-THG (9 blocks, 1 half block and 6 cores)
S59	16.335	THM-THG (14 blocks and 6 cores)

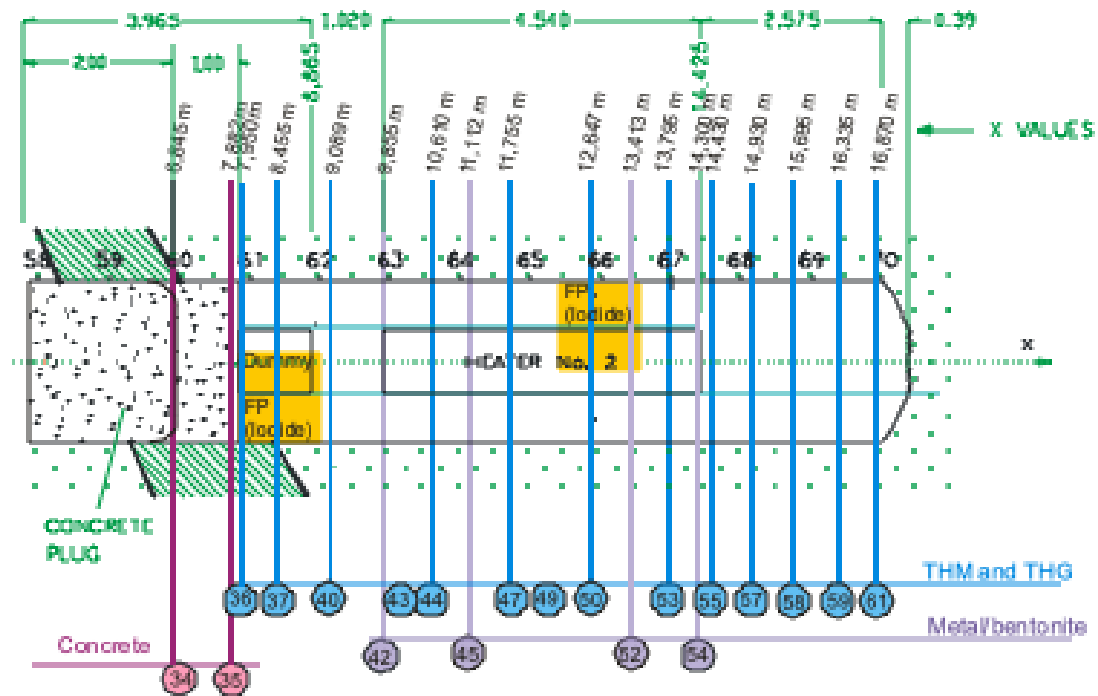


Fig. 9: Distribution of sampling sections for THM-THG and interfaces studies of CIEMAT (modified from Bárcena & García-Siñeriz 2015)

The samples were preserved in plastic film, two layers of aluminised PET-sheets and vacuum-sealed plastic bags immediately after their extraction. The PET-sheets were vacuum-sealed. Protection against mechanical actions was used to ensure the integrity of the material. On the wrapping of every sample, its reference and the position with respect to the gallery entrance was clearly indicated. The samples were referred to according to the key given in the Sampling Book (Bárcena & García-Siñeriz 2015).

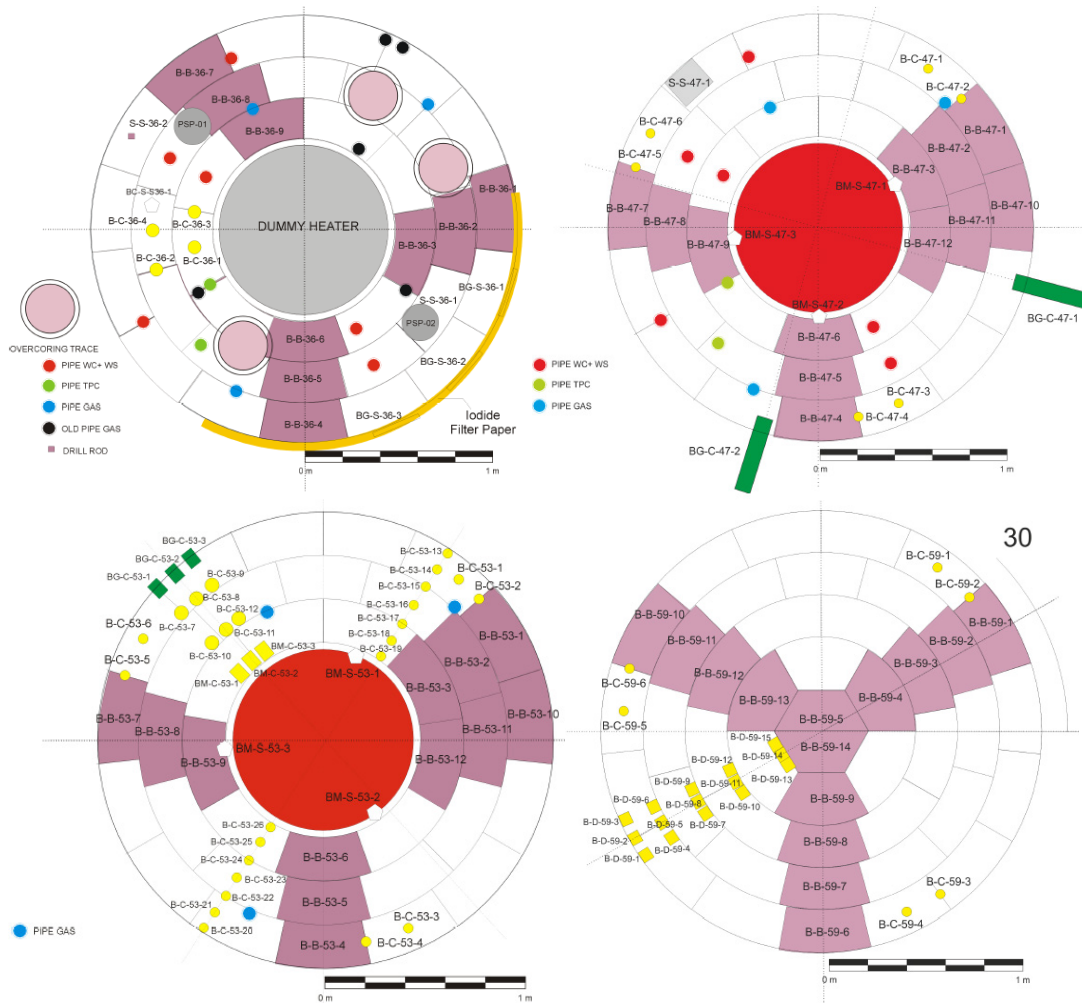


Fig. 10: Position of blocks received at CIEMAT for THM and THG tests in sampling sections S36, S47, S53 and S59 (the position of blocks BB-36-7 and BB-36-9 is interchanged) (Bárcena & García-Siñeriz 2015)

Tab. 4 shows the blocks sampled at CIEMAT laboratories and the radius of the section along which they were taken, according to Fig. 11. The radii have been named according to the same key used for the on-site determinations (Villar et al. 2016a). The same information is given in Tab. 5 for the core samples used in the gas permeability tests. The date of the block or core retrieving at Grimsel (Retrieving GTS), of its arrival at CIEMAT (Arrival CIEMAT) and of its sampling at CIEMAT's laboratories (Sampling CIEMAT) are indicated, along with the time elapsed from the day they were taken until they were sampled in the laboratory. This time span for the blocks is quite broad, between 84 and 189 days, mainly because it took three months for the first samples to get to CIEMAT. In the case of the core samples the time elapsed between retrieving and testing in the laboratory was much longer, because the experimental setup for the gas permeability tests had to be fine-tuned. Also, three blocks (BB44-1, BB44-3 and BB-57-1) were sampled in 2017 to perform suction measurements and swelling pressure determinations that had not been initially planned. Hence, the samples from these blocks were tested two years after retrieval, and they have been treated separately. Except for some samples that were brought by CIEMAT's personnel coming back from Grimsel, most of the samples were received on August 2015. Tables 4 and 5 also show if the samples were still vacuum sealed

when they were sampled at CIEMAT or not. Note that not all the blocks and cores received (Tab. 3) were sampled.

Tab. 4: Summary of blocks sampled at CIEMAT for THM and THG determinations

Section	Radius	Block reference	Retrieving GTS	Arrival CIEMAT	Sampling CIEMAT	Time elapsed (days)	Vacuum
S36	B-C	BB-36-1	8/5/15	21/8/15	27/10/15	172	no
S36	B-C	BB-36-2	8/5/15	7/8/15	14/10/15	159	no
S36	B-C	BB-36-3	8/5/15	7/8/15	24/8/15	108	no
S36	D	BB-36-4	8/5/15	7/8/15	25/8/15	109	no
S36	D	BB-36-5	8/5/15	7/8/15	22/9/15	137	no
S36	D	BB-36-6	8/5/15	7/8/15	11/9/15	126	no
S36	F	BB-36-7	8/5/15	7/8/15	18/8/15	102	no
S36	F	BB-36-8	8/5/15	7/8/15	17/8/15	101	no
S36	F	BB-36-9	8/5/15	7/8/15	19/8/15	103	no
S44	B	BB-44-1 <sup>a</sup>	17/6/15	7/8/15	1/3/17	623	yes
S44	B	BB-44-3 <sup>a</sup>	18/6/15	7/8/15	16/8/17	790	no
S47	B	BB-47-1	26/6/15	7/8/15	8/9/15	74	yes
S47	B	BB-47-2	26/6/15	7/8/15	21/9/15	87	yes
S47	B	BB-47-3	26/6/15	7/8/15	9/9/15	75	yes
S47	D	BB-47-4	29/6/15	7/8/15	21/10/15	114	no
S47	D	BB-47-5	29/6/15	7/8/15	22/10/15	115	yes
S47	D	BB-47-6	29/6/15	7/8/15	26/10/15	119	no
S47	E-F	BB-47-7	29/6/15	7/8/15	15/9/15	78	yes
S47	E-F	BB-47-8	29/6/15	7/8/15	14/9/15	77	no
S47	E-F	BB-47-9	29/6/15	7/8/15	19/10/15	112	yes
S53	B	BB-53-1	15/7/15	21/8/15	23/11/15	131	yes

Section	Radius	Block reference	Retrieving GTS	Arrival CIEMAT	Sampling CIEMAT	Time elapsed (days)	Vacuum
S53	B	BB-53-2	15/7/15	21/8/15	5/1/16	174	yes
S53	B	BB-53-3	15/7/15	21/8/15	13/1/16	182	no
S53	D	BB-53-4	15/7/15	21/8/15	21/12/15	159	no
S53	D	BB-53-5	15/7/15	21/8/15	11/1/16	180	yes
S53	D	BB-53-6	15/7/15	21/8/15	19/1/16	188	no
S53	E-F	BB-53-7	15/7/15	21/8/15	28/10/15	105	yes
S53	E-F	BB-53-8	15/7/15	21/8/15	12/1/16	181	yes
S53	E-F	BB-53-9	15/7/15	21/8/15	20/1/16	189	yes
S57	B	BB-57-1 <sup>a</sup>	23/7/15	21/8/15	1/3/17	587	yes
S59	B	BB-59-1	28/7/15	21/8/15	30/10/15	94	yes
S59	B	BB-59-2	28/7/15	21/8/15	5/11/15	100	yes
S59	B	BB-59-3	28/7/15	21/8/15	10/11/15	105	yes
S59	B	BB-59-4	28/7/15	21/8/15	11/11/15	106	yes
S59	B	BB-59-5	28/7/15	21/8/15	16/11/15	111	yes
S59	D	BB-59-6	29/7/15	21/8/15	17/11/15	141	yes
S59	D	BB-59-7	29/7/15	21/8/15	30/11/15	154	yes
S59	D	BB-59-8	29/7/15	21/8/15	9/12/15	133	yes
S59	D	BB-59-9	29/7/15	21/8/15	15/12/15	139	yes
S59	D	BB-59-14	29/7/15	21/8/15	16/12/15	140	yes
S59	F	BB-59-10	29/7/15	21/8/15	1/12/15	125	yes
S59	F	BB-59-11	29/7/15	21/8/15	2/12/15	126	yes
S59	F	BB-59-12	29/7/15	21/8/15	26/1/16	181	yes
S59	F	BB-59-13	29/7/15	21/8/15	27/1/16	182	yes

<sup>a</sup> Sampled exclusively for suction and swelling pressure measurement after the main testing campaign

Tab. 5: Summary of cores used at CIEMAT for gas permeability determinations

Section	Radius	Sample reference	Retrieving GTS	Arrival CIEMAT	Sampling CIEMAT	Time elapsed (days)	Vacuum
S36	E-F	BC-36-1	8/5/15	27/5/15	28/5/15	20	yes
S44	A-B	BC-44-1	16/6/15	7/8/15	20/9/16	462	yes
S44	D-E	BC-44-2	18/6/15	7/8/15	17/8/16	426	yes
S44	E	BC-44-7	18/6/15	7/8/15	18/8/16	427	yes
S47	A	BC-47-1	26/6/15	7/8/15	18/7/16	388	yes
S47	A	BC-47-2	26/6/15	7/8/15	10/12/15	167	yes
S47	A	BC-47-3	26/6/15	7/8/15	14/6/16	354	yes
S47	A	BC-47-4	26/6/15	7/8/15	18/11/15	145	yes
S47	F-A	BC-47-5	26/6/15	7/8/15	7/6/16	347	yes
S47	F	BC-47-6	26/6/15	7/8/15	20/7/16	390	yes

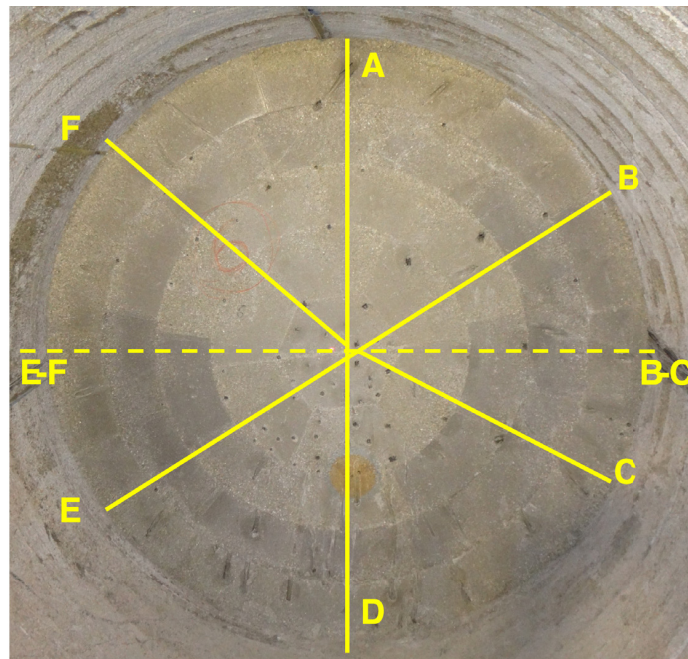


Fig. 11: References for the radii along which the blocks were taken

From the moment of their arrival, the samples were kept in a RH-controlled room (Fig. 12). The RH was initially set to 70% and then to 80%, although because the samples were vacuum-sealed, this value is not considered relevant. In fact, from February 2016 on, the RH control stopped working. The evolution of temperature and RH in this room for the period in which the FEBEX-DP samples were stored in it for analysis is shown in Fig. 13.



Fig. 12: RH-controlled room for the storage of samples

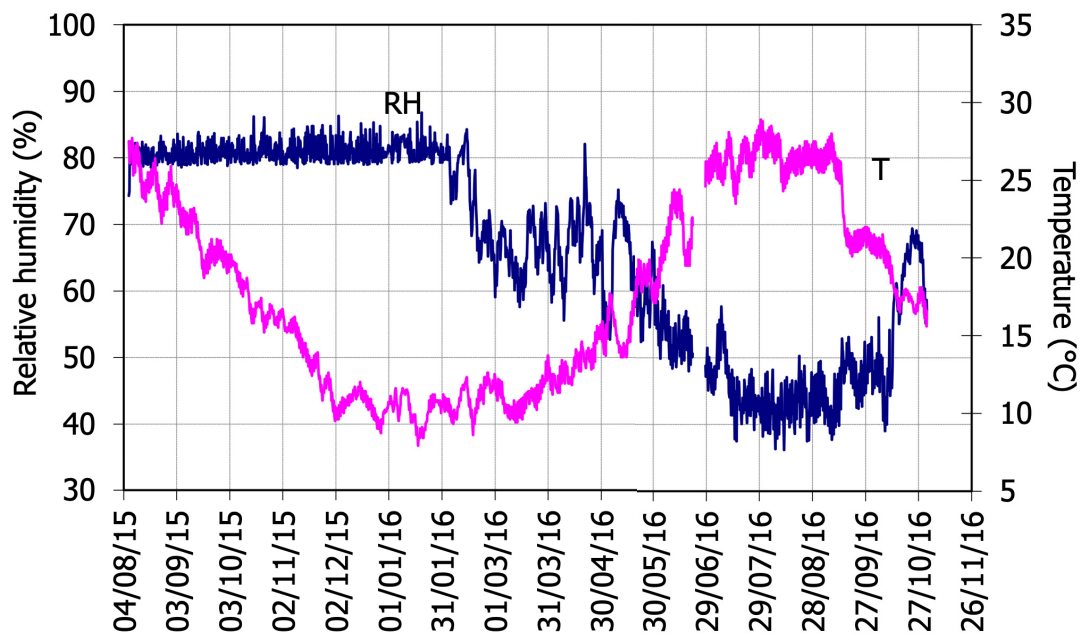


Fig. 13: Relative humidity and temperature in the storage room



### 3 Methodology

The laboratory determinations presented in this report were carried out at CIEMAT facilities mostly from August 2015 to October 2016. The tests for the determination of the water retention curve took very long, until December 2017 and the gas permeability tests went beyond 2017. For this reason they are not completely reported here. Also, three blocks were sampled in 2017 for measurement of suction and swelling pressure (BB-44-1, BB-44-3, BB-57-1). During the main testing period, between one and three blocks were sampled every week in the laboratory. The block to be sampled every day was taken early in the morning from the storage room to the laboratory where the subsampling was made. Some blocks were taken out from the storage room a day before sampling, since thermal equilibrium is necessary for the correct measurement of thermal conductivity and suction, and during the winter the temperatures were much lower in the storage room than in the laboratory.

The plastic and aluminium foil bags were removed and, with the block wrapped in the plastic foil, thermal conductivity and relative humidity were measured. In some blocks, a qualitative measure of moisture was taken with a microwave technique (Trotec T610). To perform these measurements only the indispensable surface of the block was uncovered, thus avoiding unnecessary humidity losses (Fig. 14).



Fig. 14: Measurement of thermal conductivity, relative humidity and moisture before sampling the blocks

Each block was unpacked only once in order to take the subsamples for the different determinations. The sampling was coordinated to make the tests immediately after unpacking and sampling. The blocks were sectioned along the radius, in order to obtain material for the hydro-mechanical (THM) and geochemical and mineralogical (THG) tests (Fig. 15). The latter are reported in Fernández et al. (2018). In order to obtain a more detailed sampling, subsamples from two (three in a few cases) different positions along the radius of the block were taken. The subsamples obtained in this way were referenced by adding a correlative number to the initial reference of the block, 1 for the part closest to the granite and 2 for the part closest to the gallery axis.



Fig. 15: Sectioning of blocks for THM and THG determinations

The samples for the different HM determinations were obtained by drilling (Fig. 16). The block remaining after sampling was sectioned in the direction transversal to the radius (Fig. 17), and the two pieces obtained were individually wrapped with plastic film, packed with two vacuumed aluminium foil bags and stored again in the RH-controlled room. The aim of this separation was to avoid additional water diffusion between the two parts of the block during long storage.

The sampling logs of the blocks analysed for THM and THG tests are presented in Iglesias et al. (2018).



Fig. 16: Drilling of a block to obtain subsamples 1 (closest to the granite) and 2 (closest to the gallery axis) for HM determinations

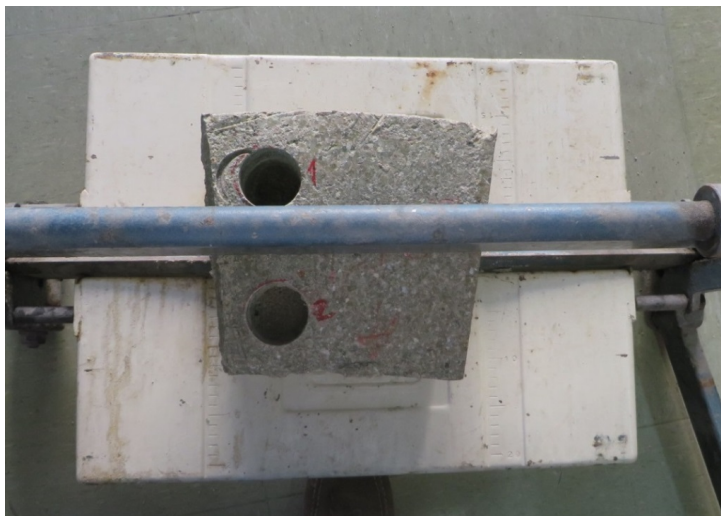


Fig. 17: Sectioning of the THM part of a block before packaging and final storage

### 3.1 Basic properties

#### 3.1.1 Thermal conductivity

The superficial thermal conductivity of the bentonite blocks was measured using a Kemtherm QTM-D3 system by Kyoto Electronics (1987), which operates on the basis of the transient hot wire method (Fig. 18). Transient methods have the advantage over steady-state methods that the movement of water in response to the thermal gradients applied for determination is minimised, more notably if these gradients are small. Consequently, transient methods for the measurement of thermal conductivity are to be recommended over steady-state methods for humid soils.



Fig. 18: Kemtherm QTM-D3 conductivity meter with probe and standard plates

The transient hot wire method is based on the exponential increase in the temperature of a thin hot wire that occurs when a constant power is applied (heat flux), while the wire is stretched in

the centre of a cylindrical sample or a rectangular parallelepiped of infinite length. This allows the thermal conductivity of the material to be calculated on the basis of heat flux (power and intensity), the characteristics of the heating wire (length, radius and resistance) and the increase in temperature of the wire over a given period of time.

The measuring equipment used is based on the probe method, a variation of the transient hot wire method in which the wire, instead of being inserted into the sample, is placed between the sample and an insulating material of known thermal conductivity (Kyoto Electronics 1987). This insulating material and the wire, along with a K-type thermocouple for the measurement of temperature variation, constitute the measuring probe. If this probe method is applied, thermal conductivity ( $\lambda$ , W/(m·K)) is calculated by means of the following equation (Eq. 1):

$$\lambda = K \frac{I^2 \ln(t_2/t_1)}{V_2 - V_1} - H \quad (\text{Eq. 1})$$

where  $V_1$  and  $V_2$  are the initial and final output voltage of the measuring equipment ( $V$ );  $I$  is current intensity (A);  $t_2$  and  $t_1$  are the end and beginning of the measuring time (s); and  $K$  and  $H$  are the constants of the probe, calculated on the basis of the resistance of the wire, the thermoelectric power of the thermocouple and the thermal conductivity of the insulating material. The constants that have to be used also depend on the thermal conductivity of the material measured. For thermal conductivities between 0.02 and 0.2 W/m·K constants  $H_1$  and  $K_1$  are used, whereas for thermal conductivities between 0.2 and 10 W/m·K constant  $K_2$  and  $H_2$  are used.

The values of thermal conductivity obtained using this method or the conventional hot wire method coincide, since the relation between temperature variation and time is practically the same in both cases (Kyoto Electronics 1987).

The superficial thermal conductivity was measured in the sampled blocks just after unpacking. The plastic film was kept around the blocks during the measurement and only the rectangular section necessary to apply the probe was uncovered. This surface was smoothed with a scraper and brushed to remove any loose material. The thermal conductivity was usually measured on the surface of the block that faced the gallery entrance in two positions transversal to the radius, 1 (closer to the granite) and 2 (closer to the gallery axis) (Fig. 14). At the same positions water content and dry density were determined (see [3.1.3](#)), which allowed to relate these parameters to the thermal conductivity measured.

The measurement was performed at laboratory temperature, at least 1 h after the block had been taken from the storage room to the laboratory. The probe was placed on the flat surface of the specimen and the temperature of both was allowed to stabilise to equilibrium for at least 15 min. A heat flux (known power) was applied via the wire for 60 s, causing a temperature increase of some 20°C. Given that this is a short period of time, the sample was heated only in the area surrounding the heater wire, this implying that the value of the measurement corresponds to the thermal conductivity of the surface of the sample to which the probe was applied. For values of thermal conductivity of between 0.02 and 10 W/(m·K), which are usual in geological materials, the flux generated by the heater wire is between 3 and 30 kcal/m·h. A check must be made to ensure that the temperature increase caused was within the range 10 to 30°C. If this is not the case, the measurement will not be valid, as a result of which the heater current intensity should be modified and the test repeated. All the samples were measured with the same current

intensity of 1.41 A. Three valid measurements were performed on each sample, separated by a period of time, guaranteeing cooling of the sample and the probe to laboratory temperature (15 minutes). The results were recorded by a printer connected to the equipment.

### 3.1.2 Suction measurement

The relative humidity and temperature of the blocks was measured before unpacking either with psychrometers or with capacitive sensors, depending on the bentonite water content. The relative humidity of the blocks with higher water content was measured with 8 psychrometers Wescor Elitech PST-55-30-SF with stainless steel filters (Fig. 19) connected to a Wescor Elitech PSYPRO datalogger. These sensors, 6 mm in diameter and 30 mm in length, operate in a suction range from 50 to 6200 kPa, with a precision of  $\pm 1\%$  FS. The capacitive transmitters used for the samples with lower water content were Sensirion SHT75, which have a precision of 2% RH in the range from 20 to 80%.

The blocks were taken to the laboratory at least 1 h before the measurements. The plastic and aluminium foil bags were removed and, with the block wrapped in plastic foil, holes were drilled in the block to install the sensors inside (Fig. 20). The stabilisation of the measurement took about 1 h. To convert the values of relative humidity (RH, %) to suction values ( $s$ , MPa) Kelvin's law is used (Eq.2):

$$s = -10^{-6} \frac{R \times T}{V_w} \ln\left(\frac{RH}{100}\right) \quad (\text{Eq. 2})$$

where  $R$  is the universal constant of gases ( $8.3143 \text{ J/mol}\cdot\text{K}$ ),  $T$  the absolute temperature (K) and  $V_w$ , the molar volume of water ( $1.80 \cdot 10^{-5} \text{ m}^3/\text{mol}$ ).

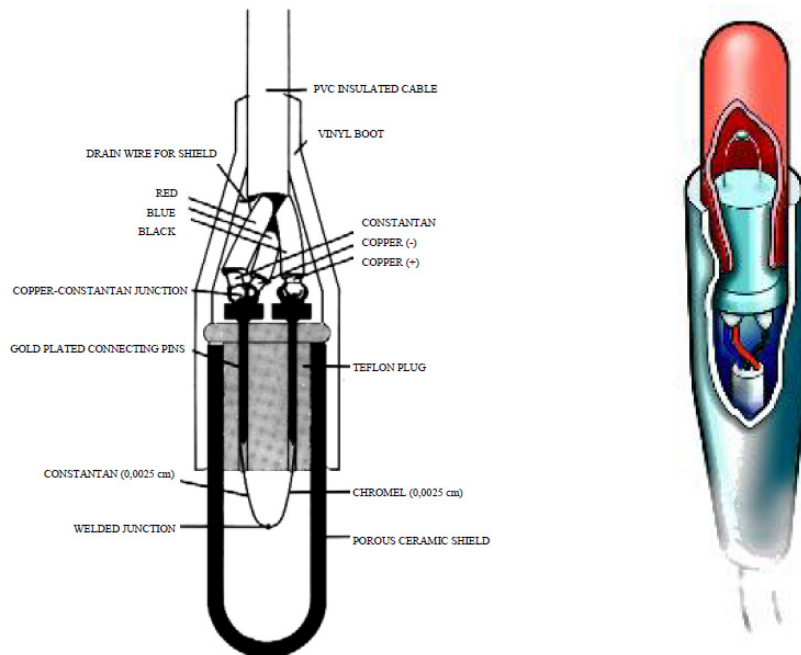


Fig. 19: Schematic representation of the psychrometers



Fig. 20: Psychrometers inserted into a block prior to unpacking

### 3.1.3 Water content and dry density

The samples for water content and dry density determinations were obtained by drilling with a crown drill bit of internal diameter 4.5 cm. Two or three positions were drilled in each block, and from every core 1 or 2 subsamples were obtained (Fig. 21). The volume of the subsamples was between 2 and 24 cm<sup>3</sup> (average volume 11 cm<sup>3</sup>) and the mass between 4 and 47 g (average mass 21 g). The external part of the subsamples that was in contact with the crown drill bit, was removed. In each of these subsamples water content and dry density were determined.

The gravimetric water content ( $w$ ) is defined as the ratio between the mass of water and the mass of dry solid expressed as a percentage. Consequently, all the values given in this report are weight percentages. The mass of water was determined as the difference between the mass of the sample and its mass after oven-drying at 110°C for 48 h (mass of dry solid). Dry density ( $\rho_d$ ) is defined as the ratio between the mass of the dry sample and the volume occupied by it prior to drying. The volume of the specimens was determined by immersing them in a recipient containing mercury and by weighing the mercury displaced (Fig. 22), with a value of 13.6 g/cm<sup>3</sup> for the density of mercury. The absolute error of this measurement is in the order of 10<sup>-2</sup> g/cm<sup>3</sup>. The same samples whose volumes had been determined were used for the water content determination. The balance used was an AND GF2000, with a capacity up to 2100 g and a precision of 0.01 g.



Fig. 21: Location in the blocks of sampling positions for water content and dry density (and most of the other determinations)



Fig. 22: Determination of sample volume by immersion in mercury

### 3.1.4 Specific weight of solid particles

The specific weight of the solid particles of a soil ( $\gamma_s$ ) is defined as the ratio between the weight of a given quantity of dry soil and its volume. In order to obtain the specific weight of solid particles, the weight of the water displaced by a known mass of dry soil is determined. This analysis requires the use of deionized, de-aired water for soil suspension and pycnometers of capacity 50 cm<sup>3</sup>. The procedure is as follows:

- Pycnometer calibration: the clean and dry pycnometer with its stopper are weighed ( $W_p$ ). Then the pycnometer is filled with deionised water at 20°C, assuring that the bottom of the meniscus reaches the end of the capillary tube inside the pycnometer stopper. The assemblage full of water is weighed again ( $W_a$ ).
- Sample preparation: A 50 g portion of sample is dried in the oven at 110°C for at least 24 h and ground to pass through a 2 mm sieve. This sample is subsequently ground until all of it passes through the 0.4 mm sieve and dried again at 110°C for 48 h. Three 4-g aliquots obtained by quartering of this sample were used for the determinations.
- Suspension preparation: the pycnometer is half filled with deionised water and weighed ( $W_b$ ). About 4 g of the soil previously prepared are added to the pycnometer. The pycnometer with water and sample is weighed ( $W_c$ ). The weight of the sample ( $W_s$ ) is computed as  $W_c - W_b$ . In order to eliminate the air trapped in the suspension, this procedure is followed:
  1. The pycnometers with the sample and water inside are agitated on a vibrating shaker for 24 hours.
  2. Sonicate pycnometers for 15 min to reduce the air content.
  3. Finally, the pycnometers are placed inside a desiccator connected to a vacuum extraction system. The pressure value is reduced until getting close to the boiling point (below 25 mbar) in order to achieve the elimination of air. Between 1.5 and 2 h are needed, depending on the sample.
- Final weighing and volume computation: the pycnometer containing water and sample is completely filled with de-aired, deionised water and weighed ( $W_d$ ). The weight of the volume of water equivalent to the soil volume ( $W_{dw}$ ) (at 20°C) is determined as:  $W_{dw} = W_a + W_s - W_d$ . This weight is converted into volume ( $V_s$ ) by using a water specific gravity of 1 g/cm<sup>3</sup>.

The specific weight of solid particles is finally computed as the ratio  $W_s/V_s$ . All measurements of water and solids weight were made at a fixed temperature of 20°C.

### 3.1.5 Measurement of basal spacing

The (001) reflection or basal spacing gives the distance along the crystallographic c-axis between clay lamellae, and for a given clay depends on the exchangeable cations present in the interlayer and their degree of hydration.

From all the blocks sampled at CIEMAT, subsamples were preserved in paraffined foil and the X-ray profile of a plane surface of them was registered at laboratory temperature after removing the foil and without any further treatment. An anticatode of Cu ( $\text{CuK}\alpha$ ) radiation was used with a Philips model X'Pert-MPD diffractometer at 40 mA, 45 kV operating condition. X-ray diffraction (XRD) experimental profiles were obtained with a 0.1 mm entrance slit and a scanning rate of 0.025 °2 $\theta$ /s. Data were collected between 2 and 10°2 $\theta$ . The goniometer settings

were: automatic divergence slit and diffracted beam slit 2 mm. The position of the peaks was adjusted by using the quartz in the samples as an internal standard. The complete mathematical description of the scan pattern was obtained by combining a polynomial function that describes the background and a profile function that fits the experimental peaks in order to obtain better peak parameters (peak position, net intensity and full width at half maximum (FWHM)). The pseudo-Voigt profile function, which is the weighted mean between a Lorentz and a Gaussian function, was used to fit the peaks as well as to deconvolute overlapped peaks.

After the determination of the water retention curves (subchapter 4.4.1) and the consolidation tests (subchapter 4.5.3), a fragment of the samples tested was also used for measuring the basal spacing. For these samples an anticathode of Cu ( $\text{CuK}\alpha$ ) radiation was used with a Bruker D8 Advance diffractometer at 40 mA and 40 kV operating conditions. XRD experimental profiles were obtained with a 1 mm entrance slit,  $0.05^\circ$   $2\theta$  step size and a counting time of 3 s per step. Data were collected between  $2$  and  $30^\circ$   $2\theta$ , except for the samples from the consolidation tests BB-47-7-2 and BB-47-8-2, for which the data were collected between  $2$  and  $10^\circ$   $2\theta$ . Goniometer settings were fixed divergence slit and diffracted beam slit, both of 1 mm. A profile function was fitted to the observed intensities to obtain better peak parameters (peak position, net intensity and full width at half maximum (FWHM)) completely describing the measured scan. The Pearson VII function was used. It was also used to deconvolute overlapping peaks.

### 3.1.6 Pore size distribution

The pore size distribution of each subsample was determined by mercury intrusion porosimetry (MIP). This technique determines the pore size distribution by injecting mercury into the sample at different pressures while controlling the volume intruded. The pressure applied may be related to the minimum pore diameter intruded, taking into account the characteristics of the fluid. The ratio of the volume of mercury intruded (pore volume) to the applied pressure (which conditions the minimum pore diameter) allows obtaining distribution curves thereby establishing the percentage of a specific pore size included within a given range.

In order to alter as least as possible, the clay microstructure during drying, the samples were put in the ice condenser of a Telstar LioQuest equipment at  $-50^\circ\text{C}$  for 3 h. Afterwards they were lyophilised for 19 h at a temperature of  $-50^\circ\text{C}$  under a vacuum of 0.2 mbar, so to eliminate the water in the pores by sublimation. Before the MIP tests the samples were heated to  $35^\circ\text{C}$  for 2 h. The porosimeter used was a Micromeritics AutoPore Series IV 9500, which allowed the exploration of pore diameters between 0.006 and 600  $\mu\text{m}$ . Prior to mercury injection the sample was outgassed by applying a vacuum of 50  $\mu\text{m-Hg}$ . Afterwards the mercury injection pressure was increased from 2.7 kPa to 220 MPa in 109 steps. To determine the extrusion branch of the curve, the pressure was released in 56 steps down to a pressure of 68.6 kPa. An advancing and receding contact angle of mercury on the clay surface equal to  $139^\circ$  was considered.

The mercury intrusion method only accesses the macroporosity and part of the mesopores (those of sizes between 50 and 6 nm), since mercury does not intrude the microporosity (pores of a size of less than 2 nm, according to the classification of Sing et al. 1985). In the high-density clay materials retrieved from the FEBEX-DP, pores larger than those quantifiable by MIP are not expected. However, the pores connected to the external surface by narrow openings will not be intruded until sufficient pressure is applied to intrude the entryways. All of the volume of such pores will be allocated to the threshold radius class of the most restricted part of the entryway (bottleneck effect). Nevertheless, considering that most of the non-intruded porosity corresponds to pores with sizes smaller than the limit of the apparatus, an estimation of the percentage of pores actually intruded can be made by comparing the actual void ratio of the

samples ( $e$ , computed from their dry density and density of solid particles) and the apparent void ratio calculated from mercury intrusion ( $e_{nw}$ , mercury being a non-wetting ( $_{nw}$ ) fluid). Thus, the pore size distribution curves obtained by MIP were corrected to take into account the percentage of pores not intruded.

### 3.1.7 Specific surface area

The specific surface area (SSA) of the bentonite samples was determined using the BET method (Brunauer et al. 1938) that analyses the adsorption isotherms of nitrogen gas. This parameter represents the external surface ( $a_s$ ), i.e. the surface of the intra-aggregate and inter-aggregate voids but not that of the interlayer space. Thus, it is a measure of the available area for solute transport in the compacted bentonite and of the degree of coherent stacking of smectite platelets (Sposito 1992).

- The sorption isotherms were determined in an ASAP 2020 of Micromeritics (Fig. 23). The unaltered samples (i.e. not ground) were lyophilised prior to degassing. Samples of between 0.8 and 1.8 g were degassed at 90°C for the time necessary to reach a vacuum of 50  $\mu\text{m Hg}$ , which was kept for 10 min. Afterwards the samples were kept at 90°C under vacuum for 8 h. The isotherms obtained had 55 points, 32 in the range of relative pressures between 0.01 and 0.995 and 23 points in the range 0.995 and 0.14. The BET method was applied in the range of  $P/P_0$  0.06-0.2.



Fig. 23: Equipment used for the determination of  $\text{N}_2$  sorption isotherms (Micromeritics ASAP 2020)

## 3.2 Hydraulic properties

### 3.2.1 Water retention curves

The water retention curves (WRC) were determined with the aim of checking the effect of prolonged drying on the water retention capacity of the bentonite. For this reason, samples from the internal ring of the barrier in contact with the liner were tested. The three blocks in contact with the liner in sections S47 and S53 were sampled, but also two blocks close to the axis of the gallery in cool section S59 (Fig. 10, Tab. 4). These two blocks had water contents close to those blocks taken from sections S47 and S53 and were sampled to check the effect of the thermal

treatment on the water retention capacity, since the blocks from sections S47 and S53 were submitted to much higher temperatures during operation than those from section S59 (Tab. 2). Two samples were obtained by drilling from each block with a crown drill bit of internal diameter 4.5 cm. In the blocks from section S47 these two samples were drilled at two different distances from the axis of the gallery, 1 and 2, as shown in Fig. 16. In the rest of the blocks the two subsamples, a and b, were drilled at the same distance from the gallery axis but at different depths in the block. The cores obtained were trimmed with cylindrical cutters to adjust their diameter to 3.8 cm and pushed into stainless steel rings which are the body of a cell (Fig. 24, left). The height of the resulting bentonite cylinders was between 1.1 and 1.3 cm. Filter papers and porous plates were placed on top and on the bottom of the sample and the steel covers of the cell were tightened. The cells were placed in desiccators with sulphuric acid solutions (Fig. 24, right), to apply a given suction to the samples by controlling the relative humidity (vapour transfer technique). The relative humidity inside the desiccators is related to total suction through Kelvin's equation (Eq. 2).

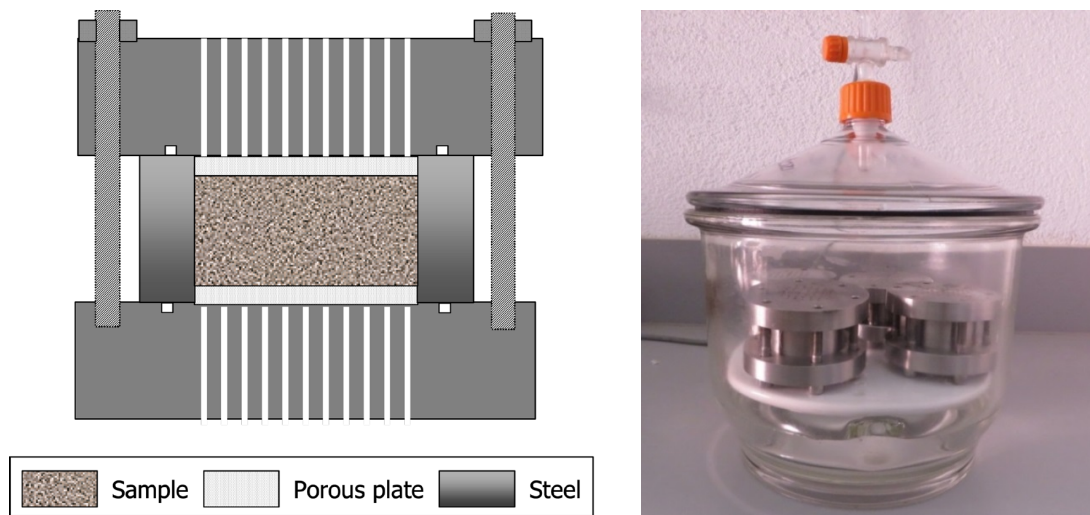


Fig. 24: Schematic representation of the constant volume cell for WRC determination (left) and desiccator with perforated cells inside (right)

The samples were initially submitted to suctions of 19-23 MPa, which were suction values measured in the blocks following the procedure described in section 3.1.2. Afterwards, the samples were submitted progressively to lower suction values. The evolution of water content in the samples was checked by periodical weighing, and the suction step was not changed until stabilisation was reached. Once equilibrium was reached for the final suction value, the cells were opened, the samples were extracted by pushing with a hydraulic press and they were weighed, and their dimensions measured. Small parts of the samples were used for measurement of the basal spacing and determination of the pore size distribution according to the procedures described in 3.1.5 and 3.1.6. All the remaining part of the samples was used for water content determination.

The final density of the sulphuric acid solution in the desiccator was checked using a Density Meter (A-110M-Mettler Toledo,  $\pm 0.0001 \text{ g/cm}^3$  resolution). From this the water activity of the solution ( $a_w = RH/100$ ) can be computed, and this gives the value of suction to which the samples were subjected through Kelvin's law (Eq. 2). The lowest suction value applied was 0.47 MPa,

corresponding to a RH of 99.67% (Eq. 2). This RH was generated using a  $10^{-4}$  M NaCl solution. The determinations were performed at 20°C.

### 3.2.2 Hydraulic conductivity

The hydraulic conductivity was measured in 17 samples taken from sections S47 and S53 at different distances from the heater. It was measured according to a method developed at CIEMAT for expansive soils (Villar 2002). The method is based on the theoretical principle of the constant head permeameter. Basically, it consists in measuring against time the volume of water that passes through a specimen, confined in a rigid cell preventing it from deforming, to which a constant hydraulic gradient between the upper and lower parts is applied. The complete saturation of the sample and associated swelling guarantee perfect contact with the walls of the cell, preventing the flow of water between these and the sample. At the same time, the flow of water passing through the specimen is measured versus time.

The measuring system consists of the following elements (Fig. 25):

- Stainless steel cell with water inlet and outlet, in which the sample is confined. It comprises a ring with covers tightened with rods. The nominal dimensions of the sample are 19.63 cm<sup>2</sup> in surface area and a length about 2.5 cm.
- An injection pressure system. An oil/water pump or a piston pump connected to the bottom of the cell was used for this purpose, in the first case with an intermediate exchanger that separated the water in the pressure system from the deionised water injected to the sample.
- A GDS pressure/volume controller to apply the downstream pressure on top of the sample and at the same time measure the water outflow. The GDS controller allows fixing the pressure with an accuracy of 1 kPa and measuring water volume changes resolved to 1 mm<sup>3</sup>.
- Data acquisition system to record the water outflow.

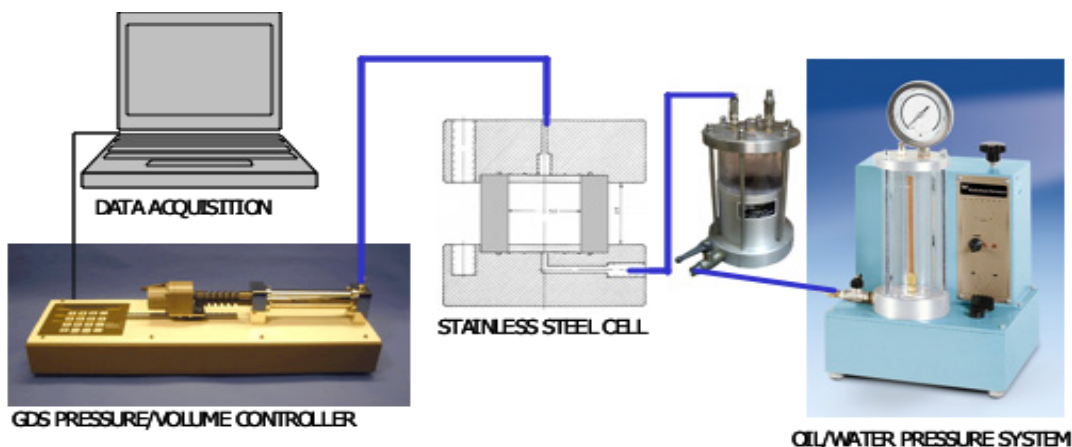


Fig. 25: Schematic representation of the setup for permeability measurement of expansive soils (using an oil/water pump to apply injection pressure and a pressure/volume controller for backpressure application and outflow measurement)

The samples were drilled at two locations in each block using a crown drill bit of 5.7 cm internal diameter (Fig. 26) and were later adapted to the diameter of the cell ring by working them with a cylindrical cutter, attempting not to modify either their moisture or density. They were then pushed inside the cell ring (Fig. 27), filter papers and porous stones were placed on top and on the bottom and the covers of the cell were tightened.



Fig. 26: Drilling of cores to obtain samples for the hydraulic conductivity tests



Fig. 27: Appearance of the samples drilled from the blocks inside the permeability cell rings

The sample was saturated from both faces with deionised water injected at a pressure of 0.6 MPa over the necessary time period. This was checked by measuring the water intake until stabilisation. Once the sample was saturated, a hydraulic gradient was applied by increasing the pressure at the bottom of the cell ( $P_i$ ), while the downstream pressure on top was maintained lower ( $P_b$ ). In this way a hydraulic head corresponding to the difference between the lower and

upper pressure ( $\Delta P = P_i - P_b$ ) was achieved. The supposedly linear hydraulic gradient is the ratio existing between the hydraulic head and the length of the specimen, the values applied in these tests being of between 1600 and 11700. The water volume passing through the sample was measured online. The tests ran over a time period long enough to determine a stable volume of water passing through the specimen for a given hydraulic gradient. Two or three different hydraulic gradients were applied to each sample.

Once constant flow was achieved, the volume of water passing through the sample ( $\Delta V$ , cm<sup>3</sup>) was determined over a given time period ( $\Delta t$ , s). Hydraulic conductivity  $k_w$  (cm/s) was calculated by applying Darcy's law for flow in porous media (Eq. 3):

$$k_w = \frac{\Delta V \times l}{A \times \Delta t \times \Delta P} \quad (\text{Eq. 3})$$

where  $\Delta P$  is the hydraulic head in cm of water,  $A$  is the surface area of the cell (19.63 cm<sup>2</sup>) and  $l$  the length of the specimen (in cm).

The tests were performed at room temperature. At the end of the test, the sample was weighed, measured and oven-dried at 110°C for 48 h to check the actual water content.

### 3.2.3 Gas permeability

Two different experimental setups were used to determine the gas permeability, a low-pressure and a high-pressure one. The aim of the tests performed in the low-pressure equipment was to determine the influence of water content and degree of saturation on gas permeability, whereas the aim of the tests performed on the high-pressure permeameter was to analyse the effect of boundary conditions, such as gas pressure and confining pressure, on gas permeability. Since most of the samples were close to saturation, it was expected that the permeabilities would be very low or even zero. In those cases, the aim of the tests was to determine the breakthrough pressures, which could only be done with the high-pressure equipment.

When there are two fluids present in the porous material (gas and water in this case), the permeability of each fluid depends upon the saturation of the material in each fluid: these are called apparent (or effective) permeabilities. Hence, the value obtained in the determinations (apart from the gas permeability,  $k_g$ ) is the intrinsic permeability measured with gas flow,  $k_{ig}$ , multiplied by the relative permeability to gas,  $k_{rg}$ . In turn, the relative permeability to gas is the ratio of the apparent (effective) permeability of gas at a particular saturation to the absolute permeability of gas at total gas saturation, *i.e.* in completely dry material, where the  $k_{rg}$  value would be 1.

Most samples were initially tested in the low-pressure equipment and afterwards in the high-pressure equipment. The first device worked as an unsteady-state (or falling-head) permeameter in which only pressure was measured (LP). The second one was used under two major different configurations: as an unsteady-state permeameter, in which only pressures were measured (HP-US), and as a steady-state (constant-head) permeameter (HP-S) in which pressure and gas flow were measured. The second configuration consisted of two lines, a low confining pressure one (LCP) and a high confining pressure one (HCP). Tab. 6 shows the experimental setups used and their characteristics, which are described in more detail below.

Tab. 6: Characteristics of the experimental setups used for the gas permeability tests

Equipment		Working principle	Variables measured	Range confining P (MPa)	Range injection P (MPa)
LP		Unsteady-state permeameter	Pressure	0.6-1.0	<0.1
HP-US		Unsteady-state permeameter	Pressure	1.0-14.0	0.2-13.0
HP-S	LCP	Steady-state permeameter	Pressure, gas flow	0.6-2.0	0.1-0.6
	HCP	Steady-state permeameter	Pressure, gas flow	0.6-9.0	0.1-1.2

Two kinds of samples were used: core samples drilled on site and core samples drilled from blocks in the laboratory. Most of the samples tested were drilled on site in the same sections where the blocks for THM and THG characterisation were taken, i.e. S36, S44, S47, S50, S53, S57 and S59. Half of them were drilled in the middle of blocks and the other half at the contact between two blocks, so as to have a vertical interface along the core (Fig. 28, left). The other group of samples, only a few of them, was drilled in the laboratory from blocks received for the THM and THG determinations (Fig. 28, right).

To prepare the samples the core diameter was fit to that of the testing cells (36 or 50 mm) by using a cutting ring and a knife (Fig. 29) and sand paper in some cases. The cylindrical surface of the samples was smoothed and the parallelism of the cylinder's ends was assured. The resulting specimens were between 2.4 and 5.2 cm in height and 10-20 cm<sup>2</sup> in surface area. In some cases the interface along the core became evident only after preparing the specimen (Fig. 30). In order to determine the initial water content and dry density of the samples, a small spare fragment resulting from the sample preparation was used.



Fig. 28: Sample drilled on site at the contact between blocks (left) and in the laboratory (right)



Fig. 29: Sample preparation: adjusting the diameter



Fig. 30: Appearance of a specimen prepared for gas test with interface between blocks

Filter paper and porous plates were placed on top and on the bottom of the samples. Perforated PVC discs were used in some cases to adapt the specimen height to the cell dimensions. The assemblage thus prepared was laterally wrapped in different ways. Some samples were laterally wrapped in double latex membranes or in EPDM ([ethylene propylene diene](#) monomer) rubber over a latex membrane. Other samples were wrapped in duct tape and finally in an EPDM rubber membrane. Vacuum grease was applied between membranes in order to prevent the loss of gas. The wrapped samples were placed in triaxial cells that were filled with water and pressurised to ensure perfect adherence of the membranes to the surface of the sample. The subsequent procedure for each setup (Tab. 6) is described in the following subsections.

At the end of the tests, the bentonite specimens were measured and weighed and the water content and dry density at three different levels (two, if they were too short) along the cylindrical specimens were determined. To determine the dry mass of the samples they were oven-dried at 110°C for 48 h, and to compute the dry density, the volume of the same specimens was determined by immersing them in mercury prior to drying.

### Low-pressure equipment (LP)

Once the triaxial cell was filled with water and pressurised, the inlet at the lower part of the sample was connected to an airtight tank of known volume, in which nitrogen gas was injected at a pressure slightly higher than atmospheric. The tank was has a pressure sensor connected to a data acquisition system which recorded the pressure of the fluid contained inside. The inlet at the upper part of the sample was left open to the atmosphere. The test consisted of allowing the air in the tank to go out to the atmosphere through the specimen, while the decrease in pressure in the tank was measured as a function of time. The tests were performed at constant, room temperature. Prior to the permeability test, the airtightness of the system was checked for every new test. The cartoon of the assembly for the low-pressure determination is shown in Fig. 31.

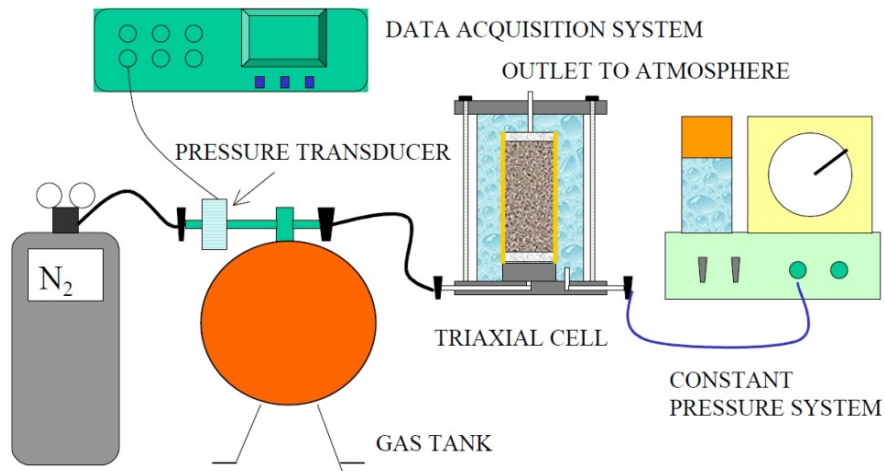


Fig. 31: Schematic representation of the low-pressure gas permeability system

The gas permeability was calculated in accordance with the following equation (Yoshimi & Osterberg 1963; Eq. 4):

$$k_{ig} \cdot k_{rg} = 2.3 \times \frac{V \times L \times \mu_g}{A \times \left( P_{atm} + \frac{P_0}{4} \right)} \times \frac{-\text{Log}_{10} \left( \frac{P(t)}{P_0} \right)}{t - t_0} \quad (\text{Eq. 4})$$

where  $k_{ig} \cdot k_{rg}$  is the effective permeability to gas (m<sup>2</sup>),  $V$  the volume of the tank (m<sup>3</sup>),  $L$  the length of the sample (m),  $A$  the surface area of the sample (m<sup>2</sup>),  $\mu_g$  the dynamic viscosity of nitrogen ( $1.78 \cdot 10^{-5}$  Pa·s),  $P_{atm}$  is atmospheric pressure (Pa),  $P_0$  is the excess pressure over atmospheric pressure at time  $t_0$  (s) and  $P(t)$  is the excess over atmospheric pressure in the tank at time  $t$ . The volume of the spherical tank used was  $2.21 \cdot 10^{-2}$  m<sup>3</sup> and the gas used for the tests was nitrogen, for which a density of  $1.12$  kg/m<sup>3</sup> was taken.

Taking into account the density of nitrogen ( $\rho_g$ ,  $1.12$  kg/m<sup>3</sup>), the following relation between gas permeability ( $k_g$ , m/s) and the product of intrinsic permeability measured with nitrogen gas ( $k_{ig}$ , m<sup>2</sup>) times the relative permeability to gas ( $k_{rg}$ ) is obtained (Eq. 5):

$$k_g = \frac{\rho_g \times g}{\mu_g} \times k_{ig} \cdot k_{rg} = 6.2 \cdot 10^5 \times k_{ig} \cdot k_{rg} \quad (\text{Eq. 5})$$

The triaxial cell was initially pressurised to 0.6 MPa and gas was injected at a pressure close to 0.1 MPa through the bottom of the sample. If flow took place, the confining pressure was increased to 1 MPa, and the test was repeated. Afterwards, the cell with the sample was moved to the high-pressure equipment.

### High-pressure equipment (HP)

Two different configurations of the gas permeability setup were used for these tests, which were performed on the same samples previously tested in the low pressure equipment described above (LP). The details of the experimental setups and equations used to compute permeability are given in Villar et al. (2013). For all the configurations, a data acquisition system under LabView running on a PC recorded the data and monitored the tests in progress.

The first tests were performed in a setup in which a small gas cylinder was connected to the upper part of the sample, the pressure in it was initially fixed with nitrogen gas to 200 kPa and allowed to decrease as flow took place through the sample, following the working principle of an unsteady-state (falling-head) permeameter (HP-US). Another small cylinder was connected to the bottom of the sample and initially set under vacuum. If no changes in pressure were recorded for 24 h, the injection pressure was increased by 200 kPa. The process was repeated until gas started to flow through the sample, causing a decrease of pressure in the upstream cylinder and an increase in the downstream one. The pressure change in the cylinders was converted to flow (mean volume flow rate  $Q_m$ ) using the following Equation 6 (Loosveldt et al. 2002):

$$Q_m = V_v \times \left( \frac{\Delta P}{P_{av}} \right) \times \frac{1}{\Delta t} \quad (\text{Eq. 6})$$

where  $V_v$  is the volume of the cylinder,  $\Delta t$  is the time interval in which the change in pressure took place,  $\Delta P$  is the pressure change and  $P_{av}$  is the average pressure (upstream or downstream) in the cylinder (inlet or outlet) during the time interval considered.

To compute permeability the gas inflow or outflow can be used, applying the following equation for incompressible media with compressible pore fluids (Scheidegger 1974; Eq. 7):

$$k_{ig} \cdot k_{rg} = \frac{Q_m \times \mu_g \times L \times 2 P_m}{A \times (P_{up}^2 - P_{dw}^2)} \quad (\text{Eq. 7})$$

where  $Q_m$  is the flow obtained applying Equation 6 (other symbols as in Equation 4).

At a later stage the setup was modified and flowmeters were installed to measure gas outflow. Under this configuration the tests were performed by keeping constant confining and injection pressures and atmospheric backpressure, i.e. following the working principle of a steady-state (constant-head) permeameter (HP-S). The setup consisted of two lines that allowed performing two tests simultaneously. In one of the lines the injection pressure could reach values of up to 12 MPa and the confining pressure, which was applied with a pressure/volume piston controller,

of up to 16 MPa (low confining pressure setup, LCP). In the other line (Fig. 32), the injection pressure could reach 24 MPa and the confining pressure could be increased to as high as 33 MPa (high confining pressure setup, HCP).

Outflow gas rates, upstream and downstream pressure, confining pressure and temperature were monitored online. To compute the apparent (or effective) permeability, the inflow or outflow measurements could be used in Equation 7. The values computed from the outflow ( $Q_m$ ) have been used in this work. In this kind of test,  $P_{dw}$  is the actual atmospheric pressure (because the inlet for the sample bottom was opened to atmosphere), and  $P_m$  is the atmospheric pressure, because of the measurement conditions of the gas mass flowmeters.

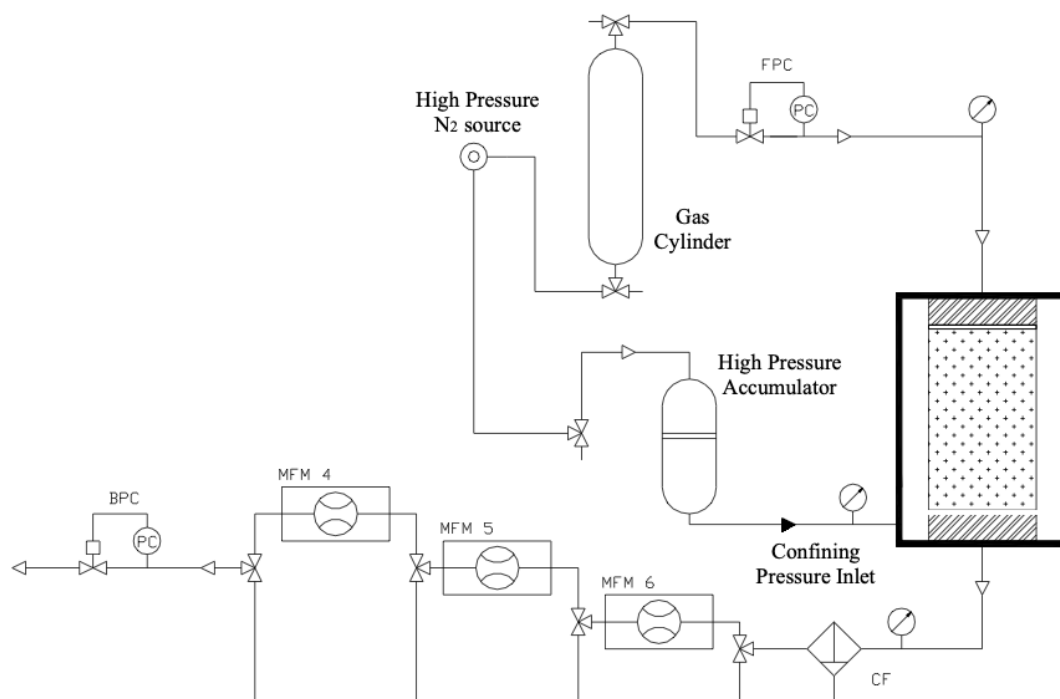


Fig. 32: Experimental setup of the high confining pressure line (HCP) (CF: coalescing filter, FPC: forward-pressure controller, BPC: back-pressure controller, MFM: mass flow meter)

To analyse the effect of injection and confining pressures on permeability, the tests consisted of several steps. Usually the tests started under confining pressure of 0.6 or 1 MPa (depending on the last confining pressure applied in the low-pressure equipment) and atmospheric backpressure. In most tests the injection pressure was initially set to 0.1 MPa and increased by 0.1 MPa every step until flow took place or was sufficiently high to be correctly measured ( $\sim 0.5$  mL/min). If noticeable flow had been reached, and the difference between confining and injection pressure was below a certain value (0.2 MPa in most cases), the confining pressure was progressively increased until gas could not flow through the sample. Finally, the confining pressure was stepwise released.

### 3.3 Mechanical properties

#### 3.3.1 Swelling under load tests

The saturation (or swelling) under load test makes it possible to determine the strain capacity of the soil when it saturates under a previously established pressure. The swelling capacity was tested under a vertical load of 0.5 MPa on 20 samples taken at different distances from the heater from three different sections (S36, S47 and S53). Additionally, it was measured in six samples from section S36 to check the effect of the proximity to the shotcrete (three of them under a vertical stress of 50 kPa) and in two “oxidised” samples from section S59 and two others from section S36.

The tests were performed in standard oedometers (Fig. 33) following approximately ASTM D 4546-03 Method A. Two samples from each block (external and internal position) were drilled at two locations using a crown drill bit of either 5.7 or 4.5 cm internal diameter (Fig. 26), and were later adapted to the diameter of the oedometer ring, which was between 3.6 and 5.0 cm, by working them with a cylindrical cutter, attempting not to modify either their moisture content or density. They were then pushed inside the oedometer ring (Fig. 34). Once in the oedometer, a vertical pressure of 0.5 MPa was applied to the samples. After stabilisation of the deformation, the samples were saturated with deionised water at atmospheric pressure from the bottom porous plate. The swelling strain experienced by the specimens on saturation was recorded by linear strain transducers connected to a data acquisition system. During most of the tests, the electrical conductivity of the water in the oedometer cell’s reservoir was measured with an electrical conductivity meter, which was submerged in the oedometer water every time the reservoir was refilled with deionised water (Fig. 33, right). Water refilling was done to keep the water level in the cell always approximately constant.

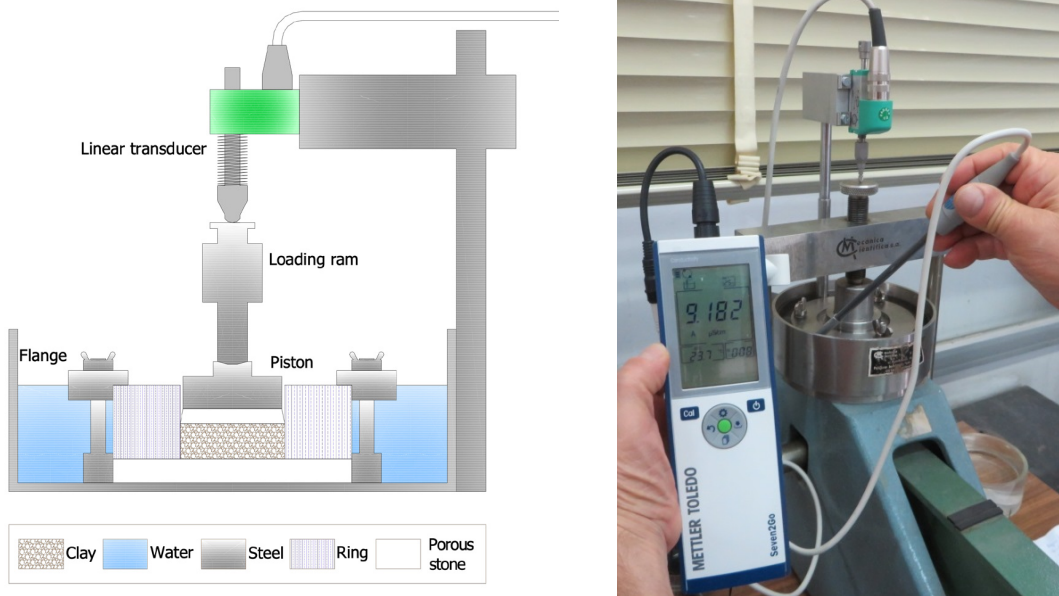


Fig. 33: Schematic cross-section of an oedometric cell (left) and daily measurement of electrical conductivity of the water in the cell (right)

The ratio between the final length increase undergone by the sample in equilibrium with the load applied and its initial length gives the strain value of the material on saturating, the negative values indicate swelling strains. The final result is, therefore, the percentage of strain of a sample of given initial dry density and water content on saturating under a fixed load. On completion of the tests, the height of the sample was checked and the water content of the specimen was determined by oven-drying at 110 °C for 48 hours. The tests were performed at laboratory temperature.



Fig. 34: Appearance of the base and the upper part of a sample inserted in the oedometer ring

### 3.3.2 Swelling pressure

The swelling pressure of two samples was tested in the standard oedometers described in the previous subchapter (Fig. 33). The procedure for preparation of the sample and mounting in the oedometer cell and frame was the same as described above. Once the oedometer cell was filled with deionised water, the deformation was continuously monitored and avoided by manually adding lead weights to the oedometer frame lever arm, with the aim of keeping the volume of the specimen constant during saturation. Ideally the vertical strain shall not drift excessively from  $\pm 0.005$  mm, thus preventing both the swelling and the consolidation of the sample. The test was considered to be completed when, under a constant vertical load, no strain was observed for at least 24 h. With this system the swelling pressure exercised by the sample is determined from the load that has to be applied in order for the volume of the sample to be kept constant during saturation, taking into account the sample surface area and the value of the lever arm. The deformation experienced by the equipment upon loading was previously calibrated and taken into account when the loads were added and for computation of the final strain of the specimens.

The electrical conductivity of the water in the oedometer was also checked periodically (Fig. 33, right). On completion of the tests, the height of the sample was checked and the water content of the specimen was determined by oven-drying at 110 °C for 48 hours. The tests were performed at laboratory temperature.

### 3.3.3 Swelling pressure and permeability tests

A custom-built high-pressure oedometer that keeps the samples at constant volume while measuring the water intake and the swelling pressure developed on saturation was used to

measure swelling pressure and hydraulic conductivity in four samples of the external ring of the barrier. This device observes the swelling pressure development kinetics on saturation, and once the sample is saturated, the hydraulic conductivity can be measured in the same equipment.

The tests were performed in the oedometer equipment shown in Fig. 35. The oedometer ring has 5.0 cm inner diameter, and the length of the specimens—which were obtained by trimming from the blocks as described above—was between 1.2 and 1.8 cm. The sample, confined between porous stainless steel sinters, was hydrated at constant volume through the bottom face with deionised water from a water column (pressure of 15 kPa), while the upper outlet remained open to atmosphere. At the same time, a load cell installed in the loading frame measured the swelling pressure exerted by the clay. The small vertical deformation of the specimen, due mainly to load cell and frame deformability, was measured by two linear strain transducers. An automatic volume change apparatus measured the water intake of the specimen. The values of load, strain and water intake were automatically recorded.

After complete saturation (which was assumed by the stabilisation of water intake and swelling pressure development), the pressure registered was considered the swelling pressure value for the dry density attained. The actual density may differ slightly from the initial one due to the small displacement allowed by the equipment (about 10  $\mu\text{m}$  when a vertical stress of 2.2 MPa is applied), and this is taken into account.

Afterwards, hydraulic conductivity was determined in the same equipment and on the same samples, which were kept at constant volume. In order to perform this determination, the water pressure at the bottom of the samples was increased to 2.0, 2.3 and 3.0 MPa consecutively, while a backpressure of 0.6 MPa was applied on top, resulting in hydraulic gradients between 8000 and 20000. The water outflow was measured with the same volume change apparatus used to measure the water intake during saturation. The hydraulic conductivity was calculated by applying Darcy's law for each installed gradient (Eq. 3).

On completion of the tests, the height of the sample was checked, and the water content of the specimen was determined by oven-drying at 110 °C for 48 hours. The tests were performed at laboratory temperature. The procedure followed is described in detail as CIEMAT's internal standard PT-MA-04-01 (Gómez-Espina & Villar 2008).

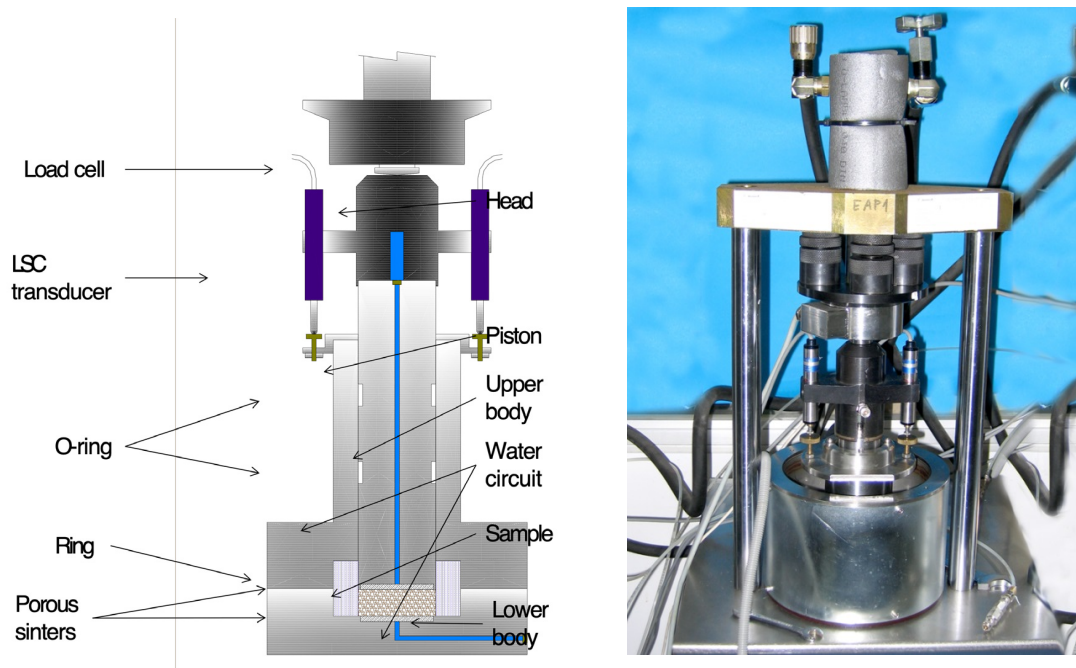


Fig. 35: Schematic layout and picture of the high-pressure oedometric equipment

### 3.3.4 Consolidation tests

The blocks installed in the FEBEX *in-situ* test at Grimsel were manufactured by applying uniaxial vertical pressures between 40 and 45 MPa (ENRESA 2000), which would correspond approximately to the preconsolidation stress of the clay. However, the modification of the structure of the sample –for example as a result of hydration under low load, with which more open structures with higher levels of porosity are obtained–, may cause the value of preconsolidation to decrease. This may be analysed through determination of the preconsolidation pressure ( $\sigma'_p$ ) in graphs showing the evolution of void ratio due to increasing load under constant suction. To this end, the preconsolidation pressure, pre- and post-yield compressibility of samples from Grimsel were determined under oedometric conditions and controlled suction pressure values. This knowledge verifies possible changes these parameters underwent during the long-term experiment, and thus identifies alterations on the hydro-mechanical properties of the bentonite.

To perform these tests, two oedometric cells (Fig. 36) adapted to withstand the high pressure supplied by an oedometric frame equipped with a load cell (Fig. 37) were used. Cylindrical samples of height between 1.4 and 1.8 cm and diameter 3.9 cm were drilled from the bentonite blocks and laterally sanded to fit the diameter of the oedometer ring (Fig. 38). The vertical deformation of the specimen during the test was measured by two LVDTs.

The samples were tested under the suction measured with psychrometers or capacitive sensors in the blocks from which they were taken (subchapter 3.1.2). The water content and dry density of the adjacent clay was checked. The suction inside the cells was set by means of sulphuric acid solutions. The sample was let to equilibrate at the target suction under a low vertical load. Afterwards, the sample was loaded progressively up to 32 MPa. Each loading step was kept until stabilisation of the deformation. The tests were performed at laboratory temperature.

Five samples taken at different distances from the heater along one sampling radius of section S47 and two samples from the reference bentonite were tested.

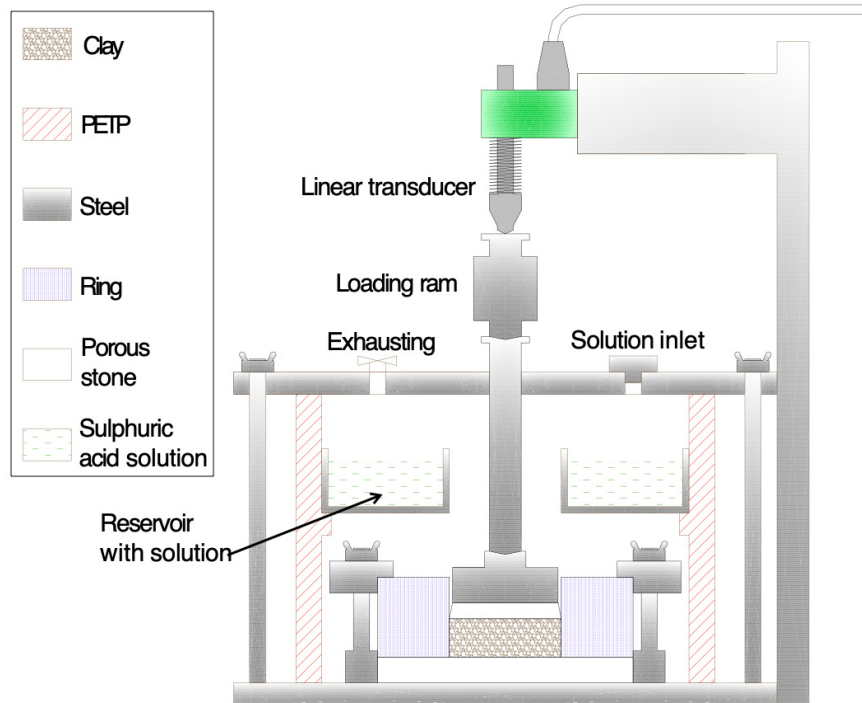


Fig. 36: Schematic cross-section of an oedometric cell with vessel for solutions



Fig. 37: Suction-controlled oedometer cells installed in the frames to perform high pressure consolidation tests



Fig. 38: Preparation of samples for the consolidation tests



## 4 Results

### 4.1 Calculating the degree of saturation

The bentonite water degree of saturation ( $S_r$ ), which is the ratio of volume of water to volume of voids, has been computed using Equation (8):

$$S_r = \frac{w \times \rho_d}{n} \quad (\text{Eq. 8})$$

where  $w$  is the water content,  $\rho_d$  is the dry density, and  $n$  is the porosity of the bentonite, in turn computed using the dry density and the solid specific weight ( $\gamma_s$ ). This Equation assumes that water has a density of 1 g/cm<sup>3</sup>. The degree of saturation obtained will depend thus on the solid specific weight used. If a value lower than the actual one were used, the degrees of saturation would be fictitiously high and *vice versa*. For the FEBEX bentonite used to manufacture the blocks placed at the GTS, a solid specific weight for the solids component of 2.70±0.04 g/cm<sup>3</sup> (average of 20 measurements) was determined in pycnometers using water for soil suspension (Villar 2002, ENRESA 2000, 2006). In 22 samples taken from Grimsel during the 2015 dismantling campaign, this parameter was determined again, and the same average value was found (see subchapter 4.2.2).

In addition to the uncertainties in the specific weight value determination, there is another reason for computing inaccurate degrees of saturation: the assumption of taking 1 g/cm<sup>3</sup> as the value for the density of the water. Although it is known to be higher in water adsorbed in bentonites. There is increasing evidence from the fields of neutron diffraction, Monte Carlo computer simulations and quasi-elastic neutron scattering that the density of water attached to clay minerals may be greater than 1.0 g/cm<sup>3</sup> (Skipper et al. 1991, Monsalvo et al. 2006, Chávez-Páez et al. 2001, Tambach et al. 2004, Huang et al. 1994), with values of water density in phyllosilicates of up to 1.38 g/cm<sup>3</sup>, higher in smectites with divalent cations in the interlayer (such as FEBEX) than with monovalent ones (Jacinto et al. 2012). This fact becomes more evident in highly compacted expansive clays close to water saturation, in which degrees of saturation much higher than 100% can be computed if a water density value of 1.0 g/cm<sup>3</sup> is considered (Villar 2002, Marcial, 2003, Lloret & Villar, 2007). Thus, a computed degree of saturation of 115% for a saturated sample would indicate that the average density of the water in it is 1.15 g/cm<sup>3</sup>. Furthermore, the proportion of adsorbed water (with a density higher than 1 g/cm<sup>3</sup>) over free water (with a density of 1 g/cm<sup>3</sup>) increases as the dry density of the bentonite is higher.

Since there is no accurate knowledge of the values that the density of water can take (which would depend on the particular bentonite, its density and water content), the customary value of 1 g/cm<sup>3</sup> has been used in the calculations presented in the following subchapters, which would partially explain the degrees of saturation higher than 100% found in some cases.

### 4.2 Basic properties

Blocks intended for THM and THG determinations were also sampled for water content and dry density, which were determined in two (three in some cases) different positions of each block along a radius (named 1 and 2, Fig. 16). Consequently, at least six determinations were made along a given radius of the barrier, whose length was about 114 cm in the sections without heater and 65 cm in the sections with heater. The values of water content ( $w$ ), dry density ( $\rho_d$ ) and degree of saturation ( $S_r$ ) obtained are shown in Tab. 7 and Tab. 8. The Tables also show the thermal conductivity ( $\lambda$ ), total suction, the specific weight of solid particles ( $\gamma_s$ ) and basal

spacing ( $d(001)$ ) measured in the same positions, which are analysed in other subchapters below.

Tab. 7: Summary of properties determined in the blocks sampled in sections S36, S44 and S47

Block reference	Distance <sup>a</sup> (cm)	Radius (Fig. 11)	$w$ (%)	$\rho_d$ (g/cm <sup>3</sup> )	$S_r$ (%)	$\lambda$ (W/m·K)	Suction (MPa)	$\gamma_s$ (g/cm <sup>3</sup> )	$d(001)$ (nm)
BB-36-1-1	111	B-C	29.1	1.51	100	1.26	4.6	2.66	
BB-36-1-2	102		27.7	1.55	101	1.27	4.9	2.70	
BB-36-2-1	87		27.0			1.25	5.2		
BB-36-2-2	77		26.3	1.58	100	1.18	4.3		
BB-36-3-1	67		27.5	1.55	101	0.98	5.4		1.554
BB-36-3-2	57		27.6	1.55	101	1.22	5.7		1.673
BB-36-4-1	111	D	33.4	1.42	100	1.11	3.1		1.734
BB-36-4-2	102		31.6	1.45	99		3.9		1.760
BB-36-5-1	87		27.3	1.55	99	1.20	5.4		1.699
BB-36-5-2	77		26.7	1.56	98	1.19	5.7		1.625
BB-36-6-1	67		27.5	1.53	98		5.3		
BB-36-6-2	57		27.6	1.54	99		5.7		
BB-36-9-1	111	F	31.4	1.47	102	1.22	3.7		1.634
BB-36-9-2	103		29.7	1.50	100		4.3		1.698
BB-36-9-3	96		29.0	1.52	100	1.17	4.8		1.664
BB-36-8-1	88		27.6	1.55	100	1.21	5.6		
BB-36-8-2	81		27.5	1.55	100		5.8		
BB-36-8-3	73		27.1	1.56	100	1.20	5.8		
BB-36-7-1	65		27.0	1.55	98	1.28	5.7		
BB-36-7-2	58		27.1	1.55	99		6.0		

Block reference	Distance <sup>a</sup> (cm)	Radius (Fig. 11)	w (%)	$\rho_a$ (g/cm <sup>3</sup> )	$S_r$ (%)	$\lambda$ (W/m·K)	Suction (MPa)	$\gamma_s$ (g/cm <sup>3</sup> )	$d(001)$ (nm)	
BB-36-7-3	50		27.3	1.54	97	1.20	5.4			
BB-44-1-1 <sup>b</sup>	111	B	28.3	1.54	101		5.7			
BB-44-1-2 <sup>b</sup>	102		27.3	1.56	101		5.3			
BB-44-3-1 <sup>b</sup>	67	B	22.0	1.64	92		23.0			
BB-44-3-2 <sup>b</sup>	57		22.0	1.63	91		23.2			
BB-47-1-1	111	B	28.1	1.54	100	1.18	4.9		1.711	
BB-47-1-2	102		26.3	1.56	97	1.26	5.0		1.671	
BB-47-2-1	87		24.5	1.61	97	1.20	18.8		1.635	
BB-47-2-2	77		23.4	1.62	96	1.18	20.9		1.569	
BB-47-3-1	67		22.2	1.65	94	1.17	29.2		1.584	
	62		21.5	1.64	90		28.8			
BB-47-3-2	57		20.8	1.63	86	1.06			1.727	
BB-47-4-1	111		D	26.5	1.56	98	1.22	3.7	2.71	1.608
BB-47-4-2	102			25.6	1.57	95	1.21	1.6	2.72	1.646
BB-47-5-1	87			23.9	1.60	93	1.13	20.8	2.74	1.682
	82	23.8		1.60	94		20.1			
BB-47-5-2	77	23.8		1.60	94	1.14	20.4	2.74	1.632	
BB-47-6-1	67	19.4		1.65	82	1.10	43.5	2.76	1.563	
	62	18.7		1.65	79		46.1			
BB-47-6-2	57	18.1		1.65	76		49.8	2.77	1.674	
BB-47-7-1	111	E-F		27.7	1.54	99	0.84	4.5	2.72	1.746
BB-47-7-2	102			26.0	1.57	97	1.21	2.8	2.69	1.709

Block reference	Distance <sup>a</sup> (cm)	Radius (Fig. 11)	$w$ (%)	$\rho_d$ (g/cm <sup>3</sup> )	$S_r$ (%)	$\lambda$ (W/m·K)	Suction (MPa)	$\gamma_s$ (g/cm <sup>3</sup> )	$d(001)$ (nm)
BB-47-8-1	87		24.9	1.60	98	0.93	19.3	2.72	1.680
BB-47-8-2	77		24.5	1.60	96	1.15	20.6	2.70	1.735
BB-47-9-1	67		20.0	1.62	81	1.20	28.1	2.61	1.615
BB-47-9-2	57		20.9	1.65	89		32.5	2.67	1.674

<sup>a</sup> approximate distance to gallery axis; <sup>b</sup> sampled 2 years after retrieving

Tab. 8: Summary of properties determined in the blocks sampled in sections S53, S57 and S59

Block reference	Distance <sup>a</sup> (cm)	Radius (Fig. 11)	$w$ (%)	$\rho_d$ (g/cm <sup>3</sup> )	$S_r$ (%)	$\lambda$ (W/m·K)	Suction (MPa)	$\gamma_s$ (g/cm <sup>3</sup> )	$d(001)$ (nm)
BB-53-1-1	111	B	28.1	1.54	100	1.12	2.7		1.643
BB-53-1-2	102		26.4	1.59	101	1.20	13.5		1.567
BB-53-2-1	87		24.3	1.62	98	1.19	21.5		1.700
BB-53-2-2	77		24.0	1.62	98	1.19	20.7		1.633
BB-53-3-1	67		22.8	1.65	98	1.22	22.9		1.574
BB-53-3-2	57		21.9	1.64	91	1.14	25.1		1.585
BB-53-7-1	111	E-F	27.7	1.54	99	1.21	5.2		1.672
BB-53-7-2	102		26.0	1.57	97	1.20	1.4		1.665
BB-53-8-1	87		24.3	1.62	99	1.24	17.2		1.611
BB-53-8-2	77		23.9	1.63	98	1.19	18.4		1.583
BB-53-9-1	67		20.8	1.66	90	1.18	31.3		1.575
BB-53-9-2	57		19.0	1.62	77	1.06	35.6		1.574
BB-53-4-1	111	D	26.5	1.59	103	1.24	2.4		
BB-53-4-2	102		25.5	1.59	99	1.16	0.4		

Block reference	Distance <sup>a</sup> (cm)	Radius (Fig. 11)	w (%)	$\rho_d$ (g/cm <sup>3</sup> )	$S_r$ (%)	$\lambda$ (W/m·K)	Suction (MPa)	$\gamma_s$ (g/cm <sup>3</sup> )	$d(001)$ (nm)	
BB-53-5-1	87		23.8	1.62	97	1.16	22.9		1.592	
BB-53-5-2	77		23.2	1.64	96	1.21	25.1		1.595	
BB-53-6-1	67		18.7	1.67	81	1.16	33.9		1.599	
BB-53-6-2	57		18.2	1.65	77	0.89	39.9		1.574	
BB-57-1-1 <sup>b</sup>	111	B	29.2	1.52	101		5.7			
BB-57-1-2 <sup>b</sup>	102		28.6	1.53	101		5.3			
BB-59-1-1	111	B	29.5	1.51	100	1.19	5.0	2.72	1.681	
BB-59-1-2	102		28.2	1.52	99	1.17	5.1	2.70	1.614	
BB-59-2-1	87		27.0	1.54	97	1.12	2.7	2.72	1.602	
BB-59-2-2	77		26.6	1.56	99	1.22	0.7	2.68	1.664	
BB-59-3-1	67		26.4	1.56	97	1.17	1.6	2.68	1.602	
BB-59-3-2	57		25.9	1.56	91	1.17	0.1	2.69	1.652	
BB-59-4-1	40		25.2	1.62	102	1.14	19.0		1.599	
BB-59-4-2	28		25.7	1.57	97	1.20	18.4		1.555	
BB-59-5-1	15		25.5	1.57	96	1.22	18.9		1.639	
BB-59-5-2	5		25.3	1.56	94	1.24	19.8		1.611	
BB-59-6-1	111		D	29.7	1.50	100	1.19	4.8		1.657
BB-59-6-2	102			28.1	1.52	98	1.21	2.6		1.656
BB-59-7-1	87	27.4		1.55	100	1.13	1.3		1.690	
BB-59-7-2	77	27.0		1.56	99	1.19	0.1		1.475	
BB-59-8-1	67	26.3		1.56	97	1.23	24.2	2.74	1.669	
BB-59-8-2	57	25.7		1.56	95	1.20	22.7		1.673	
BB-59-9-1	40	25.6		1.55	94	1.15	21.9	2.66	1.571	

Block reference	Distance <sup>a</sup> (cm)	Radius (Fig. 11)	w (%)	$\rho_d$ (g/cm <sup>3</sup> )	$S_r$ (%)	$\lambda$ (W/m·K)	Suction (MPa)	$\gamma_s$ (g/cm <sup>3</sup> )	$d(001)$ (nm)
BB-59-9-2	28		25.7	1.59	99	1.21	18.6		1.577
BB-59-14-1	15		25.4	1.58	97	1.15	18.5		1.664
BB-59-14-2	5		25.2	1.57	95	1.06	20.1		1.645
BB-59-10-1	111	F	31.1	1.48	102	1.13	4.7		1.466
BB-59-10-2	102		29.1	1.48	96	1.16	2.5		1.720
BB-59-11-1	87		28.2	1.53	100	1.24	3.5		1.652
BB-59-11-2	77		28.0	1.53	99	1.25	1.4		1.733
BB-59-12-1	67		27.2	1.54	98	1.25	14.4		1.644
BB-59-12-2	57		26.7	1.56	98	1.23	17.9		1.617
BB-59-13-1	40		26.3	1.56	98	1.24	16.3		1.761
BB-59-13-2	28		25.5	1.57	96	1.19	17.6		1.612

<sup>a</sup> approximate distance to gallery axis; <sup>b</sup> sampled almost 2 years after retrieving

#### 4.2.1 Water content and dry density

The results obtained for the different sections sampled are plotted in Fig. 39 to Fig. 42. The water content decreased from the granite towards the inner part of the barrier in all sections, whereas dry density increased. In the three radii sampled in every section the changes were similar. In the sections around the heater (S47 and S53) the change along the radii was approximately linear. The physical state of section S36 was conditioned by the fact that it was a section affected by Heater #1 for five years followed by 13 years of no heating. Section S59 was always a cool section and the water content in every point was much higher than the initial one (14%).

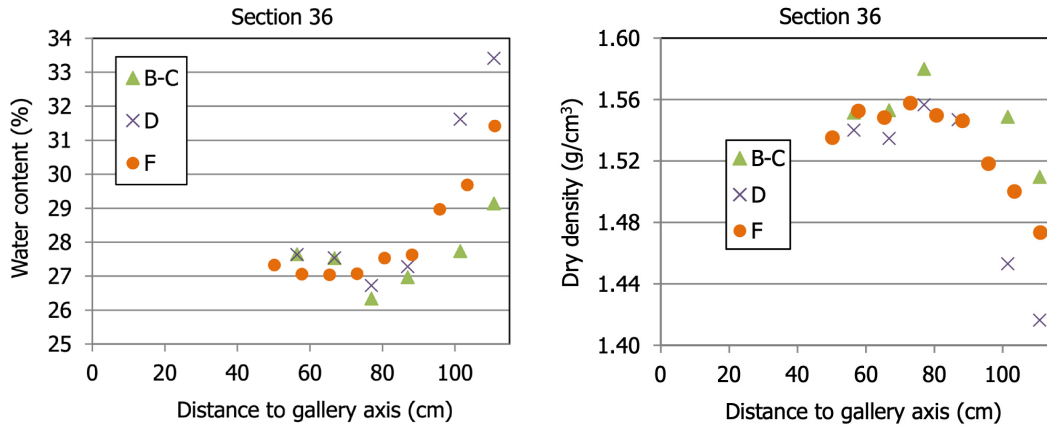


Fig. 39: Water content and dry density measured in the laboratory in blocks taken from section S36 (the sampling radii are indicated in the legend according to Fig. 11)

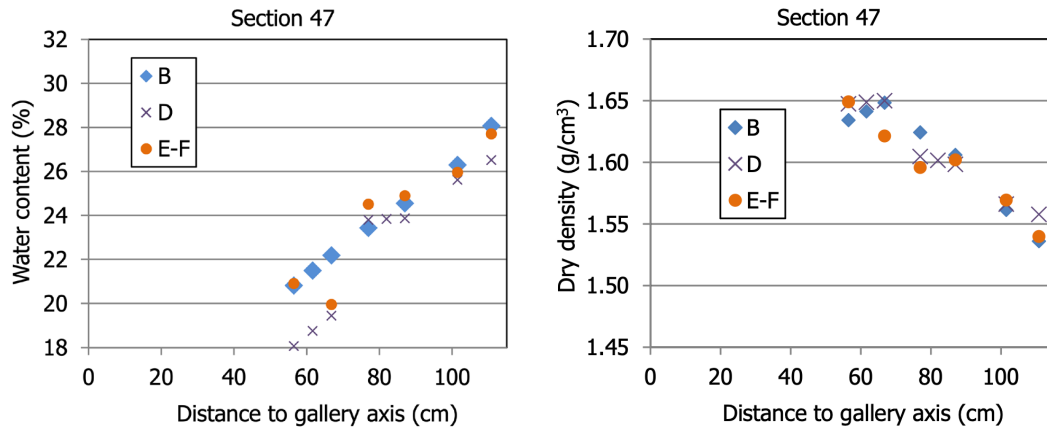


Fig. 40: Water content and dry density measured in the laboratory in blocks taken from section S47 (the sampling radii are indicated in the legend according to Fig. 11)

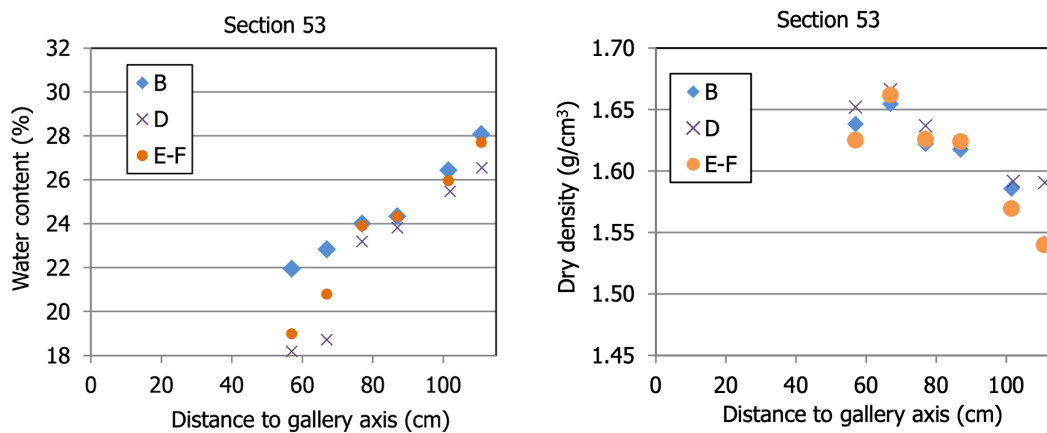


Fig. 41: Water content and dry density measured in the laboratory in blocks taken from section S53 (the sampling radii are indicated in the legend according to Fig. 11)

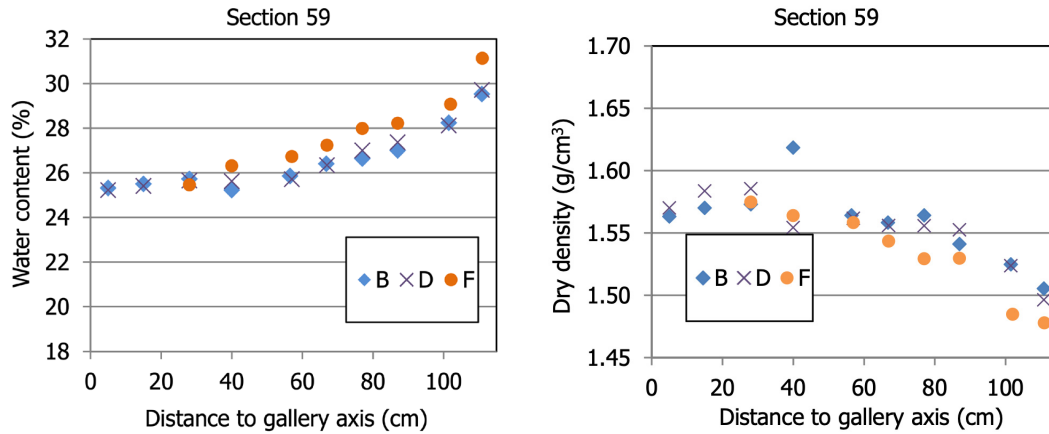


Fig. 42: Water content and dry density measured in the laboratory in blocks taken from section S59 (the sampling radii are indicated in the legend according to Fig. 11)

The thermal and hydraulic gradients during operation had caused significant water content changes in the barrier and hence, inside the blocks (Villar et al. 2016a). When the heater was switched off and the blocks retrieved, the thermal gradient disappeared, and this could trigger the homogenisation of the water content inside the blocks by pure diffusion. The time from the retrieving and packing of the blocks at the GTS and the sampling at CIEMAT’s laboratories varied between 74 to 189 days (Tab. 4). During this time the blocks were kept stored inside the vacuum-packed aluminium bags and water diffusion could take place inside them. This hypothesis has been analysed by comparing the relation between the water content measured in the external part of the block and that in the internal part (i.e. the part closest to the granite and the one closest to the axis of the gallery, subsamples 1 and 2, respectively, in Tab. 7 and Tab. 8, Fig. 17). In the sections around the heater, where the water content gradient was quite linear (Villar et al. 2016a), this ratio should be clearly higher than 1. The ratio between the water content in the external part of the block (subsample 1) and that in the internal part (subsample 2) has been computed and plotted in Fig. 43 as a function of the time since retrieval of the block to its sampling in the laboratory. The average values of this relationship for the blocks sampled on site in nearby sections have also been plotted. The value is clearly higher for the blocks sampled on site, which would mean that during the storage of the blocks prior to sampling in the laboratory, the water content tended to homogenise. The process must have started very quickly, since even the blocks sampled earlier after retrieving had lower water content gradient than the blocks sampled on site. Although not systematically, this gradient tends to be lower over time (values closest to 1), which suggests that the water redistribution was still taking place when the blocks were sampled in the laboratory. This water redistribution could also have resulted in some dry density changes inside the blocks.

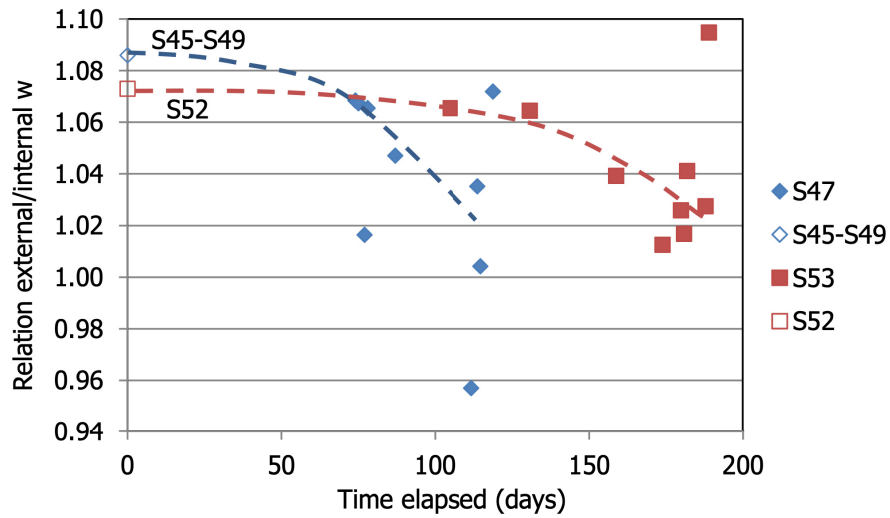


Fig. 43: Relationship between the water content determined in subsamples 1 and 2 of the blocks in the laboratory as a function of the time since their retrieval at GTS (filled symbols, sections S47 and S53). The values for time 0 correspond to the average value for this relationship obtained in the blocks of nearby sections analysed on site (S45-S49 and S52)

The results obtained in the laboratory have been compared with those obtained on site by AITEMIN for nearby sections (Villar et al. 2016a), which have been plotted in Fig. 44 to Fig. 46. The agreement between both measurements is very good, what suggests that the packing and transport conditions were appropriate to maintain the *in-situ* state of the blocks even several months after their retrieval. However, as it has been discussed above (Fig. 43), certain water content homogenisation took place inside the blocks that had been kept stored before sampling in the laboratory.

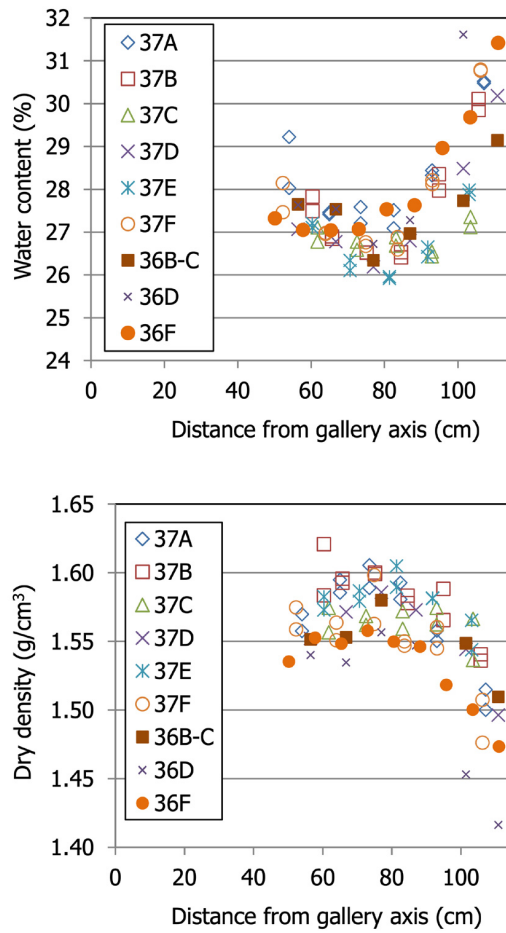


Fig. 44: Comparison of water content and dry density measured in close-by sections S36 (CIEMAT’s lab, filled symbols and small crosses) and S37 (on site). The sampling radii are indicated in the legend according to Fig. 11

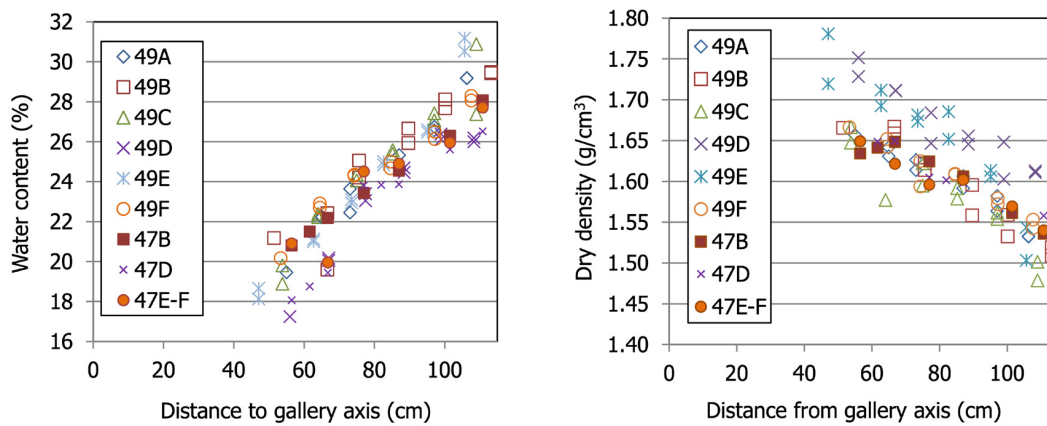


Fig. 45: Comparison of water content and dry density measured in close-by sections S47 (CIEMAT’s lab, filled symbols and small crosses) and S49 (on site). The sampling radii are indicated in the legend according to Fig. 11

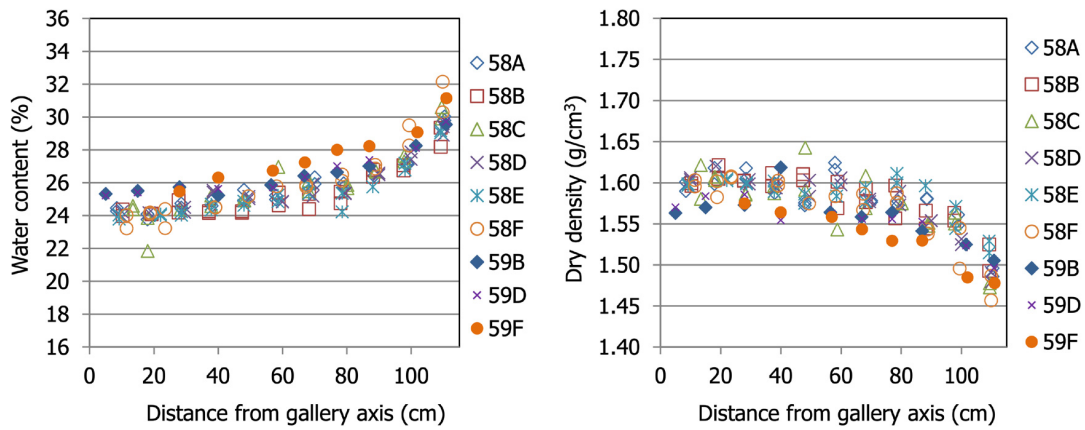


Fig. 46: Comparison of water content and dry density measured in close-by sections S59 (CIEMAT’s lab, filled symbols and small crosses) and S58 (on site) . The sampling radii are indicated in the legend according to Fig. 11

As it was mentioned at the beginning of Chapter 3, before subsampling the blocks in the laboratory, a qualitative measurement of their moisture was made with a microwave technique (Fig. 14), using the same equipment as during the dismantling at GTS, a Trotec T610. This was done in samples from section S53 and S59. The values obtained were correlated to the water content actually determined in the laboratory (shown in Tab. 7 and Tab. 8), as shown in Fig. 47 (left). The linear correlation shown in the Figure between the Trotec value (TV) and the water content ( $w$ , %) was used to compute the water content and compare it with the actually measured water content of the blocks (Fig. 47, right). A direct correlation with degree of saturation was also found, as well as an inverse correlation with dry density, although less good than for water content.

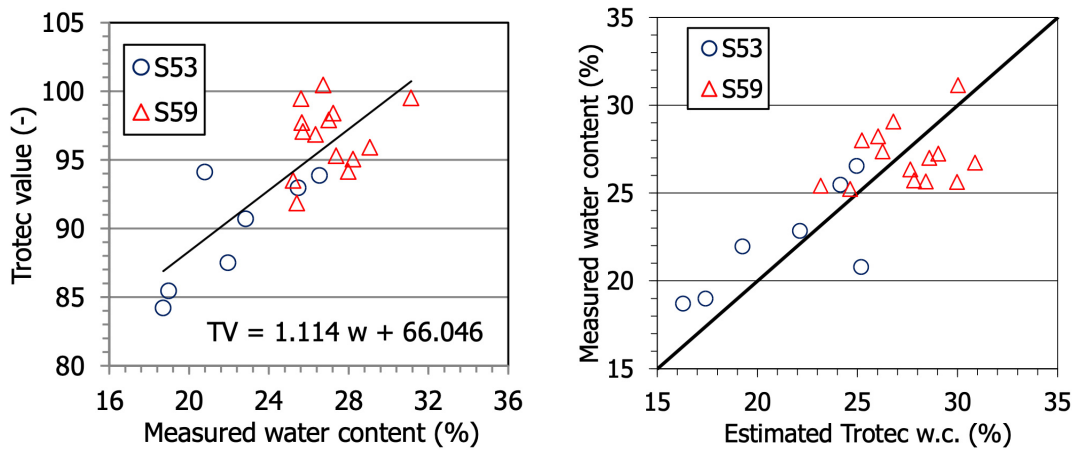


Fig. 47: Microwave measurement of the moisture of blocks

**4.2.2 Specific weight of solid particles**

The specific weight of solid particles was determined in some samples to check if changes had taken place during operation and because this is a key value to accurately compute the degree of saturation. The determination was performed in 22 samples of sections S36, S47 and S59 (Tab. 7, Tab. 8) and an average value of  $2.70 \pm 0.04 \text{ g/cm}^3$  was found, which is the same found years ago for the reference bentonite (Villar 2002). The dispersion of the measurements is relatively large and does not seem to be related to the position of the samples in the barrier, although the highest values were found close to the heater (Fig. 48).

Since the solid specific gravity depends on mineralogy, and consequently on chemical composition, the values obtained were compared to the chemical composition of the same samples detailed in Fernández et al. (2018), to find an explanation of the variability in solid specific weight values measured. The correlation between specific weight and major oxides, trace elements and free Al, Si and Fe was investigated, but no conclusive results were found. The specific weight tends to increase with the content in  $\text{SiO}_2$  and  $\text{Na}_2\text{O}$  and to decrease with the loss on ignition, which in turn is related to the organic matter, diverse types of water and sulphide contents. The content of Cr and Ba as trace elements is also directly correlated with the specific weight.

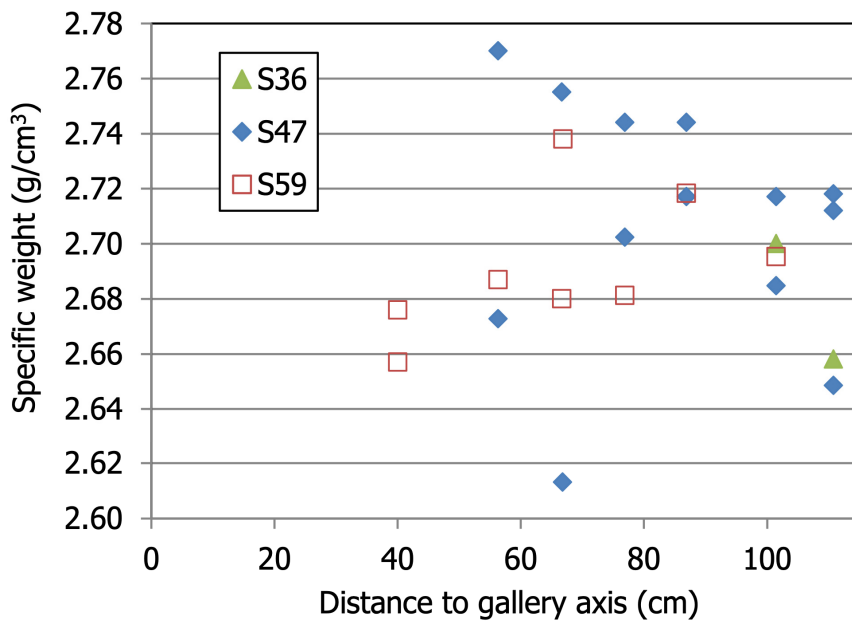


Fig. 48: Specific weight of solid particles determined in samples from different sampling sections

**4.2.3 Suction measurement**

Figure 49 plots the suction values calculated with Eq. 2 from psychrometer or capacitive sensor measurements as a function of distance to the gallery axis. The two sections around the heater (S47 and S53) show a clear increase of suction from the external part of the barrier towards the heater. In fact, capacitive sensors had to be used to measure the suction in the two internal rings of the barrier, because it was out of the psychrometers' range. Although the suction values were

much lower, they also increased from the external part of the barrier towards the internal part in S36.

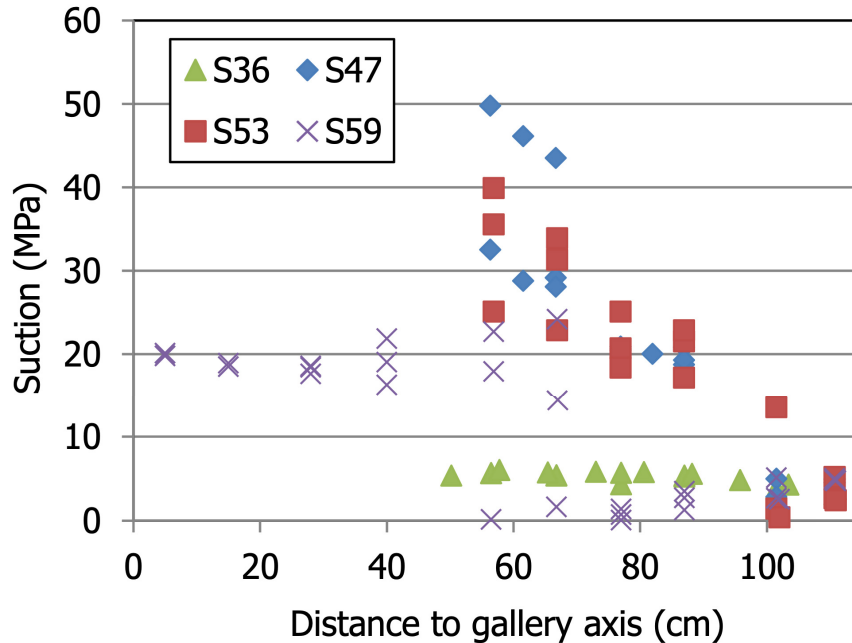


Fig. 49: Total suction values measured in blocks from different sampling sections at CIEMAT's laboratory

Figure 50 draws the water retention curves (WRC) by plotting the suction values measured versus water content values and degrees of saturation determined in the same blocks and at the same positions (Tab. 7 and Tab. 8). For water content values and degrees of saturation lower than 25% and 95% respectively (i.e. for suction values above 10 MPa), suction values increased linearly as water content or degree of saturation decreased. However, suction did not vanish when approaching full saturation. This remaining total suction would be a consequence of the block retrieval operation (undrained unloading): the samples retrieved suffered relaxation during dismantling and this possibly increased their suction, because of the changes in porosity. It has to be taken into account that during operation the bentonite blocks were exposed to high temperatures, and consequently the suction values in the barrier could have been lower than those measured in the laboratory.

The relationship between suction and water content or degree of saturation for the lowest suction values (those below 7 MPa that were measured basically with psychrometers) does not seem clear in these Figures. To analyse the lower suction range, the values were grouped according to the dry density of the samples in Fig. 51 (Villar et al. 2016a). The relationship between suction and water content or degree of saturation for suction pressures below 7 MPa (those measured with psychrometers) appeared dependent on dry density: the higher the dry density the lower the water content for a given suction pressure. Samples of lower density have higher water retention capacity, since their porosity is higher. For larger suction pressures the effect of density cannot be evaluated, because the range of densities was not large enough. In terms of degree of saturation, the effect of density on the WRC was not noticeable.

Although, the samples analysed had been submitted to wetting or wetting-after-drying paths during in-situ operation, the measurements performed with the sensors did not show any clear hysteresis effects. Fig. 51 (left) also shows the water retention curve for the FEBEX reference bentonite obtained previously (Villar 2002, 2007, Villar & Gómez-Espina 2009) for the same density as the average dry density of the barrier (1.6 g/cm<sup>3</sup>). The comparison of the WRC of the blocks retrieved with that of the reference material points to the preservation of the water retention capacity during operation.

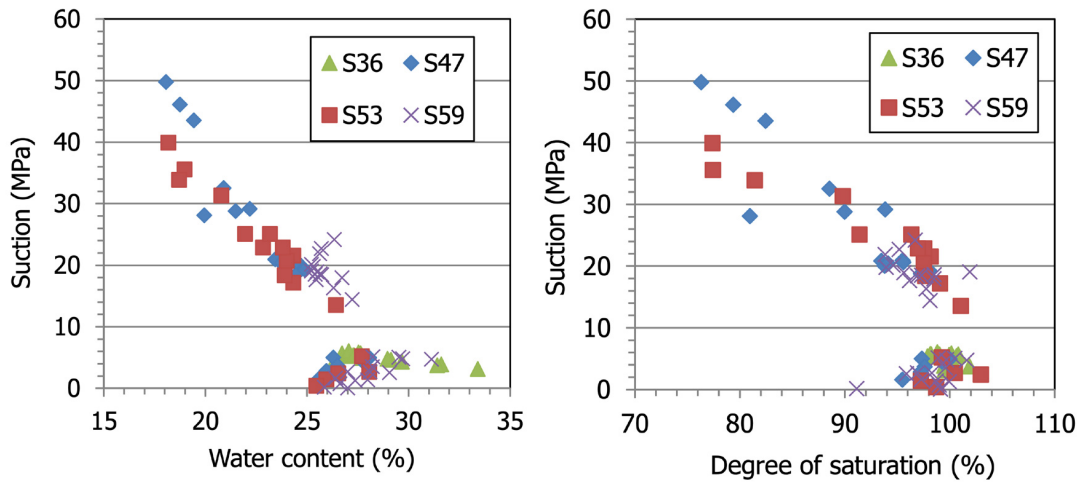


Fig. 50: Relationship between suction and water content and suction and degree of saturation in the blocks sampled at CIEMAT’s laboratory

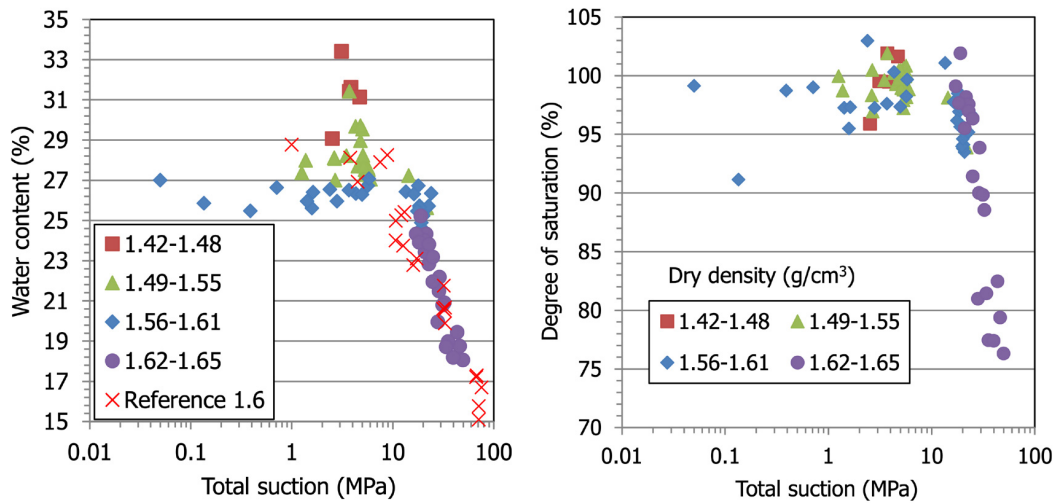


Fig. 51: Relationship between suction values measured and water content and degree of saturation in the blocks sampled at CIEMAT’s laboratory (range of dry density indicated in g/cm<sup>3</sup>)

#### 4.2.4 Interlayer space

The basal reflection ( $d_{001}$  value) gives a measure of the interlayer distance between smectite particles, a minimum value of about 1 nm corresponding to a collapsed interlayer with no water in it. It is considered that smectites display basal reflections of about 1.25, 1.55 and 1.85 nm for the homogeneous 1, 2 and 3 water layers hydration states, respectively. The exact values mainly depends, for a given smectite type, on the exchangeable cations. Under hygroscopic water content (14%), which was the condition of the bentonite used to manufacture the blocks in 1996, the basal spacing of the FEBEX bentonite is about 1.48 nm (Villar et al. 2012).

The smectite basal reflection of the FEBEX-DP samples was determined from X-ray profiles recorded on a sufficiently flat surface at room temperature, without any previous treatment of the samples. The values obtained were given in Tab. 7 and Tab. 8 (Gutiérrez-Nebot 2016a, b) and plotted in Fig. 52 as a function of distance to the gallery axis. Fig. 53 plots the basal spacing values as a function of water content. All the values measured were above the initial ones and corresponded mostly to a completely developed 2-layer hydrate, except for those samples of sections S47 and S53 that were taken at less than 20 cm from the heater. Fig. 53 shows that these samples have a water content below 25%, which agrees with the results shown in Fig. 40 and Fig. 41. Above this water content the basal spacing tended to increase with water content, i.e. as the distance from the axis of the gallery increased. A few samples had basal spacings close to those corresponding to the 3-layer hydrate. It has not been possible to assess the influence of the time elapsed from sampling at GTS to X-ray diffraction (which went from 76 to 196 days) on the basal spacings measured.

For most of the samples the 001 reflection was a double one that could be decomposed into two peaks, the one shown in Tab. 7 and Tab. 8 and plotted in the Figures 52 and 53 and another one towards lower angles, i.e. higher spacings. The two peaks could be told apart by profile fitting of the XRD pattern. An example of this is shown in Fig. 54 for radius B of section S47. The average value of the main peak was  $1.562 \pm 0.028$  nm and of the second one  $1.724 \pm 0.89$  nm, the first one corresponding to the full development of the 2-layer hydrate and the second one to the transition between the 2- and 3-layer hydrate. Overall, the ratio between the intensities of the main and the secondary peaks was higher for the drier samples, i.e. those closer to the heater, which would indicate a predominance of the 2-layer hydrate as becomes clear in Fig. 55 for the samples of section S47. These samples were subjected to higher temperatures and the temperature in this part of the barrier decreased considerably before dismantling. The water vapour present in the pore network would condensate because of cooling and the liquid water could migrate into the interlayer, causing an increase in the basal spacing from that corresponding to the 2-layer hydrate –that would have been predominant under high temperature– to the 3-layer hydrate. In the coolest samples the 3-layer hydrate would have been already predominant during operation, for which reason the ratio between the main (corresponding to the 2-layer hydrate) and secondary peaks (corresponding to the 3-layer hydrate) would be lower. This is not so in the samples from section S53, despite the fact that it was also a section around the heater. The main difference between the measurements performed in both sections is that the samples from section S47 were X-rayed shortly after sampling the block in the laboratory (the same day or the next day), whereas the samples from section S53 were X-rayed between 5 and 13 days after block sampling. A hypothesis to explain the differences between both sections could be that the longer time elapsed between sample release from the block and X-ray measurement allowed for water redistribution inside the microstructure. In a few samples (all of them with water contents above 25%) the highest intensity peak was the one towards the smallest angles, i.e. higher basal spacings.

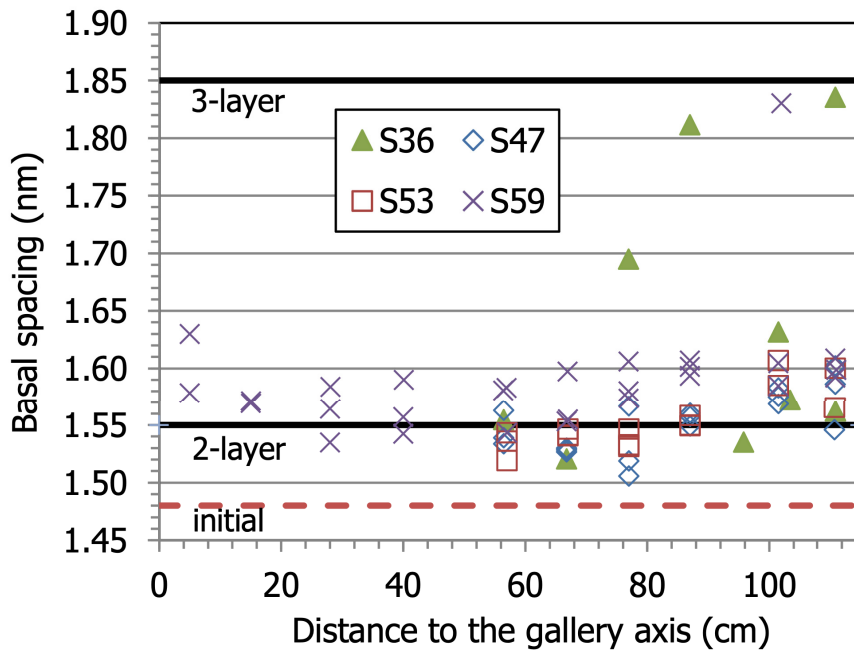


Fig. 52: Basal spacing of the smectite in FEBEX-DP samples of different sections as a function of the distance to the axis

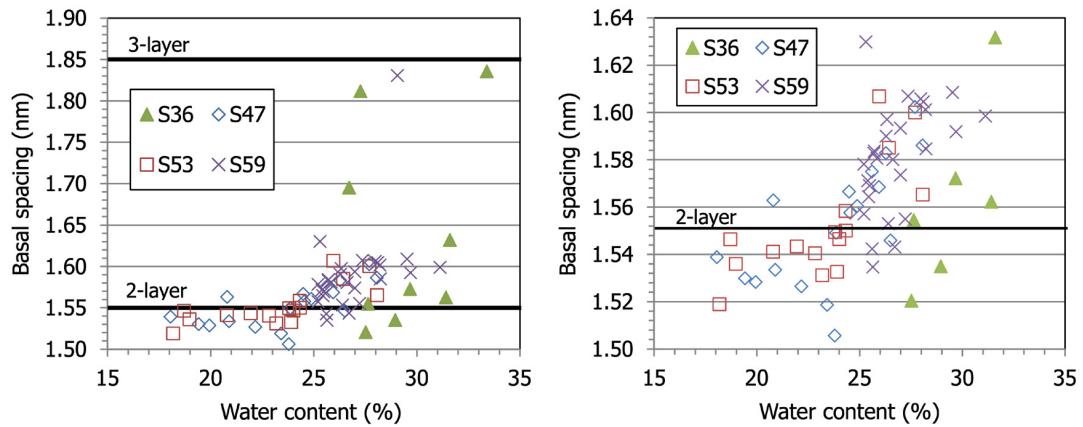
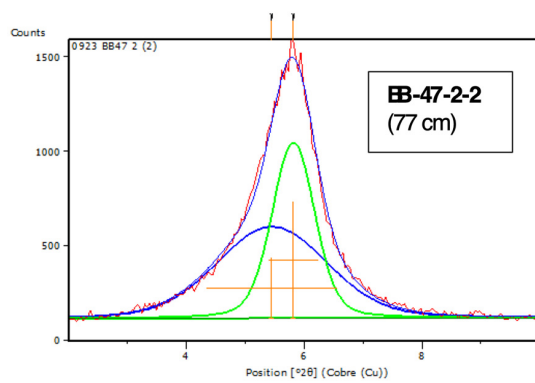
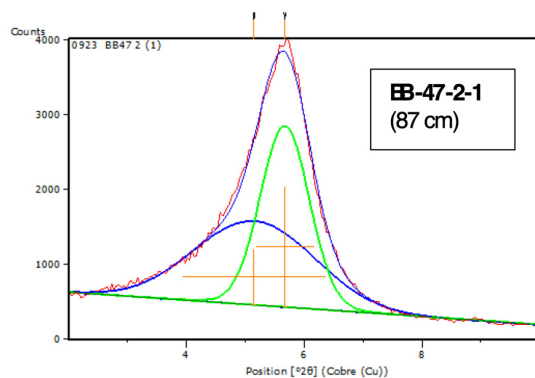
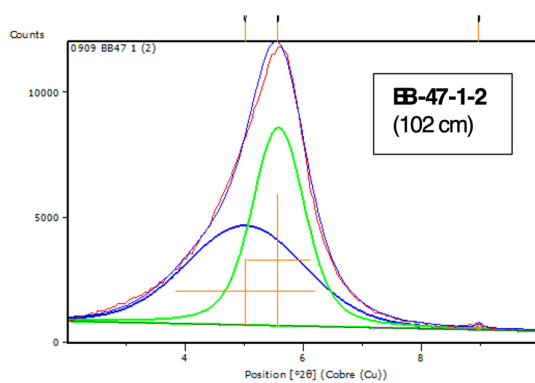
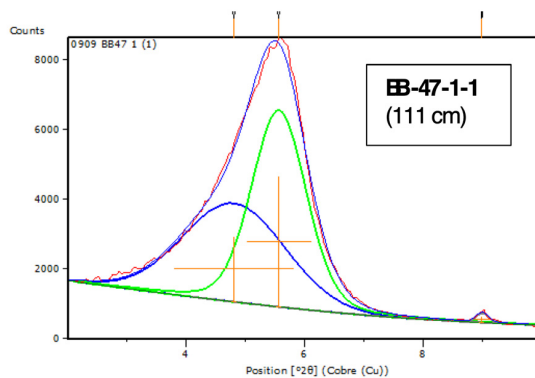


Fig. 53: Basal spacing of the smectite in FEBEX-DP samples of different sections as a function of water content (the figure on the right is an enlargement)



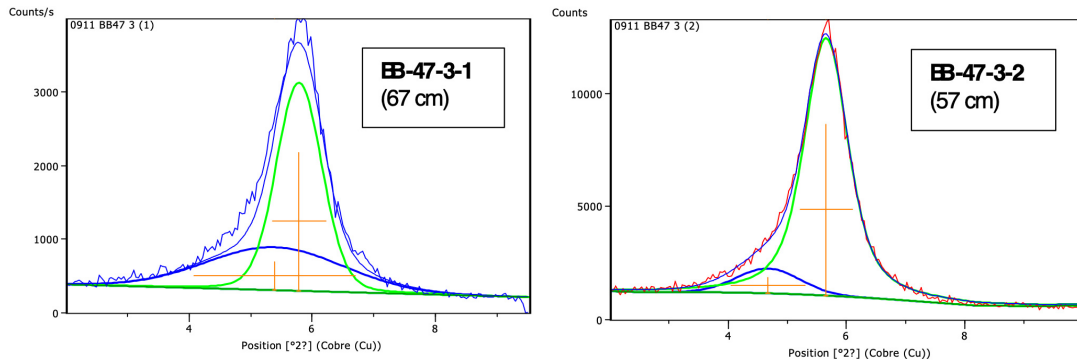


Fig. 54: Profile fitting of the XRD pattern of samples from radius B in section S47 (Gutiérrez-Nebot 2016a). The distance to the axis of the gallery is indicated in parentheses

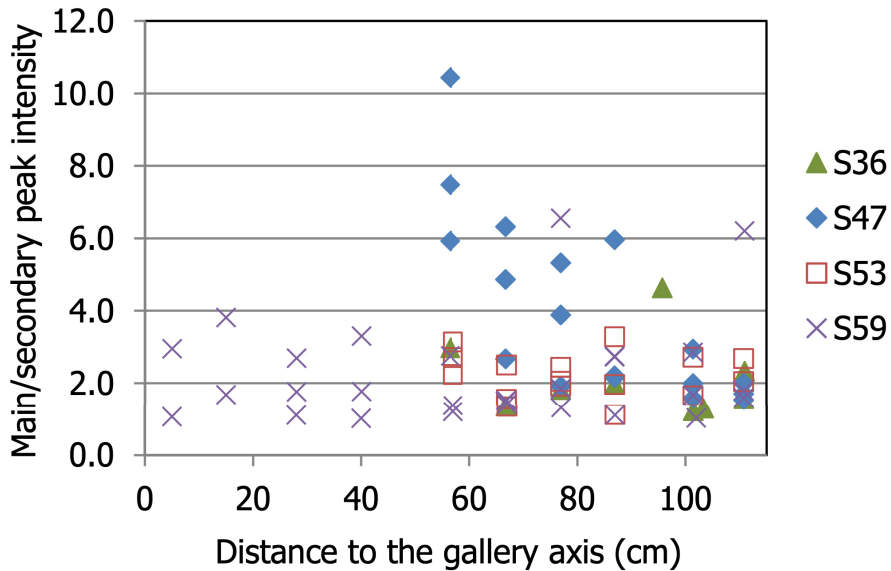


Fig. 55: Relation between the intensities of the main and secondary reflections of the basal spacing for samples of different sections

The values of the maximum intensity peaks have been plotted along with values obtained for the FEBEX bentonite saturated in different ways with deionised water (Villar et al. 2012, 2016b and other unpublished data) in Fig. 56. Most of them were samples obtained from compaction to a wide range of dry densities (from 1.1 to 1.75 g/cm<sup>3</sup>) saturated either prior to compaction or afterwards. The values obtained for the FEBEX-DP samples for water contents below 27% are similar to those measured in FEBEX bentonite samples of the same water content saturated with deionised water. For higher water contents there is a larger dispersion, both among the samples from the dismantling and among the other FEBEX samples.

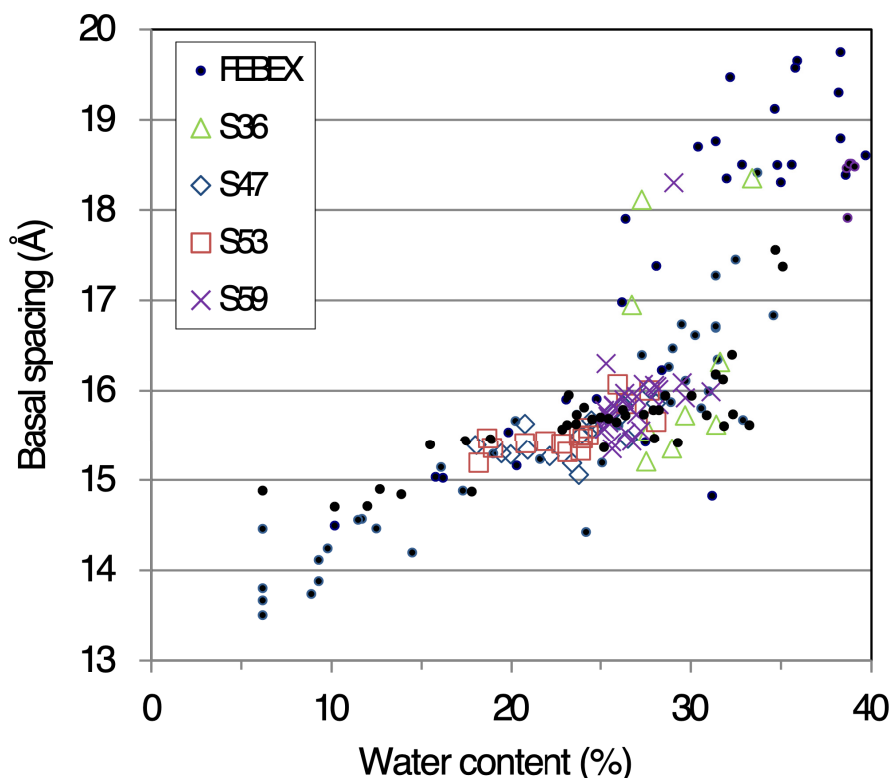


Fig. 56: Basal spacings of FEBEX samples saturated in different ways with deionised water (Villar et al. 2012, 2016b) and of samples from the FEBEX-DP

#### 4.2.5 Pore size distribution

The pore size distribution of samples taken from the blocks was analysed by mercury intrusion porosimetry (Campos et al. 2017). The equipment used, gained access to pores between 540  $\mu\text{m}$  and 7 nm. Fig. 57 to Fig. 60 show examples of the curves obtained along a sampling radii in four barrier sections. Two pore families appeared systematically in all the samples, one in the size range of macropores and another one in the size range of mesopores. This is the usual pore size distribution pattern obtained by MIP in compacted FEBEX bentonite, irrespective of the water content or dry density. The result also indicated the presence of a new pore family of larger size in some of the more saturated samples taken in the external part of the barrier (e.g. BB-47-7-1, BB-59-6-1).

Because of limitations of the method and equipment, only part of the macropores (pores of sizes between  $5.4 \cdot 10^5$  and 50 nm) and part of the mesopores (pores between 50 and 7 nm) were explored. Pores larger than  $6 \cdot 10^5$  nm in compacted clay materials are not expected, but the number of pores smaller than 7 nm can be very relevant. To overcome this undervaluation of porosity, an estimation of the percentage of pores not intruded by mercury can be made by comparing the actual void ratio of the samples ( $e$ , computed from their dry density and density of solid particles) and the apparent void ratio calculated from mercury intrusion ( $e_{nw}$ , mercury being a non-wetting (<sub>nw</sub>) fluid). Thus, the pore size distribution obtained by MIP was corrected to take into account the percentage of pores not intruded.

The corrected results are detailed in Tab. 9 to Tab. 12. The porosity decreased in all the radii towards the axis of the gallery, which is related to the decrease of dry density towards the granite as observed in Fig. 39 to Fig. 42. As it has been explained above, these values do not correspond to the actual porosity of the samples, since mercury is not able to intrude all the pores. In fact, the non-intruded void ratio was between 35 and 58% in these samples, with an average of between 40 and 50%, depending on the sampling section. Fig. 61 shows a comparison of the porosity determined by MIP and the porosity of the samples as determined from the dry density actually measured. There is a good linear correlation between both, but the porosity determined by MIP is considerably lower than the actual one.

Tables 9 to 12 also show the percentage of macropores (>50 nm) and their mode, and the percentage of mesopores and micropores (i.e. those of diameter <50 nm), along with the mode of mesopores. The separate quantification of mesopores and micropores is not accurate, because the limit of the two pore sizes is 2 nm, whereas the lower limit of the equipment is 7 nm. An average of 66% of the void ratio of all the samples corresponded to pores that had a diameter smaller than 50 nm after operation. The pore size distribution along three radii of sections S36, S47, S53 and S59 is plotted in Fig. 63 to Fig. 65. The horizontal lines indicate the average pore percentages of samples compacted at dry density 1.6 g/cm<sup>3</sup> with their hygroscopic water content, which would represent approximately the original state of the blocks. The proportion of void ratio corresponding to pores smaller than 50 nm increased with respect to that in the reference sample (66% vs. 54%), while the proportion of pores larger than 50 nm decreased (34% vs. 46%). This would point to the homogenisation of the pore sizes towards the smaller ones. The difference between the percentage of pores larger and smaller than 50 nm increased on the whole from the granite towards the internal part of the barrier, although the maximum difference between the proportions of the two pore sizes was mostly found in the middle part of the barrier, particularly in those barrier sections around the heater. It must be remembered that the total void ratio was higher for the samples from the external part of the barrier than for those in the internal part, because by the end of FEBEX operation, the dry density clearly increased with distance from the granite surface (see for example Fig. 45). Close to the heater, where the samples were dried, there was a small relative increase in the macropore void ratio.

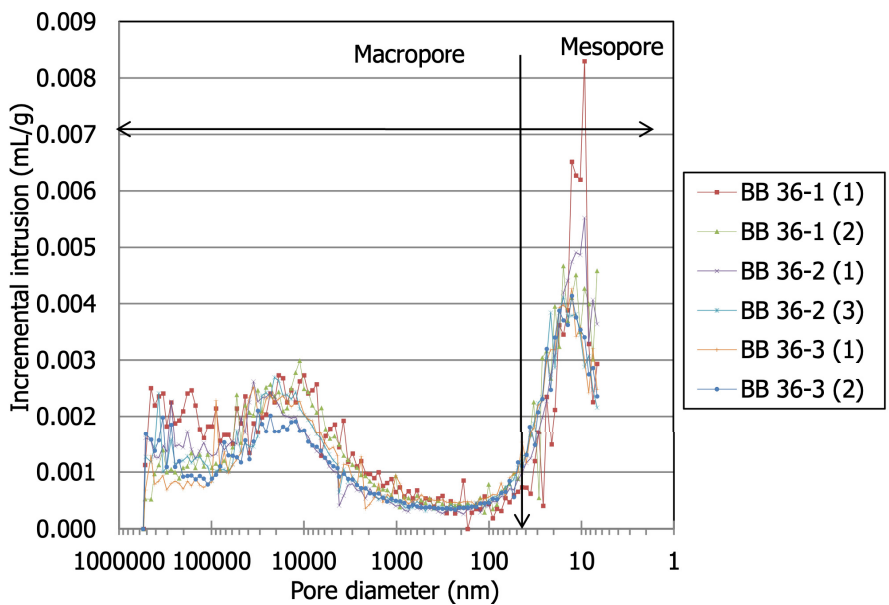


Fig. 57: Pore size distribution of samples from radius B-C in section S36

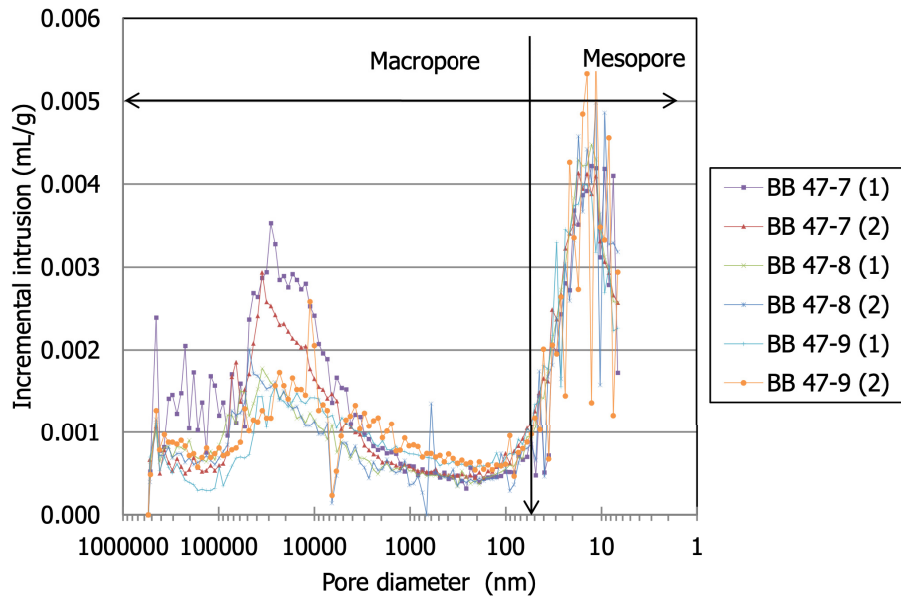


Fig. 58: Pore size distribution of samples from radius E-F in section S47

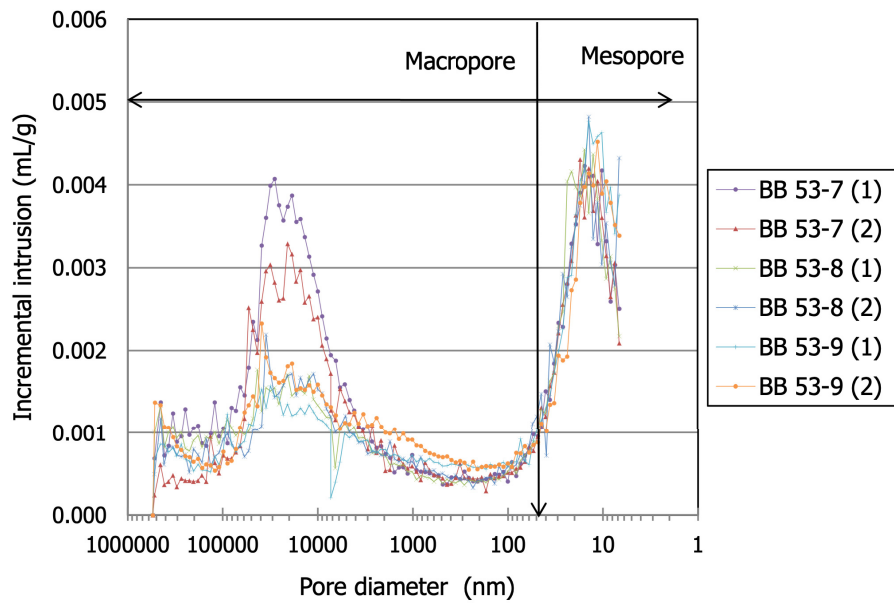


Fig. 59: Pore size distribution of samples from radius E-F in section S53

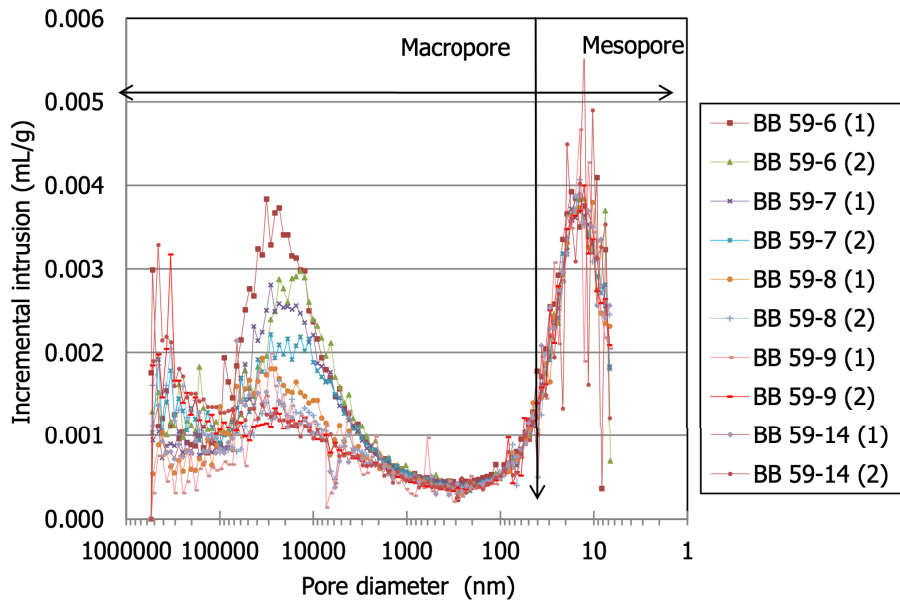


Fig. 60: Pore size distribution of samples from radius D in section S59

Tab. 9: Pore size distribution obtained with MIP of samples from section S36 (*n*: porosity, *e*: void ratio)

Reference	Distance to axis (cm)	<i>n</i> MIP (%)	Intruded <i>e</i> (% of total)	Macro (% vol)	Mode macro (nm)	Meso+micro (% vol)	Mode meso (nm)
FEBEX		29	68	46	16760±3484	54	8.59±2.04
BB-36-1-1	111	30	65	43	451770	57	6.7
BB-36-1-2	102	28	61	40	13736	60	15.4
BB-36-2-1	82	27	60	39	453582	61	9.1
BB-36-2-2 <sup>a</sup>	82	26	55	35	35165	65	13.9
BB-36-2-3 <sup>a</sup>	82	27	57	37	20860	63	15.4
BB-36-2-4 <sup>a</sup>	82	27	58	38	454088	62	12.5
BB-36-3-1	67	26	54	35	35164	65	12.5
BB-36-3-2	57	25	51	32	31645	68	12.5
BB-36-4-1	111	33	63	47	28525	53	11.2

Reference	Distance to axis (cm)	<i>n</i> MIP (%)	Intruded <i>e</i> (% of total)	Macro (% vol)	Mode macro (nm)	Meso+micro (% vol)	Mode meso (nm)
BB-36-4-2	102	32	61	44	23161	56	12.5
BB-36-5-1	87	27	54	35	31643	65	19.0
BB-36-5-2	77	27	56	36	28527	64	12.5
BB-36-6 <sup>b</sup>	49	29	62	42	31644	58	12.5
BB-36-7 B	59	24	46	27	99182	73	13.9
BB-36-8	85	27	57	35	335356	65	15.4
BB-36-9	111	27	52	34	48131	66	13.9

<sup>a</sup> samples taken at different depths into the blocks; <sup>b</sup> close to liner

Tab. 10: Pore size distribution obtained with MIP of samples from section S47 (*n*: porosity, *e*: void ratio)

Reference	Distance to axis (cm)	<i>n</i> MIP (%)	Intruded <i>e</i> (% of total)	Macro (% vol)	Mode macro (nm)	Meso+micro (% vol)	Mode meso (nm)
FEBEX		29	68	46	16760±3484	54	8.59±2.04
BB-47-1-1	111	27	57	37	369759	63	8.2
BB-47-1-2	102	25	53	32	48124	68	13.9
BB-47-2-1	87	25	55	31	452738	69	15.4
BB-47-2-2	77	23	51	27	25693	73	15.4
BB-47-3-1	67	23	54	30	25699	70	10.1
BB-47-3-2	57	24	53	31	1138	69	13.9
BB-47-4-1	111	25	51	30	35145	70	17.1
BB-47-4-2	102	25	53	32	25690	68	12.5
BB-47-5-1	87	25	57	34	274973	66	17.1
BB-47-5-2	77	24	51	28	48103	72	15.4

Reference	Distance to axis (cm)	<i>n</i> MIP (%)	Intruded <i>e</i> (% of total)	Macro (% vol)	Mode macro (nm)	Meso+micro (% vol)	Mode meso (nm)
BB-47-6-1	67	24	55	31	53452	69	12.5
BB-47-6-2	57	23	53	32	18784	68	19.0
BB-47-7-1	111	28	60	41	28509	59	12.5
BB-47-7-2	102	26	56	34	35166	66	17.1
BB-47-8-1	87	24	52	28	35157	72	12.5
BB-47-8-2	77	23	50	27	48116	73	11.2
BB-47-9-1	67	24	53	30	25697	70	15.4
BB-47-9-2	57	25	59	35	11123	65	11.2

Tab. 11: Pore size distribution obtained with MIP of samples from section S53 (*n*: porosity, *e*: void ratio)

Reference	Distance to axis (cm)	<i>n</i> MIP (%)	Intruded <i>e</i> (% of total)	Macro (% vol)	Mode macro (nm)	Meso+micro (% vol)	Mode meso (nm)
FEBEX		29	68	46	16760±3484	54	8.59±2.04
BB-53-1-1	111	28	46	31	370373	69	13.9
BB-53-1-2	102	27	62	39	516611	61	11.2
BB-53-2-1	87	24	54	32	35158	68	13.9
BB-53-2-2	77	24	55	32	39020	68	12.5
BB-53-3-1	67	24	58	32	334163	68	10.1
BB-53-3-2	57	24	58	32	370968	68	10.1
BB-53-4-1	111	27	62	38	7327	62	13.9
BB-53-4-2	102	25	55	32	28514	68	13.9
BB-53-5-1	87	25	58	35	523025	65	23.4
BB-53-5-2	77	24	56	32	25695	68	12.5

Reference	Distance to axis (cm)	<i>n</i> MIP (%)	Intruded <i>e</i> (% of total)	Macro (% vol)	Mode macro (nm)	Meso+micro (% vol)	Mode meso (nm)
BB-53-6-1	67	25	63	36	28518	64	12.5
BB-53-6-2	57	26	64	40	48118	60	12.5
BB-53-7-1	111	29	62	42	28519	58	15.4
BB-53-7-2	102	26	56	36	20870	64	17.1
BB-53-8-1	87	24	54	31	43320	69	15.4
BB-53-8-2	77	24	55	31	35169	69	13.9
BB-53-9-1	67	24	57	32	31644	68	13.9
BB-53-9-2	57	25	59	36	39029	64	11.2

Tab. 12: Pore size distribution obtained with MIP of samples from section S59 (*n*: porosity, *e*: void ratio)

Reference	Distance to axis (cm)	<i>n</i> MIP (%)	Intruded <i>e</i> (% of total)	Macro (% vol)	Mode macro (nm)	Meso+micro (% vol)	Mode meso (nm)
FEBEX		29	68	46	16760±3484	54	8.59±2.04
BB-59-1-1	111	28	57	38	272891	62	12.5
BB-59-1-2	102	28	58	39	333313	61	12.5
BB-59-2-1	87	27	56	37	273309	63	17.1
BB-59-2-2	77	26	54	36	12341	64	11.2
BB-59-3-1	67	28	53	35	1742	65	11.2
BB-59-3-2	57	26	54	35	15247	65	11.2
BB-59-4-1	40	19	56	35	28505	65	15.4
BB-59-4-2	28	24	50	31	12342	69	11.2
BB-59-5-1	15	23	46	28	35148	72	12.5
BB-59-5-2	5	25	51	32	446897	68	15.4

Reference	Distance to axis (cm)	<i>n</i> MIP (%)	Intruded <i>e</i> (% of total)	Macro (% vol)	Mode macro (nm)	Meso+micro (% vol)	Mode meso (nm)
BB-59-6-1	111	29	58	40	28509	60	8.2
BB-59-6-2	102	27	55	37	13740	63	12.5
BB-59-7-1	87	26	54	35	28534	65	17.1
BB-59-7-2	77	26	53	35	28503	65	15.4
BB-59-8-1	67	24	47	28	35160	72	10.1
BB-59-8-2	57	24	48	29	334604	71	13.9
BB-59-9-1	40	22	42	23	28513	77	13.9
BB-59-9-2	28	24	50	30	334860	70	12.5
BB-59-10-1	111	30	59	42	31641	58	11.2
BB-59-10-2	102	28	55	38	15249	62	13.9
BB-59-11-1	87	28	60	41	12375	59	11.2
BB-59-11-2	77	27	55	36	11124	64	13.9
BB-59-12-1	67	26	54	34	12374	66	11.2
BB-59-12-2	57	28	59	39	18781	61	12.5
BB-59-13-1	40	27	61	41	447825	59	15.4
BB-59-13-2	28	27	60	39	333920	61	13.9
BB-59-14-1	15	23	48	27	65821	73	13.9
BB-59-14-2	5	24	51	31	454325	69	12.5

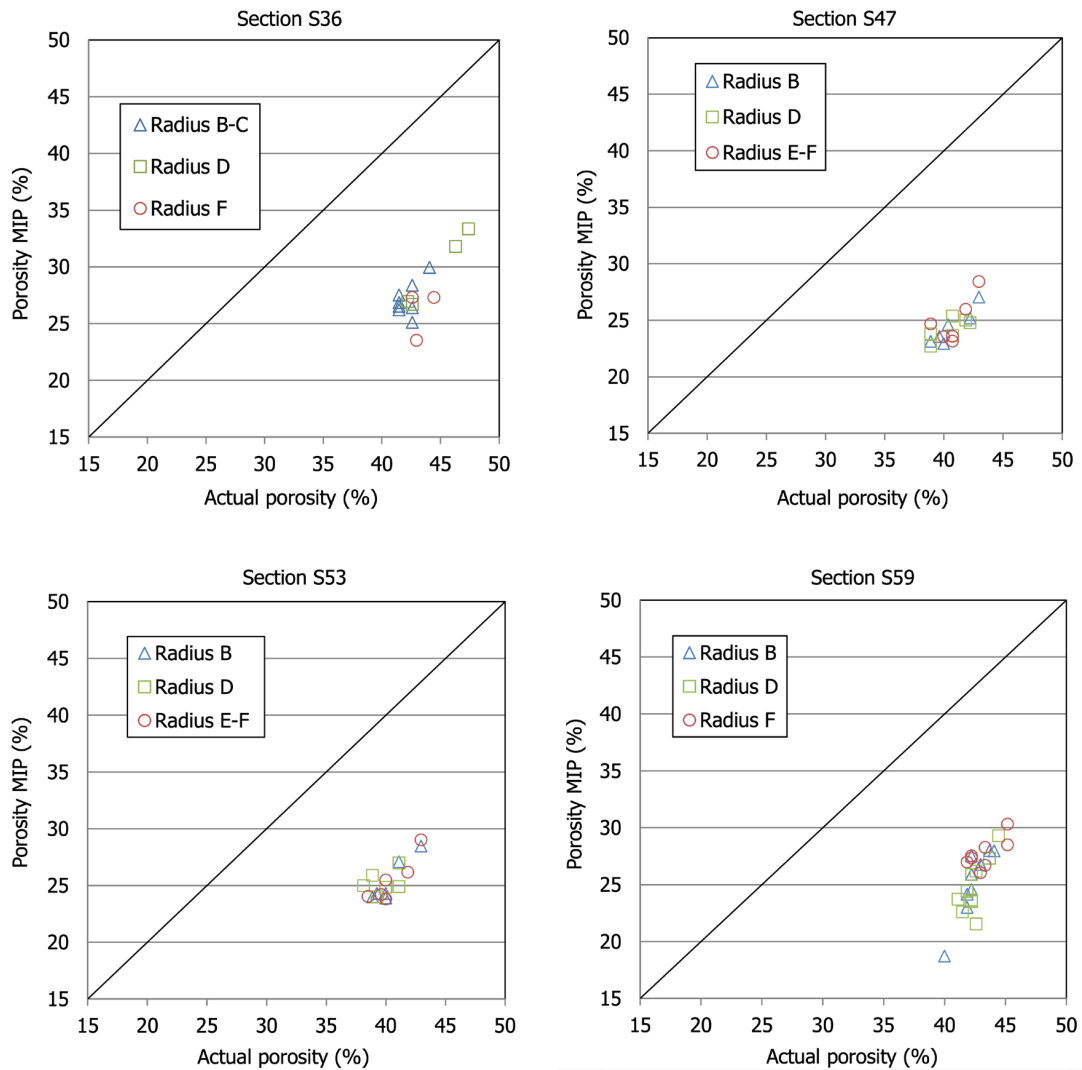


Fig. 61: Comparison of the porosity determined by MIP and calculated from the dry density and specific weight in Tab. 7 and Tab. 8 for different sampling sections

Tables 9 to 12 also show a systematic increase in the diameter mode of the macropores and the mesopores with respect to the reference material (123  $\mu\text{m}$  vs. 17  $\mu\text{m}$  and 13 nm vs. 9 nm, respectively), probably related to the overall increase in the water content of the bentonite. The percentage of mesopores and micropores (diameter <50 nm) as a whole increased over the course of the experiment and the average size of the mesopores (diameter 50-7 nm) increased. Consequently, it is assumed that the hydration occurring during operation led to an increase in the percentage of micropores, i.e. those that cannot be intruded by mercury. These conclusions are consistent with the average increase in basal spacing reported in the previous section.

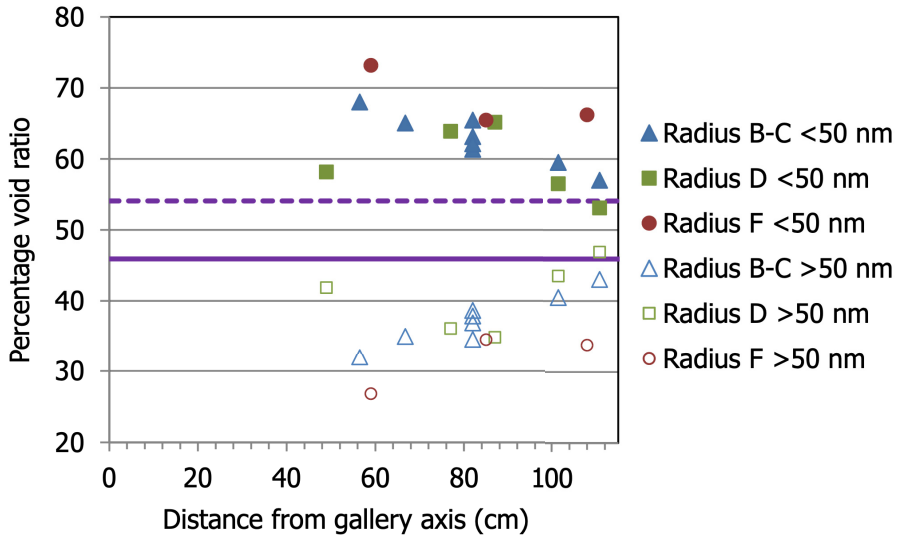


Fig. 62: Void ratio along three radii of section S36 (the solid and dotted thick horizontal lines indicate the values of pores larger and smaller than 50 nm, respectively, for the reference FEBEX compacted at 1.6 g/cm<sup>3</sup> with 14% water content)

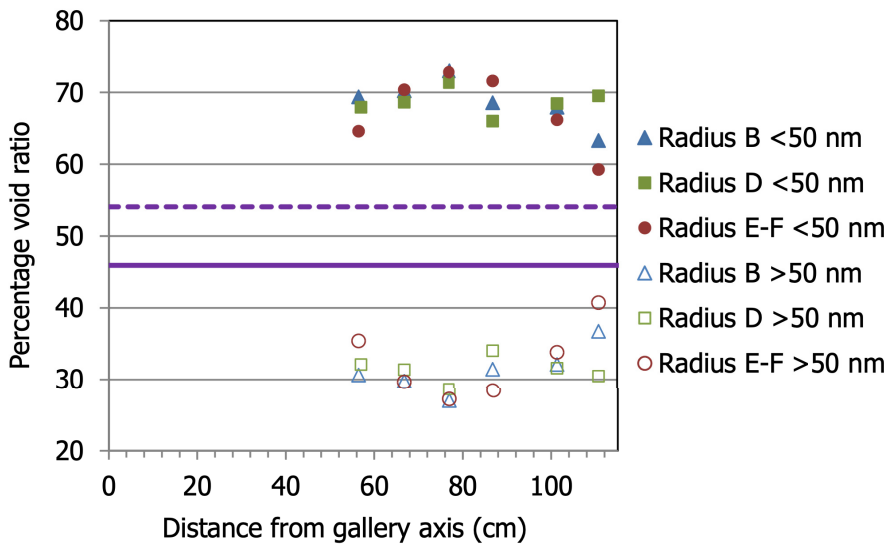


Fig. 63: Void ratio along three radii of section S47 (the solid and dotted thick horizontal lines indicate the values of pores larger and smaller than 50 nm, respectively, for the reference FEBEX compacted at 1.6 g/cm<sup>3</sup> with 14% water content)

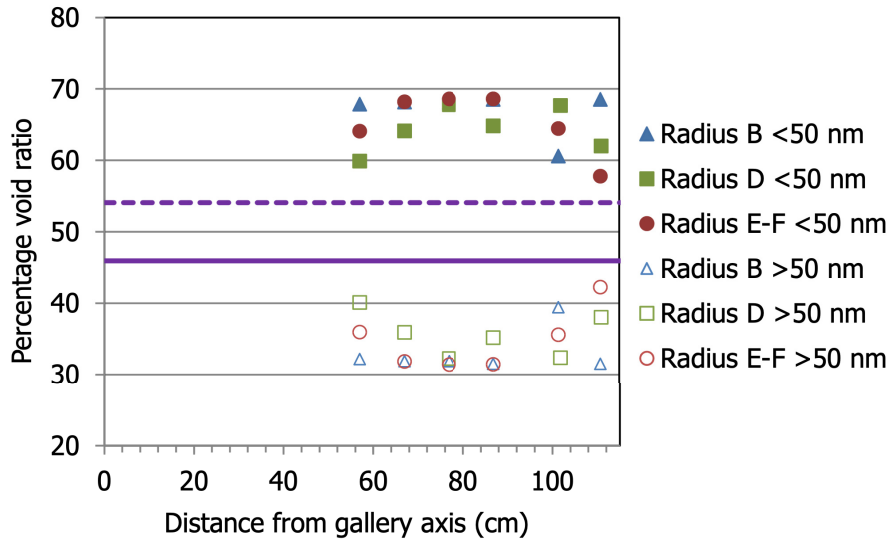


Fig. 64: Void ratio along three radii of section S53 (the solid and dotted thick horizontal lines indicate the values of pores larger and smaller than 50 nm, respectively, for the reference FEBEX compacted at 1.6 g/cm<sup>3</sup> with 14% water content)

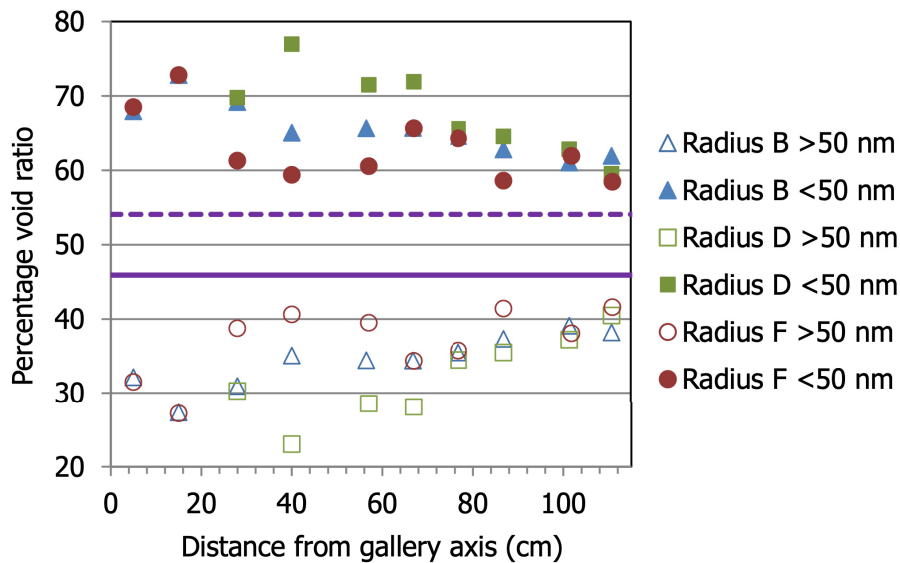


Fig. 65: Void ratio along three radii of section S59 (the solid and dotted thick horizontal lines indicate the values of pores larger and smaller than 50 nm, respectively, for the reference FEBEX compacted at 1.6 g/cm<sup>3</sup> with 14% water content)

#### 4.2.6 Specific surface area

The BET specific surface area (SSA) was determined from the nitrogen adsorption isotherms. The samples analysed were taken along one radius in sections S36, S47, S53 and S59. The results obtained in terms of BET SSA are shown in Fig. 66, the entire isotherm results can be found in Campos et al. (2017). Figure 66 also shows the value for the reference untreated

bentonite. The values in the proximity of the granite were higher than the reference one in the four sections analysed, and then tended to decrease towards the internal part of the barrier. The decrease recorded was not very sharp, although previous investigations had shown a drop of BET specific surface area towards drier and heated areas (Cuevas et al. 2002a). Lower values of SSA were also found in the samples taken during the first dismantling close to the heater (Villar et al. 2006). The reason for not finding even lower values could be that no samples at less than 17 cm away from the heater were analysed. In the cool section S59 the specific surface area was slightly higher than the reference one, particularly in the external part of the barrier (approximately the 30 cm closest to the granite), where it was noticeably higher. Hence, it seems the specific surface area is related to the water content the samples had before being analysed. This becomes clear in Fig. 67, in which the specific surface area values have been plotted as a function of the water content of the samples after dismantling. The samples analysed had on average SSAs 7% higher than the reference value.

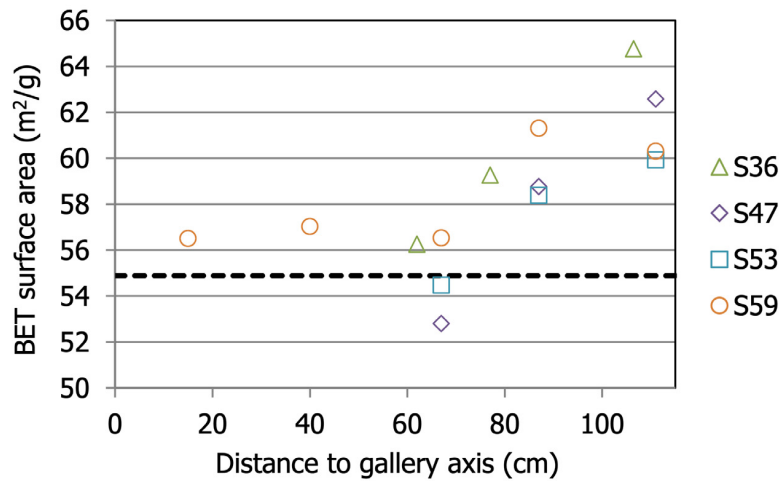


Fig. 66: BET specific surface area of samples taken along a radius from different sections (the dotted line indicates the value for the reference FEBEX bentonite)

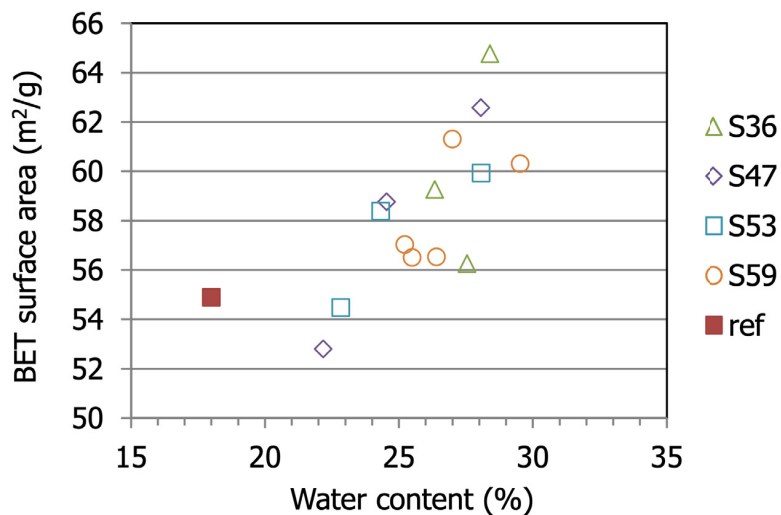


Fig. 67: BET specific surface area of the reference FEBEX and of samples taken along a radius from different sections as a function of their water content at the time of dismantling

### 4.3 Thermal conductivity

The thermal conductivity measured at two different positions on the surface of the blocks is shown in Fig. 68. There is no clear relationship between the position of the blocks in the barrier and the thermal conductivity, which is mostly clustered between 1.1 and 1.3 W/m·K.

It is known that thermal conductivity depends on water content and dry density and consequently on degree of saturation. The values have been plotted again in Fig. 69, where a trend for the thermal conductivity to decrease with the degree of saturation can be observed. Nevertheless, there is a large dispersion, possibly because the samples tested had a broad range of water content and dry density values. The fact that most of the samples were close to full saturation makes it difficult to establish clear dependences, as the range of thermal conductivities measured was too narrow.

In Fig. 70 the values have been plotted again grouped according to the dry density as a function of the water content of the samples. Although the dispersion is still large, it becomes clear that samples with the same thermal conductivity have different water content values, and, as before, the dry density of these samples is lower when water content values are higher. In order to check if the thermal conductivity of the bentonite changed during operation, empirical relationships between thermal conductivity ( $\lambda$ , W/mK) and water content ( $w$ , %) as a function of the bentonite dry density ( $\rho_d$ , g/cm<sup>3</sup>) have also been plotted in the Figure:

$$\ln \lambda = \ln (0.8826 \rho_d - 0.8909) + 0.003 w \quad (\text{Eq. 9})$$

These relationships were determined from measurements performed with the same methodology as used in FEBEX-DP on samples of untreated FEBEX bentonite compacted to different dry densities with various water contents (Villar 2002). Despite the dispersion of the values, the comparison points to a preservation of the thermal conductivity of the bentonite after operation.

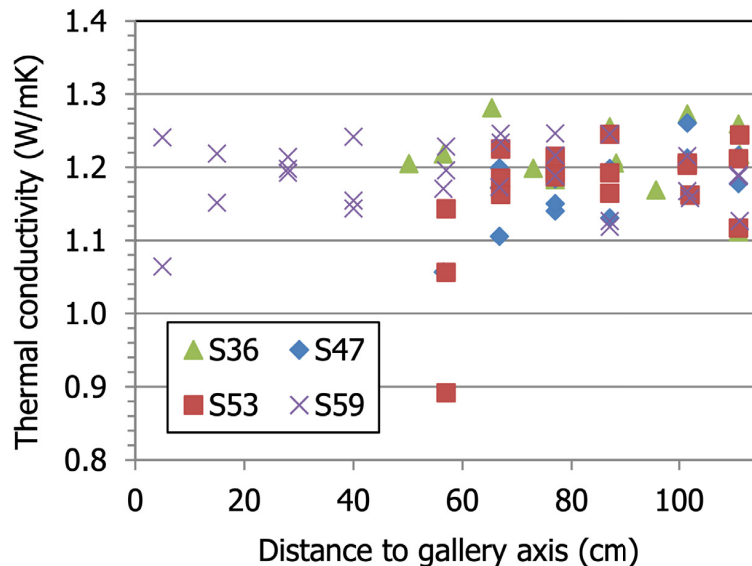


Fig. 68: Thermal conductivity measured on blocks taken from different sampling sections

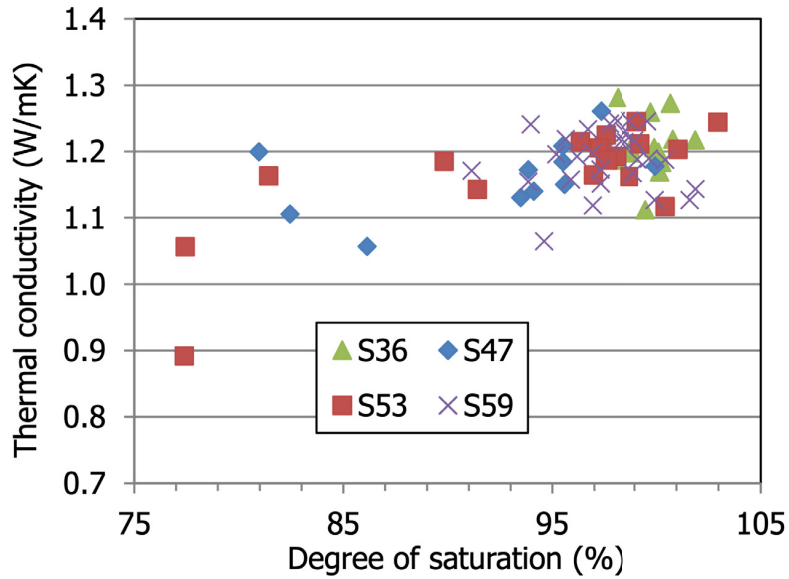


Fig. 69: Thermal conductivity measured for different sections as a function of degree of saturation

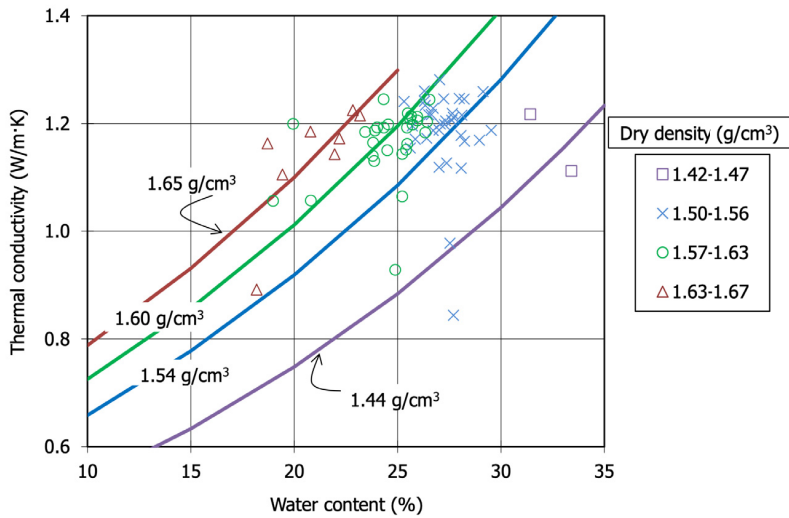


Fig. 70: Dependence of thermal conductivity measured in blocks on water content and dry density (symbols) and empirical relationships for FEBEX reference bentonite (lines)

## 4.4 Hydraulic properties

### 4.4.1 Water retention curve

The samples for the water retention curve determination were obtained by drilling in the laboratory blocks from sections S47, S53 and S59 at the locations shown in Fig. 71. They were drilled from blocks in contact with the heater in sections S47 and S53. Samples were also taken from the cool section S59. These samples were trimmed from the most internal blocks of the barrier, which were those with the lowest water content. This was done to start the determination of the WRCs from water contents as similar as possible between the two sets of samples (heated and non-heated). Nevertheless, the samples from sections S47 and S53 were drier, and in fact, because of the bad consistency of the blocks, particularly those of S47, it was difficult to obtain good-shaped samples. Because of their higher water content, the blocks from section S59 were more consistent and it was easier to trim samples from them.

After trimming, the samples were placed into perforated cells which were submitted to controlled suction pressures in desiccators, following the procedure described in subchapter 3.2.1. The initial suction pressure was selected to be equal to the suction pressure measured in the blocks from which the samples were drilled (Tab. 7, Tab. 8), and was subsequently reduced by steps, waiting for water content stabilisation in each step. This way the samples were saturated and the WRCs were determined following a wetting path under constant-volume conditions.

The initial characteristics of the samples from sections S47, S53 and S59 are shown in Tab. 13, Tab. 14 and Tab. 15, respectively. They include the dry density ( $\rho_d$ ) and water content ( $w$ ) of the blocks from which they were drilled, and the suction values measured in them (those shown in Tab. 7 and Tab. 8), the initial characteristics of the samples trimmed ( $\rho_d$ ,  $w$ ,  $S_r$ ) and the evolution of these values in the subsequent suction pressure steps. The time necessary to reach water content stabilisation for each step is also indicated. The dry density of the trimmed samples was generally lower than that of the blocks from which they were trimmed, and this is because of the difficulty in trimming samples from blocks that were relatively dry and crumbled easily. There was also a difference between the initial and final dry densities of the samples. This is because the initial height and diameter of the samples –although intended to be as close as possible to the internal dimensions of the cells– did not allow to completely fill the internal volume of the cells, and this was filled in the course of the first suction step, which resulted in a slight increase of the water content of the samples and associated swelling. The subsequent steps brought, as expected, further increases in water content and degree of saturation, since the volume of the samples remained constant during the determination.

The equilibrium water content values for each suction step are plotted as a function of suction pressure in Fig. 72 to Fig. 74 for the different sections. The initial water content values of the blocks from which the samples were trimmed are also plotted in Figures 72 to 74 linked to the suction pressure measured in the same blocks at the approximate locations where the samples were drilled from (Tab. 7, Tab. 8). The first suction step resulted in a decrease in water content for the samples from section S59, whereas for the samples from the other sections the water content slightly increased.

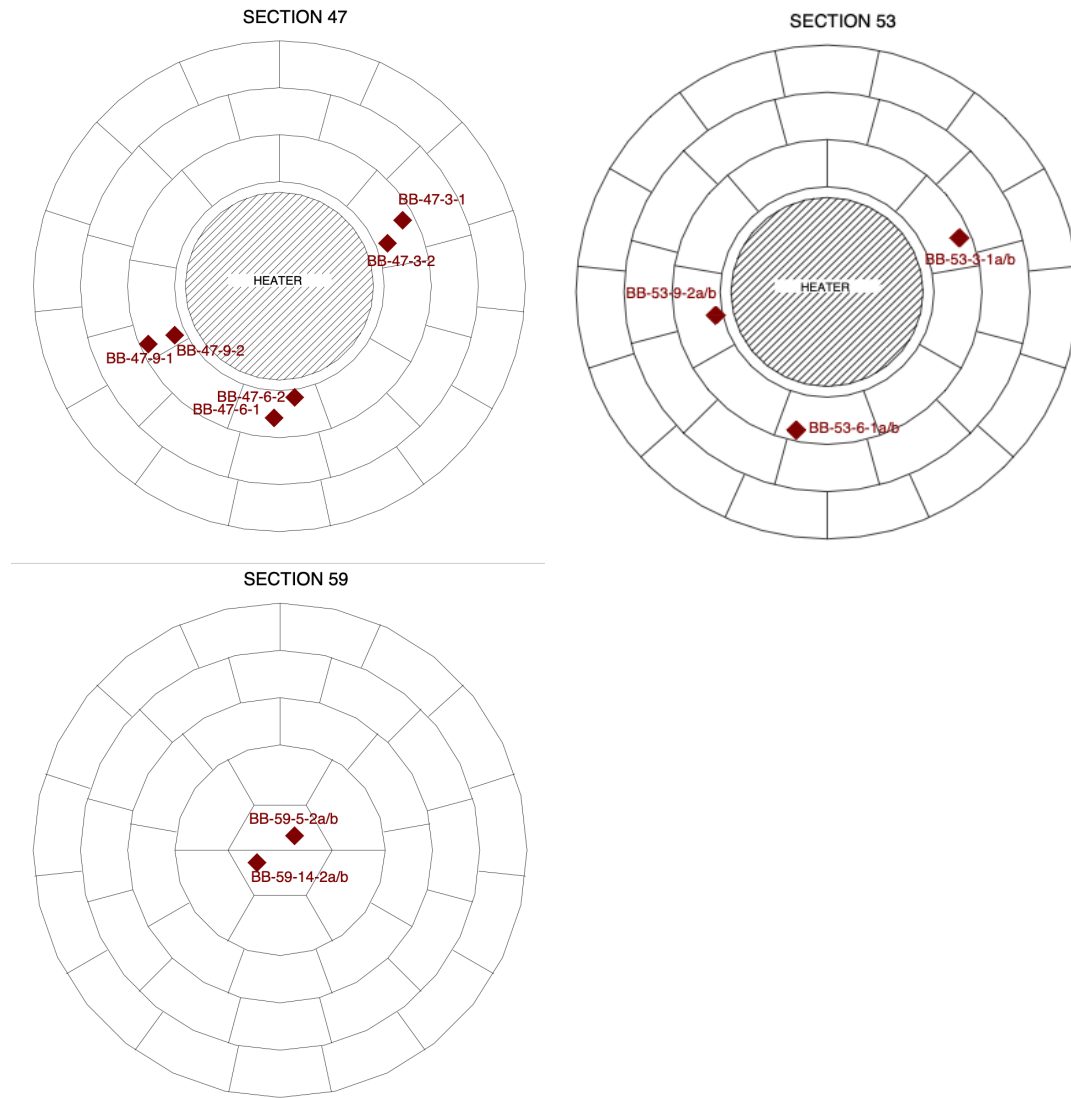


Fig. 71: Location of samples used for water retention curve determination

Tab. 13: Results of the water retention curves with samples from section S47

Reference	1. BB47-9-1	2. BB47-9-2	3. BB47-3-1	4. BB47-3-2	5. BB47-6-1	6. BB47-6-2
Distance to axis (cm)	67	57	67	57	67	57
Block $\rho_d$ (g/cm <sup>3</sup> )	1.62	1.65	1.65	1.63	1.65	1.65
Block $w$ (%)	20.0	20.9	22.2	20.8	19.4	18.1

Reference	1. BB47-9-1	2. BB47-9-2	3. BB47-3-1	4. BB47-3-2	5. BB47-6-1	6. BB47-6-2
Initial suction (MPa)	28	33	29	29	44	50
Initial $\rho_d$ (g/cm <sup>3</sup> )	1.42	1.64	1.68	1.65	1.56	1.54
Final $\rho_d$ (g/cm <sup>3</sup> )	1.39	1.52	1.55	1.55	1.50	1.52
Initial $w$ (%)	20.1	20.2	21.1	20.8	18.8	19.9
Initial $S_r$ (%)	60	85	94	88	69	71
Suction (MPa)	23	23	23	23	23	23
Days	49	49	49	49	49	49
$w$ (%)	21.2	21.1	21.8	21.7	20.2	22.5
$S_r$ (%)	61	73	80	79	68	78
Suction (MPa)	13	13	13	13	13	13
Days	105	105	105	105	105	105
$w$ (%)	22.1	22.7	22.8	23.0	21.2	24.4
$S_r$ (%)	63	78	83	83	72	85
Suction (MPa)	11	11	11	11	11	11
Days	198	198	198	198	198	198
$w$ (%)	23.7	24.3	23.8	24.5	22.7	26.8
$S_r$ (%)	68	84	87	89	77	93
Suction (MPa)	6.6	6.6	6.6	6.6	6.6	6.6
Days	113	113	113	113	113	113
$w$ (%)	24.7	24.8	24.2	25.4	23.6	27.9
$S_r$ (%)	71	86	88	92	80	97
Suction (MPa)	0.5	0.5	0.5	0.5	0.5	0.5
Days	291	291	291	228	291	228

Reference	1. BB47-9-1	2. BB47-9-2	3. BB47-3-1	4. BB47-3-2	5. BB47-6-1	6. BB47-6-2
$w$ (%)	33.6	31.3	29.1	31.9	30.0	36.3
$S_r$ (%)	96	108	106	115	101	126

Tab. 14: Results of the water retention curves with samples from section S53

Reference	7. BB53-3-1a	8. BB53-3-1b	9. BB53-6-1a	10. BB53-6-1b	11. BB53-9-2a	12. BB53-9-2b
Distance to axis (cm)	67	67	67	67	57	57
Block $\rho_d$ (g/cm <sup>3</sup> )	1.65	1.65	1.67	1.67	1.62	1.62
Block $w$ (%)	22.8	22.8	18.7	18.7	19.0	19.0
Initial suction (MPa)	23	23	37	37	33	33
Initial $\rho_d$ (g/cm <sup>3</sup> )	1.60	1.57	1.61	1.63	1.58	1.61
Final $\rho_d$ (g/cm <sup>3</sup> )	1.57	1.54	1.56	1.52	1.52	1.57
Initial $w$ (%)	22.2	21.7	19.7	22.4	20.7	19.0
Initial $S_r$ (%)	87	81	79	93	78	76
Suction (MPa)	22.6	22.6	22.6	22.6	22.6	22.6
Days	81	81	76	76	75	75
$w$ (%)	22.3	22.0	20.4	20.9	21.2	19.9
$S_r$ (%)	84	79	75	73	74	75
Suction (MPa)	13.2	13.2	13.2	13.2	13.2	13.2
Days	141	141	141	141	141	141
$w$ (%)	23.4	23.0	21.6	22.1	22.4	21.3
$S_r$ (%)	88	83	80	77	78	79
Suction (MPa)	11.5	11.5	11.5	11.5	11.5	11.5
Days	97	97	97	97	97	97

Reference	7. BB53-3-1a	8. BB53-3-1b	9. BB53-6-1a	10. BB53-6-1b	11. BB53-9-2a	12. BB53-9-2b
w (%)	23.9	23.4	22.1	22.5	22.9	21.8
$S_r$ (%)	90	84	81	78	80	81
Suction (MPa)	6.3	6.3	6.3	6.3	6.3	6.3
Days	73	73	73	73	73	73
w (%)	24.2	24.1	22.7	23.4	24.0	22.9
$S_r$ (%)	91	86	84	81	83	85
Suction (MPa)	0.5	0.5	0.5	0.5	0.5	0.5
Days	112	228	228	228	228	112
w (%)	27.2	27.6	27.3	27.5	29.4	25.7
$S_r$ (%)	102	99	101	96	102	96

Tab. 15: Results of the water retention curves with samples from section S59

Reference	13. BB59-14-2a	14. BB59-14-2b	15. BB59-5-2a	16. BB59-5-2b
Distance to axis (cm)	5	5	5	5
Block $\rho_d$ (g/cm <sup>3</sup> )	1.57	1.57	1.57	1.57
Block w (%)	25.2	25.2	25.5	25.5
Initial suction (MPa)	20	20	20	20
Initial $\rho_d$ (g/cm <sup>3</sup> )	1.54	1.51	1.50	1.53
Final $\rho_d$ (g/cm <sup>3</sup> )	1.53	1.48	1.50	1.53
Initial w (%)	26.0	26.1	26.9	23.6
Initial $S_r$ (%)	93	89	91	84
Suction (MPa)	18.7	18.7	18.7	18.7
Days	87	87	87	87

<b>Reference</b>	<b>13. BB59-14-2a</b>	<b>14. BB59-14-2b</b>	<b>15. BB59-5-2a</b>	<b>16. BB59-5-2b</b>
$w$ (%)	23.4	24.7	25.0	21.3
$S_r$ (%)	82	81	84	75
Suction (MPa)	13.4	13.4	13.4	13.4
Days	140	140	140	140
$w$ (%)	24.2	25.4	26.0	22.4
$S_r$ (%)	85	84	88	79
Suction (MPa)	11.5	11.5	11.5	11.5
Days	97	97	97	97
$w$ (%)	24.7	26.0	26.5	22.6
$S_r$ (%)	87	85	89	80
Suction (MPa)	6.5	6.5	6.5	6.5
Days	73	73	73	73
$w$ (%)	25.8	27.2	27.6	23.9
$S_r$ (%)	91	89	93	85
Suction (MPa)	0.5	0.5	0.5	0.5
Days	112	112	291	112
$w$ (%)	29.0	31.0	33.4	27.1
$S_r$ (%)	102	102	113	96

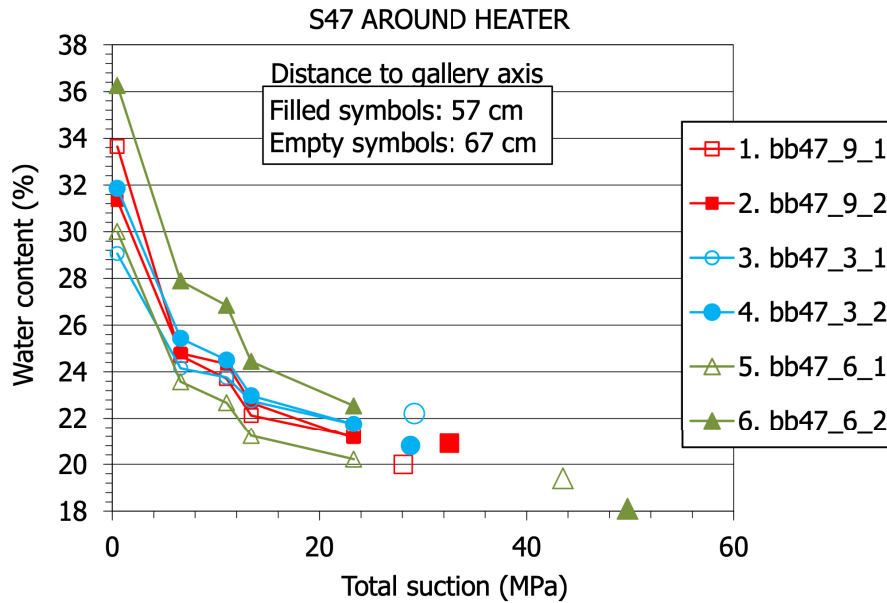


Fig. 72: Water retention curves determined for samples of section S47. The highest suction value for each sample (largest symbols) is that measured in the block from which it was trimmed and reported in Tab. 7

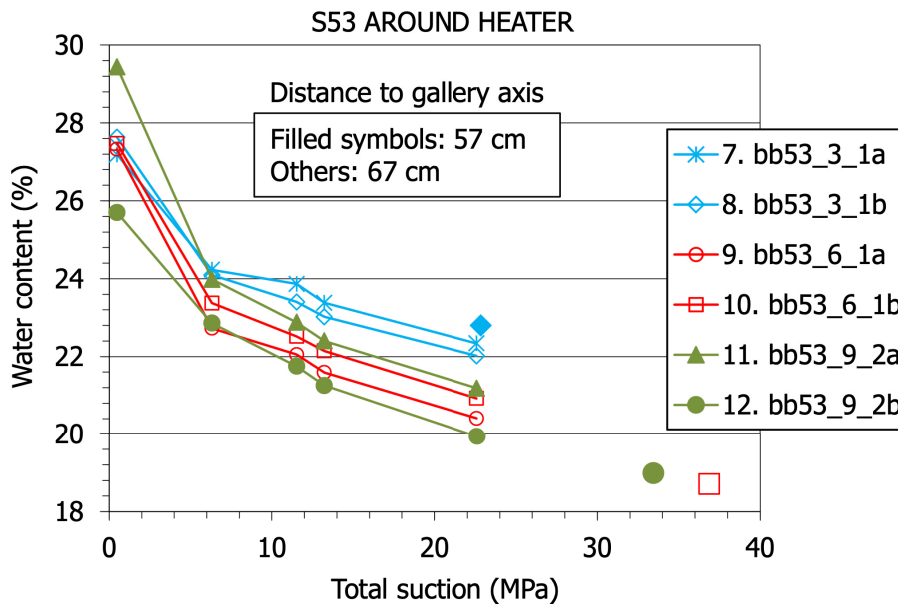


Fig. 73: Water retention curves determined for samples of section S53. The highest suction value for each sample (largest symbols) is that measured in the block from which it was trimmed and reported in Tab. 8

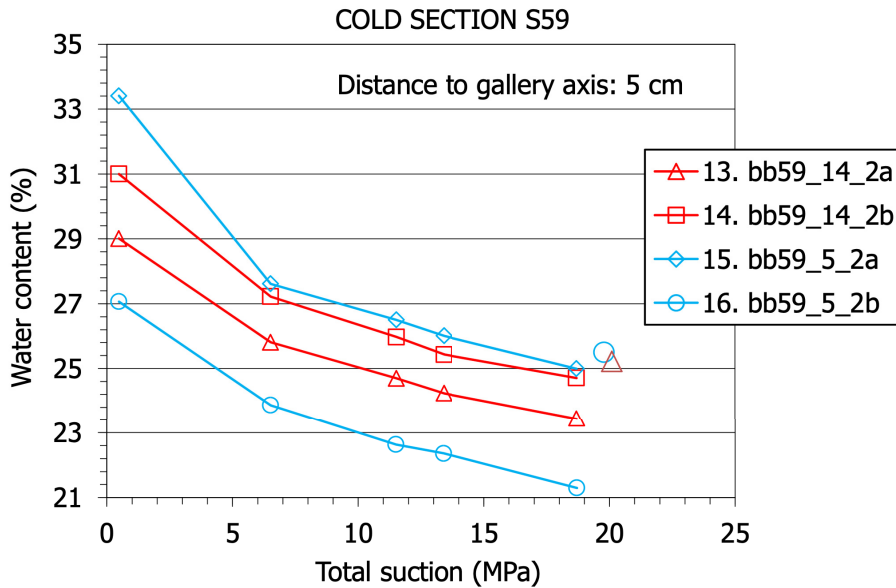


Fig. 74: Water retention curves determined for samples of section S59. The highest suction value for each sample (largest symbols) is that measured in the block from which it was trimmed and reported in Tab. 8

The Figures above show that even inside the same block, the behaviour of the samples was different. A possible explanation is the wide range of variation in dry densities, which spanned between 1.39 and 1.58 g/cm<sup>3</sup>, since dry density has an effect on the water retention capacity, particularly for the lowest suctions. However, in the results for the FEBEX-DP samples just presented this relation was not clear and the divergence between samples cannot be explained solely by their different dry densities. In contrast, the initial water content seems to also have a significant influence on the water content evolution during wetting, particularly for suction pressures above 10 MPa. This means that the initial water content difference between samples was more or less preserved until suction reached values around 10 MPa: samples with higher initial water content kept having higher water contents than the other samples during the wetting path. But when suction decreased below 10 MPa the trend changed.

Additionally, the samples have been grouped according to their position in the barrier, particularly their distance to the gallery axis, which in the samples around the heater conditions the maximum temperature to which they were submitted. The results for the samples that were taken closer to the heater, i.e. at 57 cm from the gallery axis in sections S47 and S53, have been plotted in Fig. 75. Since section S47 was located in the middle part of the heater whereas section S53 was towards the back of it, the temperatures during operation were very likely higher in section S47 (Tab. 2). However, the initial water contents were higher for the samples from section S47, and they remained so during the whole wetting path, the difference with samples from section S53 increasing as suction pressure decreased. The results for the rest of the samples, i.e. those taken at 67 cm from the gallery axis in sections S47 and S53, and from cool section S59 are plotted in Fig. 76. In this case the initial water content values of samples from sections S47 and S53 were similar but wetting for suction pressures below 10 MPa brought a higher increase in water content for samples of section S47. In fact, although the samples from section S59 had higher initial water contents than the rest of the samples, the final water contents at the end of the wetting path were similar for the two sets of samples (S47 and S59). It could be

concluded that the samples submitted to the highest temperatures (above 90°C according to Tab. 2) had the highest water adsorption capacity for the lowest suction pressures.

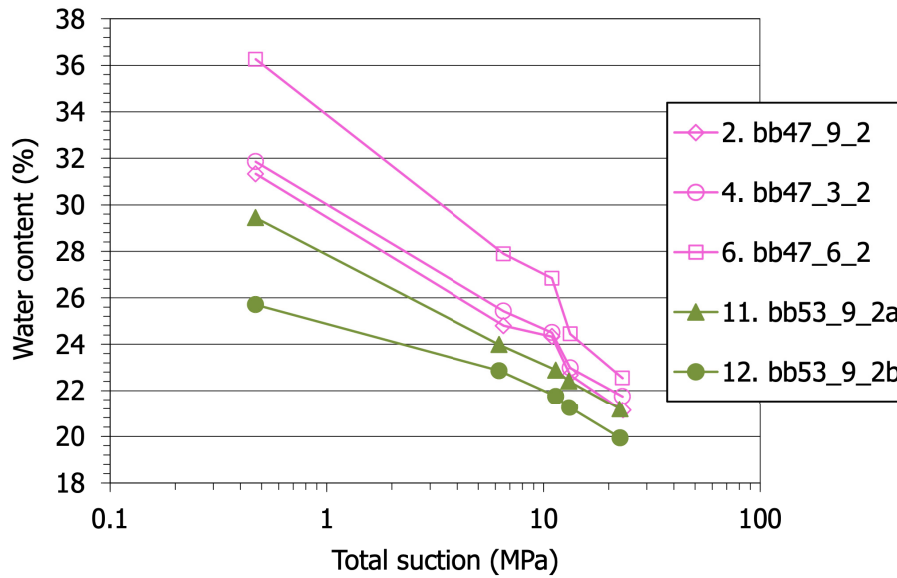


Fig. 75: Water retention curves of samples located at 57 cm from the gallery axis in sections S47 and S53

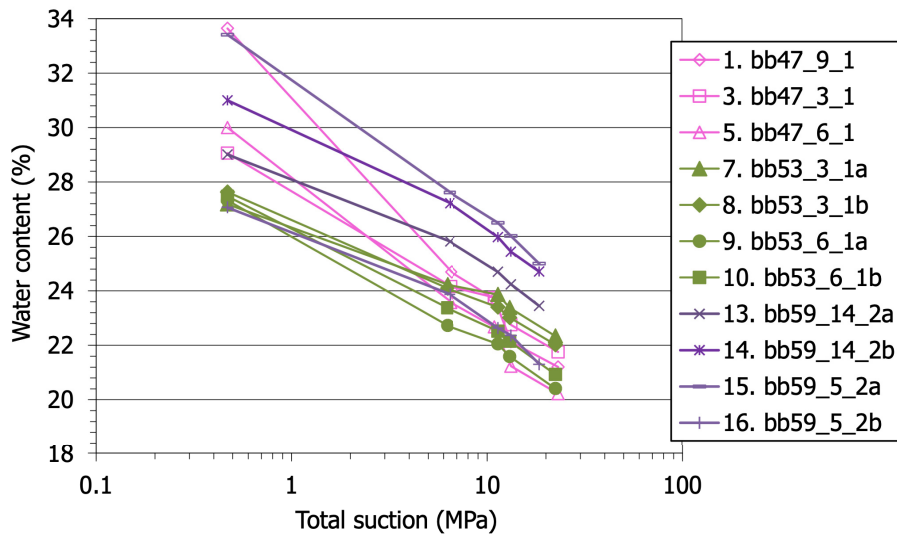


Fig. 76: Water retention curves of samples located at 67 cm from the gallery axis in sections S47 and S53 and 5 cm from the gallery axis in section S59

As it was reported in subchapter 4.2.3 the suction of the blocks was measured in the laboratory before being unpacked. The values obtained were related to the water content values measured in the same samples and it was possible to draw water retention curves for different ranges of

dry density (Fig. 51). These results are plotted in Fig. 77 along with the water retention curves shown above. For suction pressures below 20 MPa the samples of lower density had higher water retention capacity, since their porosity was higher. This was very clear for the results obtained by measuring suction but could also be stated from the results obtained in cells. For higher suctions the effect of density cannot be evaluated solely based on the results obtained with sensors, because the range of densities was too narrow. As it has been explained above, the effect of density was not clear either in the results obtained in cells. Nevertheless, the samples tested under different suction pressures in the desiccators (empty symbols) reached lower water contents than those measured in blocks of the same suction pressures (filled symbols). This can be explained by the differences in dry density, since the dry densities of the samples tested in cells were mostly below  $1.6 \text{ g/cm}^3$  whereas those of the blocks in which suctions higher than 20 MPa were measured were above  $1.6 \text{ g/cm}^3$ . Experiments performed with the FEBEX bentonite compacted at different dry densities showed that for high suction pressures the water retention capacity was higher with higher dry density, although the trend inverted towards lower suction pressures (Villar 2002). Overall, if the different densities are taken into account, the results obtained with both methods are quite consistent.

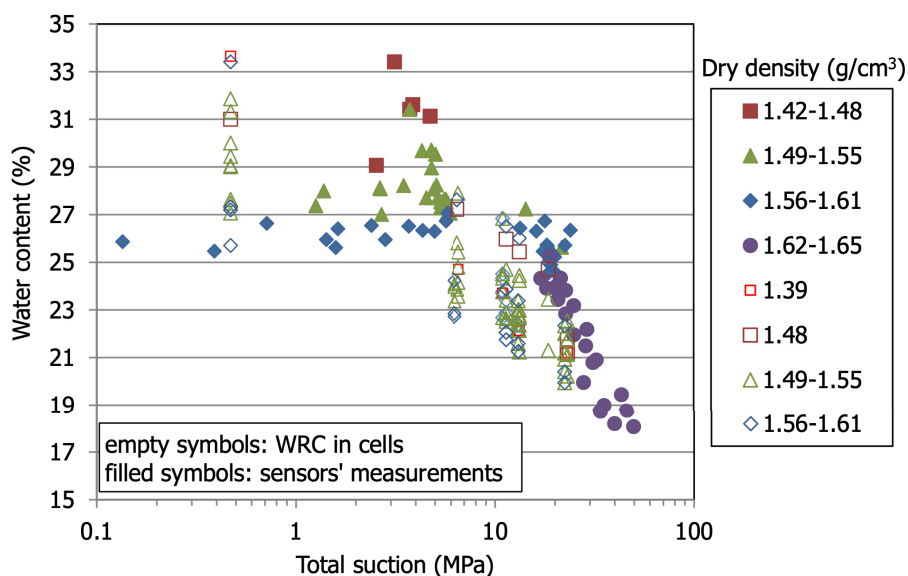


Fig. 77: Water retention curves obtained by measuring the suction pressure of blocks with different water content values (subchapter 4.2.3, filled symbols) and obtained in cells (this subchapter, empty symbols)

The water retention capacity of a material depends on its mineralogical composition –which is assumed to be the same in all the FEBEX-DP samples, since no relevant mineralogical changes were observed (Fernández et al. 2018)–, the hydraulic path (drying paths resulting in higher water content values than wetting paths), the temperature, the dry density and the stress conditions (both aspects particularly relevant in expansive materials). Other factors such as the salinity of the water available or the nature of the exchangeable cations may also affect the water retention capacity of a bentonite. Some of the influencing factors were not reproduced in the laboratory determinations, such as the temperature (which for some of the samples tested was higher during operation, whereas it was kept at  $20^{\circ}\text{C}$  during the laboratory determinations), kind of available water (particularly its salinity, since water was taken by the samples in the

laboratory in the vapour phase) or the precise stress conditions (which were isochoric in the laboratory tests, whereas the barrier was submitted to different stresses). For these reasons, the aim of the tests reported here was not to define the WRC of the samples under the operational conditions in situ, but to check if the material retrieved had the same water retention capacity that could be expected for the FEBEX reference bentonite under similar conditions (temperature, dry density and hydraulic path). Hence, all the factors possibly affecting the results have to be analysed before assessing the preservation of the water retention capacity. Some of these aspects are further discussed in Campos & Villar (2018). For example, the samples from sections S47 and S53 had a hydraulic history different to those from cool section S59, since the former had been dried during operation whereas the latter had been continuously wetted. Hence, the determination of the water retention curve for samples from sections S47 and S53 followed a “wetting after drying” path, whereas the samples from section S59 continued in the laboratory the wetting path started in the barrier.

To better evaluate the possible changes occurred in the water retention capacity during operation, the water retention curves obtained in the FEBEX-DP samples have been compared in Fig. 78 to those obtained for the reference bentonite compacted to different dry densities and submitted under confined conditions to different suction pressures, following the same procedure presented in this report. All the values were obtained in wetting paths (Villar 2007, Villar et al. 2012 and unpublished results). The results of the FEBEX-DP samples have been grouped in dry density ranges close to those available for the reference bentonite. Despite the scatter of the data, it can be said that the water retention capacity did not noticeably change during operation, and certainly did not decrease.

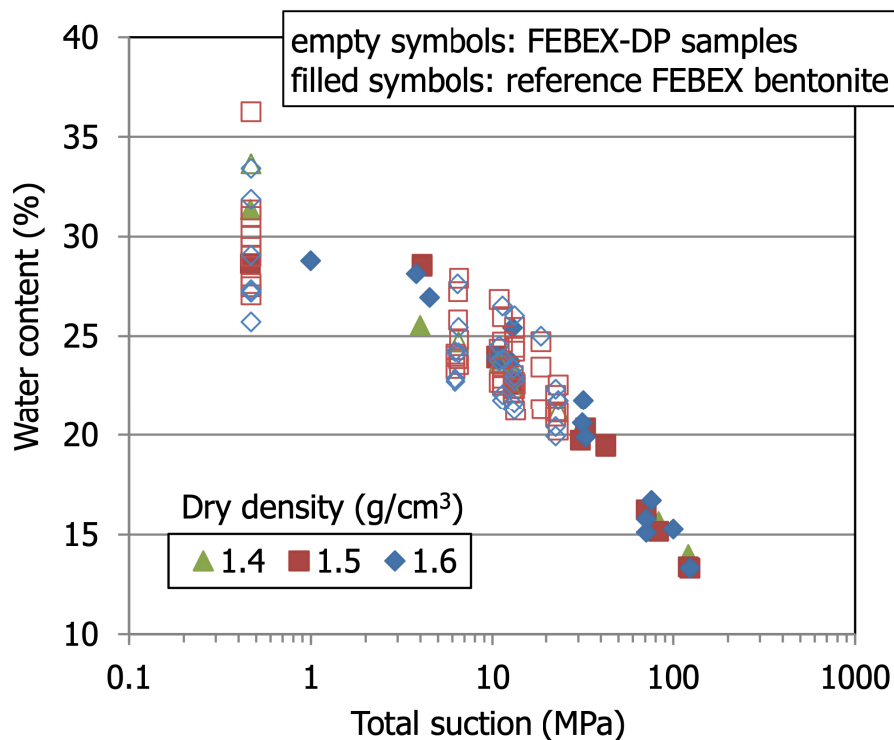


Fig. 78: Water retention curves obtained in cells for the reference bentonite compacted at different dry densities (filled symbols) and for the FEBEX-DP samples (this report, empty symbols)

### 4.4.2 Hydraulic conductivity

The hydraulic conductivity was measured in 17 samples drilled from blocks of sections S47 and S53 at different distances from the heater evenly distributed along sampling radii (Fig. 79). In section S47 the samples were drilled along radius B and D (samples BB-47-1-1, BB-47-1-2, BB-47-2-1, BB-47-2-2, BB-47-3-1, BB-47-3-2, BB-47-4-1, BB-47-4-2, BB-47-5-1, BB-47-5-2, BB-47-6-1) and in section S53 along sampling radius B (samples BB-53-1-1, BB-53-1-2, BB-53-2-1, BB-53-2-2, BB-53-3-1, BB-53-3-2).

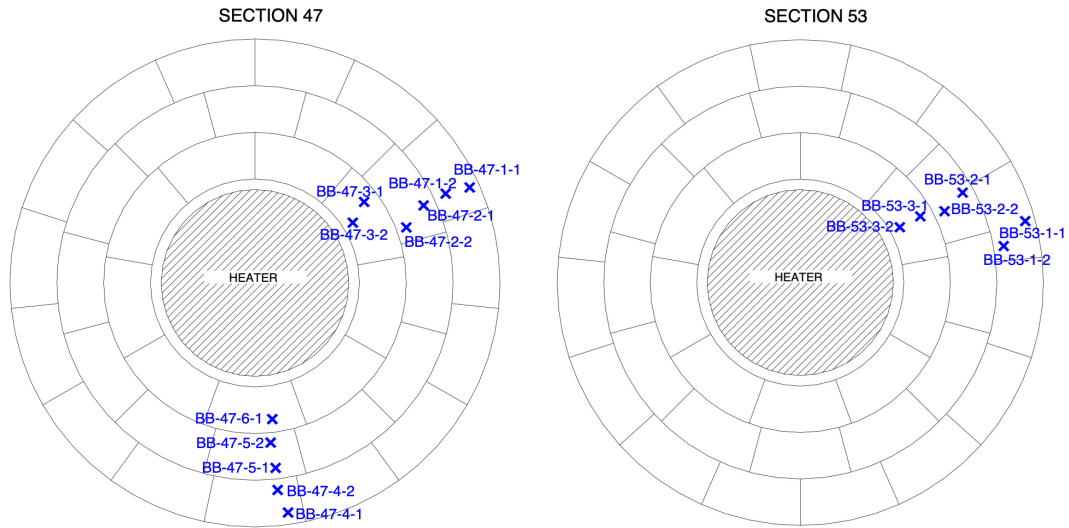


Fig. 79: Location of samples used for hydraulic conductivity tests

The samples were initially saturated for periods of time of between 13 and 86 days. Although many samples had a high initial degree of saturation, they took water because, once in the cell, their density decreased with respect to the original value, due to the filling of some irregularities that could have been created during trimming. In fact, there was a clear decrease in dry density of the samples tested in the permeability cells with respect to that of the blocks from which they were trimmed. Trimming caused changes in the original dry density of the samples, for which reason dry densities lower than those measured in adjacent samples of the same blocks –those shown in Tab. 7 and Tab. 8– were found (Fig. 80).

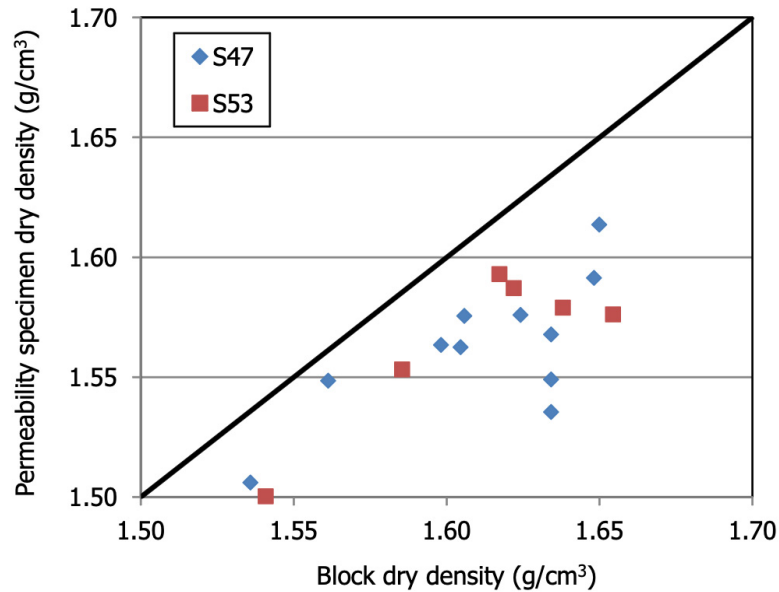


Fig. 80: Comparison of the dry density measured in adjacent samples in the same block and the dry density of the samples trimmed for permeability tests

Fig. 81 shows the water intake during the saturation of some of the samples tested. The samples with lower initial water content, i.e. those closer to the heater, took more water. Also, the specimens in section S47 took overall more water than those of section S53 because their initial water content was on average lower.

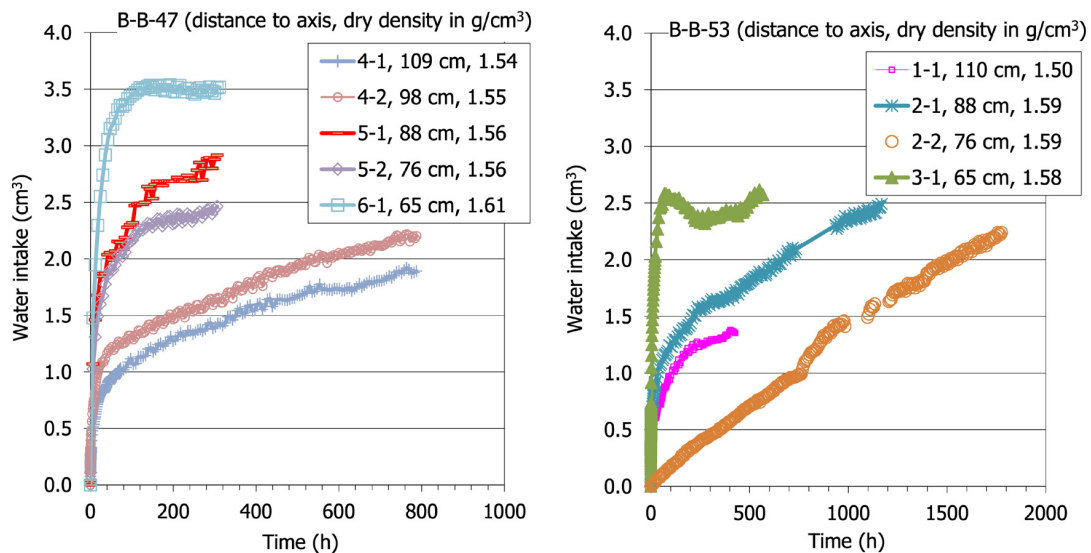


Fig. 81: Water intake during saturation of samples from sections S47 and S53

After saturation, hydraulic gradients of between 1600 and 11700 were applied to the samples and maintained until the outflow rate was constant. Afterwards, the hydraulic gradient was

changed and maintained until constant outflow rate. In some cases a third hydraulic gradient was applied. The whole measuring process took between 28 and 106 days. For the first samples tested, those from radius B in section S47, lower hydraulic gradients were applied (below 4000). As an example, the outflow curves for a sample from section S47 and another one from section S53 are shown in Fig. 82. These flows values were used to compute permeability using Equation 3, and the values obtained are shown in Tab. 16. The values obtained for all the samples have been plotted as a function of the hydraulic gradient applied in Fig. 83 and Fig. 84. Although there is not a clear relationship between hydraulic conductivity and gradient (only the values obtained for the same sample should be compared), the lowest permeabilities were measured when hydraulic gradients below 5000 were used. In fact, a previous research analysing the effect of hydraulic gradient on permeability of the FEBEX bentonite found that – in some cases– the permeability tended to be slightly lower as the hydraulic gradient decreased (Villar & Gómez-Espina 2009).

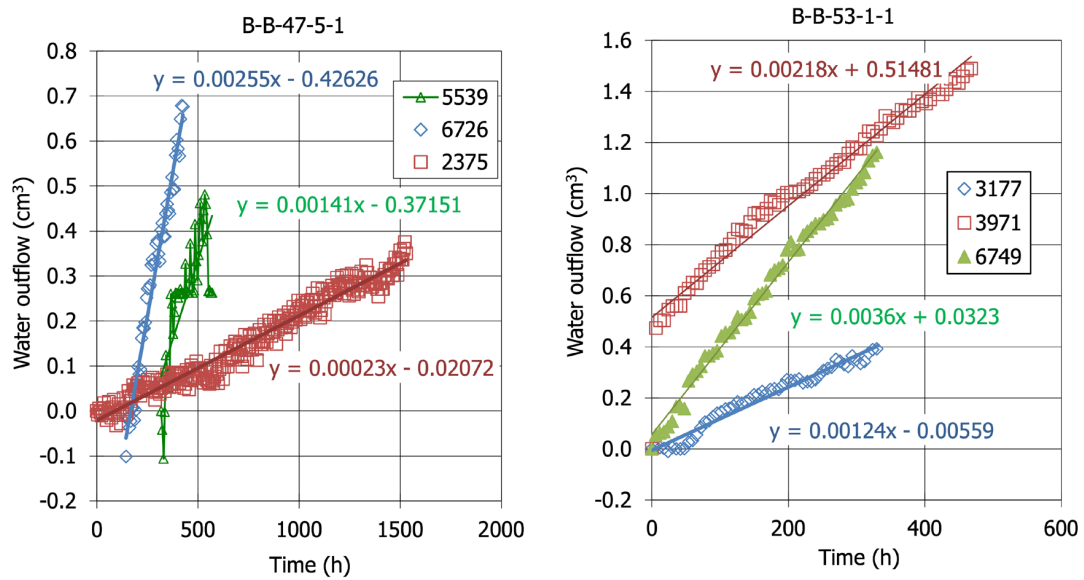


Fig. 82: Water outflow during the permeability tests of two samples. The hydraulic gradients applied are indicated in the legends (m/m)

Tab. 16: Results of the hydraulic conductivity measurements of the samples in Fig. 81

Reference	Hydraulic head (kPa)	Hydraulic gradient	Duration (days)	$k_w$ (m/s)	$k_{iw}$ (m <sup>2</sup> )	$T$ (°C)
BB-47-5-1	14000	5539	10	$3.6 \cdot 10^{-14}$	$3.7 \cdot 10^{-21}$	25.9±1.3
	17000	6726	18	$5.4 \cdot 10^{-14}$	$5.5 \cdot 10^{-21}$	23.4±0.4
	6003	2375	64	$1.4 \cdot 10^{-14}$	$1.4 \cdot 10^{-21}$	23.4±0.7
BB-53-1-1	8001	3177	14	$5.5 \cdot 10^{-14}$	$5.6 \cdot 10^{-21}$	20.8±0.7
	10000	3971	22	$7.8 \cdot 10^{-14}$	$7.9 \cdot 10^{-21}$	21.6±0.8
	16997	6749	10	$7.6 \cdot 10^{-14}$	$7.7 \cdot 10^{-21}$	

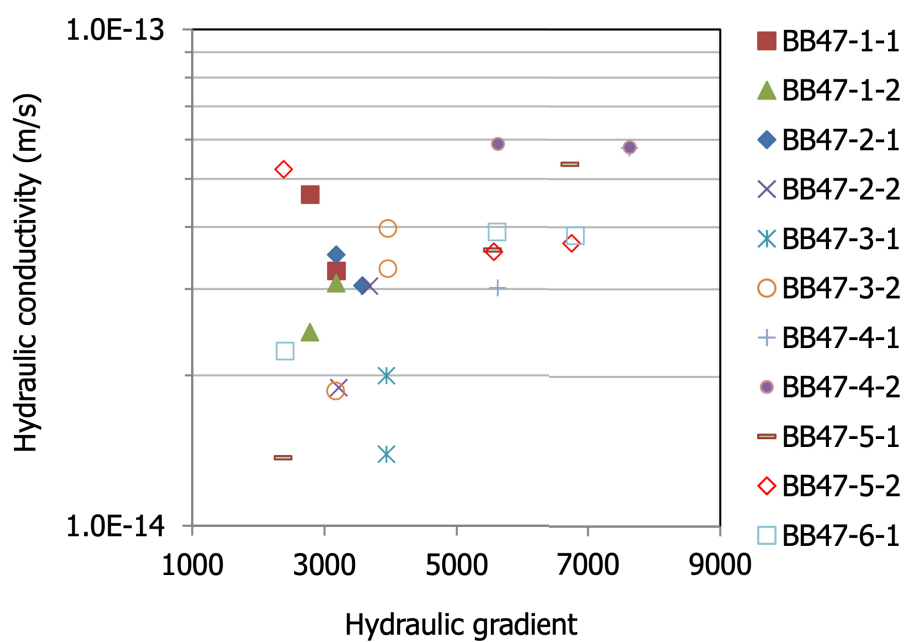


Fig. 83: Hydraulic conductivity of samples from section S47 as a function of the hydraulic gradient applied

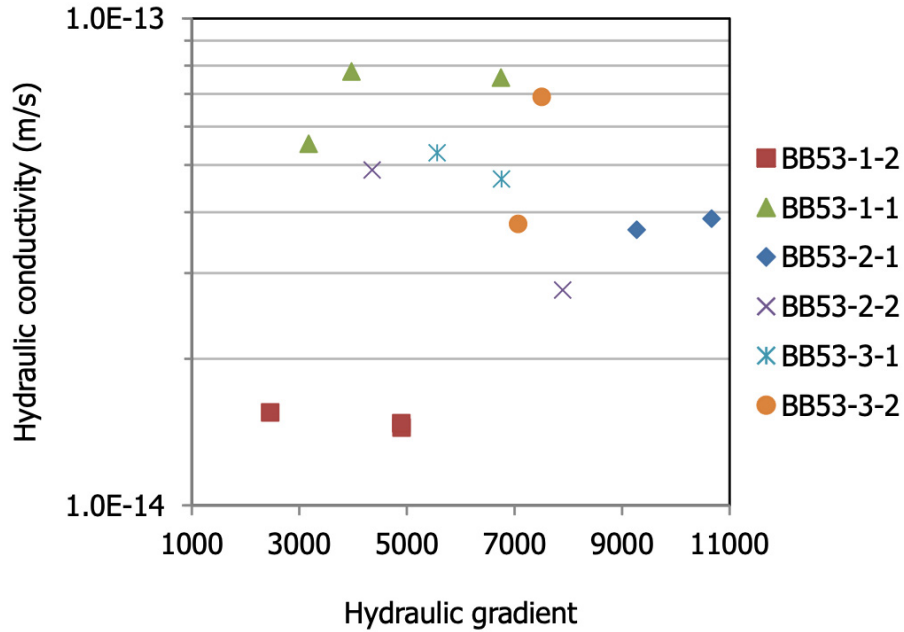


Fig. 84: Hydraulic conductivity of samples from section S53 as a function of the hydraulic gradient applied

A summary of the characteristics of all the tests, including the average permeability value obtained for the measurements performed under different hydraulic gradients is given in Tab. 17 for section 47 and in Tab. 18 for section S53. The time needed to saturate the sample and for the measurement of hydraulic conductivity, the average value of hydraulic conductivity ( $k_w$ ), the temperature during the measurement and the initial and final conditions of the samples are indicated. The hydraulic conductivities measured in the samples retrieved were in the order of  $10^{-14}$  m/s. As it has been explained above, because of trimming the dry density of the samples used for the permeability tests was lower than those measured in adjacent samples of the same blocks (Fig. 80). Consequently, the values measured do not correspond to the permeability of the bentonite at the moment it was retrieved, not only because the dry densities are lower, but also because the samples were saturated with deionised water to perform the determinations, and permeability depends greatly on the degree of saturation and pore fluid composition. Hence, the aim of these tests was not to determine the absolute value of the property in situ but evaluate any potential substantial changes in the hydraulic conductivity of the bentonite that may have occurred during FEBEX operation. This is why the values measured in the samples retrieved are compared to those of reference, untreated samples of the same dry density, which is the main parameter controlling permeability in expansive materials.

Tab. 17: Results of the hydraulic conductivity determinations performed in samples from section S47

Reference	Saturation (days)	$\rho_d$ (g/cm <sup>3</sup> )	Initial $w$ (%)	Initial $S_r$ (%)	Duration (days)	$k_w$ (m/s)	Final $w$ (%)	Final $S_r$ (%)	$T$ (°C)
BB-47-1-1	27	1.51	29.1	99	43	$4.0 \cdot 10^{-14}$	31.4	107	22
BB-47-1-2	27	1.55	27.7	100	71	$2.8 \cdot 10^{-14}$	30.3	110	22
BB-47-2-1	58	1.58	25.6	97	28	$3.3 \cdot 10^{-14}$	28.0	106	21
BB-47-2-2	86	1.58	25.6	97	47	$2.5 \cdot 10^{-14}$	29.0	110	22
BB-47-3-1	57	1.59	22.8	88	59	$1.7 \cdot 10^{-14}$	27.1	105	22
BB-47-3-2	57	1.57	22.1	83	59	$3.0 \cdot 10^{-14}$	28.9	108	22
BB-47-4-1	32	1.54	28.9	103	32	$4.4 \cdot 10^{-14}$	30.1	107	22
BB-47-4-2	32	1.55	27.3	99	32	$5.8 \cdot 10^{-14}$	29.6	108	21
BB-47-5-1	13	1.56	25.2	94	92	$3.4 \cdot 10^{-14}$	29.0	108	24
BB-47-5-2	13	1.56	26.3	97	106	$4.2 \cdot 10^{-14}$	30.4	113	24
BB-47-6-1	13	1.61	21.6	87	106	$3.3 \cdot 10^{-14}$	28.4	114	24

Tab. 18: Results of the hydraulic conductivity determinations performed in samples from section S53

Reference	Saturation (days)	$\rho_d$ (g/cm <sup>3</sup> )	Initial $w$ (%)	Initial $S_r$ (%)	Duration (days)	$k_w$ (m/s)	Final $w$ (%)	Final $S_r$ (%)	$T$ (°C)
BB-53-1-1	18	1.50	29.8	101	36	$6.6 \cdot 10^{-14}$	31.8	107	21
BB-53-1-2	22	1.55	27.5	100	33	$1.5 \cdot 10^{-14}$	29.5	108	21
BB-53-2-1	55	1.59	25.9	101	40	$3.8 \cdot 10^{-14}$	28.5	111	
BB-53-2-2	74	1.59	24.9	96	57	$3.8 \cdot 10^{-14}$	27.6	106	23
BB-53-3-1	32	1.58	23.2	88	56	$5.0 \cdot 10^{-14}$	27.8	105	
BB-53-3-2	60	1.58	22.4	85	57	$5.3 \cdot 10^{-14}$	28.0	106	23

The results are plotted in Fig. 85 as a function of the location of the samples during operation. The dry density of each sample is also indicated in the Figure. As a general rule, the hydraulic conductivity of bentonite is mainly related to dry density and the latter in turn should be related to the position of the block in the barrier. Consistently with this, the overall trend in section S47 is for the hydraulic conductivity to decrease towards the heater, where the densities were higher, whereas for section S53 there is not a clear dependence of hydraulic conductivity on the position of the sample inside the barrier. This is probably because the two samples drilled from the middle block of the barrier in section S53 had –as a consequence of trimming– higher dry density than those in the internal and external blocks, and consequently, lower hydraulic conductivity.

For this reason, the hydraulic conductivity values have been plotted in Fig. 86 as a function of the final dry density inside the permeability cell. The decrease of hydraulic conductivity with dry density is highlighted in this Figure. The fact that the change in dry density of the permeability samples during trimming with respect to the density of the blocks was not the same for all the samples (as observed in section S53), might be the reason why the relation between hydraulic conductivity and distance to the axis is not straightforward.

An empirical relationship for the reference FEBEX bentonite relating hydraulic conductivity ( $k_w$ , m/s) to dry density ( $\rho_d$ , g/cm<sup>3</sup>) was obtained for samples compacted to dry densities above 1.47 g/cm<sup>3</sup> and permeated with deionised water (Villar 2002):

$$\log k_w = -2.96 \rho_d - 8.58 \quad (\text{Eq. 10})$$

Both this curve and its range of variation (30%) are also shown in Fig. 86. When comparing these values to those expected for untreated FEBEX bentonite of the same dry density, it was found that the values for the FEBEX-DP samples were below the theoretical ones, in many cases even below the expected range of variation of this property for FEBEX bentonite. In

particular, the samples from radius B in section S47, which were tested using hydraulic gradients below 4000, had hydraulic conductivities clearly below those expected for the reference bentonite. In contrast, the samples of the same section tested with higher hydraulic gradients (those of radius D), had higher hydraulic conductivities, as had those of section S53. The determinations for the reference bentonite were performed applying hydraulic gradients on average of 15200, i.e. higher than those used for the testing of the FEBEX-DP samples. A previous research analysing the effect of hydraulic gradient on permeability of the FEBEX bentonite found that –in some cases– the permeability tended to be slightly lower as the hydraulic gradient decreased (Villar & Gómez-Espina 2009). Hence, it is considered that these low values are a consequence of using hydraulic gradients close to the critical ones in the samples of radius B in section S47.

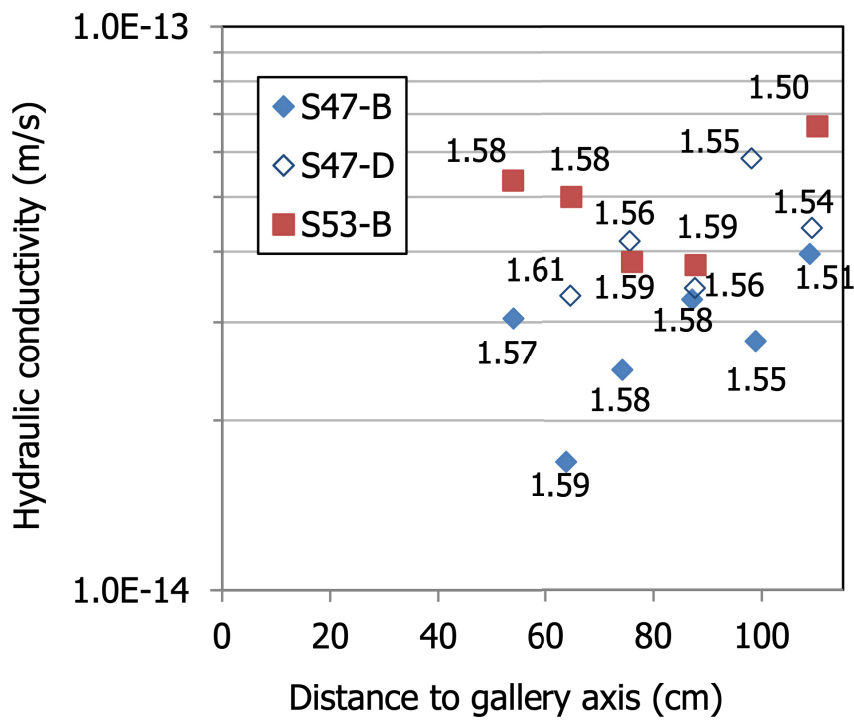


Fig. 85: Hydraulic conductivity of samples from section S47 and S53 taken along different radii (the dry density of the specimens is indicated in g/cm³)

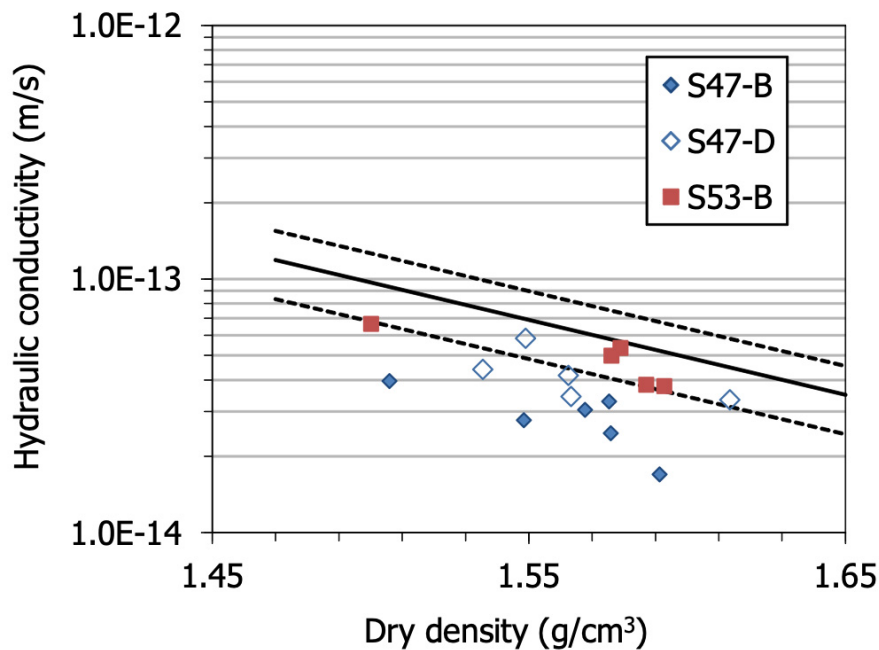


Fig. 86: Hydraulic conductivity of samples from different sections and radii (indicated in the legend) and empirical correlation for untreated FEBEX bentonite obtained with Eq. 10 (solid line, the dashed lines indicate the expected range of variation, 30%)

Nevertheless, when the values actually measured are compared with those obtained for samples of the same dry density obtained with Eq. 10 (Fig. 87), it is clear that the hydraulic conductivity of the samples retrieved decreased with respect to that of the reference bentonite and was on average on the lower range of variation of this property (about 27% below the average expected value). Unlike what was observed in the swelling capacity tests, this decrease did not seem to be related to the position of the samples in the barrier. The osmotic effect was probably not significant on the permeability samples because the samples were confined and not able to swell differently during the permeability measurement as it happened in the swelling capacity tests (see subchapter 4.5.1). There is also the possibility that, during the 18 years operation, the microstructure of the bentonite experienced changes that could affect the water flow. It is known that saturation involves a homogenisation of pore sizes towards the smaller sizes, leading to a decrease of intrinsic permeability with increasing degree of saturation (Villar & Lloret, 2001). Indeed, this process took place during the saturation of the samples in the permeability cell, and it certainly also occurred during saturation of the samples used to determine the permeability of the reference bentonite. But over the 18 years of saturation in the barrier the average pore size became lower and more homogeneous, as it has been discussed in the subchapter about the pore size distribution (4.2.5), this would explain the lower hydraulic conductivity of the samples that were exposed to barrier conditions. Interestingly, the analyses performed in samples retrieved from large-scale tests performed at the Äspö Hard Rock Laboratory also showed in some cases a slight decrease in the hydraulic conductivity of the MX-80 buffer with no spatial trend (Karnland 2009, 2011).

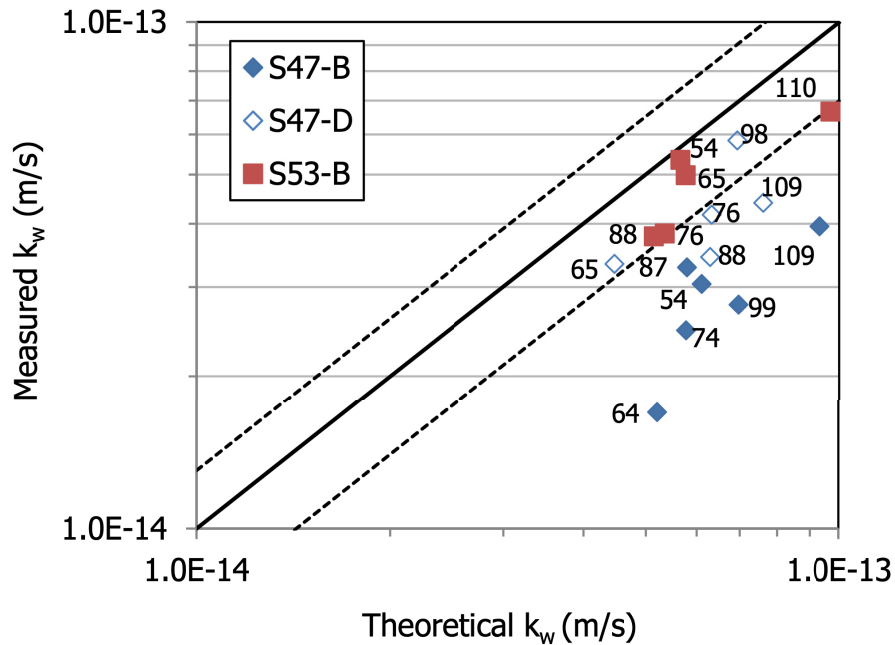


Fig. 87: Comparison between the hydraulic conductivity measured and that corresponding to samples of the reference bentonite of the same dry density obtained with Eq. 10. The distance to the gallery axis of each sample is indicated in cm

#### 4.4.3 Gas permeability

Fifteen gas permeability tests were performed in triaxial cells with bentonite core samples obtained by drilling on site or by drilling from blocks in the laboratory (Fig. 28). In every section at least six cores were drilled, two in each barrier ring: external, intermediate and internal. Of every couple of samples drilled in the same bentonite ring, one of them was drilled in the middle of a block, and the other one at the contact between that block and the neighbouring one, thereby including the vertical interface between two bentonite blocks. This sampling procedure allowed analysing the effect of sealed joints on gas permeability. Usually it is assumed that the interface has no effect on water permeability. Fig. 88 shows the location of the cores drilled in the sampling sections.

Gas permeability was measured in samples with initial dry densities values between 1.51 and 1.64 g/cm<sup>3</sup>, and with water contents between 20 and 28%, corresponding to initial degrees of saturation between 79 and 100%. Tab. 19 summarises the characteristics of the specimens tested. Most samples were initially tested in the low-pressure setup and then in the high-pressure setup. A summary of the result obtained in each setup is given in the two following subchapters (4.4.3.1 and 4.4.3.2), the results are jointly discussed in subchapter 4.4.3.3.

Tab. 19: Characteristics of the bentonite samples used for gas permeability tests

Reference	Distance to axis (cm)	Initial $\rho_d$ (g/cm <sup>3</sup> )	Initial $w$ (%)	Initial $S_r$ (%)	Height (cm)	Dia. (cm)	Drilling	Comments	Setup <sup>a</sup>
BC-36-1	59	1.52	26.7	93	3.11	3.80	On-site		HP-US
BC-44-1	103	1.57	26.2	98	3.73	3.98	On site		LP/LCP
BC-44-2	62	1.56	23.2	86	2.41	4.15	On site	Interface between blocks	LP/LCP
BC-44-4	61	1.61	24.5	97	4.11	4.19	On site		LP/LCP
BC-44-5	103	1.52	28.4	100	4.10	4.18	On site		LP/LCP
BC-44-6	102	1.51	28.4	97	3.90	4.18	On site	Interface between blocks	LP/LCP
BC-44-7	61	1.62	19.5	79	3.59	4.17	On site		LP/HCP to LCP
BC-47-1	103	1.55	26.4	96	3.86	4.12	On site		LP/LCP
BC-47-2	104	1.54	26.4	94	3.98	3.80	On site		HP-US
BC-47-3 <sup>b</sup>	82	1.61	23.7	95	3.79	4.15	On site		LCP
BC-47-4 <sup>b</sup>	81	1.59	24.8	97	3.70	3.60	On site	Interface between blocks	HP-US
BC-47-6	66	1.64	19.6	82	3.92	4.12	On site	Interface between blocks	LP/HCP
BB-53-4-2	87	1.59	25.1	96	5.21	4.96	Laboratory		LP
BB-53-5-1	76	1.63	23.3	96	4.85	4.95	Laboratory		LP/LCP

Reference	Distance to axis (cm)	Initial $\rho_d$ (g/cm <sup>3</sup> )	Initial $w$ (%)	Initial $S_r$ (%)	Height (cm)	Dia. (cm)	Drilling	Comments	Setup <sup>a</sup>
BB-53-5-2	99	1.63	22.9	94	4.99	5.00	Laboratory		LP/HCP

<sup>a</sup> LP: low pressure equipment, HP-US: high-pressure, unsteady-state, HCP: high-pressure, steady-state, high confining pressure, LCP: high-pressure, steady-state, low confining pressure (see Tab. 6)

<sup>b</sup> the position of these blocks is interchanged with respect to the Sampling Book (Bárcena & García-Siñeriz 2015)

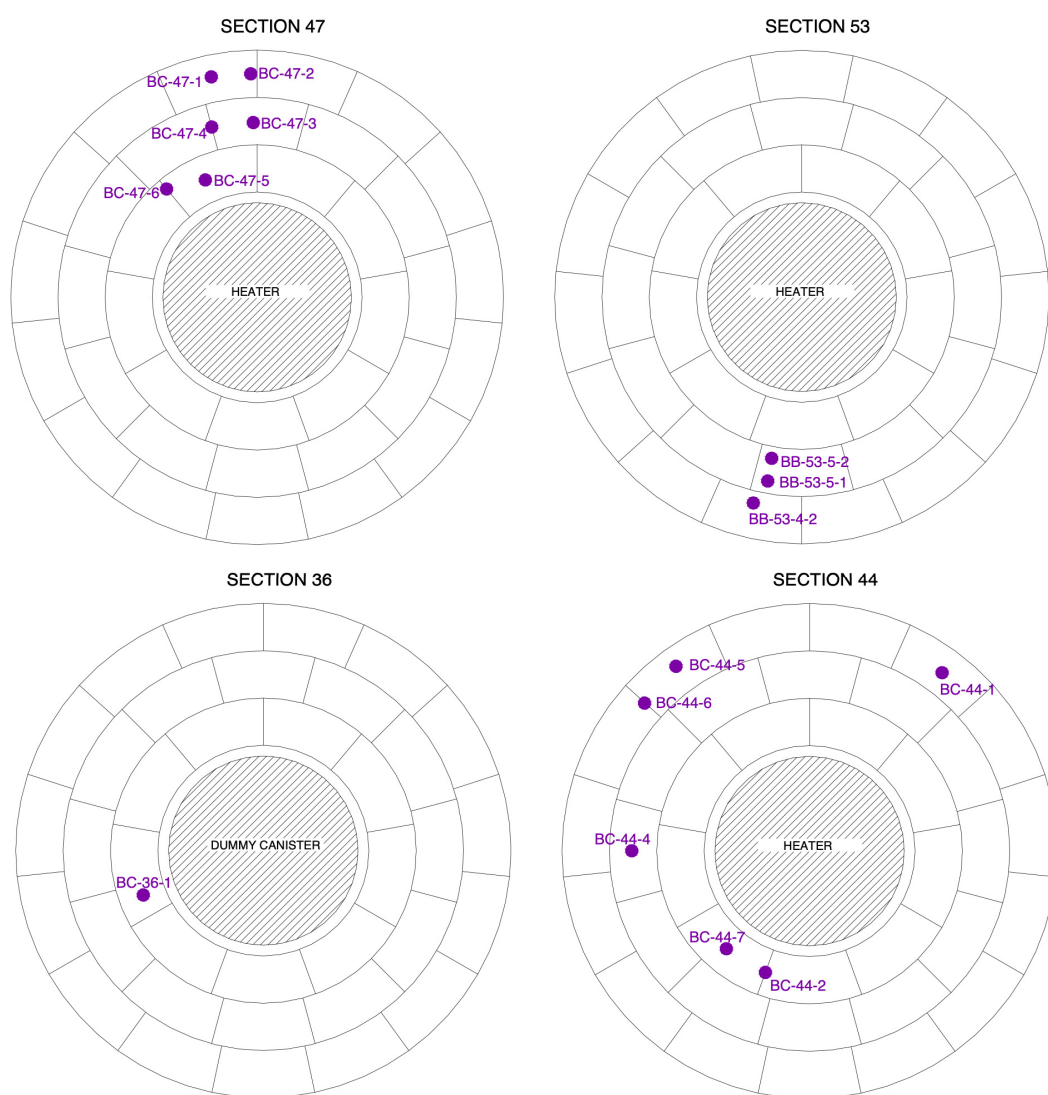


Fig. 88: Location of the samples tested for gas permeability (the actual position of the cores differs in some cases from the one in the Sampling Book (Bárcena & García-Siñeriz 2015). Samples from section S53 were drilled in the laboratory

**4.4.3.1 Low-pressure equipment (LP)**

The low-pressure tests determined the gas permeability under low confining and injection pressure conditions and assessed changes with respect to the reference bentonite. The tests followed two stages:

- Stage 1: constant confining pressure of 0.6 MPa and initial gas injection pressure of 0.1 MPa.
- Stage 2: constant confining pressure of 1.0 MPa and initial gas injection pressure of 0.1 MPa.

The effect of confining pressure was noticeable in most cases, even though the confining pressures applied were very low in relation to the swelling pressure of the bentonite or the compaction pressure applied to manufacture the blocks. Accordingly, the pressure decrease rate was lower in the samples tested under higher confining pressure. Also, when an interface was present the pressure decrease rate was higher. Both aspects can be seen in Fig. 89. Obviously, higher pressure decreases rates resulted in higher effective permeabilities (Eq. 4). Tab. 20 summarises the results obtained in each sample, expressed in terms of gas permeability ( $k_g$ ) and effective permeability ( $k_{ig} \cdot k_{rg}$ ). These results have been plotted as a function of the distance to the gallery axis in Fig. 90. The permeability is clearly lower in the samples of the external ring of the barrier that were more saturated. Indeed, the inverse relation between permeability and degree of saturation is shown in Fig. 91. The effect of the interface was not clear for the samples of the external ring that were more saturated, in which the two parts of the samples were tightly joined. Fig. 92 shows the difference between an interface between two blocks of the external ring, barely discernible, and between two blocks of the inner ring.

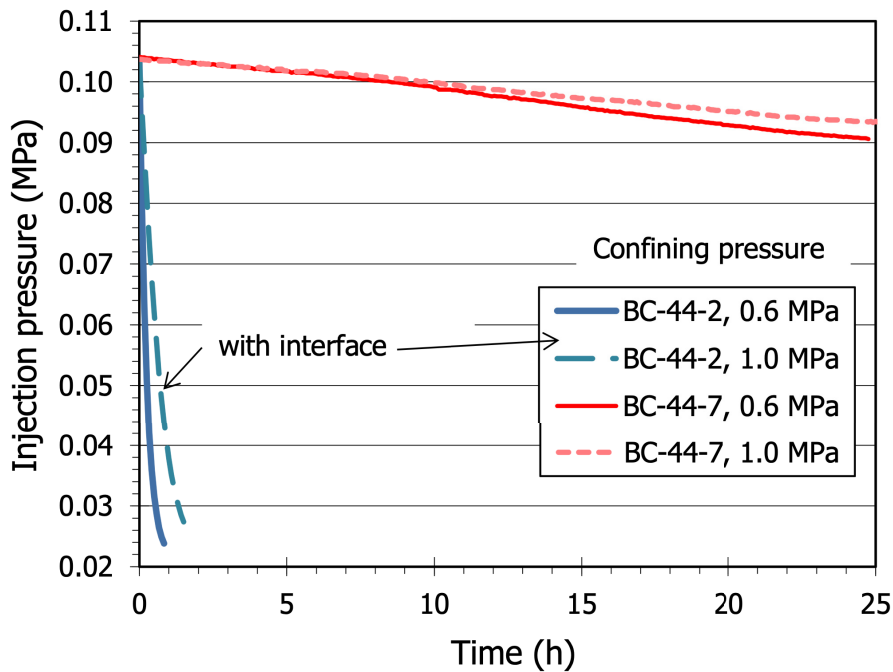


Fig. 89: Pressure decrease in the gas tank during testing of two samples of section S44 taken at ~61 cm from the gallery axis (sample BC-44-2 with an interface) under two different confining pressures

Tab. 20: Results of the gas permeability tests performed in the low-pressure setup

Sample reference	Confining $P$ (MPa)	Duration (hours)	$k_{ig} \cdot k_{rg}$ (m <sup>2</sup> )	$k_g$ (m/s)
BC-44-1	0.6	26	$4.6 \cdot 10^{-17}$	$2.9 \cdot 10^{-11}$
	1.0	224	$3.8 \cdot 10^{-17}$	$2.3 \cdot 10^{-11}$
BC-44-2 <sup>a</sup>	0.6	1	$4.4 \cdot 10^{-14}$	$2.7 \cdot 10^{-8}$
	1.0	2	$1.6 \cdot 10^{-14}$	$9.6 \cdot 10^{-9}$
BC-44-5	0.6	214		No flow
BC-44-6 <sup>a</sup>	0.6	29	$6.9 \cdot 10^{-17}$	$4.3 \cdot 10^{-11}$
	1.0	76	$2.1 \cdot 10^{-17}$	$1.3 \cdot 10^{-11}$
BC-44-7	0.6	25	$1.3 \cdot 10^{-16}$	$7.7 \cdot 10^{-11}$
	1.0	26	$9.9 \cdot 10^{-17}$	$6.1 \cdot 10^{-11}$
BC-47-1	0.6	285	$4.0 \cdot 10^{-18}$	$2.4 \cdot 10^{-12}$
BC-47-6 <sup>a</sup>	0.6	6	$2.7 \cdot 10^{-14}$	$1.6 \cdot 10^{-8}$
	1.0	5	$1.4 \cdot 10^{-14}$	$8.6 \cdot 10^{-9}$
BB-53-4-2	0.6	10		No flow
BB-53-5-1	0.6	477		No flow
BB-53-5-2	0.6	289		No flow

<sup>a</sup> samples with interface

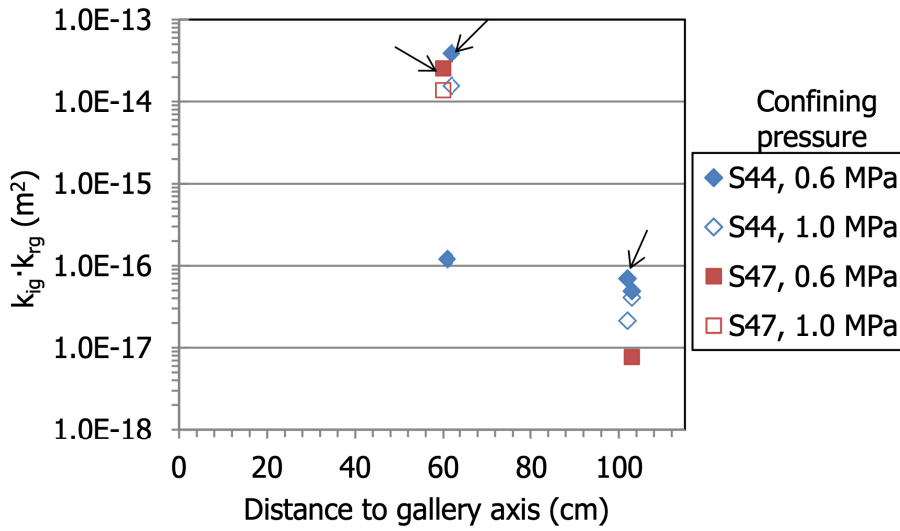


Fig. 90: Effective permeability values obtained in the low-pressure equipment as a function of the position in the barrier. The arrows point to samples with interface

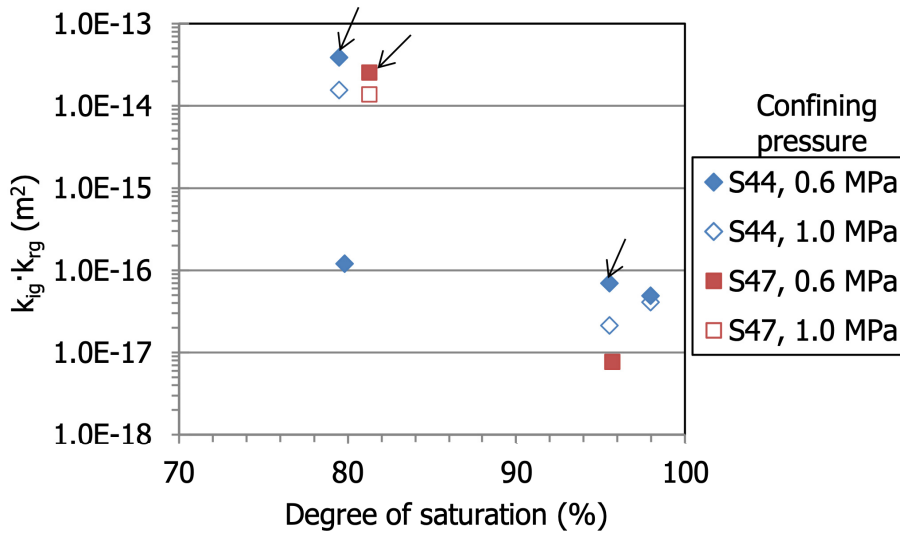


Fig. 91: Effective permeability values obtained in the low-pressure equipment as a function of the degree of saturation. The arrows point to samples with interface



Fig. 92: Interface in a sample from the external ring (indicated by an arrow, BC-44-6) and from the inner ring (BC-44-2)

#### 4.4.3.2 High-pressure equipment

The samples in which no flow had occurred or where it had been very low when tested in the low-pressure equipment were also tested in the high-pressure (HP) equipment. The HP equipment analyses the influence of boundary conditions (injection and confining pressures) on the value of permeability. To accomplish this, the tests consisted of several steps which followed a pressure path that was adjusted to each sample's characteristics. The tests started under constant confining pressure of 0.6 or 1.0 MPa and injection pressure of 0.1 MPa, equal to the pressures previously reached in the low-pressure setup. Afterwards the injection pressure was increased by 0.1 MPa every step. Once the flow was sufficiently high to be measured accurately (0.5 mL/min) or the difference between confining and injection pressures was lower than 0.2 MPa, the confining pressure was progressively increased until gas could not flow through the sample. Finally, the confining pressure was stepwise released. Tab. 21 summarises the range of pressures applied in the high-pressure equipment. Two representative tests are described below in detail.

Tab. 21: Range of pressures applied with the high-pressure equipment

Sample	Setup	Confining $P$ (MPa)	Injection $P$ (MPa)
BC-36-1	HP-US	1.0-14.0	0.2-13.0
BC-44-1	LP/LCP	1.0-2.5	0.2-0.6
BC-44-2 <sup>a</sup>	LP/LCP	1.0-9.0	0.15-0.5
BC-44-4	LP/LCP	0.6-3.5	0.2-0.5

Sample	Setup	Confining $P$ (MPa)	Injection $P$ (MPa)
BC-44-5	LP/LCP	0.6-1.5	0.2-1.4
BC-44-6 <sup>a</sup>	LP/LCP	1.0-3.0	0.2-0.6
BC-44-7	LP/HCP to LCP	1.0-9.5	0.2-0.5
BC-47-1	LP/LCP	0.6-2.5	0.2-0.7
BC-47-2	HP-US	1.5-12.0	0.2-1.6
BC-47-3	LCP	0.6-1.0	0.1-1.0
BC-47-4 <sup>a</sup>	HP-US	1.8-9.0	0.2-2.5
BC-47-6 <sup>a</sup>	LP/HCP	0.6-3.0	0.1
BB-53-5-1	LP/LCP	0.6-1.7	0.2-1.2
BB-53-5-2	LP/HCP	0.6-1.7	0.2-0.6

<sup>a</sup> samples with interface

Core sample BC-44-4 was drilled on site in the centre of a block of the intermediate ring of the barrier (Fig. 88). The dry density of the sample was 1.61 g/cm<sup>3</sup> and the water content 24.5%, corresponding to a degree of saturation of 97%.

Sample BC-44-4 was tested in the high-pressure steady-state setup, in the low confining pressure line (LCP) following the pressure path showed in Fig. 93, consisting of two phases:

- Phase 1: with an injection pressure of 0.2 MPa the confining pressure was increased from 0.6 to 1.0 MPa, and then the injection pressure was increased up to 0.5 MPa.
- Phase 2: keeping the injection pressure constant at 0.5 MPa, the confining pressure was increased up to 3.5 MPa and then decreased.

The change in injection pressure did not modify permeability, but it clearly decreased when the confining pressure increased and then increased again as the confining pressure was released (Fig. 94). Nevertheless, the permeability values measured during unloading were an order of magnitude lower than those measured for the same confining pressure during loading. The duration of the steps was between 1 and 2 hours, although between some of the steps (during night and weekends) the valves of the cell were closed, and the sample remained under the last pressure situation longer. This allowed to check that the time the sample remained under a given confining pressure also had an influence on the permeability value, which was slightly lower if the sample had remained under the same confining pressure longer (Fig. 94, right).

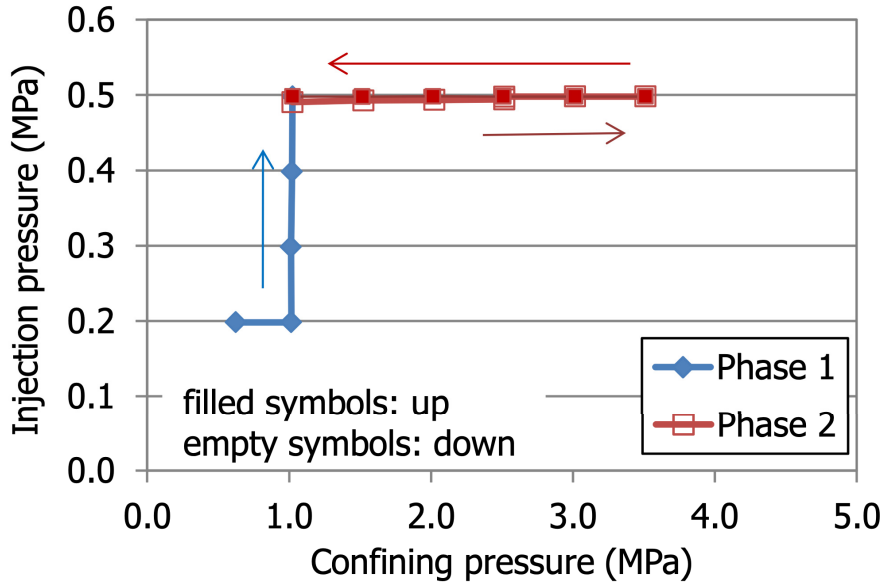


Fig. 93: Pressure path followed in the LCP setup for sample BC-44-4

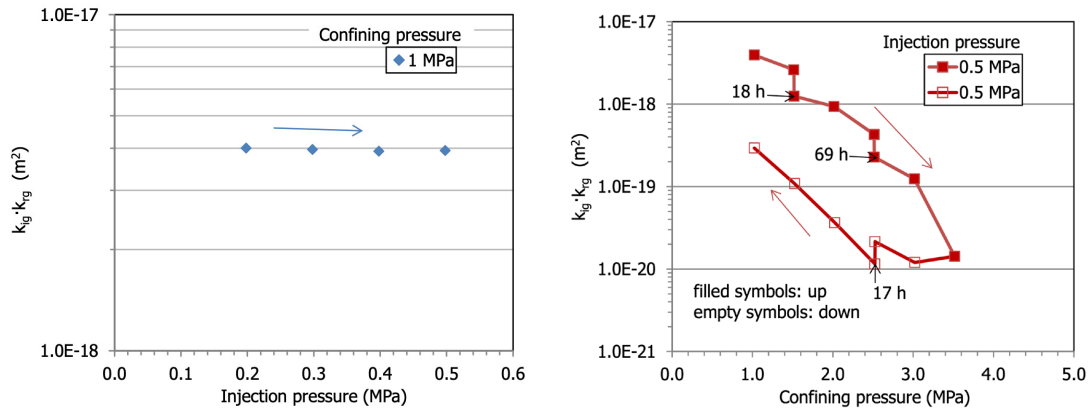


Fig. 94: Evolution of gas effective permeability at constant confining pressure (left) and constant injection pressure (right) for sample BC-44-4 (the duration of longer steps is indicated in hours)

Core sample BC-47-4 was drilled on site between two blocks of the middle ring of the bentonite barrier (Fig. 88), hence the core had a longitudinal interface (although according to the Sampling Book (Bárcena & García-Siñeriz 2015) it should have been drilled in the central part of a block). Although the interface was not initially visible, upon trimming of the sample the two parts of it detached. The initial dry density and water content of the specimen once trimmed were 1.59 g/cm<sup>3</sup> and 24.8%, respectively.

This sample was only tested in the high-pressure, unsteady-state (HP-US) equipment, following these phases (Fig. 95):

- Phase 1: the injection pressure was set to values between 0.1 and 0.3 MPa and the confining pressure was increased from 2 to 7 MPa; afterwards, keeping this confining pressure constant, the injection pressure was increased up to 2 MPa.
- Phase 2: the confining pressure was increased from 7 to 9 MPa.
- Phase 3: the confining pressure was decreased from 9 to 3 MPa and then the injection pressure was decreased to 1.5 MPa.

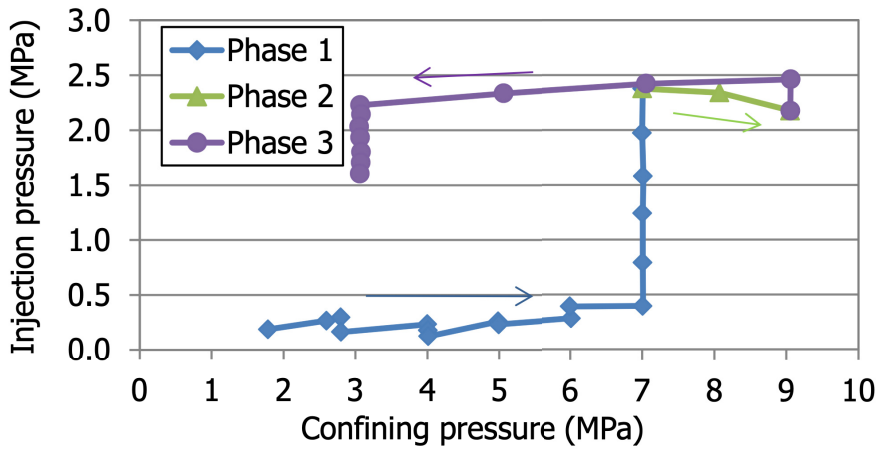


Fig. 95: Pressure path followed in the HP-US setup for sample BC-47-4

The evolution of pressure on the upstream and downstream pressure vessels from which permeability was computed is shown in Fig. 96. The duration of most of the steps was between 1 and 3 days, although there were some steps that took very long, and thus the total duration of the test increased to 172 days. The permeability values computed from the pressure increase in the downstream pressure vessel are shown in Fig. 97 as a function of the confining pressure. There was a clear trend for the permeability to decrease as the confining pressure increased. Nevertheless, a dispersion is visible which can be explained by the effect of a variable injection pressure, and of the hysteresis in loading-unloading cycles. Fig. 98 shows the permeability values as a function of the injection pressure for different confining pressures without a clear trend. The Figure also shows the effect of the confining pressure, which was very clear. The duration of the steps may also have an influence on the permeability measured, since permeability decreased noticeably when the confining pressure was applied for a long time. However, when the confining pressure decreased again to 3 MPa after loading up to 9 MPa, the permeability values measured were lower than the values measured initially for similar or even higher confining pressures. This would mean that some irreversible closure of gas pathways took place during consolidation. In fact, the interface between the two halves of the specimen appeared completely sealed after the test (Fig. 99) and separated only after drying in the oven.

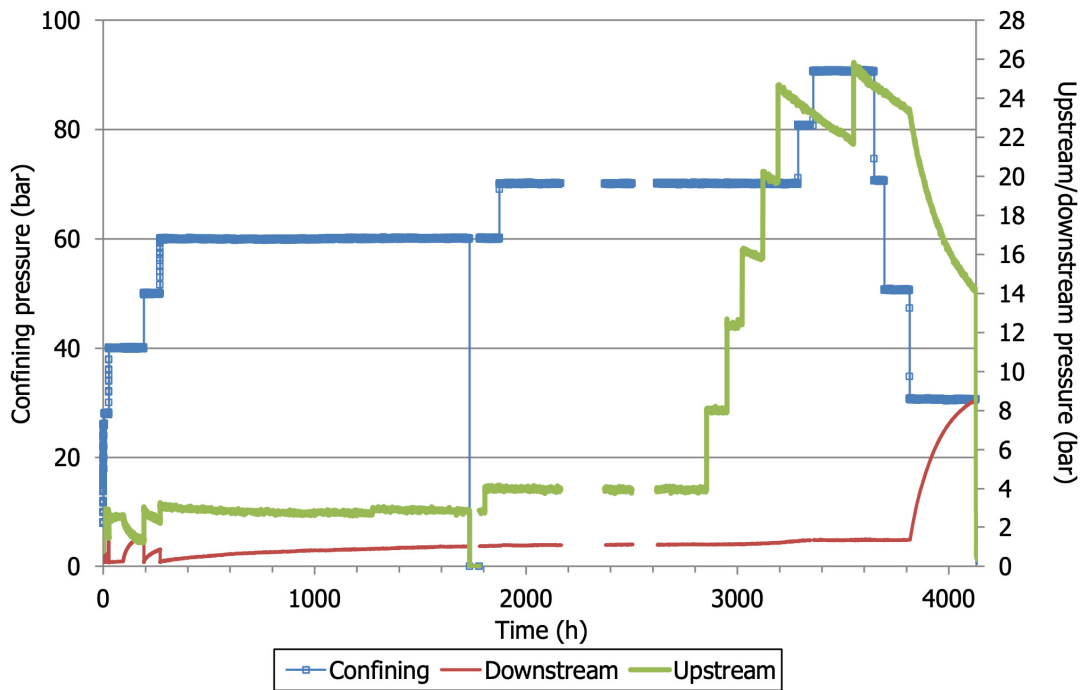


Fig. 96: Evolution of confining pressure and of pressure on the upstream and downstream vessels during test BC-47-4

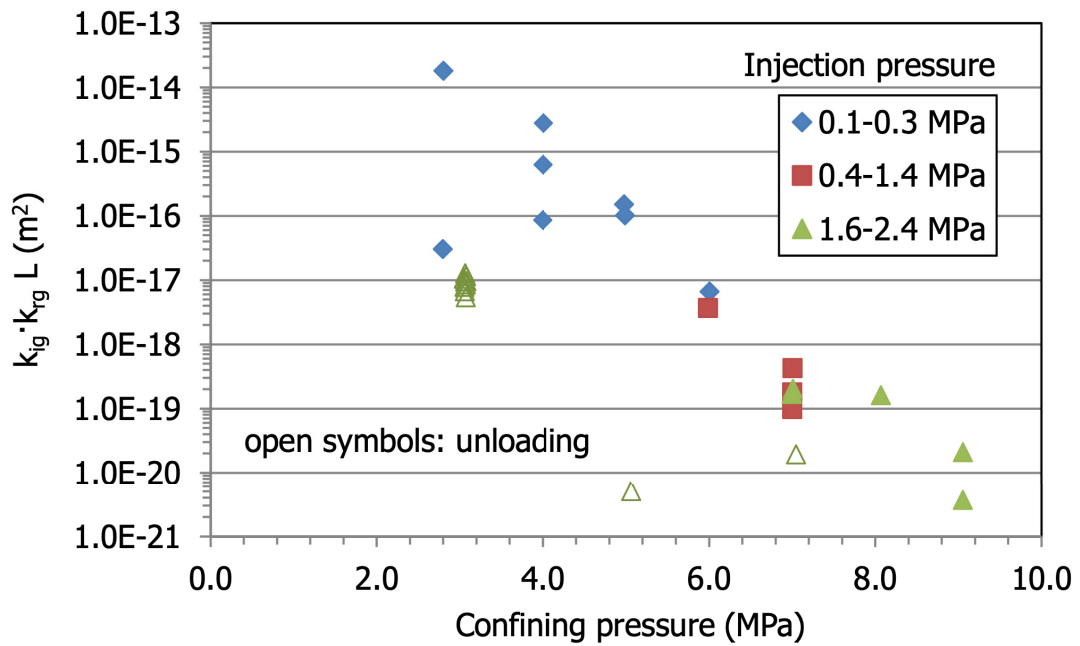


Fig. 97: Evolution of gas effective permeability ( $k_{ig} \cdot k_{rg}$ ) for sample BC-47-4 as a function of confining pressure

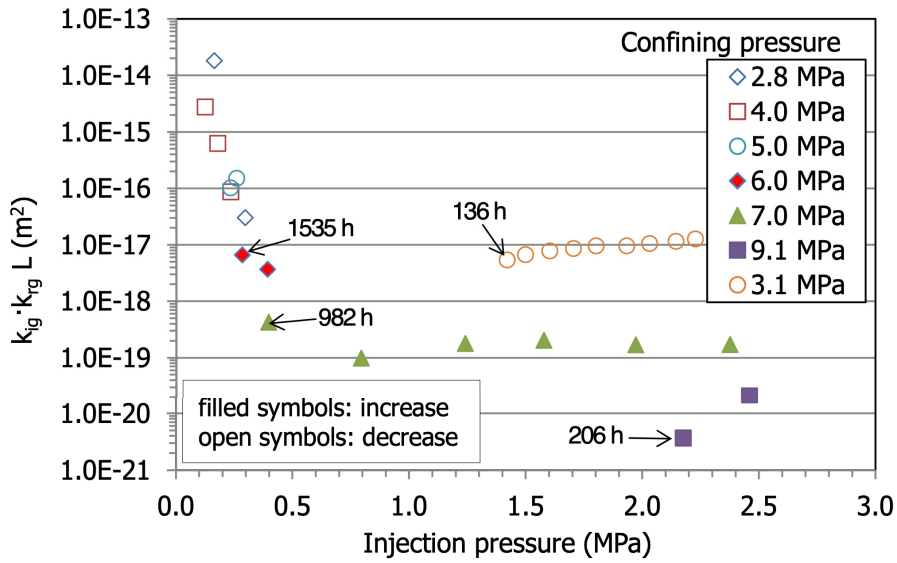


Fig. 98: Evolution of gas permeability at constant confining pressure for sample BC-47-4 (the duration of longer steps is indicated in hours)

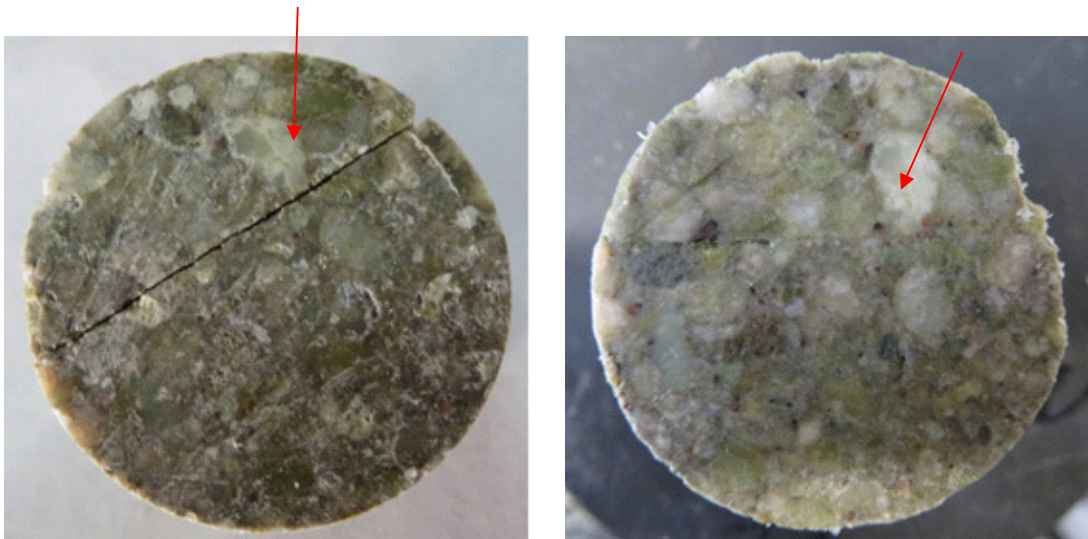


Fig. 99: Initial and final appearance of sample BC-47-4 (the arrows indicate the same position before and after testing)

#### 4.4.3.3 Summary and discussion

Fifteen gas permeability tests were performed in triaxial cells with bentonite samples obtained by drilling on site (12 samples) or core samples drilled from blocks in the laboratory (3 samples). The average dry density of the samples was  $1.58 \pm 0.04 \text{ g/cm}^3$  and water content of  $24.6 \pm 2.7\%$  ( $S_r = 93 \pm 6\%$ ). The sample conditions upon retrieval were preserved during gas testing, i.e. the samples were carefully trimmed in order to minimise changes in dry density and water content. All the tests started with a confining pressure of 0.6 or 1.0 MPa. The injection

pressure was slowly increased until a noticeable flow was reached and then the confining pressure was increased. Finally, the confining pressure was reduced to the initial values in most of the tests. The precise pressure path followed, depended on the characteristics of the samples and consequently they were quite heterogeneous.

A summary of the initial and final characteristics of the samples and of the results obtained both in the LP permeameter and in the HP one (including the testing time in each setup) is shown in Tab. 22 to Tab. 24 for the different sampling sections. The effective permeability values given in these tables are the average of all values obtained for consecutive steps of the same confining pressure, irrespective of the injection pressure applied. As seen above and explained further in this report, the effect of injection pressure on permeability in the range of pressures tested is negligible. The initial void ratio accessible for gas flow, which is computed as  $e(1-S_r)$ , is also shown in Tables 22 to 24.

Tab. 22: Results of the gas permeability tests in core samples from section S44

	BC-44-1	BC-44-2	BC-44-4	BC-44-5	BC-44-6	BC-44-7
Comments		Interface			Interface	
Initial $\rho_d$ (g/cm <sup>3</sup> )	1.57	1.56	1.61	1.52	1.51	1.62
Initial $w$ (%)	26.2	23.2	24.5	28.5	28.4	19.5
Initial $S_r$ (%)	98	86	97	100	97	79
Initial $e(1-S_r)$	0.015	0.102	0.021	0.003	0.020	0.137
Final $\rho_d$ (g/cm <sup>3</sup> )	1.58	1.62	1.61	1.53	1.53	1.65
Final $w$ (%)	25.7	22.3	24.4	27.5	26.7	19.9
Final $S_r$ (%)	98	91	97	98	94	84
Confining $P$ (MPa)	$k_{ig} \cdot k_{rg}$ (m <sup>2</sup> ) – LP setup					
0.6	$4.9 \cdot 10^{-17}$	$3.9 \cdot 10^{-14}$		No flow	$6.9 \cdot 10^{-17}$	$1.2 \cdot 10^{-16}$
1.0	$4.1 \cdot 10^{-17}$	$1.6 \cdot 10^{-14}$			$2.1 \cdot 10^{-17}$	$1.1 \cdot 10^{-16}$
Duration test LP (days)	6	1	Not tested	16	4	2
Confining $P$ (MPa)	$k_{ig} \cdot k_{rg}$ (m <sup>2</sup> ) – HP setup					
0.6			$6.4 \cdot 10^{-18}$	No flow		
1.0	$2.8 \cdot 10^{-18}$	$5.0 \cdot 10^{-15}$	$4.0 \cdot 10^{-18}$	$5.9 \cdot 10^{-20}$	$1.0 \cdot 10^{-17}$	$1.1 \cdot 10^{-16}$

	<b>BC-44-1</b>	<b>BC-44-2</b>	<b>BC-44-4</b>	<b>BC-44-5</b>	<b>BC-44-6</b>	<b>BC-44-7</b>
1.5	$1.3 \cdot 10^{-18}$	$3.5 \cdot 10^{-15}$	$1.9 \cdot 10^{-18}$	$8.4 \cdot 10^{-21}$	$2.9 \cdot 10^{-18}$	
2.0	$3.5 \cdot 10^{-19}$	$3.2 \cdot 10^{-15}$	$9.4 \cdot 10^{-19}$		$5.6 \cdot 10^{-19}$	$5.2 \cdot 10^{-17}$
2.5	$2.3 \cdot 10^{-20}$	$3.1 \cdot 10^{-15}$	$3.3 \cdot 10^{-19}$		$1.6 \cdot 10^{-19}$	
3.0		$3.0 \cdot 10^{-15}$	$1.2 \cdot 10^{-19}$		$2.8 \cdot 10^{-20}$	$3.1 \cdot 10^{-17}$
3.5		$2.9 \cdot 10^{-15}$	$1.4 \cdot 10^{-20}$			
4.0		$2.9 \cdot 10^{-15}$				$2.0 \cdot 10^{-17}$
4.5		$2.9 \cdot 10^{-15}$				
5.0		$2.8 \cdot 10^{-15}$				$1.3 \cdot 10^{-17}$
5.5		$2.8 \cdot 10^{-15}$				
6.0		$2.8 \cdot 10^{-15}$				No flow
6.5		$2.6 \cdot 10^{-18}$				
7.0		$1.7 \cdot 10^{-18}$				
7.5		$6.1 \cdot 10^{-19}$				
8.0		$6.3 \cdot 10^{-19}$				
8.5		$4.7 \cdot 10^{-19}$				
9.0		$1.6 \cdot 10^{-18}$				
Duration test HP (days)	2	6	5	7	8	14
Min injection $P$ (MPa)	0.20	0.15	0.20	0.60	0.20	0.20
Conf $P$ (min injec $P$ )	1.00	1.00	0.60	1.00	1.00	1.00

Tab. 23: Results of the gas permeability tests in core samples from section S47

	<b>BC-47-1</b>	<b>BC-47-2</b>	<b>BC-47-3</b>	<b>BC-47-4</b>	<b>BC-47-6</b>
Comments				Interface	Interface
Initial $\rho_d$ (g/cm <sup>3</sup> )	1.55	1.54	1.61	1.59	1.64
Initial $w$ (%)	26.4	26.4	23.7	24.8	19.6
Initial $S_r$ (%)	96	94	95	97	82
Initial $e$ (1- $S_r$ )	0.032	0.046	0.033	0.023	0.120
Final $\rho_d$ (g/cm <sup>3</sup> )	1.55	1.55	1.57	1.61	1.64
Final $w$ (%)	26.3	25.9	23.9	23.1	19.6
Final $S_r$ (%)	95	91	90	91	82
Confining $P$ (MPa)	$k_{ig} \cdot k_{rg}$ (m <sup>2</sup> ) – LP setup				
0.6	$7.7 \cdot 10^{-18}$				$2.5 \cdot 10^{-14}$
1.0					$1.4 \cdot 10^{-14}$
Duration test LP (days)		Not tested	Not tested	Not tested	
Confining $P$ (MPa)	$k_{ig} \cdot k_{rg}$ (m <sup>2</sup> ) – HP setup				
0.6	$1.7 \cdot 10^{-18}$		$3.5 \cdot 10^{-17}$		$4.4 \cdot 10^{-14}$
0.8			$2.8 \cdot 10^{-17}$		
1.0	$1.5 \cdot 10^{-18}$		$2.3 \cdot 10^{-17}$		$5.1 \cdot 10^{-14}$
1.5					$2.3 \cdot 10^{-14}$
2.0	$2.8 \cdot 10^{-20}$	$1.2 \cdot 10^{-17}$			$1.0 \cdot 10^{-14}$
2.5	$3.9 \cdot 10^{-21}$				
3.0		$1.2 \cdot 10^{-19}$		$9.1 \cdot 10^{-15}$	
4.0		$7.1 \cdot 10^{-20}$		$1.7 \cdot 10^{-15}$	
5.0		$5.3 \cdot 10^{-20}$		$5.4 \cdot 10^{-17}$	

	<b>BC-47-1</b>	<b>BC-47-2</b>	<b>BC-47-3</b>	<b>BC-47-4</b>	<b>BC-47-6</b>
6.0		$5.7 \cdot 10^{-20}$			
7.0		$3.9 \cdot 10^{-20}$		$2.1 \cdot 10^{-19}$	
8.0		$4.1 \cdot 10^{-20}$		$1.6 \cdot 10^{-19}$	
9.0		$3.8 \cdot 10^{-20}$		$3.7 \cdot 10^{-21}$	
10.0		$5.0 \cdot 10^{-20}$			
11.0		$3.8 \cdot 10^{-20}$			
12.0		$2.3 \cdot 10^{-20}$			
Duration test HP (days)	9	167	13	172	0.2
Min injection $P$ (MPa)	0.20	0.40	0.10	0.20	0.10
Conf $P$ (min injec $P$ )	0.60	2.00	0.60	2.00	0.60

Tab. 24: Results of the gas permeability tests in core samples from section S36 and drilled samples from section S53

	<b>BC-36-1</b>	<b>BB53-4-2</b>	<b>BB53-5-1</b>	<b>BB53-5-2</b>
Comments		Lab	Lab	Lab
Initial $\rho_d$ (g/cm <sup>3</sup> )	1.52	1.59	1.63	1.63
Initial $w$ (%)	26.7	25.1	23.3	22.9
Initial $S_r$ (%)	93	96	97	94
Initial $e$ (1- $S_r$ )	0.052	0.025	0.023	0.043
Final $\rho_d$ (g/cm <sup>3</sup> )	1.57	1.59	1.60	1.59
Final $w$ (%)	26.7	24.8	24.6	24.3
Final $S_r$ (%)	96	96	92	94
Confining $P$ (MPa)	$k_{ig} \cdot k_{rg}$ (m <sup>2</sup> ) – LP setup			

	<b>BC-36-1</b>	<b>BB53-4-2</b>	<b>BB53-5-1</b>	<b>BB53-5-2</b>
0.6		No flow	No flow	No flow
Duration test LP (days)	Not tested			
Confining $P$ (MPa)	$k_{ig} \cdot k_{rg}$ (m <sup>2</sup> ) – HP setup			
0.6			$2.4 \cdot 10^{-19}$	$3.3 \cdot 10^{-19}$
1.0	$8.3 \cdot 10^{-16}$		$1.6 \cdot 10^{-19}$	$5.5 \cdot 10^{-19}$
1.4			$1.8 \cdot 10^{-20}$	$1.2 \cdot 10^{-19}$
1.6			$1.4 \cdot 10^{-20}$	$6.5 \cdot 10^{-20}$
2.0	$4.0 \cdot 10^{-17}$			
3.0	$5.4 \cdot 10^{-18}$			
4.0	$6.7 \cdot 10^{-18}$			
5.0	$1.3 \cdot 10^{-18}$			
6.0	$1.5 \cdot 10^{-18}$			
7.0	$1.6 \cdot 10^{-18}$			
8.0	$5.6 \cdot 10^{-19}$			
9.0	$4.3 \cdot 10^{-19}$			
10.0	$6.4 \cdot 10^{-18}$			
11.0	$7.5 \cdot 10^{-19}$			
12.0	$4.7 \cdot 10^{-19}$			
13.0	$1.3 \cdot 10^{-18}$			
14.0	$4.4 \cdot 10^{-19}$			
Duration test HP (days)	168	Not tested	23	15
Min injection $P$ (MPa)	0.20		0.30	0.20

	<b>BC-36-1</b>	<b>BB53-4-2</b>	<b>BB53-5-1</b>	<b>BB53-5-2</b>
Conf <i>P</i> (min injec <i>P</i> )	1.00		0.60	0.60

In the range of pressures tested, no clear effect of the injection pressure on the permeability value obtained was observed. The values obtained in both setups (LP and HP) showed that, for a constant confining pressure, the gas permeability was essentially constant despite the injection pressure changes. This can be seen in Fig. 100 and Fig. 101, in which the results obtained for different samples tested under confining pressures of 0.6 and 1.0 MPa have been plotted. Only in a few cases did the gas permeability increase slightly with the increase in injection pressure, since it resulted in an increase in the void sizes. This is the case of samples BB-53-5-1, BB-53-5-2 and BC-44-5, taken from the intermediate and external rings of the barrier. It was checked that for these three samples flow was not linearly related to the difference of squared pressures along the sample, which indicates that flow was not stationary, and Darcy’s law cannot be applied strictly to compute permeability. Hence, the permeability values computed with Eq. (7) for these samples would not be reliable. The figures also show that the highest gas permeabilities for these confining pressures were measured in the samples with interface.

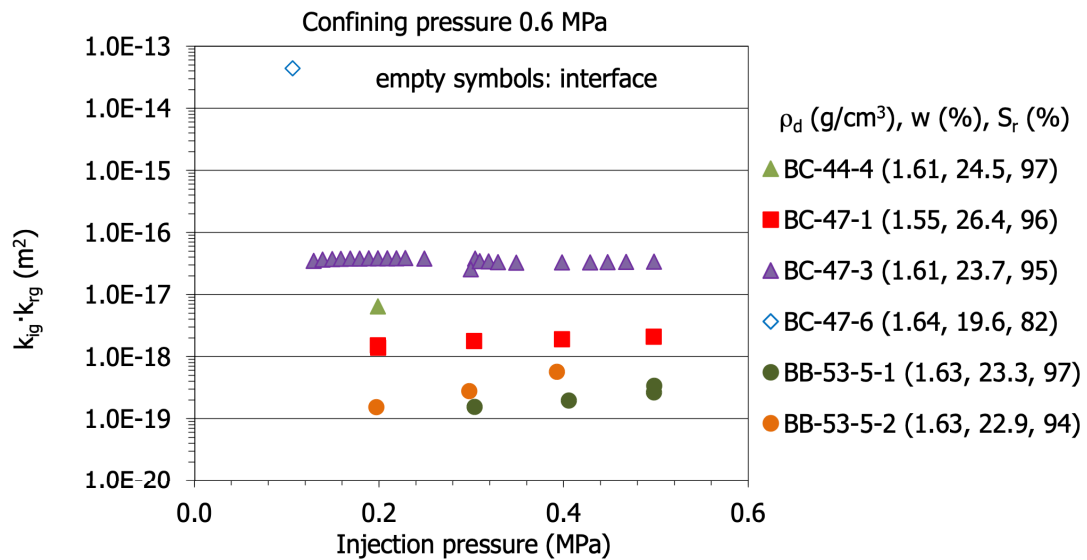


Fig. 100: Effective gas permeability measured at constant confining pressure of 0.6 MPa in the HP setup. The sample reference, dry density, water content and degree of saturation are indicated in the legend

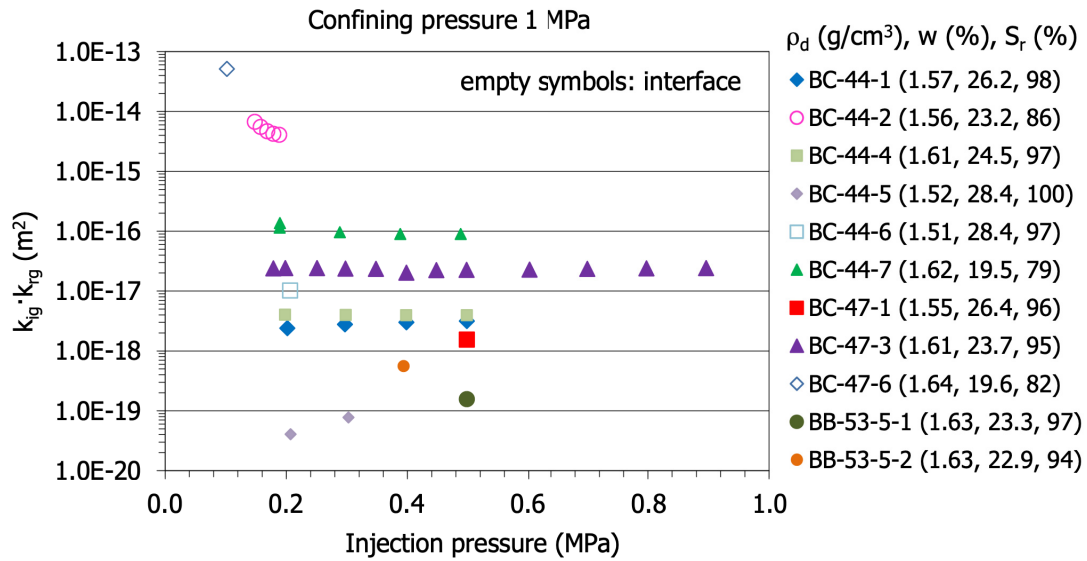


Fig. 101: Effective gas permeability measured at constant confining pressure of 1 MPa in the HP setup. The sample reference, dry density, water content and degree of saturation are indicated in the legend

Since the injection pressure did not substantially affect the permeability values obtained for a given confining pressure, the average gas permeability obtained for all the steps performed under the same confining pressure was computed (Tab. 22 to Tab. 24) Fig. 102 to Fig. 104 show the average gas permeability values measured for each confining pressure in materials recovered from different sampling sections. The decrease of gas permeability with confining pressure is clear. The distance from the sample to the axis of the gallery is also indicated in the Figures. Overall, the samples closest to the gallery axis, which were drier and had lower degrees of saturation (subchapter 4.2.1), had higher gas permeability. The decrease of gas permeability with confining pressure was significant, particularly for samples with high degree of saturation. The highest decrease of permeability (of 3 or 4 orders of magnitude) took place for confining pressures below 4 MPa. For higher confining pressures the decrease was less significant, always smaller than one order of magnitude, except when the sample had an interface or relatively low degree of saturation. The samples with interface taken from the inner bentonite ring (distances to the gallery axis around 60 cm) had higher permeability than neighbouring samples drilled in the middle of a block, and this permeability decreased for confining pressures higher than the 4 MPa previously mentioned. The permeability of sample BC-44-2, drilled between two blocks of the internal ring of section S44, decreased three orders of magnitude when the confining pressure was increased to 6 MPa, and the permeability of sample BC-47-4, which was drilled in an equivalent location in section S47 (Fig. 88), decreased four orders of magnitude when the confining pressure increased from 4 to 7 MPa. However, the samples from the external ring with and without interface behaved similarly, experiencing a clear decrease of permeability for confining pressures lower than 4 MPa. There was no flow through these samples when the confining pressure increased above 2-4 MPa.

The confining stress reduced the size of the gas pathways, also increasing their tortuosity. In the case of the highly-saturated samples there was no need to apply a high confining pressure to completely block the air passages, whereas in the less saturated samples the gas found ways out until the confining pressure was high enough to sufficiently reduce the air-filled pore space. This would also explain the fact that the effect of injection pressure increase was only

noticeable in the samples with the highest water content, in which small changes in the size of the gas pathways would imply significant changes in a permeability which was very low.

During most of the gas permeability tests the dry density of the samples increased (initial and final values are given in Tab. 22 to Tab. 24), which is consistent with the decrease in effective gas permeability occurred during the tests. Only in those tests in which the maximum confining pressure applied was low (below 1.6 MPa), did the dry density of the sample not increase after testing. In fact, there is a positive linear correlation between change in dry density and the maximum pressure applied ( $R^2=0.7$ ).

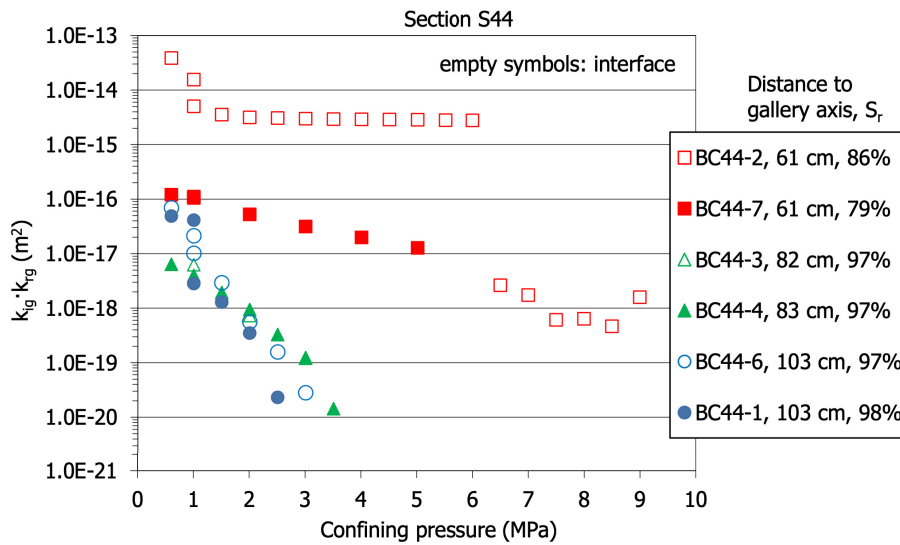


Fig. 102: Change of effective permeability with increasing confining pressure in samples of section S44 (the values are the average of all steps in which confining pressure was the same, irrespective of the injection pressure)

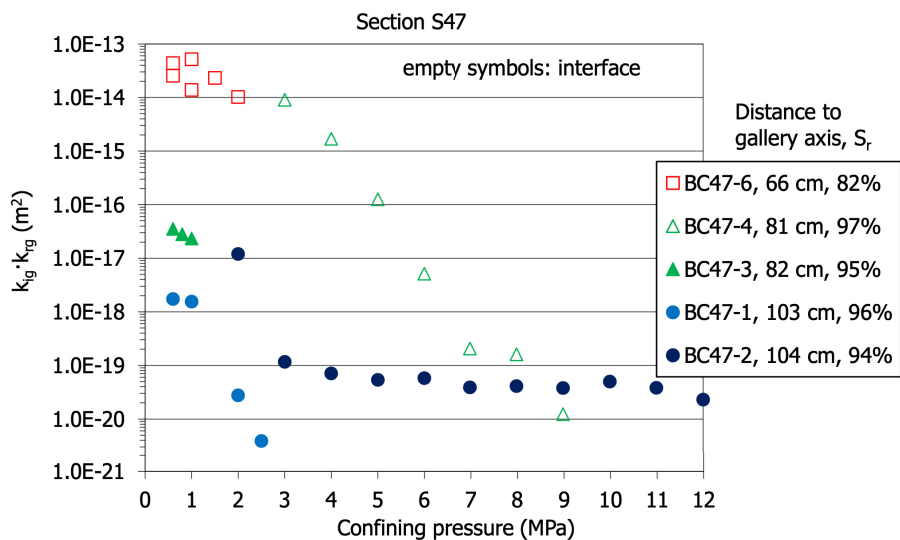


Fig. 103: Change of effective permeability with increasing confining pressure in samples of section S47 (the values are the average of all steps in which confining pressure was the same, irrespective of the injection pressure)

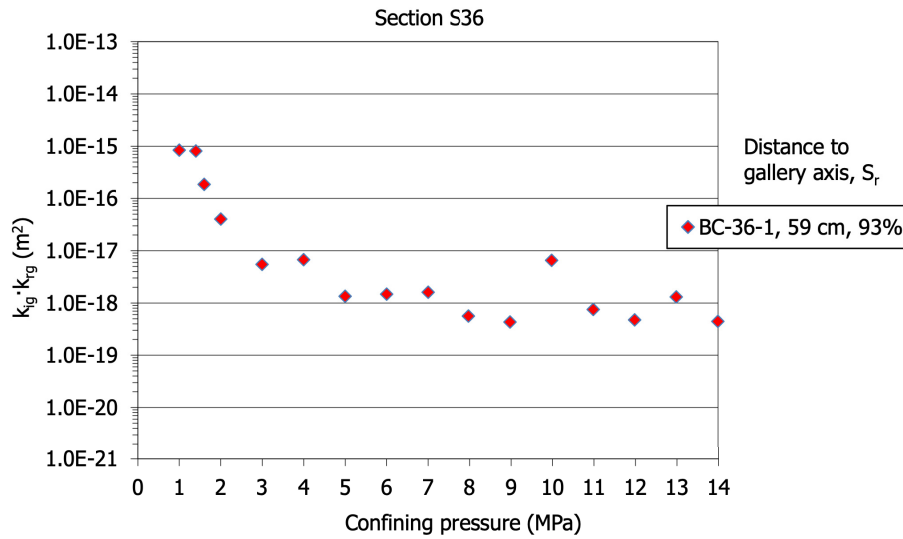


Fig. 104: Change of effective permeability with increasing confining pressure in samples of sections S36 (the values are the average of all steps in which confining pressure was the same, irrespective of the injection pressure)

After reaching a maximum confining pressure, generally corresponding to a value above which no flow took place, the samples were progressively unloaded. During unloading, as the confining pressure decreased the effective permeability increased, but the original permeability values were never recovered. Fig. 105 and Fig. 106 show the changes in permeability during loading-unloading for samples of different sections. The permeability values plotted are the average of all the consecutive steps in which confining pressure was the same, regardless the injection pressure, which –as shown above– did not affect the permeability. Overall, the samples that had higher initial permeability –either because their degree of saturation was low or because they had an interface– had to be submitted to higher confining pressures to stop flow. Also, the permanent decrease in gas effective permeability after loading was higher in the samples with interface (namely BC-44-2 and BC-47-4). In contrast, sample BC-44-6, which was drilled in the outer ring of the barrier and had a high degree of saturation, behaved similarly to other samples, despite the fact that it had a vertical interface, indicating that the interface was no longer a preferred pathway for gas movement. This had been already observed in the tests performed in the LP equipment (Fig. 90).

When flow occurred under a given pressure situation, the duration of the steps was generally short (1-2 hours). In many cases, it was observed that, if the same pressure situation was kept for longer, flow decreased, and the permeabilities computed were lower. This aspect has not been analysed in detail but could have some effect on the results obtained.

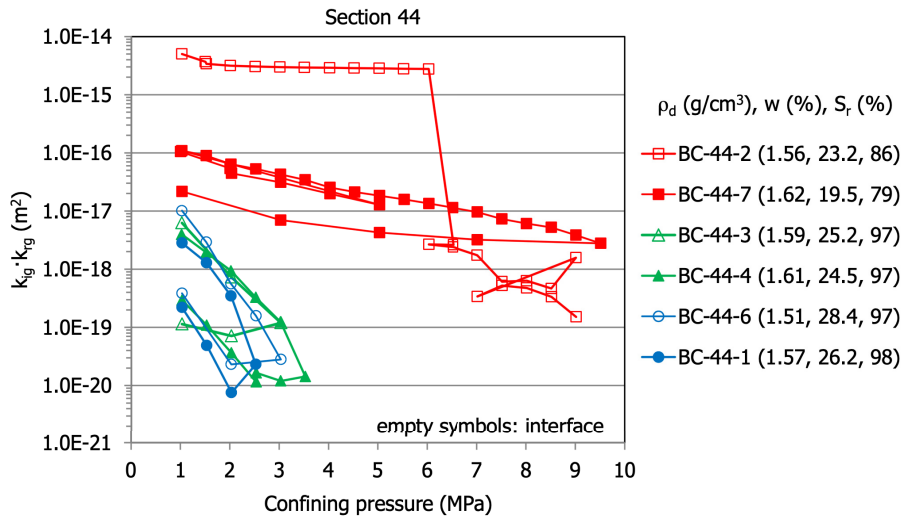


Fig. 105: Change of gas effective permeability with increase/decrease of confining pressure for samples of section S44. The sample reference, dry density, water content and degree of saturation are indicated in the legend

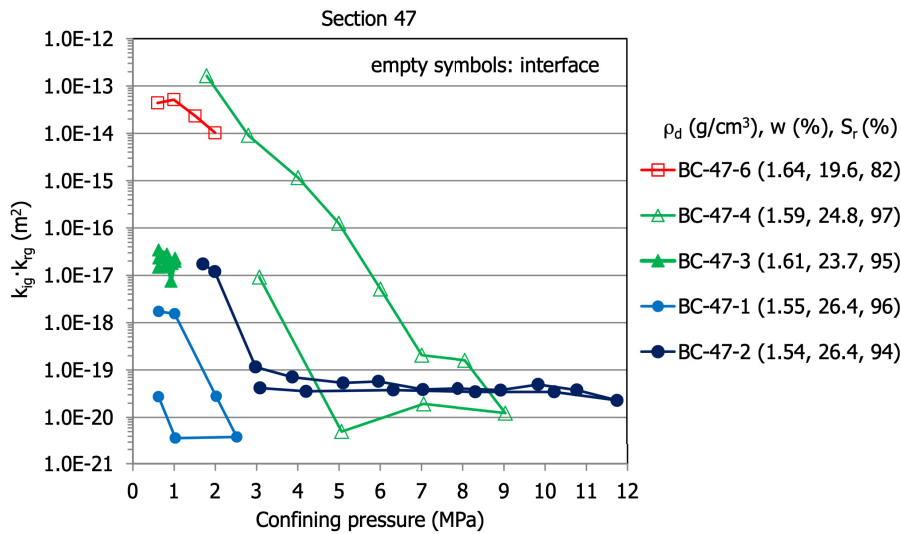


Fig. 106: Change of gas effective permeability with increase/decrease of confining pressure for samples of section S47. The sample reference, dry density, water content and degree of saturation are indicated in the legend

Final checking of water content in the samples showed that the gravimetric water content was usually lower in the upper part where gas was injected (although the differences inside a given sample were lower than 0.4%), which indicates that the upper part of the samples dried to some extent as a consequence of gas flow, with water being pushed towards the bottom of the samples by the gas. In some cases, water must have been expelled out of the sample, because the final water content was found to be lower than the initial one (Tab. 22 to Tab. 24). This would be evidence of two-phase flow being the main gas transport mechanism in these tests.

The gas permeability of the untreated FEBEX bentonite was analysed in the framework of the FEBEX and FORGE projects (Shaw 2015), and gas permeability was seen to decrease with the decrease in accessible void ratio –which is computed as  $e(1-S_r)$ – according to power laws with exponents between 3 and 4 (Villar & Lloret 2001, Villar 2002, Villar et al. 2013, Gutiérrez-Rodrigo et al. 2014). The permeability values measured in the FEBEX-DP retrieved samples for different confining pressures (Tab. 22 to Tab. 24) have been plotted in Fig. 107 as a function of their accessible void ratio. The accessible void ratio values of the samples tested were below 0.15, and the permeability was clearly higher with higher accessible void ratios. The scatter in the data is high because the range of dry densities and water contents involved was large. There were also samples with and without interface included in the data set. Figure 107 also shows the effect of confining pressure on gas effective permeability for samples of different accessible void ratio with and without interface. In the range of confining pressures from 0.6 to 7.0 MPa, the permeability decreased with increasing confining pressure, as discussed above. Overall, for similar values of accessible void ratio the samples with an interface had higher permeability for the entire range of confining pressures analysed, although differences tended to be lower towards the smaller accessible void ratios.

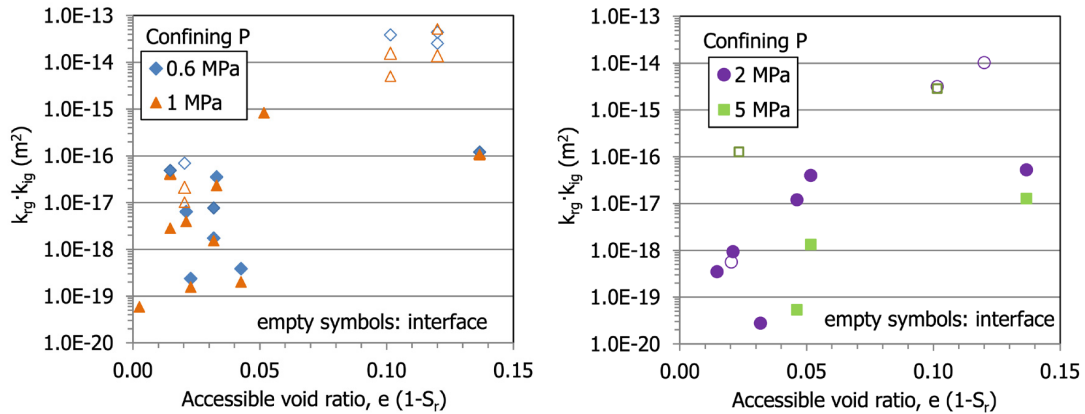


Fig. 107: Effect of confining pressure on gas effective permeability for samples with and without interface (The accessible void ratio plotted is the initial one. The values for confining pressure 0.6 and 1.0 MPa were obtained in the LP and HP setups)

The gas permeability of the reference FEBEX bentonite samples compacted to different dry densities with various water contents was measured during the FEBEX project in the same LP setup used in the current research (Villar 2002) and during the FORGE project in the same HP-S setup used in this work (Villar et al. 2013). In the first case (falling-head or unsteady-state permeameter) the confining pressure applied was 0.6 MPa and the injection pressure decreased during the tests from an initial value of 0.1 MPa. In the second case (constant pressure or steady-state permeameter), confining pressures of 0.6 and 1 MPa were applied. For gas pressures below 1.2 MPa no effect of the injection or confining pressures on the value of permeability was detected in those tests. The results obtained in FEBEX and in FORGE are plotted in Fig. 108, along with the correlation curve between gas effective permeability,  $k_{ig} \cdot k_{rg}$  ( $m^2$ ), and accessible void ratio,  $e(1-S_r)$ , which has the following expression (Villar et al. 2013; Eq. 11):

$$k_{ig} \cdot k_{rg} = 1.25 \cdot 10^{-12} (e(1-S_r))^{3.22} \quad (\text{Eq. 11})$$

The values measured in the samples retrieved during the FEBEX-DP have also been plotted in Figure 108 and are more clearly seen in the enlargement presented in Fig. 109. In order to make the results strictly comparable, only those values obtained under confining pressures of 0.6 and 1 MPa have been represented. These values were obtained in the same two setups as the values obtained for the reference sample. The accessible void ratio of the FEBEX-DP samples is in the low range, because their degree of saturation was very high. Nevertheless, the values obtained for material recovered in FEBEX-DP are generally consistent with those of the reference bentonite. The exceptions are the samples containing block interfaces, with overall gas permeabilities clearly higher than those obtained with Equation 11. The samples with an interface that had a very low accessible void ratio (high saturation), such as BC-44-6 drilled in the external ring of the barrier, had permeabilities closer to that of the reference bentonite. This can be interpreted as evidence of effective sealing of this interface as the result of water uptake and clay swelling.

Summarising, the gas permeability of the samples from the FEBEX-DP depended on the accessible void ratio in the same way as the FEBEX reference bentonite. Consequently, it seems that no changes on the gas transport properties took place during operation. The void ratio accessible for gas flow was below 0.15 in all the samples tested, given their high degree of saturation. If the correlation between accessible void ratio and gas permeability is extrapolated towards a value close to null accessible void ratio (say 0.002), which would almost correspond to completely saturated samples, the intrinsic permeability would be in the order of  $10^{-21}$  m<sup>2</sup>, which is also the order of the intrinsic permeability measured in saturated samples of dry density 1.6 g/cm<sup>3</sup> with water flow (subchapter 4.4). The gas permeability of the samples also depended on their stress state, decreasing noticeably as the confining pressure increased up to 4 MPa. For higher confining pressures the decrease of gas permeability with stress was less significant, except in samples with interface. The decrease in permeability that occurred during loading was not reversible, and the gas permeability of the samples after unloading was lower than the initial one. The time in which the sample remained under a given pressure step also affected the permeability value: the longer the sample remained under a given confining pressure, the lower the permeability. Samples with an interface had higher permeability than samples of similar accessible void ratio with no interface, and it was necessary to apply higher confining pressures to reduce or suppress gas flow in them. Nevertheless, the samples drilled along interfaces of the external ring of the barrier had permeabilities closer to that corresponding to the same accessible void ratio in the reference bentonite.

Previous laboratory studies showed that, in the FEBEX compacted bentonite and under isochoric condition, two-phase flow seemed to take place for degrees of saturation lower than about 97%, whereas for higher degrees of saturation, pathway dilation could be the predominant mechanism (Villar et al. 2013, Gutiérrez-Rodrigo et al. 2014, 2015). The threshold pressure for gas entry into the bentonite was higher than the swelling pressure and seemed to be lower than the gas pressure required for fracturing the material (macroscopically). On the contrary, in the research reported here, two-phase flow seems to have taken place in all cases, even for samples with a degree of saturation higher than 97%. The fact that these samples were tested under constant confining stress instead of under no volume change conditions (isochoric), would have made the transport of gas easier, with opening of gas flow trajectories. As the confining stress increased, the tortuosity of these gas pathways would increase, which would have caused the decrease in gas permeability, and eventually the pathways would have been closed.

These results and some additional ones are analysed in more detail, also taking into account the microstructure changes caused by gas testing, in Villar et al. (2018).

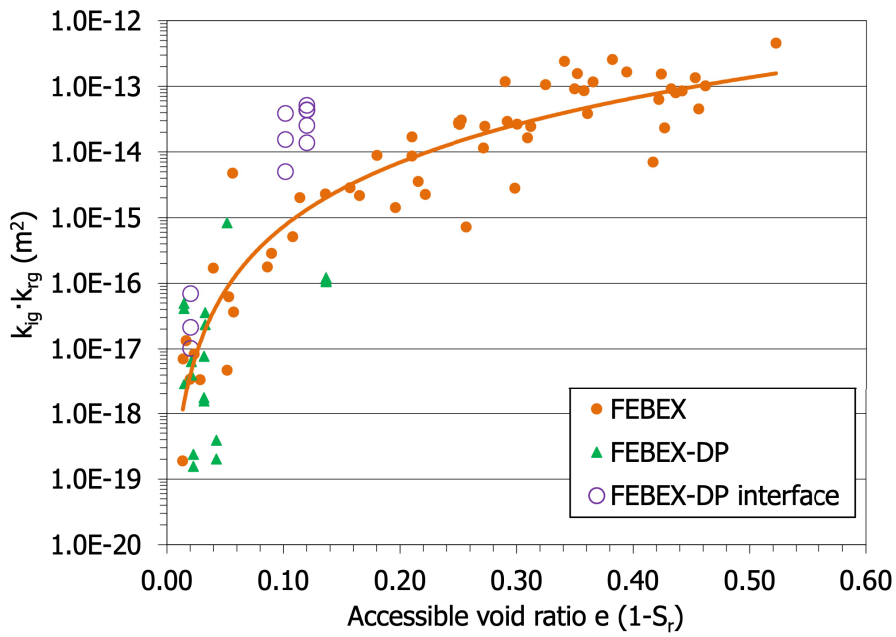


Fig. 108: Gas permeability as a function of the accessible void ratio for FEBEX samples tested during the FEBEX and FORGE projects and for FEBEX-DP samples with and without interface (Eq. 11)

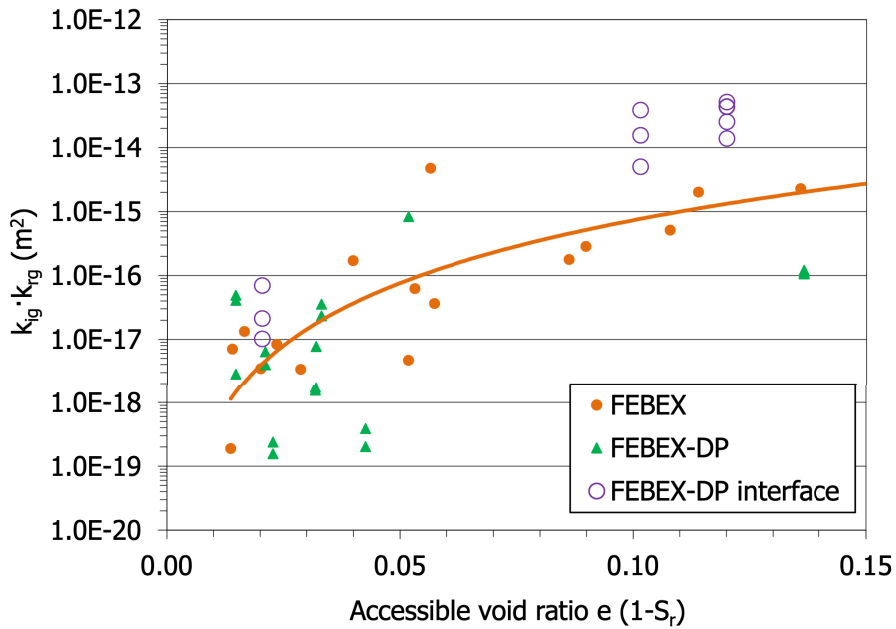


Fig. 109: Gas permeability as a function of the accessible void ratio for FEBEX samples tested during the FEBEX and FORGE projects and for FEBEX-DP samples with and without interface (enlargement of Fig. 108; Eq. 11)

## 4.5 Mechanical properties

### 4.5.1 Swelling deformation tests

The swelling capacity was tested in 20 samples taken at different distances from the heater from three different sections (S36, S47 and S53): two along radius B-C in section S36, six along radius D in section S47 and twelve along radii B and E-F in section S53 (Fig. 110). Additionally, in order to check the effect of the proximity to shotcrete on bentonite swelling, six samples from section 36 taken along radius F were tested, three of them under a vertical stress of 50 kPa. These samples were drilled from the block surface that had been in contact with the shotcrete plug during operation. Moreover, the swelling capacity of bentonite affected by oxidation was tested in two samples drilled from a block in contact with the liner in section S36 and in two samples close to an extensometer in section S59.

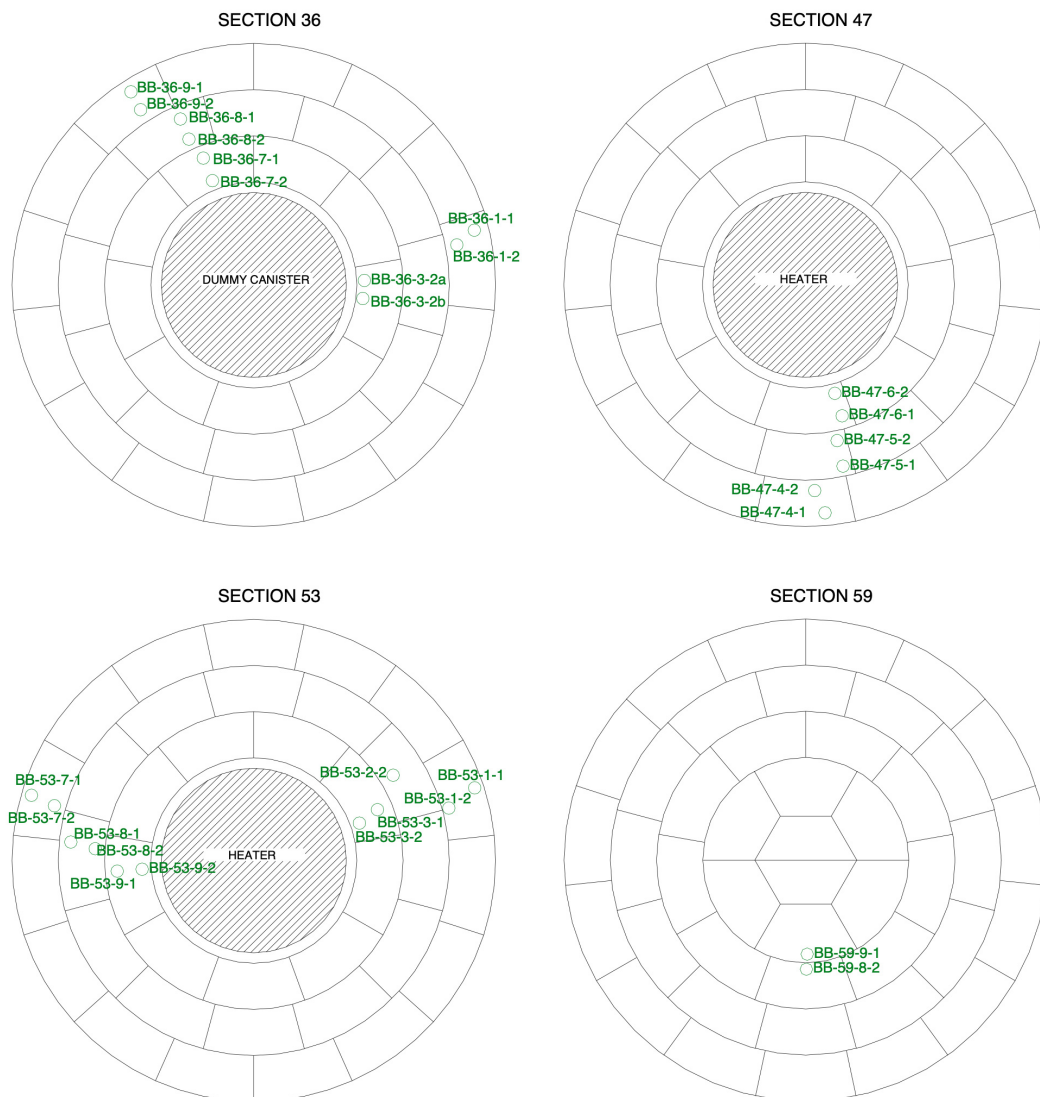


Fig. 110: Location of samples used for the swelling capacity tests

To perform the swelling under load tests, the specimens were obtained by drilling from the blocks and subsequently trimming as detailed in subchapter 3.3.1. The samples thus prepared were pushed into the oedometer rings. The diameter of the oedometer rings was between 3.6 and 5.0 cm, and the initial height of the specimens was between 1.2 and 1.8 cm. In most cases this procedure meant a decrease of the density of the specimen in the oedometer ring with respect to the original dry density of the block (Fig. 111). This resulted in a smaller swelling capacity measured in the tests than actually present in the blocks, because swelling capacity increases with dry density.

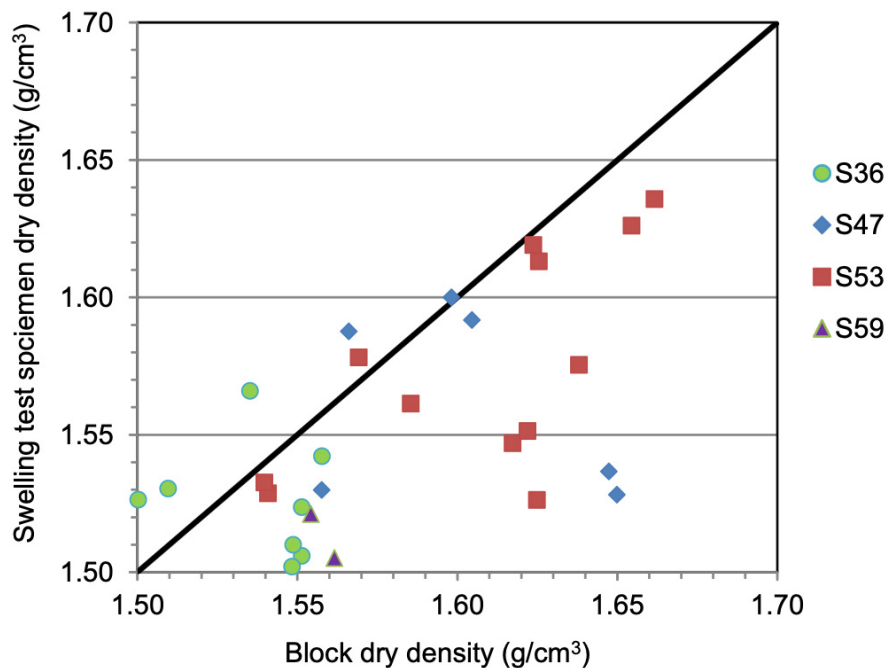


Fig. 111: Decrease of samples' density caused by the processes of trimming and fitting into the oedometer cells

Tab. 25, Tab. 26 and Tab. 27 summarise the results of the swelling under load tests and the initial and final conditions of samples not affected by interfaces (shotcrete or metallic elements) in sections 36, 47 and 53, respectively. The final vertical strain ( $\epsilon$ ) is computed as the ratio between the change in height experienced by the sample and the initial height, the negative values indicating swelling. The evolution of the vertical stress during the swelling deformation tests is shown in Fig. 112, Fig. 113 and Fig. 114 for samples of sections S36, S47 and S53 respectively. It took longer for the deformation of samples taken close to the heater to stabilise.

Indeed, the samples closer to the heater had higher initial dry density and lower initial water content. The swelling capacity is related to both, increasing with initial dry density and decreasing with initial water content. For this reason, the final strain of the samples closer to the heater was overall higher (Fig. 115). Nevertheless, there were clear exceptions, such as the extremely high swelling of sample BB-47-4-2, which also had an anomalously high dry density ( $1.59 \text{ g/cm}^3$ ) for a sample taken from the external ring of the barrier (see Fig. 40). This high dry density could have been caused inadvertently during preparation and setting of the sample.

Tab. 25: Results of the swelling under load tests with samples of section S36

Reference	Initial $\rho_d$ (g/cm <sup>3</sup> )	Initial $w$ (%)	Initial $S_r$ (%)	Vertical $P$ (kPa)	Final $\varepsilon$ (%)	$t$ (days)	Final $\rho_d$ (g/cm <sup>3</sup> )	Final $w$ (%)	Final $S_r$ (%)	$T$ (°C)
BB-36-1-2	1.51	29.2	100	502	-2.46	144	1.47	34.4	112	23.9
BB-36-1-1	1.53	29.3	104	497	-6.99	43	1.43	35.2	107	23.0

Tab. 26: Results of the swelling under load tests with samples of section S47

Reference	Initial $\rho_d$ (g/cm <sup>3</sup> )	Initial $w$ (%)	Initial $S_r$ (%)	Vertical $P$ (kPa)	Final $\varepsilon$ (%)	$t$ (days)	Final $\rho_d$ (g/cm <sup>3</sup> )	Final $w$ (%)	Final $S_r$ (%)	$T$ (°C)
BB-47-4-1	1.53	28.1	99	491	-3.33	37	1.48	32.1	105	23
BB-47-4-2	1.59	26.6	103	500	-15.70	40	1.37	39.4	110	23
BB-47-5-1	1.60	24.2	95	493	-11.13	35	1.44	36.0	111	23
BB-47-5-2	1.59	23.9	93	517	-10.69	33	1.44	34.1	105	24
BB-47-6-1 <sup>a</sup>	1.53	22.1	78	515	-14.56	46	1.33	42.8	113	22
BB-47-6-2 <sup>a</sup>	1.54	18.7	67	494	-11.61	41	1.38	39.0	110	22

<sup>a</sup> pressure of 1 MPa applied to prepare the sample

Tab. 27: Results of the swelling under load tests with samples of section S53

Reference	Initial $\rho_d$ (g/cm <sup>3</sup> )	Initial $w$ (%)	Initial $S_r$ (%)	Vertical $P$ (kPa)	Final $\varepsilon$ (%)	$t$ (days)	Final $\rho_d$ (g/cm <sup>3</sup> )	Final $w$ (%)	Final $S_r$ (%)	$T$ (°C)
BB-53-1-1	1.53	29.3	103	476	-5.24	17	1.45	34.2	108	22
BB-53-1-2	1.56	25.9	96	502	-8.77	25	1.43	34.3	105	22
BB-53-2-1	1.55	24.2	88	509	-5.01	29	1.47	31.5	102	21

Reference	Initial $\rho_d$ (g/cm <sup>3</sup> )	Initial $w$ (%)	Initial $S_r$ (%)	Vertical $IP$ (kPa)	Final $\varepsilon$ (%)	$t$ (days)	Final $\rho_d$ (g/cm <sup>3</sup> )	Final $w$ (%)	Final $S_r$ (%)	$T$ (°C)
BB-53-2-2	1.55	25.0	91	495	-9.69	29	1.42	34.4	104	21
BB-53-3-1	1.63	23.7	97	498	-18.29	55	1.37	38.4	107	21
BB-53-3-2	1.58	23.5	89	498	-12.53	55	1.40	35.1	102	21
BB-53-7-1	1.53	28.4	101	491	-3.76	38	1.48	32.2	105	24
BB-53-7-2	1.58	26.5	101	494	-7.98	23	1.46	34.6	110	23
BB-53-8-1	1.62	24.0	97	494	-14.03	50	1.42	33.4	100	25
BB-53-8-2	1.61	24.4	98	497	-11.28	63	1.45	33.8	106	25
BB-53-9-1	1.64	20.8	86	509	-6.40	75	1.54	29.1	104	24
BB-53-9-2	1.53	20.3	71	500	-12.64	75	1.35	38.1	104	24

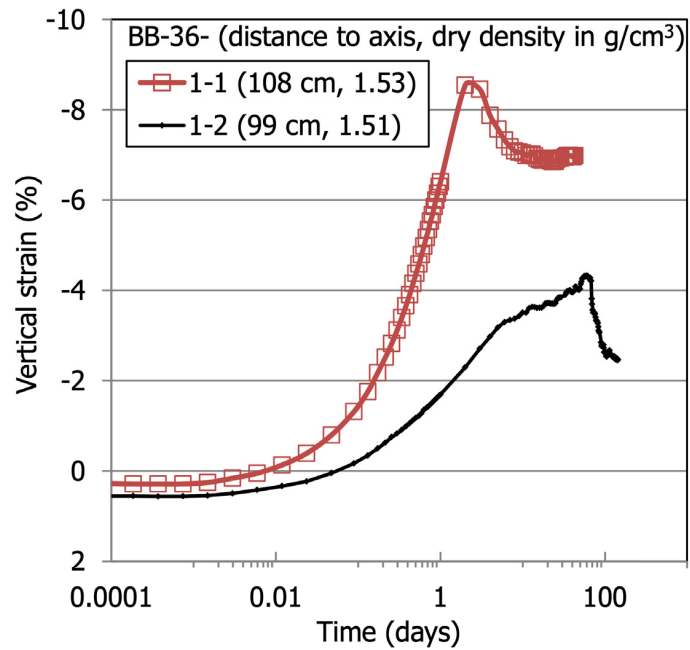


Fig. 112: Evolution of vertical strain during the swelling under 0.5 MPa stress for samples of section S36

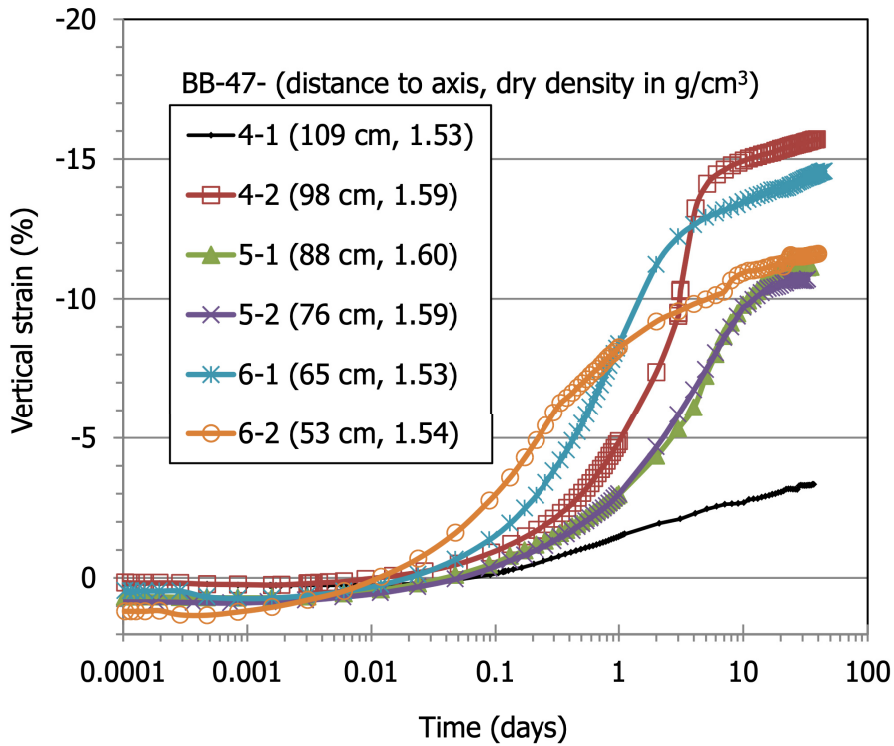


Fig. 113: Evolution of vertical strain during the swelling under 0.5 MPa stress for samples of section S47

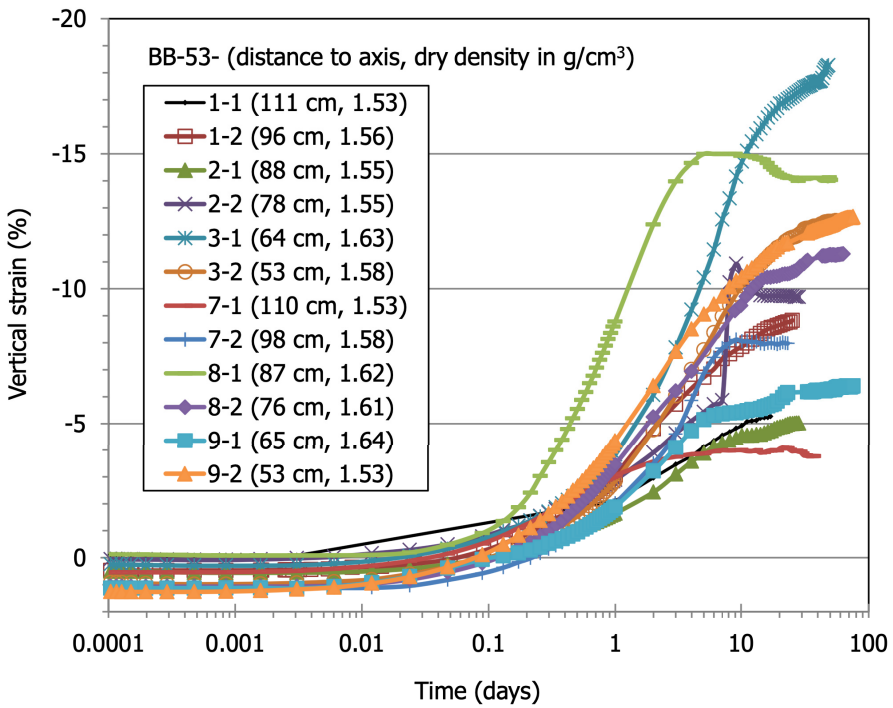


Fig. 114: Evolution of vertical strain during the swelling under 0.5 MPa stress for samples of section S53

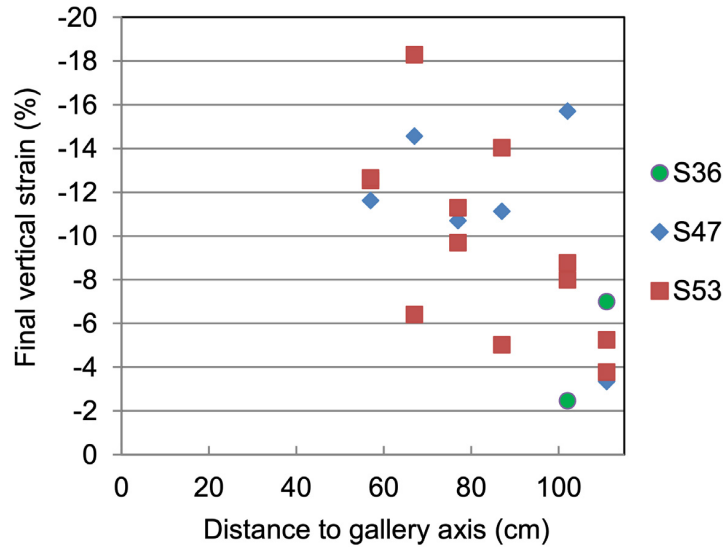


Fig. 115: Final vertical strain for samples of different sections saturated under vertical stress 0.5 MPa

In order to assess the modification of the swelling capacity of the bentonite as a result of the 18-year operation, the final vertical strain measured has to be compared with the final vertical strain of samples of the reference FEBEX bentonite of the same initial dry density and water content saturated under the same conditions, i.e. same vertical load and kind of water, since all these parameters affect the swelling capacity. Based on numerous swelling under load tests performed with the FEBEX reference bentonite compacted to different initial dry densities ( $\rho_{d0}$ , g/cm<sup>3</sup>) with different water contents ( $w_0$ , %), an empirical relation predicting the final swelling strain ( $\epsilon$ , %) after saturation with deionised water under vertical load of 500 kPa was found (Villar & Lloret 2008; Eq. 12):

$$\epsilon = (37.48 \rho_{d0} - 50.43) \ln w_0 - 154 \rho_{d0} + 204.24 \quad (\text{Eq. 12})$$

The results obtained in the samples from the FEBEX-DP have been compared with the corresponding theoretical values obtained with this expression in Fig. 116. On average the vertical strains actually measured were lower than the theoretical ones (-10% vs. -12%). Figure 116 also includes the distance to the gallery axis of the samples. Most samples from the external, more saturated bentonite ring swelled less than expected, whereas the samples from the inner, drier ring tended to swell as expected or more. This could be related to their higher initial salinity, which would have brought about some osmotically-driven swelling. The higher salinity in the pore water of the samples close to the liner was confirmed in Fernández et al. (2018), where the very low salinity (much lower than initial) of the samples from the external ring was also highlighted.

The electrical conductivity of the water in the oedometer cells was measured during the tests. In the tests performed with samples from the inner ring, the electrical conductivity increased considerably during the tests, which would indicate that the soluble salts in the bentonite were diffusing into the deionised water in the oedometer cell's reservoir, gradually reducing salinity in the specimen pore fluid. In contrast, the electrical conductivity of the water in the oedometer cells in which samples from the external ring were being tested barely increased during the tests

(Fig. 117), indicating that there were only limited soluble salts present in their pores. Fig. 118 shows the simultaneous evolution of swelling strain and electrical conductivity of the water in the oedometer cell for two samples of section S53, one of them obtained from the external ring and the other one from the internal ring. Because of trimming (Fig. 111), the initial dry density of these two specimens was similar, despite the fact that the blocks from which they were obtained had considerably different densities (Fig. 41). The sample from the internal ring swelled more and for longer, with the electrical conductivity of the water in the oedometer cell increasing considerably, particularly after 10 days, when most swelling had already been developed. This could indicate that the osmotic part of swelling (indicated by the increase in electrical conductivity as the soluble species left the bentonite) was less important and was not remarkable until the crystalline swelling had been completed. This process did not take place in the reference bentonite or in the more saturated bentonite from the external ring, because in both cases the salinity was lower. It has to be highlighted that this is a process that took place because the samples were let to swell under a low vertical stress in a relatively large volume of water, but the same conditions are not encountered in the barrier during operation.

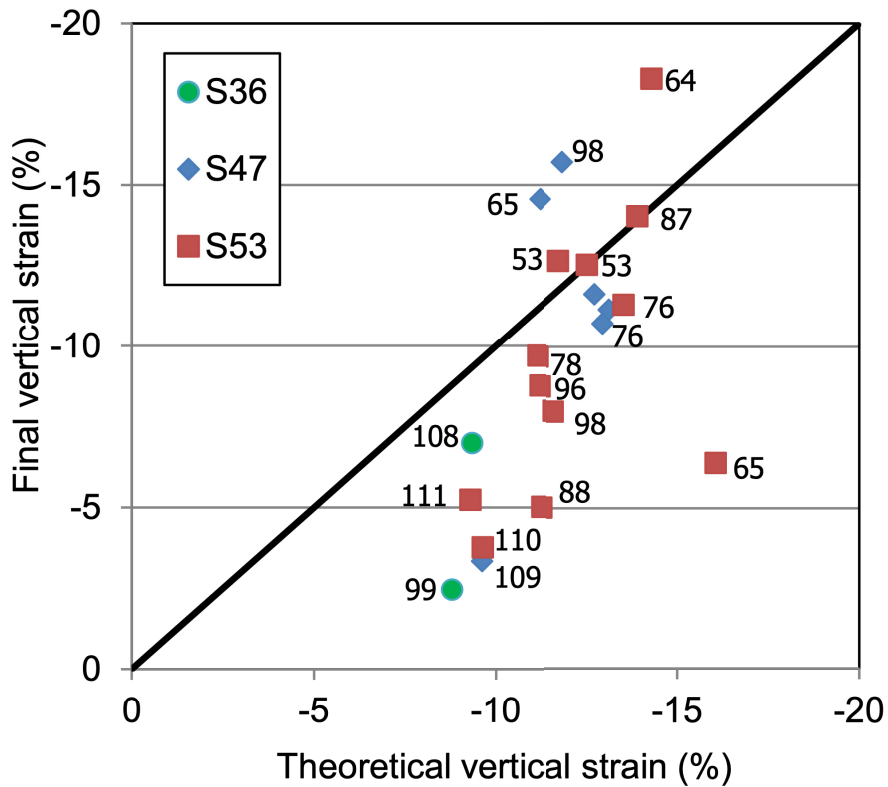


Fig. 116: Comparison between the vertical strain measured at the end of the swelling under load tests and the strain corresponding to equivalent samples of the reference bentonite tested under the same conditions obtained with Eq. 12. The distance to the gallery axis of each sample is indicated in cm

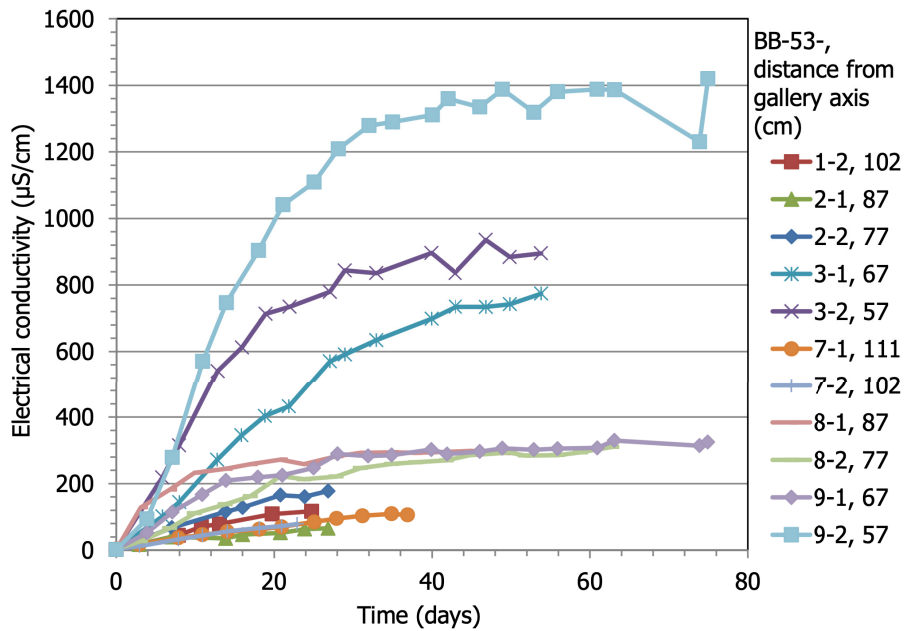


Fig. 117: Evolution of electrical conductivity of the water in the oedometer cell during swelling under 0.5 MPa stress for samples of section S53

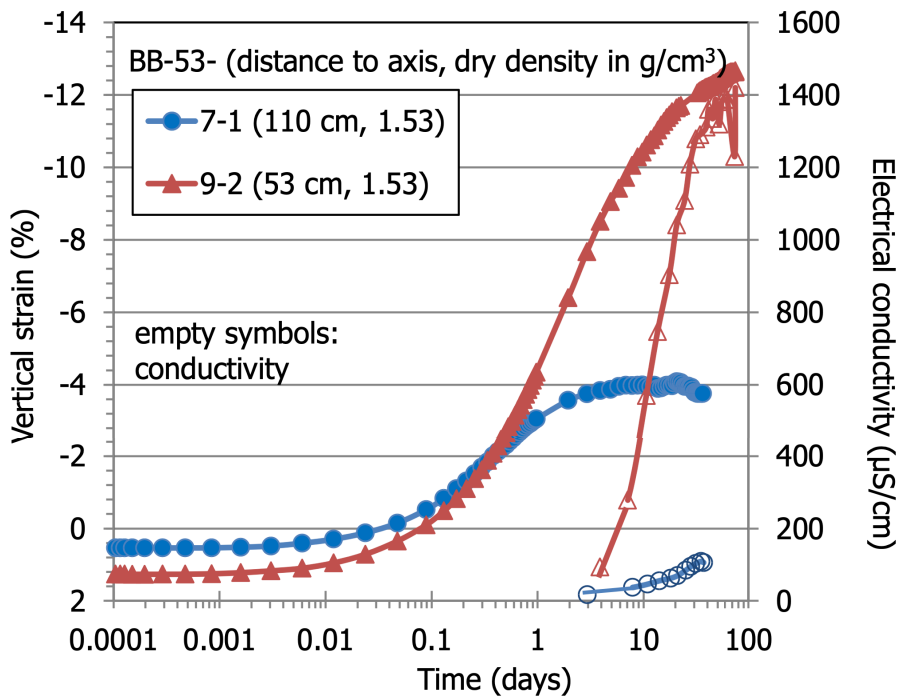


Fig. 118: Evolution of vertical strain and electrical conductivity of water in the oedometer cell during swelling under 0.5 MPa stress for two samples of section S53

The results of the tests performed in samples that had been in contact with the shotcrete plug are given in Tab. 28. Three of them were tested under 0.05 MPa and consequently they swelled

more and for a longer time, as can be seen in Fig. 119. The results obtained for samples affected by oxidation are shown in Tab. 29 and the evolution of vertical strain in Fig. 120. Two of them were drilled from a block in contact with the liner in section S36 (Fig. 121) and two others were drilled in blocks from section S59 affected by the oxidation of an extensometer (Fig. 122).

Tab. 28: Results of the swelling under load tests with samples of section S36 in contact with shotcrete

Reference	Initial $\rho_d$ (g/cm <sup>3</sup> )	Initial $w$ (%)	Initial $S_r$ (%)	Vertical $P$ (kPa)	Final $\varepsilon$ (%)	$t$ (days)	Final $\rho_d$ (g/cm <sup>3</sup> )	Final $w$ (%)	Final $S_r$ (%)	$T$ (°C)
BB-36-7-1	1.50	29.4	100	59	-15.66	96	1.30	41.5	104	22.9
BB-36-8-1	1.49	27.4	91	51	-29.13	66	1.15	51.1	103	23.4
BB-36-9-2	1.53	26.7	94	49	-25.04	64	1.22	47.3	105	23.4
BB-36-7-2	1.57	27.3	102	510	-5.42	68	1.49	32.2	106	21.7
BB-36-8-2	1.54	27.0	97	498	-5.00	68	1.47	33.9	109	21.7
BB-36-9-1	1.45	31.1	98	492	-2.35	70	1.42	36.0	108	21.7

Tab. 29: Results of the swelling under load tests with oxidised samples of sections S36 and S59

Reference	Initial $\rho_d$ (g/cm <sup>3</sup> )	Initial $w$ (%)	Initial $S_r$ (%)	Vertical $P$ (kPa)	Final $\varepsilon$ (%)	$t$ (days)	Final $\rho_d$ (g/cm <sup>3</sup> )	Final $w$ (%)	Final $S_r$ (%)	$T$ (°C)
BB-36-3-2a	1.52	28.3	99	499	-5.97	63	1.44	34.0	104	23.0
BB-36-3-2b	1.51	29.6	101	495	-9.63	37	1.37	38.3	107	23.0
BB-59-8-2	1.51	27.0	92	537	-6.23	25	1.42	33.4	100	22.4
BB-59-9-1	1.52	27.5	96	501	-11.97	42	1.36	39.3	107	22.4

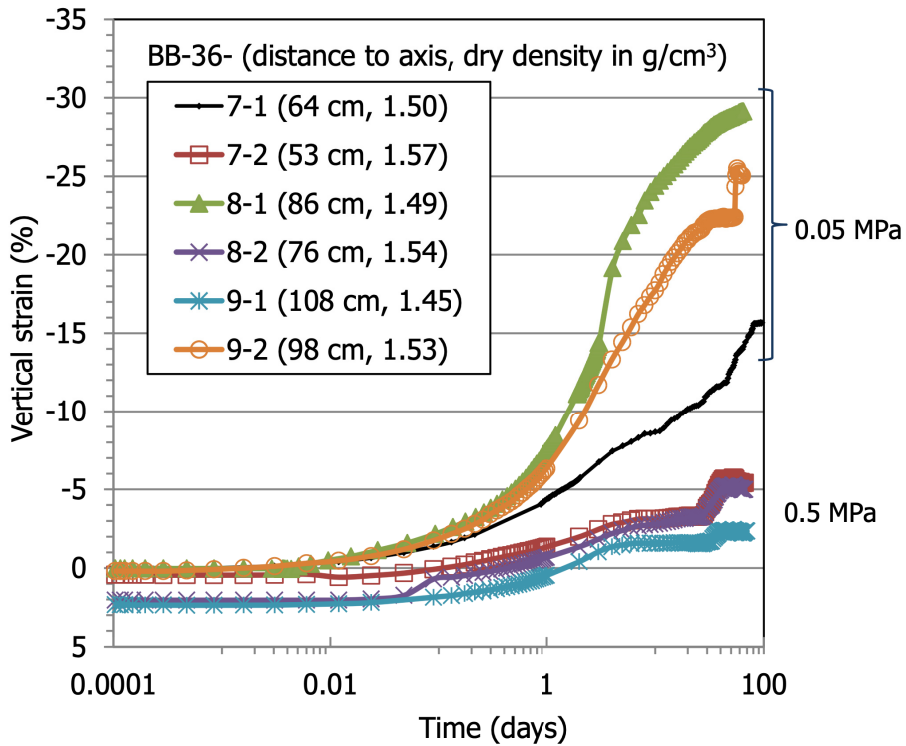


Fig. 119: Evolution of vertical strain during the swelling under 0.5 or 0.05 MPa vertical stress for samples of section S36 in contact with shotcrete

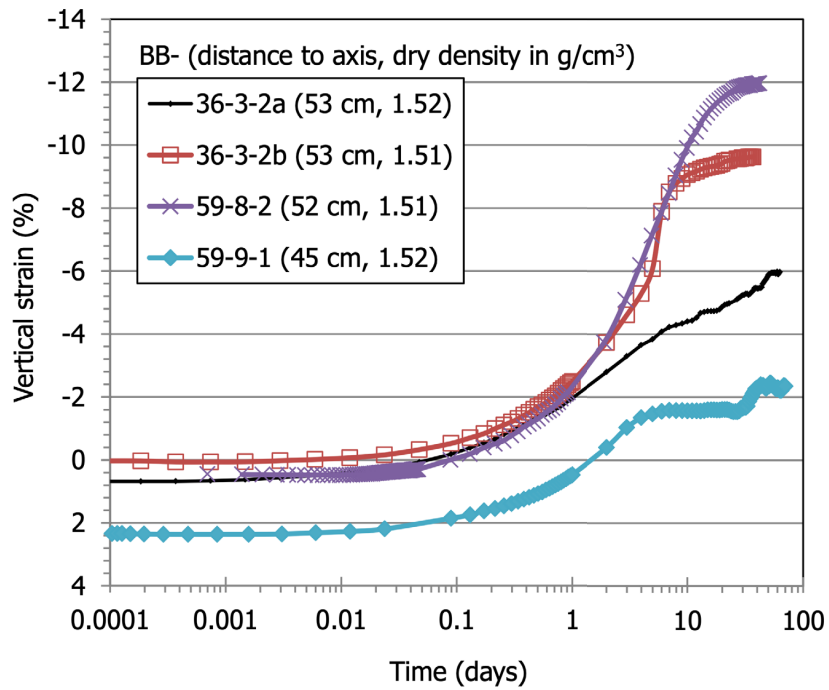


Fig. 120: Evolution of vertical strain during the swelling under 0.5 MPa vertical stress for samples drilled on oxidised bentonite



Fig. 121: Location of samples (2a and 2b) drilled close to the liner in block BB-36-3



Fig. 122: Drilling of sample BB-59-8-2 in an area affected by the oxidation of an extensometer

The final strains of the samples that were in contact with interfaces (shotcrete or metals) are shown in Fig. 123. They seem to be related to the density of the samples, since they increased towards the gallery axis, where the dry density of the samples was higher. In order to check if the swelling capacity changed with respect to that of the reference FEBEX compacted to the same dry density and water content, the final strains measured have been compared to the theoretical strains computed with Eq. 12 (Fig. 124). For the three samples tested under vertical stress 0.05 MPa, a different empirical expression was used to compute the theoretical final strain (Villar & Lloret 2008). Although the swelling strain values measured on the oxidised samples tended to be lower than the theoretical ones, the decrease was on average only around

1% swelling. Taking into account that for the rest of samples tested, i.e. those that were not affected by interfaces, the decrease in swelling capacity with respect to the theoretical one was of the same order (Fig. 116), it is considered that oxidation (samples in contact with liner, sensors) had no effect on the swelling capacity of the bentonite. However, most of the samples that were in contact with the shotcrete plug swelled less than expected for samples of the same initial dry density and water content. This could be related to the lower salinity of the samples of section S36 (Fernández et al. 2018), which was a consequence of its position in relation to the heater: there was a thermal gradient between section S36 and the front of Heater #2 (1.9 m apart) and this triggered the movement of soluble elements towards the heater, depleting them from S36 (Villar et al. 2018). For three of the samples tested, the electrical conductivity of the water in the oedometer was measured during the tests. The results are shown in Fig. 125, where it can be observed that the values were relatively low (below 300  $\mu\text{S}/\text{cm}$ ) if they are compared with those obtained in other sections for samples located at the same distance from the gallery axis (Fig. 117). The lower salinity of these samples with respect to the reference bentonite could explain their lower swelling capacity, because of the absence of osmotically-driven swelling. Hence, the swelling capacity of these samples would have been conditioned by their position with respect to the heater and not by the effect of shotcrete, which in any case was checked to be spatially very limited (Turrero & Cloet 2017). Nevertheless, it is acknowledged that the number of samples analysed was too small to draw strong conclusions.

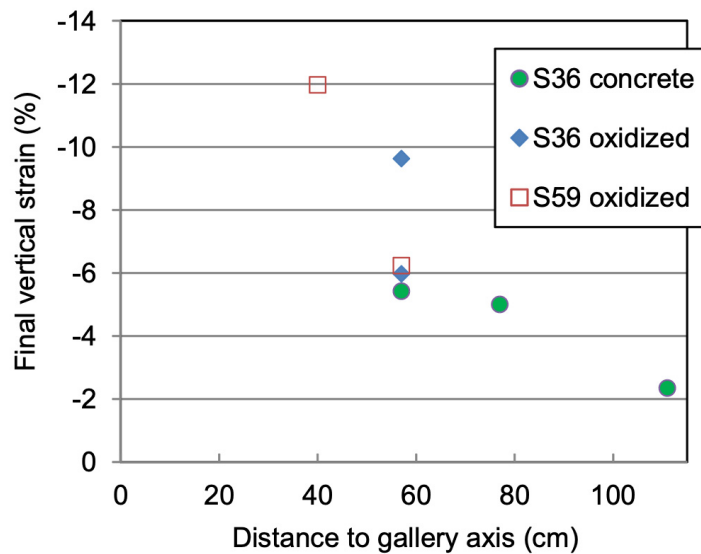


Fig. 123: Final vertical strain for samples of different sections taken close to interfaces and saturated under vertical stress 0.5 MPa

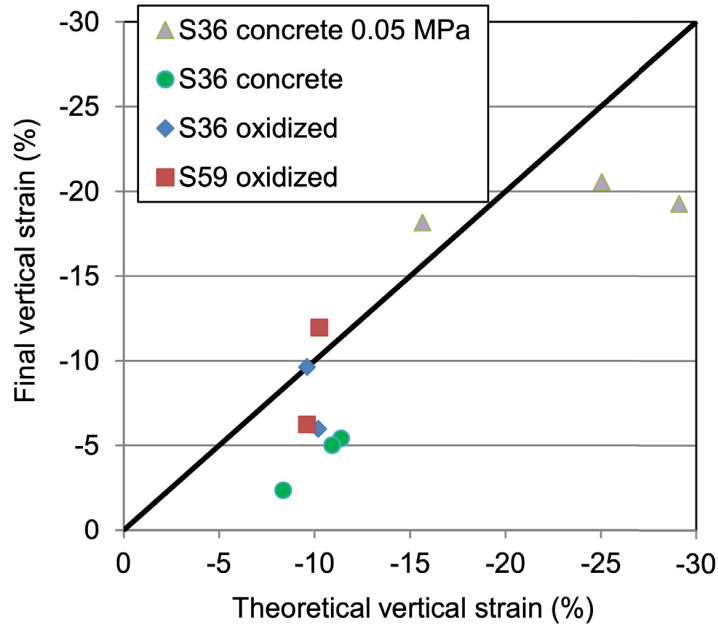


Fig. 124: Comparison between the vertical strain measured at the end of the swelling under load tests and the strain corresponding to equivalent samples of the reference bentonite tested under the same conditions. Samples taken close to interfaces.

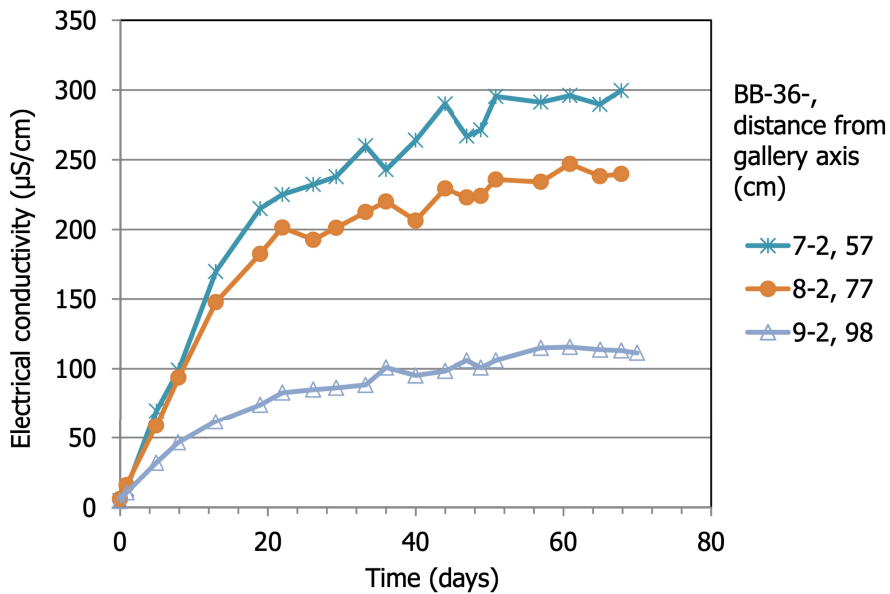


Fig. 125: Evolution of electrical conductivity of the water in the oedometer cell during the swelling stress for samples of section S36 taken in contact with the shotcrete (see Tab. 28 for characteristics of the tests)

#### 4.5.2 Swelling pressure (and hydraulic conductivity)

The swelling pressure of samples from the external ring was measured using two different experimental setups (standard oedometers and high-pressure oedometer devices) as described in subchapters 3.3.2 and 3.3.3. In two experiments the sample volume was maintained constant during saturation, but in the standard oedometers the samples were flooded whereas in the high-pressure equipment water was injected at a low pressure (15 kPa) only through the bottom surface. The initial height of the samples was between 1.2 and 1.8 cm.

These tests investigated the relationship between suction pressure of the samples, which was higher than 0 even in the saturated samples of the external ring of the barrier (see subchapter 4.2.3), and the developed swelling pressure, which theoretically should be in the same order of magnitude as the suction pressure (shown in Tab. 7 and Tab. 8).

The swelling pressure results for both procedures are shown in Tab. 30. The final values for those tests performed in the high-pressure oedometer are tentative, since on completion of the swelling pressure test the samples remained in the cell for measurement of the hydraulic conductivity, and consequently they were not assessed with the actual measurements taken upon dismantling.

Tab. 30: Results of the swelling pressure tests

Reference	Position <sup>a</sup> (cm)	Suction (MPa)	Initial $\rho_d$ (g/cm <sup>3</sup> )	Initial $w$ (%)	Initial $S_r$ (%)	$P_s$ (MPa)	Duration (days)	Final $w$ (%)	Final $\rho_d$ (g/cm <sup>3</sup> )	Final $S_r$ (%)	$T$ (°C)
BB-44-1-2 <sup>b</sup>	98	5.3	1.53	27.1	96	4.3	44	33.4	1.53	118	23.0
BB-57-1-2 <sup>b</sup>	97	5.3	1.55	27.0	98	4.3	44	28.9	1.55	105	23.0
BB-44-1-1 <sup>c</sup>	110	5.7	1.53	26.9	95	2.7	14	30.3	1.52	101	23±1
BB-44-3-1 <sup>c</sup>	65	23.0	1.62	22.0	89	3.9	47	27.6	1.61	105	23±1
BB-44-3-2 <sup>c</sup>	54	23.2	1.61	22.0	88	3.3	47	27.1	1.62	110	23±1
BB-57-1-1 <sup>c</sup>	110	5.7	1.51	27.8	96	2.1	13	34.8	1.50	118	23±1

<sup>a</sup> Distance to the gallery axis; <sup>b</sup> Tested in standard oedometers; <sup>c</sup> Tested in high-pressure equipment

In the high-pressure oedometer tests, it was possible to monitor the vertical pressure evolution as the samples saturated, which is shown in Fig. 126. The samples taken from the external ring (BB-44-1-1 and BB-57-1-1) had lower swelling pressure and it was almost completely developed after one day. However, the samples from the inner ring (BB-44-3-1 and BB-44-3-2) had higher swelling pressures, as expected from their higher dry density (see Tab. 30). It also took longer for the main part of swelling pressure to be developed in these samples (about 5 days), and there was also a significant proportion of the total swelling pressure that was developed later at a slower rate. This later swelling was probably related to the higher salinity of the samples from the inner ring, which triggered some osmotic swelling as explained in the

previous subchapter. In contrast, the swelling pressure of samples from the external ring of the barrier, where the soluble ions were leached during the 18-year operation, was probably triggered only by crystalline swelling. In fact, the electrical conductivity of the water in the cell of the two samples tested in the standard oedometers –which were taken from the external ring of the barrier– was daily measured during testing and values lower than  $160 \mu\text{S}/\text{cm}$  were found. The comparison with values measured in the swelling capacity tests described in subchapter 4.5.1 (Fig. 117) highlights again the low salinity of the samples from the external ring.

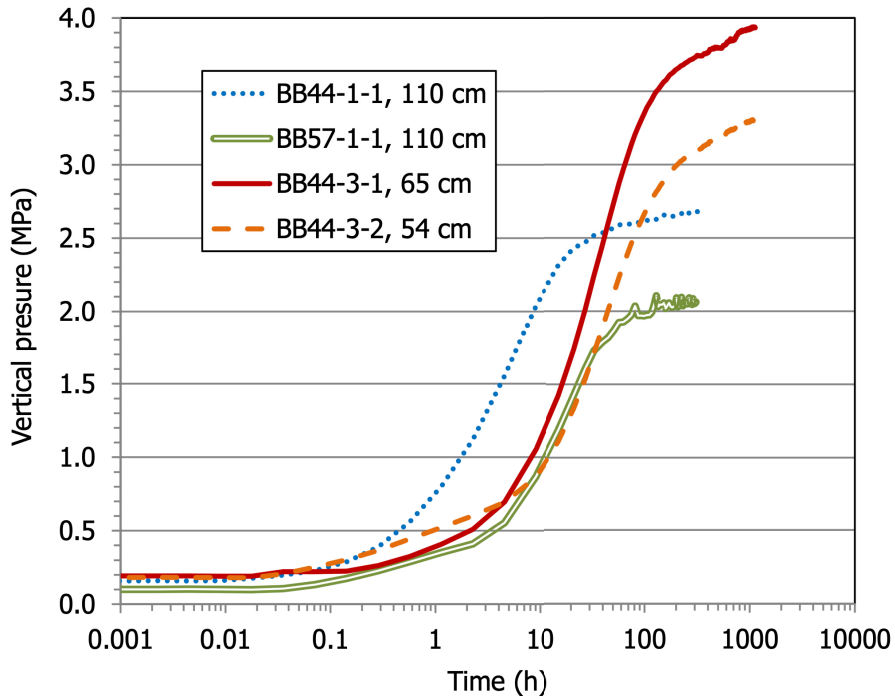


Fig. 126: Evolution of swelling pressure of samples saturated with deionised water in the high-pressure oedometer (the distance to the gallery axis is indicated in the legend)

The swelling pressure values obtained with the two methods are plotted in Fig. 127 as a function of the total suction measured at the locations in the blocks from which the specimens were trimmed. There is no clear relationship: for samples from the external ring the suction measured was around 5-6 MPa in all cases, as already mentioned in subchapter 4.2.3. However, the range of swelling pressures measured in these samples was broad (from 2 to 4.5 MPa) and seemed more related to dry density, as discussed next.

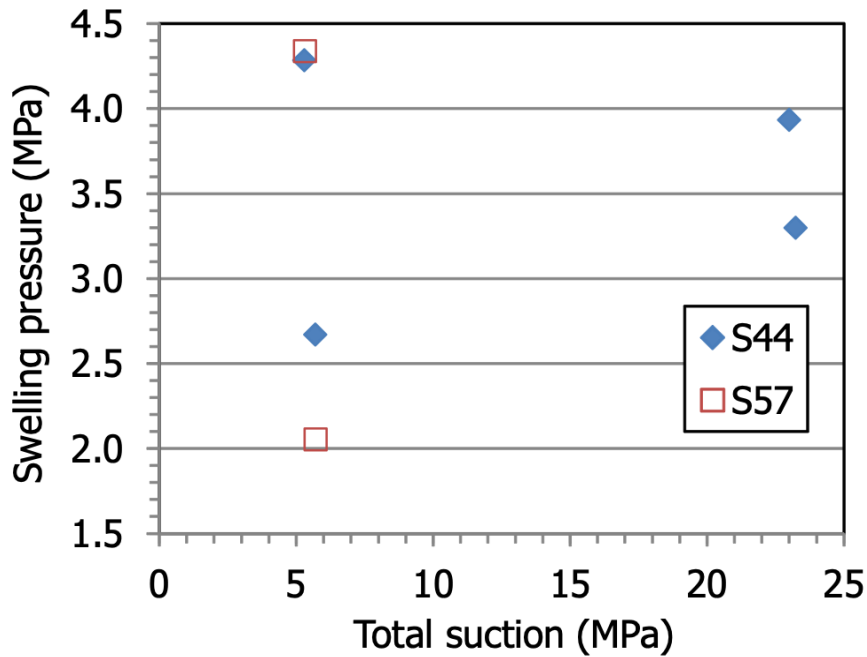


Fig. 127: Relationship between suction measured in the blocks and swelling pressure for specimens trimmed from the blocks (Tab. 30)

Fig. 128 shows the relation between swelling pressure and dry density for the samples tested. The empirical correlation between the two variables for the FEBEX reference bentonite as well as its range of variation (25%) are also shown in Figure 128. The swelling pressure ( $P_s$ , MPa) of compacted samples is exponentially related to the bentonite dry density ( $\rho_d$ , g/cm<sup>3</sup>), according to the empirical expression in Eq. 13 (Villar 2002):

$$\ln P_s = 6.77 \rho_d - 9.07 \quad \text{Eq. 13}$$

In addition to the values in Tab. 30, Fig. 128 also shows the values obtained after the hydraulic conductivity tests for the samples tested in the high-pressure oedometers. These values were obtained after the injection and backpressures applied during the permeability test had been reduced to 0.1 MPa and kept so for at least two days. The values obtained after the hydraulic conductivity tests were considerably higher, probably because in the course of the permeability test, during which water was injected into the sample from top and bottom, the water content, and consequently saturation, of the sample could have increased. This is shown in Tab. 31, with water content before and after the hydraulic conductivity tests indicated. Also, since the cell inlets on top and bottom were closed, the water pressure applied during the hydraulic conductivity testing could have dissipated incompletely and contribute to the vertical pressure measured.

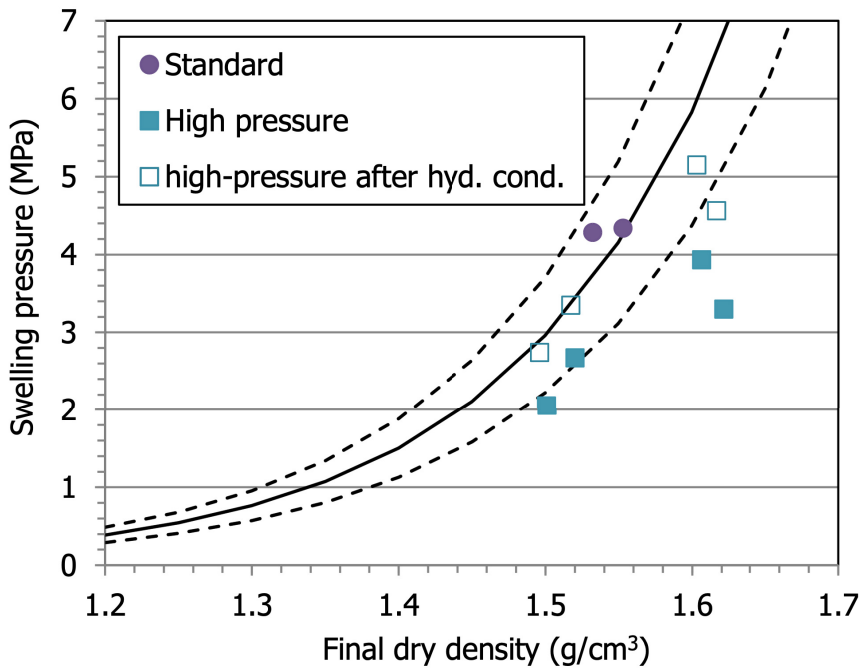


Fig. 128: Relationship between swelling pressure and dry density for the samples tested (the lines correspond to the empirical correlation for the reference bentonite in Eq. 13)

Tab. 31: Results of the hydraulic conductivity tests in the high-pressure oedometer

Reference	Position <sup>a</sup> (cm)	Initial <sup>b</sup> w (%)	k <sub>w</sub> (MPa)	Hydraulic gradient (m/m)	Duration (days)	Final w (%)	Final ρ <sub>d</sub> (g/cm³)	Final S <sub>r</sub> (%)	T (°C)
BB-44-1-1	110	26.9	5.1 · 10 <sup>-14</sup>	12000-18000	39	32.6	1.51	107	23±0
BB-44-3-1	65	22.0	1.3 · 10 <sup>-14</sup>	10000-14000	46	29.5	1.60	103	22±1
BB-44-3-2	54	22.0	1.9 · 10 <sup>-14</sup>	10000-14000	46	30.3	1.62	109	22±1
BB-57-1-1	110	27.8	6.1 · 10 <sup>-14</sup>	14000-20000	39	33.0	1.49	102	23±0

<sup>a</sup> Distance to the gallery axis; <sup>b</sup> After the swelling pressure test

Tab. 31 also shows other characteristics of the tests and the permeability values obtained after saturation (average of two or three hydraulic gradients applied, the range of which is indicated). The values obtained for the higher hydraulic gradient applied are plotted in Fig. 129 along with the values obtained in the steady-state permeameter setup (subchapter 4.4.2) and the empirical correlations for the reference FEBEX bentonite. The values obtained are consistent with those obtained in other hydraulic conductivity measurements and, as was observed before, the values

tended to be in the low range of those expected for the reference bentonite or even lower, particularly for the high dry densities. The tests also confirmed that the lower the hydraulic gradient applied, the lower the permeability value obtained. It is acknowledged that the hydraulic gradients applied could have been lower than they should (too close to the critical hydraulic gradient), particularly for the higher-density samples.

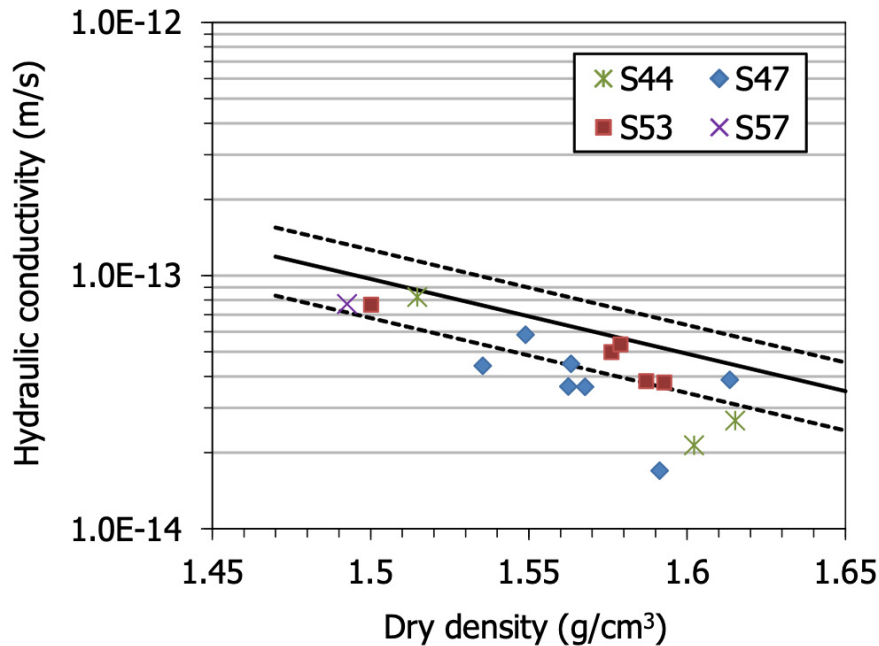


Fig. 129: Hydraulic conductivity measured as described in 4.4.2 (filled symbols) and after the swelling pressure tests (in the two cases only the values obtained for hydraulic gradients higher than 10000 m/m are included)

### 4.5.3 Volume change behaviour on loading

The compression and consolidation tests presented in this section aimed at defining the pre- and post-yield compressibility parameters and the preconsolidation stress of the bentonite recovered from the in-situ test. Compression refers to the volume change behaviour on loading starting from partially saturated conditions and with virtually no outflow of pore water, whereas consolidation involves the expulsion of pore water on loading. These data are important to complement the available information on intrinsic material parameters of FEBEX bentonite used in constitutive models. Their knowledge also allows investigating if these parameters (related mainly to volume change behaviour) underwent changes during the long term *in-situ* experiment, and thus identify alterations on the hydromechanical properties of the bentonite. The preconsolidation pressure of samples from Grimsel was determined under oedometric conditions and control of suction by performing oedometric tests. Four samples from radius E-F in section S47 and two from radius D were used (Fig. 130). The dry density ( $\rho_d$ ) and water content ( $w$ ) of adjacent fragments were initially determined and the values obtained are shown in Tab. 32 along with the suction measured in the corresponding blocks and shown in Tab. 7. The tests were performed under these suction pressures, using sulphuric acid solutions to control them. The sample was left to equilibrate at the target suction under a low vertical load. Afterwards, the sample was loaded progressively up to 32 MPa. Each loading step was

maintained until stabilisation of the deformation. The tests were performed at laboratory temperature.

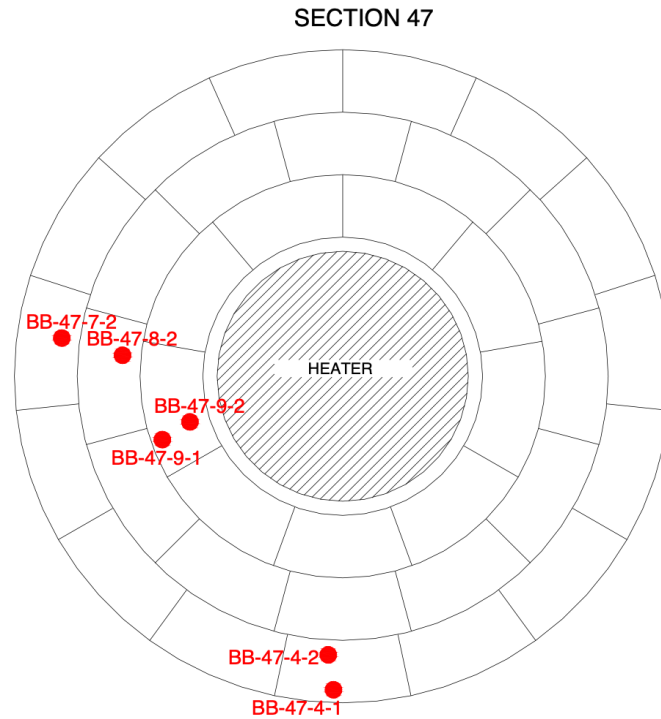


Fig. 130: Location of samples used for the oedometer tests

Tab. 32: Initial conditions of the samples used in the oedometer tests

Reference	Radius	Position <sup>1</sup> (cm)	$\rho_d$ (g/cm <sup>3</sup> )	$w$ (%)	$S_r$ (%)	Suction (MPa)
BB-47-7-2	E-F	102	1.58	26.2	100	4
BB-47-4-1	D	109	1.53	27.9	99	4
BB-47-4-2	D	98	1.56	26.9	99	2
BB-47-8-2	E-F	77	1.48	23.8	78	21
BB-47-9-1	E-F	67	1.61	20.5	82	28
BB-47-9-2	E-F	57	1.60	19.0	75	33

<sup>1</sup> Distance to gallery axis

The results obtained are shown in Tab. 33 to Tab. 38. Sample BB-47-7-2 started extruding from the oedometer ring when the vertical pressure was increased to 17 MPa (Fig. 131). At the end of the test more than half of the sample had gone out of the ring, probably because of the high initial degree of saturation of the sample. Consequently, the test was not analysed. The same happened to both samples from block BB-47-4, which started to extrude out of the ring when the vertical load was 32 MPa.

The consolidation curves of the six tests are shown in Fig. 132 to Fig. 134. The compression during the first steps, corresponding to the low stresses, was on average relatively fast, indicating that the material was still partially saturated. As loading proceeded, the samples became saturated and the consolidation rate decreased, because the material required more time to dissipate the excess pore pressure generated on loading. In fact, the degrees of saturation computed for the different steps considering the density of water as 1 g/cm<sup>3</sup> turned out to be considerably higher than 100%, since in high-density bentonite there is a predominance of interlayer-adsorbed water –whose density is higher than 1 g/cm<sup>3</sup> – over free water. After loading at 32 MPa the unloading did not cause much swelling strain.

Tab. 33: Results of the oedometer tests in sample BB-47-7-2 (external ring), performed under suction 4 MPa (test ended by clay extrusion and specimen damage)

Step	Vertical $P$ (MPa)	Final $\rho_a$ (g/cm <sup>3</sup> )	Final $e$	Duration (days)
1	2.0	1.62	0.666	7
2	5.1	1.63	0.653	22
3	11.8	1.70	0.591	26

Tab. 34: Results of the oedometer tests in sample BB-47-4-1 (external ring), performed under a suction pressure of 4 MPa

Step	Vertical $P$ (MPa)	Final $\rho_a$ (g/cm <sup>3</sup> )	Final $e$	Duration (days)
1	0.4	1.54	0.756	16
2	3.2	1.56	0.732	26
3	6.5	1.57	0.716	6
4	12.0	1.63	0.655	9
5	18.9	1.71	0.577	7
6	33.2 <sup>a</sup>	1.84	0.469	8
7	21.2	1.80	0.501	5

Step	Vertical $P$ (MPa)	Final $\rho_d$ (g/cm <sup>3</sup> )	Final $e$	Duration (days)
8	10.7	1.74	0.556	5
9	3.2	1.69	0.598	3

<sup>a</sup> Clay extrusion and specimen damage

Tab. 35: Results of the oedometer tests in sample BB-47-4-2 (external ring), performed under a suction pressure of 2 MPa

Step	Vertical $P$ (MPa)	Final $\rho_d$ (g/cm <sup>3</sup> )	Final $e$	Duration (days)
1	0.4	1.58	0.709	16
2	3.7	1.58	0.707	26
3	6.2	1.59	0.694	6
4	11.5	1.68	0.607	9
5	18.2	1.77	0.525	7
6	31.8 <sup>a</sup>	1.93	0.400	8
7	20.6	1.88	0.437	5
8	7.3	1.81	0.494	5
9	3.2	1.75	0.544	3

<sup>a</sup> Clay extrusion and specimen damage

Tab. 36: Results of the oedometer tests in sample BB-47-8-2 (middle ring), performed under a suction pressure of 21 MPa

Step	Vertical $P$ (MPa)	Final $\rho_d$ (g/cm <sup>3</sup> )	Final $e$	Duration (days)
1	2.0	1.54	0.757	7
2	5.0	1.56	0.730	22
3	11.6	1.62	0.668	26
4	18.0	1.66	0.630	45

Step	Vertical $P$ (MPa)	Final $\rho_d$ (g/cm <sup>3</sup> )	Final $e$	Duration (days)
5	32.0	1.73	0.565	39
6	20.0	1.71	0.581	1
7	10.4	1.68	0.612	12
8	5.7	1.66	0.627	14
9	2.0	1.54	0.757	7

Tab. 37: Results of the oedometer tests in sample BB-47-9-1(internal ring), performed under a suction pressure of 28 MPa

Step	Vertical $P$ (MPa)	Final $\rho_d$ (g/cm <sup>3</sup> )	Final $e$	Duration (days)
1	0.2	1.60	0.685	12
2	2.1	1.63	0.654	7
3	9.3	1.68	0.610	9
4	11.6	1.70	0.592	12
5	18.6	1.75	0.544	27
6	32.3	1.84	0.465	14
7	20.4	1.82	0.484	21
8	10.5	1.79	0.508	10
9	7.8	1.78	0.519	19
10	3.5	1.75	0.544	7

Tab. 38: Results of the oedometer tests in sample BB-47-9-2 (internal ring), performed under a suction pressure of 33 MPa

Step	Vertical $P$ (MPa)	Final $\rho_d$ (g/cm <sup>3</sup> )	Final $e$	Duration (days)
1	0.4	1.61	0.681	12
2	2.2	1.64	0.647	7

Step	Vertical $P$ (MPa)	Final $\rho_d$ (g/cm <sup>3</sup> )	Final $e$	Duration (days)
3	9.2	1.69	0.594	9
4	11.4	1.72	0.573	12
5	18.4	1.78	0.516	27
6	32.3	1.89	0.425	14
7	20.7	1.88	0.436	21
8	10.5	1.85	0.458	10
9	8.0	1.84	0.469	19
10	3.5	1.81	0.496	7



Fig. 131: Sample BB-47-7-2 extruding out of the oedometer ring after loading step at 17 MPa

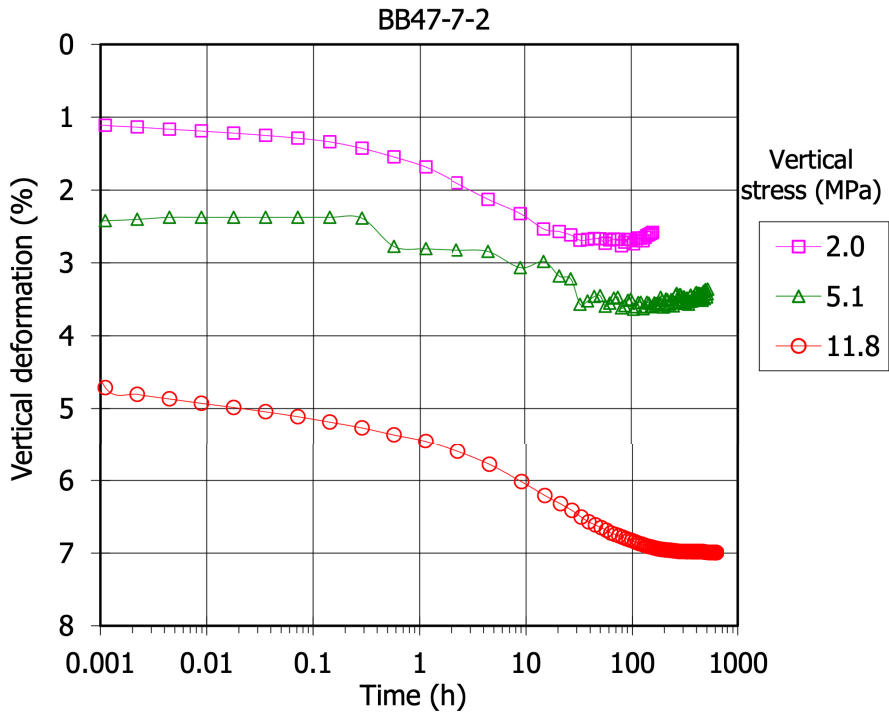


Fig. 132: Evolution of strain during the different steps of the process of loading under a suction pressure of 4 MPa for sample BB-47-7-2 (see Fig. 110 for location of sample)

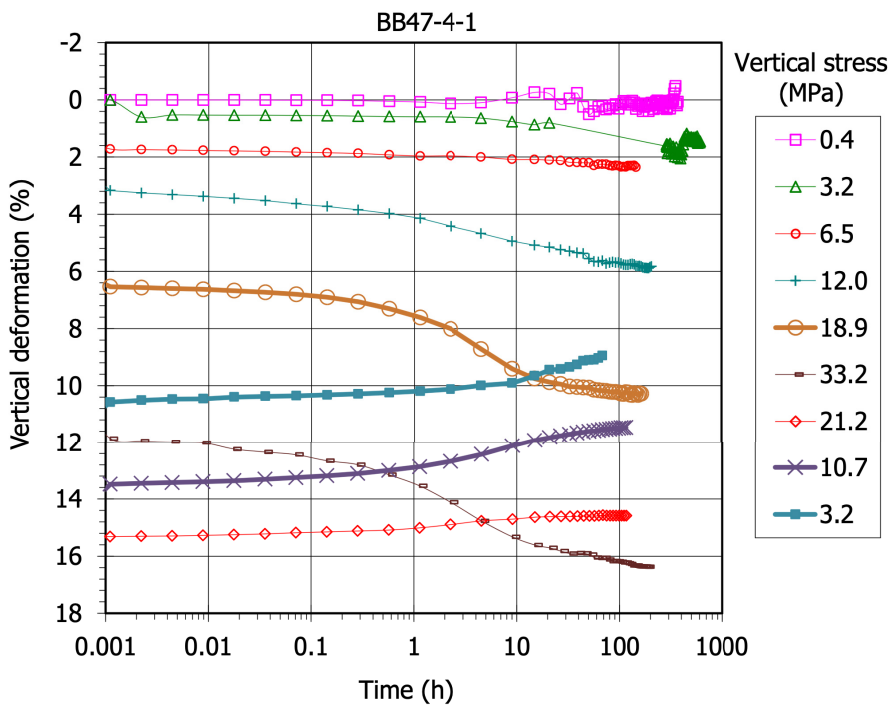


Fig. 133: Evolution of strain during the different steps of the process of loading under a suction pressure of 4 MPa for sample BB-47-4-1(see Fig. 110 for location of sample)

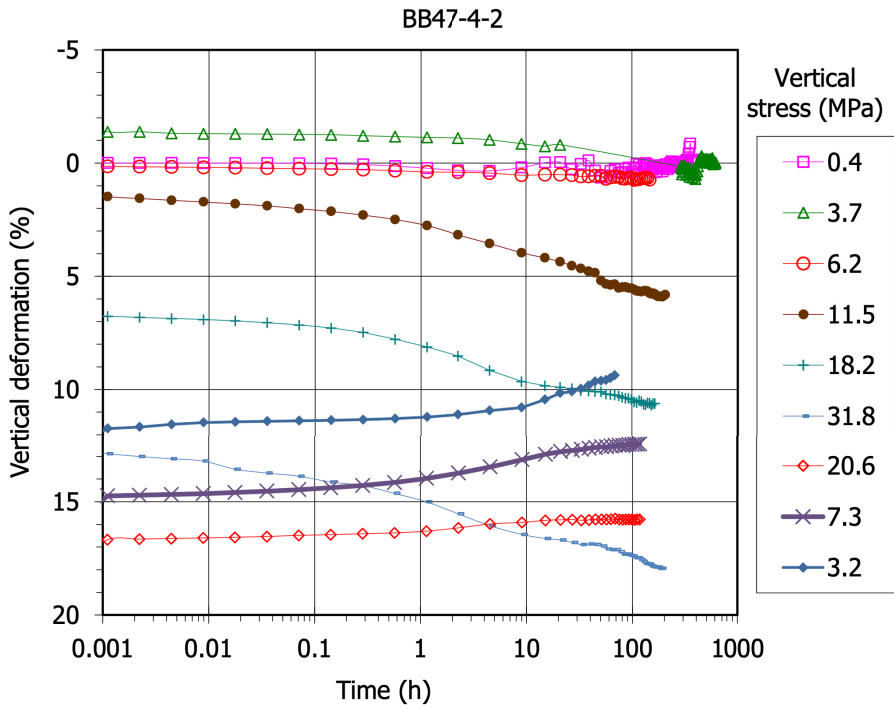


Fig. 134: Evolution of strain during the different steps of the process of loading under a suction pressure of 2 MPa for sample BB-47-4-2 (see Fig. 110 for location of sample)

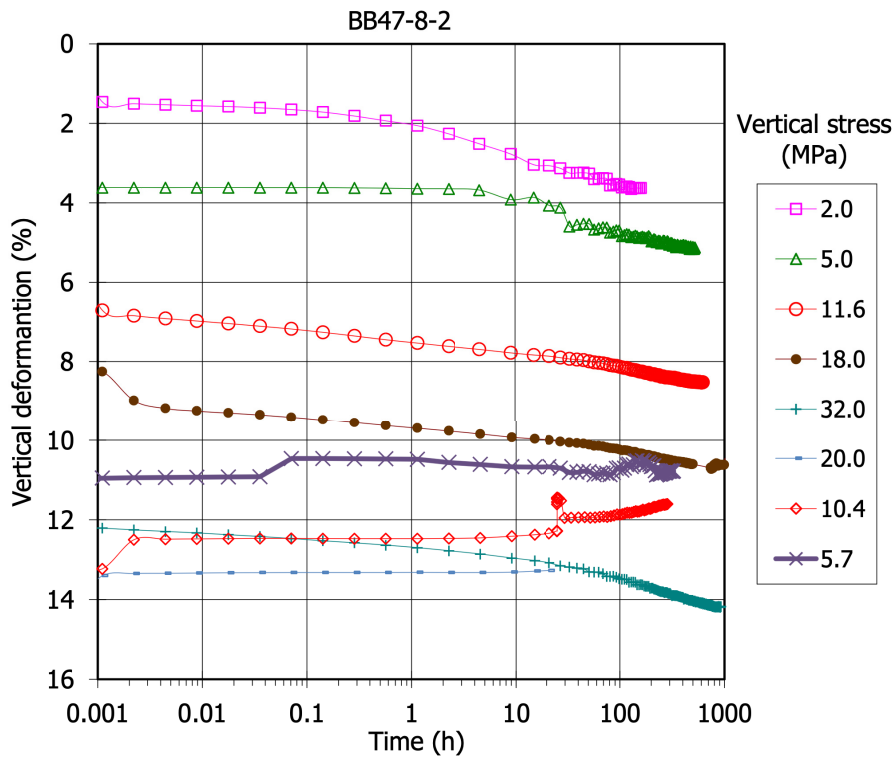


Fig. 135: Evolution of strain during the different steps of the process of loading under a suction pressure of 21 MPa for sample BB-47-8-2 (see Fig. 110 for location of sample)

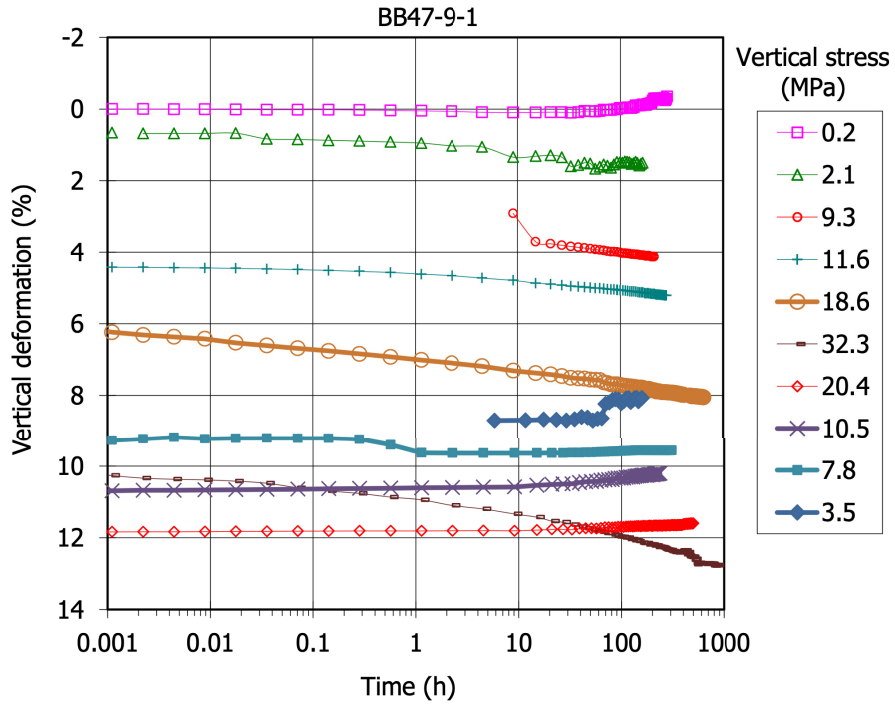


Fig. 136: Evolution of strain during the different steps of the process of loading under a suction pressure of 28 MPa for sample BB-47-9-1 (see Fig. 110 for location of sample)

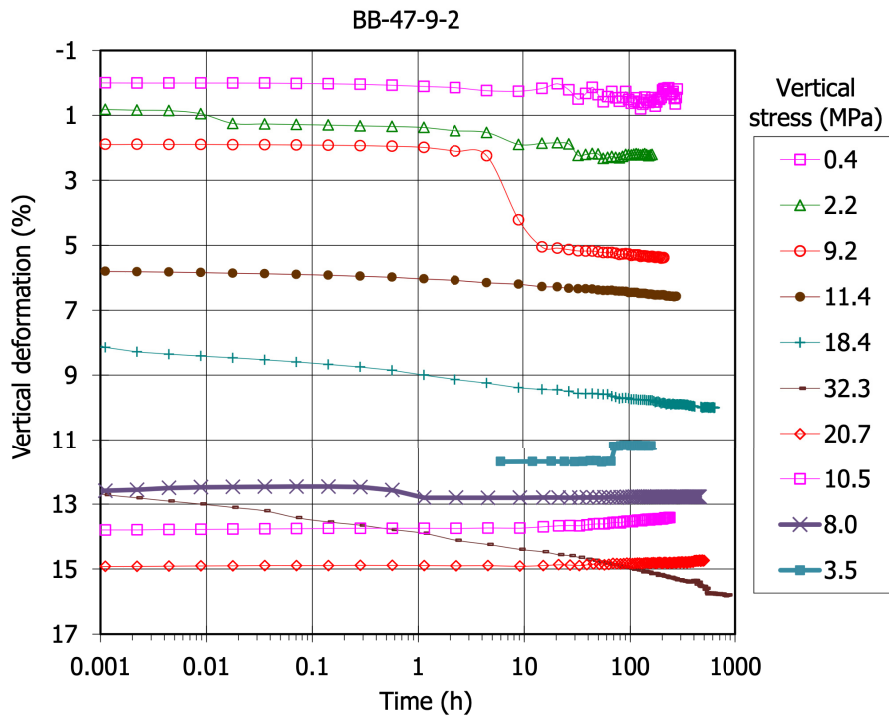


Fig. 137: Evolution of strain during the different steps of the process of loading under a suction pressure of 33 MPa for sample BB-47-9-2 (see Fig. 110 for location of sample)

The time evolution of soil deformation under saturated conditions was interpreted by back-analysis to determine the different parameters used in consolidation analysis following Terzaghi's theory (Romero et al. 2017). These parameters are:  $d_o$  (initial displacement mainly due to cell deformability),  $E'_m$  (drained constrained modulus of elasticity),  $c_v$  (coefficient of consolidation) and  $k_w$  (water permeability determined using results on  $c_v$  and  $E'_m$ ) and are shown in Annex II for each test. These coefficients were fitted only for those steps in which the computed degree of saturation indicated clearly that the sample was fully saturated despite the controlled suction condition, but even so their validity is limited, and the values obtained must be taken cautiously. Fig. 138 shows the fitted hydraulic conductivity values along with those directly measured (subchapter 3.2.2). The permeability values fitted from the oedometer tests were mostly lower than those directly measured and those expected for the reference bentonite.

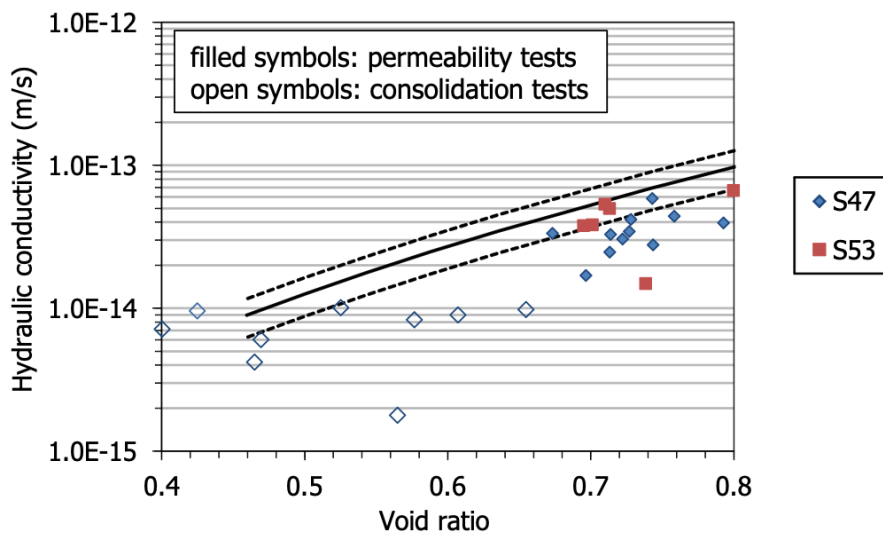


Fig. 138: Water permeability obtained by back-analysis of the oedometer tests and by direct measurement under controlled gradient (subchapter 3.2.2). The lines correspond to the empirical relation for untreated FEBEX (Eq. 10)

The oedometric curves are shown in Fig. 139. The initial void ratio was higher for the samples located farther away from the heater. The estimated values of the vertical preconsolidation stress ( $\sigma_v^*$ ) were estimated with the Casagrande method (Fig. 141 and Fig. 140) and from the cumulated work input to the soil per unit of initial volume, as described in Tavenas et al. (1979) and used in other FEBEX-DP samples by Romero et al. (2017). The values obtained with both methods are shown in Tab. 39. The second method gave higher values systematically and are considered more reliable. Lower values were found for the two samples taken from the external ring of the barrier (BB-47-4-1 and 2), i.e. those tested under lower suction. The values are plotted as a function of initial void ratio and of suction in Fig. 142, in which the values obtained in two tests performed with the untreated reference bentonite compacted to an initial dry density of  $1.7 \text{ g/cm}^3$  have also been plotted. These reference samples were prepared by applying a compaction pressure of 30 MPa to bentonite at its hygroscopic water content (14%) and they were tested under the suction pressure corresponding to these conditions (116 MPa). These two tests were intended to reproduce the initial conditions of the blocks in the barrier. However, because of the different geometry and size of the compaction moulds, the pressures applied to manufacture these blocks were higher, between 40 and 45 MPa (Fuentes-Cantillana & García-Siñeriz 1998). These compaction pressures can be assumed to approximately correspond to the

initial preconsolidation stress of the FEBEX-DP samples. Although the apparent preconsolidation pressures measured in the two reference samples tested by CIEMAT were actually lower than the compaction pressures, they were clearly higher than the apparent preconsolidation stresses measured in the retrieved samples through the oedometer tests reported in this Chapter. The decrease in the apparent preconsolidation pressure of the retrieved samples with respect to the reference samples can be explained by the volume increase experienced by the bentonite during hydration and the decrease in suction. The apparent preconsolidation pressure values of the field samples tended to be lower when the initial void ratio was higher, and the suction pressure was lower.

Tab. 39 also includes the pre-yield compressibility  $\kappa = -\Delta e / \Delta \ln \sigma_v$  for vertical stresses below 11 MPa (which is the minimum preconsolidation stress determined for the samples retrieved with the cumulated work method), as well as the post-yield compressibility  $\lambda = -\Delta e / \Delta \ln \sigma_v$ . The compressibility of the samples retrieved was higher compared to the reference sample both in the elasto-plastic and elastic zones, because of their increase in the degree of saturation and the corresponding decrease in suction (Fig. 143). The post-yield compressibility particularly increased for the samples that reached the lowest suction during barrier operation (those closest to the granite).

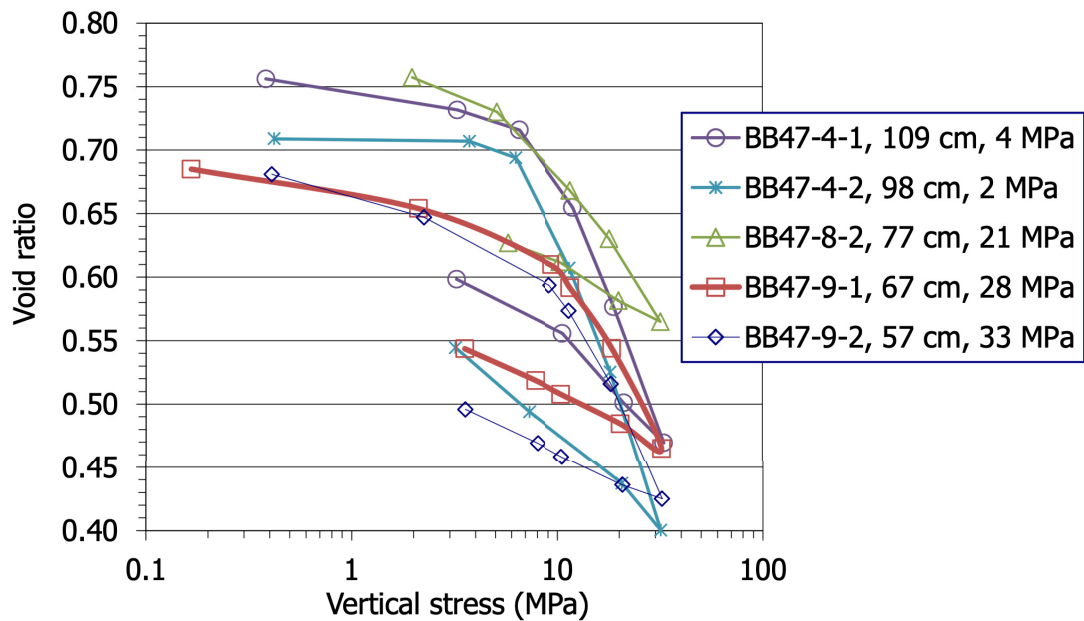


Fig. 139: Oedometric curves of the tests performed in samples from section S47 (the distance from the axis of the gallery is indicated in the legend)

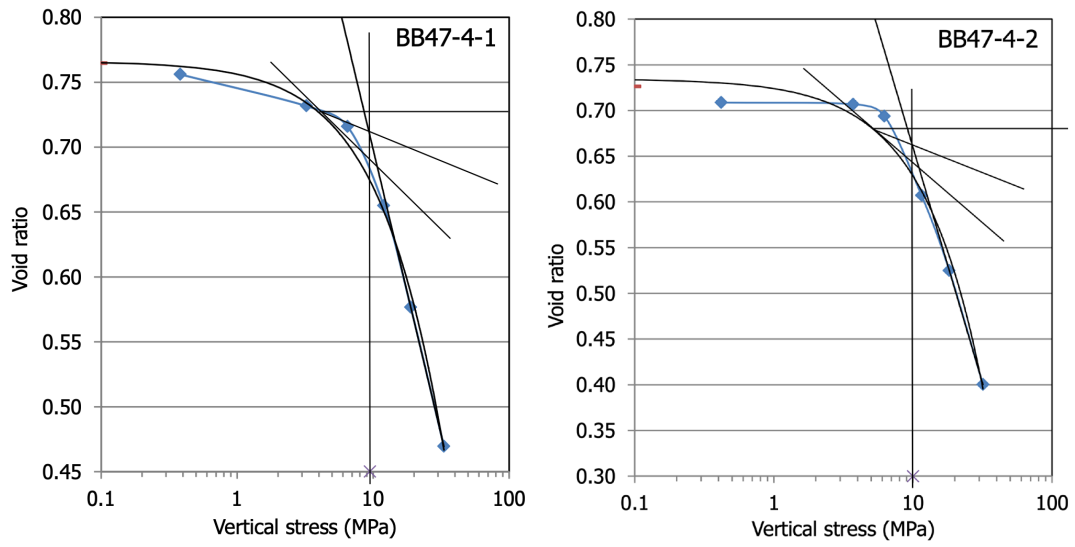


Fig. 140: Determination of the vertical preconsolidation stress of samples from radius D in section S47 using the Casagrande method

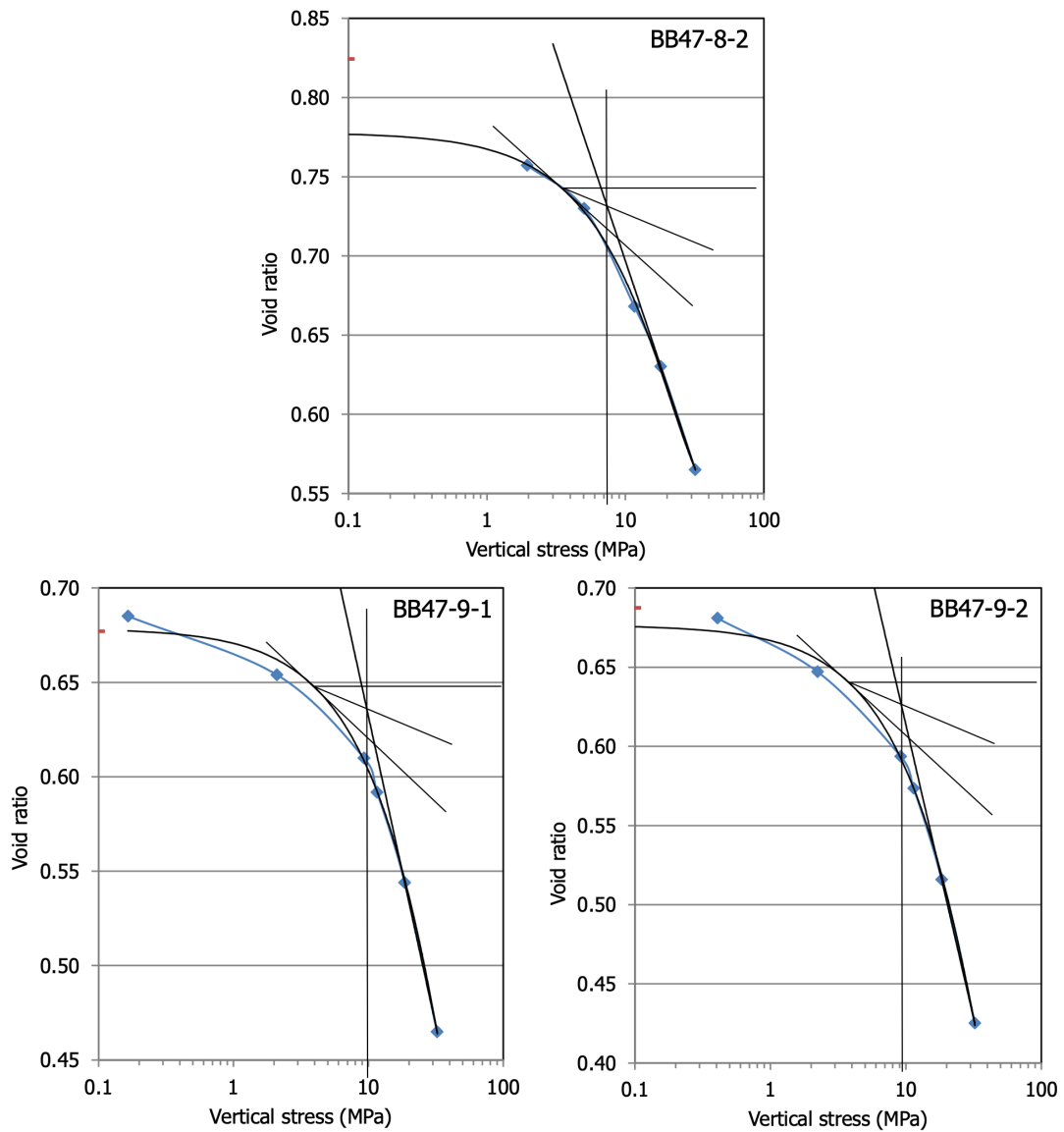


Fig. 141: Determination of the vertical preconsolidation stress of samples from radius E-F in section S47 using the Casagrande method

Tab. 39: Apparent preconsolidation stress ( $\sigma_v^*$ ), pre-yield ( $\kappa$ ) and post-yield ( $\lambda$ ) compressibility determined from the oedometer tests under constant suction for untreated and retrieved samples

Test	Distance to gallery axis (cm)	Suction (MPa)	$e_0$	$e_0^a$	$\sigma_v^{*b}$ (MPa)	$\sigma_v^{*c}$ (MPa)	$\kappa$	$\lambda$
EAP17_47	Reference	116	0.587	0.588	12.0	16.5	0.012	0.116
EAP17_47_2	Reference	116	0.579	0.579	13.0	16.0	0.009	0.099
BB-47-4-1	109	3.7	0.746	0.765	9.5	12.3	0.015	0.142
BB-47-4-2	98	1.6	0.706	0.726	10.0	12.0	0.025	0.175
BB-47-8-2	77	21	0.823	0.824	7.7	11.3	0.029	0.089
BB-47-9-1	67	28	0.679	0.677	10	13.5	0.017	0.103
BB-47-9-2	57	33	0.684	0.688	9.4	13.1	0.026	0.118

<sup>a</sup> fitted void ratio for vertical stress 0.1 MPa; <sup>b</sup> Casagrande's method; <sup>c</sup> strain energy method

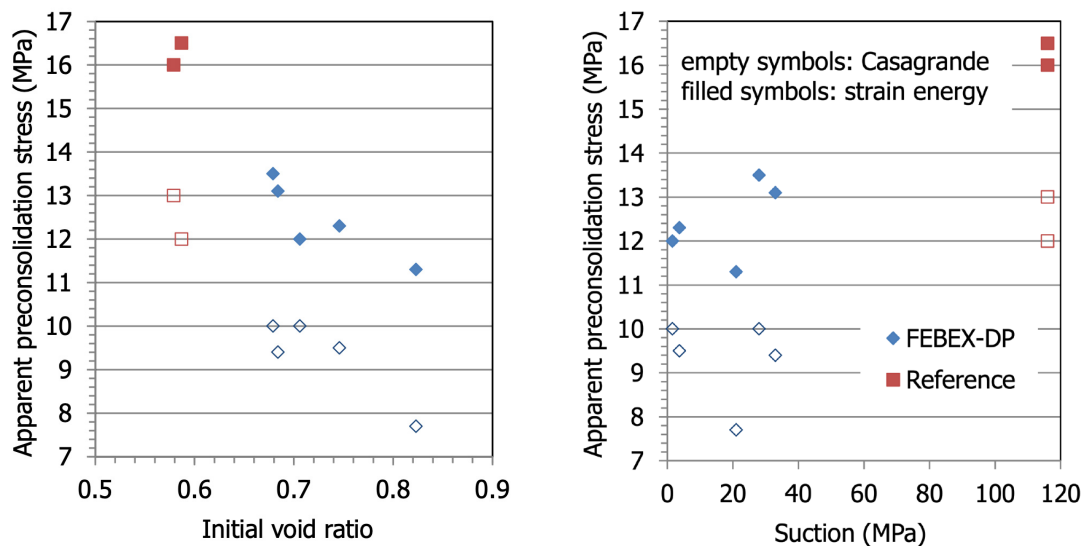


Fig. 142: Apparent preconsolidation stress estimated from the oedometer tests using two methods for samples trimmed from the blocks retrieved (FEBEX-DP) and for compacted samples of the reference bentonite



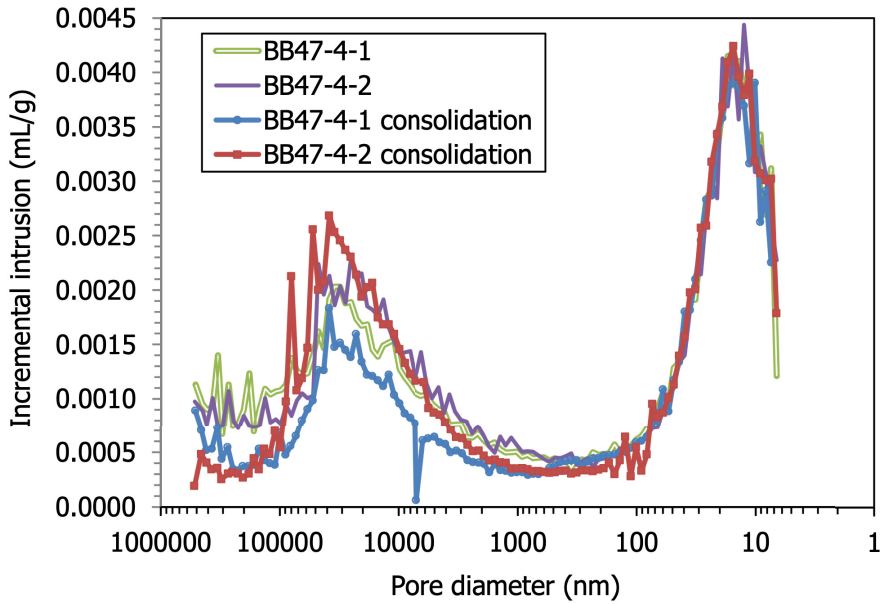


Fig. 144: Pore size distribution before and after the oedometer tests for samples of section S47

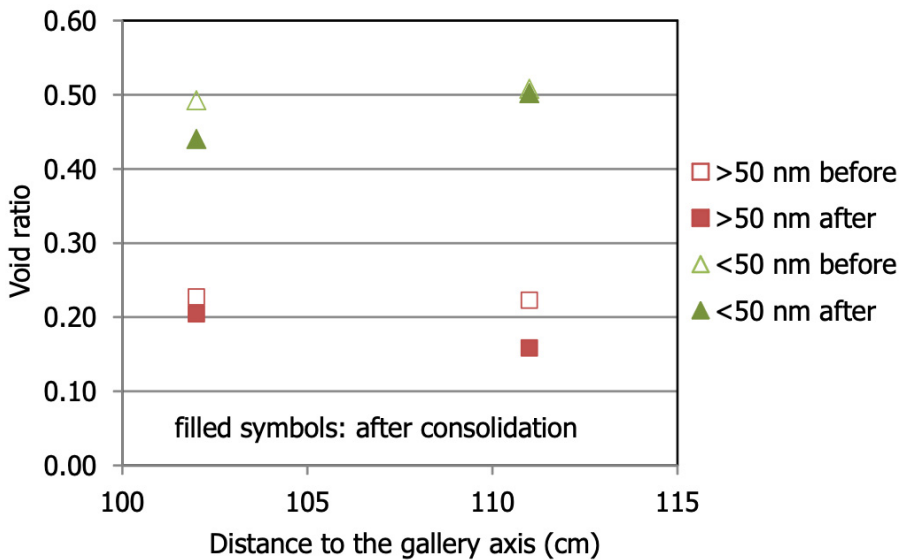


Fig. 145: Void ratio corresponding to different pore sizes before and after the oedometer tests for samples of section S47

The results from the X-ray diffraction (which was performed in four of the samples tested) are shown in Fig. 146 in terms of basal spacing of the smectite, which gives a measure of the interlayer distance. As it was explained in subchapter 4.2.4, the 001 reflection was a double one for most of the samples, and both reflections have been plotted in Figure 146, although only the main reflection was given in Tab. 40. The secondary one increased notably after the oedometer tests, which could indicate that water moved towards the interlayer during compression. This

hypothetical process seems to have been more acute as the initial water content of the samples was higher (samples closest to the granite).

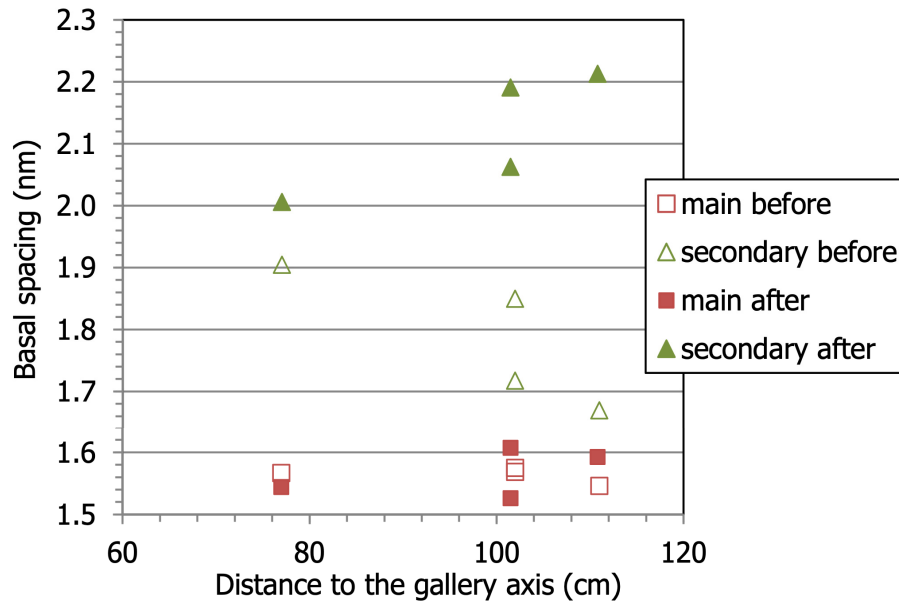


Fig. 146: Basal reflection before and after the oedometer tests for samples of section S47



## 5 Summary and discussion

The aim of the FEBEX project (Full-scale Engineered Barriers Experiment) was to study the behaviour of components in the near field of a repository in crystalline rock according to the Spanish reference concept for geological disposal of nuclear waste. As part of this project an *in-situ* test, under natural conditions and at full scale, was performed at the Grimsel Test Site (Switzerland), an underground laboratory managed by NAGRA (the Swiss agency for nuclear waste management). The heating stage of the test began in 1997. After five years of operation, half of the experiment was dismantled. The remaining part of the experiment continued running until April 2015, when the final complete dismantling of the experiment was undertaken.

At the time of dismantling, spring-summer 2015, the test had been in operation for 18 years. During this time:

- the bentonite barrier hydrated with groundwater coming from the granitic host rock,
- part of the barrier around Heater #2 –whose surface temperature was 100°C– had also been submitted to a steep thermal gradient for the entire test, and
- the bentonite slices at the front of the gallery surrounding a dummy canister that replaced Heater #1 after five years operation (i.e. after the first, partial dismantling) had been exposed to 13 years of heating. The surface temperature of the outer Heater #1 (removed in 2002) had also been set at 100°C during its operation. This means that these bentonite slices were submitted to a thermal gradient during the first five years of operation and then continued hydrating under isothermal, cooler conditions. In addition, the front bentonite slice (sampling section S36) had been in contact for the last thirteen years of operation with the shotcrete plug constructed after the partial dismantling.

Information about the temperatures measured in the bentonite during the last part of the test is given in Tab. 2.

During dismantling numerous bentonite samples, in the form of blocks, cores or irregular fragments, were taken, carefully vacuum-packed and sent to the different laboratories. These samples are called FEBEX-DP or retrieved samples. A summary of the results obtained by CIEMAT on the basic and thermo-hydro-mechanical characterisation of the bentonite retrieved during the dismantling has been presented. The laboratory sampling logs of the samples analysed at CIEMAT are compiled in Iglesias et al. (2018). The mineralogical and geochemical characteristics of the same blocks are presented in Fernández et al. (2018). Other laboratories also received bentonite samples and the results obtained by all of them (and CIEMAT) on bentonite characterisation were reported and analysed in Villar (2017). The shotcrete/bentonite interaction is dealt with in detail in NAB16-018 (Turrero & Cloet 2017). Likewise, the interaction of the bentonite with the metallic elements of the experiment (sensors, liner) is specifically analysed in NAB16-016 (Wersin & Kober 2017).

The study reported has focussed on the evaluation of the effect of temperature and hydration on the properties and characteristics of the barrier. For this reason, the analysis of results performed has taken into account the position of the samples in the barrier: if they were taken from a cool section (S36 and S59) or a section around the heater (S47 and S53) and also at which distance from the granite wall. The sample position is important because it influences the degree of hydration reached by the sample and the temperature it was submitted to during operation. Additionally, in order to assess the potential changes occurred during operation on the properties investigated, the values obtained in the FEBEX-DP samples have been compared to those of the reference, untreated FEBEX bentonite.

## 5.1 Physical state and microstructure

The laboratory determinations showed a clear radial distribution pattern: the water content decreased from the granite towards the axis of the gallery whereas the dry density increased. Hence, the void ratio of the samples (inversely related to dry density) was lower closer to the gallery axis. The physical state of section S36 was conditioned by the fact that it was a section affected by Heater #1 for five years followed by being a cool section for 13 years. There was coherence between the results obtained in the laboratory and on site (those reported in NAB16-012). This suggests that the packing and transport conditions were appropriate for maintaining the in-situ state of the blocks even several months after their retrieval. Nevertheless, when the heater was switched off and before the blocks were retrieved, the thermal gradient disappeared, and this could trigger the homogenisation of the water content inside the blocks by pure diffusion. In fact, it has been observed that during the storage of the blocks prior to sampling in the laboratory, the water content inside the blocks tended to homogenise. This water redistribution could also have resulted in some dry density changes inside the blocks.

The specific weight of the bentonite was determined in 22 FEBEX-DP samples and an average value of  $2.70 \pm 0.04 \text{ g/cm}^3$  was measured, which is the same range of variation as for the reference bentonite. The values do not seem to be related to the position of the samples in the barrier, although the highest values were found close to the heater. The specific weight tended to increase with the content in  $\text{SiO}_2$  and  $\text{Na}_2\text{O}$  and to decrease with the loss on ignition, which in turn is related to the organic matter, diverse types of water and sulphide contents. The content of Cr and Ba as trace elements was also directly correlated with the specific weight.

The water content of all the samples was above the initial condition (14%) and most were fully saturated. To analyse the hydration state from a microstructural point of view, the basal reflection ( $d_{001}$  value), which gives a measure of the interlayer distance between smectite particles, was measured by X-ray diffraction. All the values were above the initial one ( $\sim 1.48 \text{ nm}$ ). Most of them were in the range from 1.50 to 1.65 nm, which, despite the changes in the exchangeable cation complex observed, would correspond mostly to a completely developed 2-layer hydrate in transition to a 3-layer hydrate. The samples taken at less than 20 cm from the heater with water content below 25% showed lower interlayer distance. Above this water content the basal reflection tended to increase with water content, i.e. as the distance from the axis of the gallery increased. A few samples had basal reflections close to those corresponding to the 3-layer hydrate. The values obtained for the FEBEX-DP samples for water contents below 27% were similar to those measured in FEBEX bentonite samples of the same water content saturated with deionised water.

The pore size distribution was analysed with the mercury intrusion porosimetry (MIP) technique. Results indicate two major pore families in all samples: a macropore family, with sizes between 10 and 60  $\mu\text{m}$ , and a mesopore family, with sizes between 8 and 20 nm. The diameter modes of these families were higher than those of the reference material (which were  $17 \pm 3 \mu\text{m}$  and  $9 \pm 2 \text{ nm}$ , respectively), which is probably related to the overall increase in the water content of the bentonite during operation and associated swelling. The results indicate a clear increase in the proportion of void ratio corresponding to pores smaller than 50 nm (mesopores and micropores) at the end of FEBEX. More than 65% of the void ratio corresponded to this pore size at the end of FEBEX, a notable increase from the original 54%. Since the percentage of mesopores and micropores (diameter  $< 50 \text{ nm}$ ) as a whole increased after operation, whereas the average size of the mesopores (diameter 50-7 nm) increased, it is assumed that the hydration process brought about an increase in the percentage of micropores, i.e. those that cannot be intruded by mercury. This is in agreement with the average increase in

interlayer space commented in the previous paragraph and would point towards the ongoing homogenisation of the pore sizes towards a smaller size range.

The pore size distribution also changed as a function of distance to the gallery axis. It must be remembered that the total void ratio was higher for samples from the external part of the barrier compared to those in the internal part, because there was a decrease in dry density during operation towards the granite. In fact, the overall decrease in void ratio observed towards the axis of the gallery was mostly “absorbed” by the macropores, since the void ratio corresponding to pores larger than 50 nm clearly decreased towards the internal part of the barrier in cool sections. Some results indicate the presence of a new pore family of larger size in the more saturated samples taken in the external part of the barrier. Close to the heater, where the samples were dried, there was a small relative increase in the macropore void ratio.

The external specific surface area, which represents the surface of the intra-aggregate and inter-aggregate voids but not that of the interlayer space, was determined using the BET method. In the cool sections and in the external part of the barrier in sections around the heater the values obtained were higher than the reference one (55-56 m<sup>2</sup>/g), with a clear trend to increase towards the gallery wall. In fact, the external specific surface area was clearly related to the water content the samples had after dismantling, increasing for water contents above 22%.

The suction of the bentonite blocks was measured with psychrometers or capacitive sensors. Consistent with the changes in water content and dry density observed, the bentonite sections around the heater showed a clear increase of suction from the external part of the barrier towards the heater. The materials recovered from the cooler sections showed the same inwards increase, but changes were less substantial. It has to be taken into account that during operation the bentonite blocks were exposed to high temperatures, and consequently the suctions during operation could have been lower than those measured in the laboratory. By relating the suction values measured with the degree of saturation or water content of the samples in which it was measured, water retention curves (WRC) were obtained. For degrees of saturation lower than approximately 95% –corresponding to suction pressures above 10 MPa–, suction decreased linearly as the degree of saturation increased. The suction did not drop to zero when the clay approached full saturation. This remaining total suction was mainly a consequence of the block retrieval operation, which had the effect on the material of an undrained unloading: the samples retrieved suffered relaxation during dismantling and this possibly increased their suction, because of the changes in porosity. The relationship between suction pressure and water content for suctions below 7 MPa was basically dependent on dry density: the higher the dry density the lower the water content for a given suction. Although the samples analysed had been submitted during in-situ operation to wetting or wetting-after-drying paths, the measurements performed with the sensors did not show any clear hysteresis effects. The WRC curves obtained from the suction pressures measured agreed very well with the WRC of the reference bentonite obtained following different methods. This corroborates the preservation of the water adsorption capacity of the bentonite as was also confirmed by the determination of the interlayer space discussed above.

## 5.2 Thermo-hydro-mechanical properties

Most thermo-hydro-mechanical properties in bentonites depend on their dry density and water content. Changes to these properties during operation were checked on samples obtained by trimming the blocks to the appropriate size of the testing cells, while attempting to preserve their dry density and water content, i.e. the same conditions in which they were received. The results were compared to those obtained from empirical correlations resulting from previous

investigations relating these properties to the water content and dry density of the reference bentonite compacted to various dry densities and water contents.

When analysing the hydro-mechanical properties of the bentonite retrieved from the FEBEX in-situ test, the changes experienced by the bentonite during sampling on site and during preparation of specimens in the laboratory have to be kept in mind. Although the samples were preserved carefully and their water content did not seem to have changed with respect to operational period, the stresses in the barrier (which at some points were as high as 6 MPa during operation [Martínez et al. 2016]) were released on dismantling. This probably resulted in a decrease in the bentonite dry density. Additionally, the preparation of specimens to fit the testing rings required drilling and trimming, causing a decrease in the final dry density of the samples tested with respect to the bentonite blocks from which they were taken. This decrease was not of the same magnitude in all cases, since it depended on the sample conditions and on the operator. Since most THM properties depend largely on dry density, the particular values obtained for the retrieved samples are not those to be expected in the barrier during operation, because of the dry density changes just commented. Also, some boundary conditions (water availability and salinity, stress state, temperature) were different in the lab tests than during operation. The objective of the described tests, therefore, was not to determine the properties of the samples in situ during operation, but to determine changes (if any) of the FEBEX material after 18 years of operation compared to the expected response of the FEBEX reference bentonite under similar conditions.

### **5.2.1 Thermal properties**

The thermal conductivity of the bentonite blocks was measured in the laboratory and seen to increase with water content and dry density in the same way as it was observed for the reference bentonite. Hence, the thermal conductivity of the bentonite was preserved after operation. The values obtained ranged between 1.0 and 1.3 W/m·K, with no clear spatial variation (although the lowest values were measured on the blocks close to the heater), probably because the degree of saturation was very high almost everywhere in the bentonite barrier.

### **5.2.2 Hydraulic properties**

The water retention curves (WRC) of the samples retrieved were determined in wetting paths under isochoric conditions (in cells) with the vapour transfer technique. Samples taken from the driest blocks in the barrier, i.e. those closest to the heater and those from the core of the barrier in cool areas, were used, since the aim of the tests was to check the effect of prolonged and intense drying on the water retention capacity of the bentonite. The water retention capacity of bentonite is affected by temperature, hydraulic history, dry density, stress conditions and salinity, among others. Some of these factors were not reproduced in the laboratory determinations, such as the temperature (which for some of the samples tested was higher during operation), kind of available water (particularly its salinity, since in the laboratory water was taken by the samples in the vapour phase) or the precise stress conditions. For these reasons, the aim of the tests reported was not to define the WRC of the samples as when they were in the barrier during operation, but to check if the material retrieved had the same water retention capacity that could be expected for the FEBEX reference bentonite under similar conditions (temperature, dry density and hydraulic path).

The results obtained in cells have been compared and analysed together with those obtained by measuring the suctions of the blocks in the laboratory (see 5.1). This allowed to better assess the effect of dry density. For suction pressures below 20 MPa the samples of lower density had

higher water retention capacity, since their porosity was higher. For larger suctions the trend seemed to invert.

For the samples tested the initial water content also conditioned the retention capacity for suction pressures above 10 MPa. The samples closest to the heater reached higher water contents for the lowest suction pressures compared to the rest of the samples. This observation attests that the water adsorption capacity was not lost as a result of prolonged drying. The comparison of the WRCs obtained in the retrieved samples with those for the FEBEX reference bentonite compacted at similar densities shows that there were no changes in the water retention capacity during operation and that the water adsorption capacity of the bentonite under constant volume conditions is mostly conditioned by dry density.

The hydraulic conductivity was measured in samples obtained by trimming from the blocks and saturated with deionised water. The values measured do not correspond to the permeability of the bentonite at the moment the samples were retrieved, not only because the dry densities after trimming were lower, but also because the samples were saturated to perform the determinations, and permeability depends greatly on the degree of saturation. The hydraulic conductivity of the samples retrieved was in the order of  $10^{-14}$  m/s and mainly related to the dry density, with hydraulic conductivity decreasing with increasing dry density. Hence, it roughly tended to decrease towards the heater. Overall it was lower than expected for the untreated FEBEX bentonite. The fact that the hydraulic gradients applied in this work were lower than those used to determine the hydraulic conductivity of the reference bentonite, and in some cases close to the critical gradient, could have contributed to this difference. Also, the decrease of the average pore size of the bentonite during the 18-year operation discussed above and a decrease of the free/adsorbed water ratio, which was more drastic than the one expected during the relatively short period of saturation that precedes the permeability determination, could have played a part in the decrease of hydraulic conductivity that was observed, and would correspond to an actual decrease in the bentonite intrinsic permeability. This would mean that the intrinsic permeability of the barrier decreased over time during operation because of the homogenisation of pore sizes towards the smaller sizes. In any case, these tests showed that the saturated permeability of the bentonite remained very low ( $<10^{-13}$  m/s at the end-of-test densities).

The gas permeability of the FEBEX-DP samples was determined in samples taken at different positions across the barrier, some of which were taken between two blocks thereby crossing an interface. Two-phase flow seems to have been the main gas transport mechanism under testing conditions. Overall the gas permeability depended on the accessible void ratio of the samples,  $e(1-S_r)$ , in the same way as was to be expected for the FEBEX reference bentonite. Consequently, it seems no changes in gas transport properties occurred as the result of the THM conditions that the bentonite was exposed to. Since the accessible void ratio depends on water content and dry density, the gas permeability of the samples also depended on both, decreasing with the increase in water content and dry density. Thus, the gas permeability of the samples was also related to their position in the barrier, tending to be lower towards the granite, where the degree of saturation was higher, and hence, the accessible void ratio lower.

The void ratio accessible for gas flow was below 0.15 in all samples tested, given their high degree of saturation. If the correlation between accessible void ratio and gas permeability is extrapolated towards a value close to zero accessible void ratio (say 0.002), an almost completely saturated samples, the bentonite intrinsic permeability would be in the order of  $10^{-21}$  m<sup>2</sup>. This is the same order of magnitude as the intrinsic permeability for a dry density of 1.6 g/cm<sup>3</sup> measured in saturated samples with water flow.

The gas permeability of the samples also depended on their stress state, decreasing noticeably as the confining pressure increased up to 4 MPa, particularly for the wetter samples, those taken closer to the granite. As the confining stress increased, the tortuosity of the gas pathways probably increased, causing a decrease in gas permeability, and eventually the closing of pathways. In fact, beyond a confining stress of 4 MPa, no gas flow took place through any of the wetter samples, hence the breakthrough pressure for them would be higher than this value. In contrast, flow took place through the drier samples even for confining pressures as high as 9 MPa but the decrease of gas permeability with confining stress was less significant, except in samples with a vertical block interface present. This would indicate that in these less-saturated samples there was insufficient moisture to reduce or block the air-filled pore network of the specimens and minimise gas flow. The decrease in permeability that occurred during loading was not reversible, because the increase of confining pressure resulted for most samples in an irreversible increase in dry density and hence the gas permeability of the samples after unloading was lower than the initial one. Samples with an interface had higher gas permeability than samples of similar accessible void ratio with no interface, and it was necessary to apply higher confining pressures to reduce or suppress gas flow through them. Nevertheless, the samples drilled along interfaces of the external ring of the barrier had permeabilities closer to those corresponding to the same accessible void ratio in the reference bentonite, which would indicate the closing and healing of the interface, resulting in gas transport properties that are dominated by the matrix structure and not by the interface.

### 5.2.3 Mechanical properties

The swelling capacity of the samples was tested by letting the trimmed samples saturate with deionised water in oedometers under a vertical load of 0.5 MPa. The final strain of the samples closer to the heater was higher, because these samples had higher dry density and lower water content, and the swelling capacity is related to both, increasing with initial dry density and decreasing with initial water content. It also took longer for the deformation of the specimens from drier regions to stabilise. The comparison of these results with those observed for the reference bentonite tested under the same conditions showed that on average the vertical strains measured in the FEBEX-DP samples (-10%) were lower than the theoretical ones (-12%). Most samples from the external, more saturated bentonite ring swelled less than expected, whereas the samples from the inner, drier ring tended to swell as expected or more. Fernández et al. (2018) showed that the samples close to the heater had higher salinity, and this could have brought about some osmotically-driven swelling, because the soluble salts in the bentonite were dissolved by the deionised water in the oedometer cell and leached into it. This effect was remarkable once the more important crystalline swelling had been completed and did not take place in the samples from the external part of the barrier whose salinity was below that of the reference bentonite. The swelling capacity of oxidised samples (taken close to the liner or to metallic sensors) and of bentonite samples taken at the contact with the shotcrete was also analysed. It was not possible to discern any swelling capacity particularity in these samples with respect to the rest of FEBEX-DP samples analysed.

The swelling pressure on saturation with deionised water was measured in a few trimmed samples. Swelling pressure developed in a continuous way, and the major part of the swelling pressure was developed quickly. However, the swelling pressure exerted by the samples from the inner ring continued to increase at a lower rate for very long, which could be related to the osmotically-driven effect commented in the previous paragraph and triggered by their high salinity. It has not been possible to establish a relation between the swelling pressure and the suction of the samples before testing. Overall, the swelling pressure measured in samples close to saturation was related to dry density and lower than their initial suction.

The high-stress oedometric consolidation tests carried out aimed at defining under oedometric conditions the post mortem pre- and post-yield compressibility and the preconsolidation stress of the bentonite. The tests were performed at constant suction applying vertical pressures of up to 32 MPa.

The apparent preconsolidation stresses determined in the samples retrieved were between 11 and 14 MPa. The apparent preconsolidation pressure values tended to be lower as the initial void ratio was higher and the suction was lower, *i.e.* as the water content reached during operation was higher. The blocks installed in the FEBEX in-situ test at Grimsel were manufactured by applying uniaxial vertical pressures of between 40 and 45 MPa, which should correspond approximately to the preconsolidation stress of the clay. The decrease in apparent preconsolidation stress of the retrieved samples with respect to the reference one can be explained by the volume increase experienced by the bentonite during hydration and the resulting decrease in suction. The apparent preconsolidation pressure values tended to be lower as the initial void ratio was higher, and the suction pressure was lower. The pre-yield compressibility for vertical stresses below 11 MPa ( $\kappa$ ) and the post-yield compressibility ( $\lambda$ ) for higher vertical stresses were also determined. Logically, the compressibility of the samples retrieved was higher than that of the reference bentonite compacted to the initial conditions of the blocks, both in the elasto-plastic and the elastic zone, because of their higher initial void ratio. The post-yield compressibility particularly increased for the samples that reached the lowest suction pressure during barrier operation, *i.e.* those taken closest to the granite. These data are important to complement the available information on intrinsic material parameters of FEBEX bentonite used in constitutive models.

### 5.3 Conclusion

The FEBEX-DP studies just summarised confirm the good performance and stability of the bentonite barrier over a time period of 18 years. As was observed during the partial dismantling in 2002, the swelling capacity of the bentonite was after a further 13 years still able to fill all the construction gaps. It provided a continuous barrier, in which, once saturated, the interfaces between blocks did not have any role on the water content and density distribution or in the fluid transport. The thermal, hydraulic and mechanical properties analysed were consistent with the range expected for the reference bentonite, although because of the dry density gradients generated in the barrier, these properties were not homogeneous across the barrier.



## **6 Acknowledgements**

This work has been financed by the FEBEX-DP consortium (NAGRA, SKB, POSIVA, CIEMAT, KAERI) and through the Annex XLII of the ENRESA-CIEMAT framework agreement. Part of the laboratory work was performed by J. Aroz, F.J. Romero and N. Brea. The control and data acquisition systems for the gas permeability tests were developed by Dr. J.M. Barcala. The XRD measurements reported in the “Basic properties” subchapter was performed by Dr. L. Gutiérrez Nebot of the High-Level Radioactive Waste Unit of CIEMAT. The XRD measurements performed in the samples used for the water retention curve determination and the consolidation tests were performed by Dr. Xabier Alonso at the CAI Técnicas Geológicas of the Universidad Complutense de Madrid. Beatriz Carbonell was hired in the framework of the Spanish National System of Youth Guarantee in R+D 2014, with financing of the European Social Fund and the Youth Employment Initiative.



## 7 References

- ASTM D4546-03. (2003): Standard test methods for one-dimensional swell or settlement potential of cohesive soils. 7 pp.
- Bárcena, I & García-Siñeriz, J.L. (2015): FEBEX-DP (GTS) Full Dismantling Sampling Plan (in situ Experiment). Nagra Arbeitsbericht NAB 15-14. 103 pp.
- Bárcena, I., Fuentes-Cantillana, J.L. & García-Siñeriz, J.L. (2003): Dismantling of the heater 1 at the FEBEX “in situ” test. Description of operations. Publicación Técnica ENRESA 09/2003, Madrid, 134 pp.
- Bárcena, I., García-Siñeriz, J.L. & Huertas, F. (2006): FEBEX Project Final Report. Addendum sensors data report. In situ experiment. Publicación Técnica ENRESA 05-5/2006. Madrid, 157 pp.
- Brunauer, S., Emmett, P. H. & Teller, E. (1938) : Adsorption of gases in multimolecular layers. *J. Am. Chem. Soc.* 60: 309-319.
- Campos, G. & Villar, M.V. (2018) : Water retention curves of bentonite samples of the FEBEX Dismantling Project (FEBEX-DP). Informe Técnico CIEMAT 1432. Madrid, 44 pp.
- Campos, R., Castro, B. & Brea, N. (2017): FEBEX-DP: Análisis de bentonita postmortem. Caracterización petrofísica. Informe Técnico CIEMAT 1396. Madrid, 61 pp.
- Chávez-Páez, M., Van Workum, K., de Pablo, L. & de Pablo, J.J. (2001): Monte Carlo simulations of Wyoming sodium montmorillonite hydrates. *Journal of Chemical Physics* 114(3): 1405–1413.
- Cuevas, J., Villar, M.V., Martín, M., Cobeña, J.C. & Leguey, S. (2002): Thermo-hydraulic gradients on bentonite: distribution of soluble salts, microstructure and modification of the hydraulic and mechanical behaviour. *Applied Clay Science* 22 (1-2): 25-38.
- ENRESA (1995): Almacenamiento geológico profundo de residuos radiactivos de alta actividad (AGP). Diseños conceptuales genéricos. Publicación Técnica ENRESA 11/95. 105 pp. Madrid.
- ENRESA (2000): FEBEX Project. Full-scale engineered barriers experiment for a deep geological repository for high level radioactive waste in crystalline host rock. Final Report. Publicación Técnica ENRESA 1/2000, Madrid, 354 pp.
- ENRESA (2006): FEBEX Full-scale Engineered Barriers Experiment, Updated Final Report 1994-2004. Publicación Técnica ENRESA 05-0/2006, Madrid, 590 pp.
- Fernández, A.M., Sánchez-Ledesma, D.M., Melón, A., Robredo, L. M., Rey, J.J., Labajo, M., Clavero, M.A., Carretero & S., González, A.E. (2018): Thermo-hydro-geochemical behaviour of a Spanish bentonite after of the FEBEX in situ test at the Grimsel Test Site. Technical report CIEMAT/DMA/2G216/03/16. NAB16-025. Madrid, 256 pp.
- Fuentes-Cantillana, J.L. & García-Siñeriz, J.L. (1998): FEBEX. Final design and installation of the “in situ” test at Grimsel. Publicación Técnica ENRESA 12/98. Madrid, 184 pp.

- García-Siñeriz, J.L., Abós, H., Martínez, V., de la Rosa, C., Mäder, U. & Kober, F. (2016) : FEBEX-DP Dismantling of the heater 2 at the FEBEX "in situ" test. Description of operations. NAB 16-011. 92 pp.
- Gómez-Espina, R. & Villar, M.V. (2008) : Presión de hinchamiento y permeabilidad en edómetro de alta presión. Procedimiento Técnico CIEMAT PT-MA-04-01. Madrid, 19 pp.
- Gutiérrez-Nebot, L. (2016a) : Informe de caracterización de fases sólidas mediante XRD. CIEMAT, Residuos Radiactivos, Referencia 0902. Madrid, 60 pp.
- Gutiérrez-Nebot, L. (2016b) : Informe de caracterización de fases sólidas mediante XRD. CIEMAT, Residuos Radiactivos, Referencia 0911. Madrid, 18 pp.
- Gutiérrez-Rodrigo, V., Villar, M.V., Martín, P.L. & Romero, F.J. (2014): Gas transport properties of compacted bentonite. In: Khalili, N., Russell, A., Khoshghalb, A. (Eds.): *Unsaturated Soils: Research and Applications*, vol. 2: 1735-1740. Taylor & Francis Group, London. ISBN: 978-1-138-00150-3.
- Gutiérrez-Rodrigo, V., Villar, M.V., Martín, P.L., Romero, F.J. & Barcala, J.M. (2015): Gas-breakthrough pressure of FEBEX bentonite. In: Shaw, R. P. (ed.) *Gas Generation and Migration in Deep Geological Radioactive Waste Repositories*. Geological Society, London, Special Publications, 415, 47-57. First published online November 14, 2014. <http://dx.doi.org/10.1144/SP415.4>.
- Huang, W.-L., Bassett, W.A. & Wu, T.C. (1994): Dehydration and hydration of montmorillonite at elevated temperatures and pressures monitored using synchrotron radiation. *American Mineralogist* 79: 683-691.
- Iglesias, R.J., Carbonell, B. & Villar, M.V. (2018): FEBEX-DP. Postmortem analyses of bentonite performed at CIEMAT. Laboratory sampling logs. Technical Report CIEMAT/DMA/2G218/2/18. Madrid, 116 pp.
- Jacinto, A., Villar, M.V. & Ledesma, A. (2012): Influence of water density on the water-retention curve of expansive clays. *Géotechnique* 62 (8): 657-667.
- Karnland, O., Olsson, S., Dueck, A., Birgersson, M., Pedersen, K., Nilsson, S., Eriksen, T.E. & Rosborg, B. (2009): Long term test of buffer material at the Äspö Hard Rock Laboratory, LOT project. Final report on the A2 test parcel. Technical Report TR-09-29. Svensk Kärnbränslehantering AB, Stockholm, 296 pp.
- Karnland, O., Olsson, S., Sandén, T., Fälth, B., Jansson, M., Eriksen, T.E., Svärdröm, K., Rosborg, B. & Muurinen, A. (2011): Long term test of buffer material at the Äspö Hard Rock Laboratory, LOT project. Final report on the A0 test parcel. Technical Report TR-09-31, Svensk Kärnbränslehantering AB, Stockholm, 123 pp.
- Kyoto Electronics Manufacturing C. (1987): *Kemtherm QTM-D3 Quick Thermal Conductivity Meter Instruction Manual*. Tokyo, 19 pp.
- Lloret, A. & Villar, M.V. (2007): Advances on the knowledge of the thermo-hydro-mechanical behaviour of heavily compacted FEBEX bentonite. *Physics and Chemistry of the Earth Parts A/B/C* 32 (8-14): 701-715.

- Loosveldt, H., Lafhaj, Z. & Skoczylas, F. (2002): Experimental study of gas and liquid permeability of a mortar. *Cement and Concrete Research* 32: 1357–1363
- Marcial, D. (2003): Comportement hydromécanique et microstructural des matériaux de barrière ouvragée. Ph.D. Thesis. École Nationale des Ponts et Chaussées, Paris, 316 pp.
- Martínez, V., Abós, H. & García-Siñeriz, J.L. (2016): FEBEX-e: Final Sensor Data Report (FEBEX In Situ Experiment). Nagra Arbeitsbericht NAB 16-019. Madrid, 244 pp.
- Monsalvo, R., De Pablo, L. & Chávez, M.L. (2006): Hydration of Ca-Montmorillonite at basin conditions: a Monte Carlo molecular simulation. *Revista Mexicana De Ciencias Geológicas* 23(1): 84-95.
- Romero, E., Alvarado, C. Lloret, A. & Mirsalehi, S. (2017): Laboratory tests on the post mortem hydro-mechanical characterisation of FEBEX bentonite. CIMNE-UPC-GEOLAB, 84 pp.
- Scheidegger, A. E. (1974): *The Physics of Flow Through Porous Media*, 3<sup>rd</sup> ed. University of Toronto Press, Toronto.
- Shaw, R.P. (2015): The Fate of Repository Gases (FORGE) Project. In: Shaw, R. P. (ed.) *Gas Generation and Migration in Deep Geological Radioactive Waste Repositories*. Geological Society, London, Special Publications 415: 1-8.
- Sing, KSW, Everett, DH, Haul, RAW, Moscou, L, Pierotti, RA, Rouquérol, J & Siemieniowska, T. (1985): Reporting physisorption data for gas/solid systems with special reference to the determination of surface area and porosity. *Pure & Appl. Chem.* 57(4): 603-619. IUPAC.
- Skipper, N.T., Refson, K. & McConnell, J.D.C. (1991): Computer simulation of interlayer water in 2:1 clays. *Journal of Chemical Physics* 94 (11): 7434-7445.
- Sposito, G. (1992): Characterization of particle surface charge. In: Buffle J, van Leeuwen (eds.): *Environmental particles*. Chelsea, MI: Lewis Publ. p 291-314.
- Tambach, T. J., Hensen, E.J.M. & Smit, B. (2004): Molecular simulations of swelling clay minerals. *Journal of Chemical Physics B* 108: 7586-7596.
- Tavenas, F., des Rosiers, J.-P., Leroueil, S., La Rochelle, P. & Roy, M. (1979): The use of strain energy as a yield and creep criterion for lightly overconsolidated clays. *Géotechnique* 29(3): 285-303.
- Turrero M.J. & Cloet, V. (Eds.). (2017): FEBEX DP Concrete ageing and concrete-bentonite interaction studies. NAGRA NAB 16-18. 183 pp.
- Villar, M.V. (2002): Thermo-hydro-mechanical characterisation of a bentonite from Cabo de Gata. A study applied to the use of bentonite as sealing material in high level radioactive waste repositories. *Publicación Técnica ENRESA 01/2002*, Madrid, 258 pp.
- Villar, M.V. (Ed.) (2006): FEBEX Project Final report. Post-mortem bentonite analysis. *Publicación Técnica ENRESA 05-1/2006*, Madrid, 183 pp.
- Villar, M.V. (2007): Water retention of two natural compacted bentonites. *Clays and Clay Minerals* 55(3): 311-322.

- Villar, M.V. (2017): FEBEX-DP Postmortem THM/THC Analysis Report. NAB 16-017. 143 pp.
- Villar, M.V. & Lloret, A. (2001): Variation of the intrinsic permeability of expansive clay upon saturation. In: ADACHI, K., FUKUE, M.(eds.): Clay Science for Engineering. Balkema, Rotterdam. 259-266.
- Villar, M.V. & Lloret, A. (2008): Influence of dry density and water content on the swelling of a compacted bentonite. Applied Clay Science 39: 38-49.
- Villar, M.V. & Gómez-Espina, R. (2009): Report on thermo-hydro-mechanical laboratory tests performed by CIEMAT on FEBEX bentonite 2004-2008. Informes Técnicos CIEMAT 1178. Madrid, 67 pp. Agosto 2009.
- Villar, M.V., Gómez-Espina, R. & Gutiérrez-Nebot, L. (2012): Basal spacings of compacted bentonite. Applied Clay Science 65-66: 95-105.
- Villar, M.V., Gutiérrez-Rodrigo, V., Martín, P.L., Romero, F.J. & Barcala, J.M. (2013): Gas transport in bentonite. Informes Técnicos CIEMAT 1301. Madrid, 63 pp.
- Villar, M.V., Iglesias, R.J., Abós, H., Martínez, V., de la Rosa, C. & Manchón, M.A. (2016a) : FEBEX-DP onsite analyses report. NAB 16-012. 106 pp.
- Villar, M.V., Gutiérrez-Rodrigo, V., Iglesias, R.J., Campos, R. & Gutiérrez-Nebot L. (2016b) : Changes on the microstructure of compacted bentonite caused by heating and hydration. Proceedings of the 3<sup>rd</sup> European Conference on Unsaturated Soils (E-UNSAT 2016). E3S
- Villar, M.V., Carbonell, B., Martín, P.L., Gutiérrez-Álvarez, C. & Barcala, J.M. (2018): Gas permeability of bentonite samples of the FEBEX Dismantling Project (FEBEX-DP). Informe Técnico CIEMAT 1431. Madrid, 89 pp.
- Wersin, P. & Kober, F. (Eds.) (2017): FEBEX-DP. Metal corrosion and iron-bentonite interaction studies. NAB16-016. 173 pp.
- Yoshimi, Y. & Osterberg, J.O. (1963): Compression of partially saturated cohesive soils. J. Soil Mechanics and Foundations Division. ASCE 89, SM 4, 1-24.